THE RUAPEHU MAGMATIC SYSTEM: INSIGHTS FROM THE PETROLOGY AND GEOCHEMISTRY OF LAVA FLOWS

A thesis presented in partial fulfilment of the requirements for the degree of

Doctor of Philosophy

in

Earth Science

at Massey University, Palmerston North, New Zealand.

TE KUNENGA KI PŪREHUROA | MASSEY UNIVERSITY
UNIVERSITY OF NEW ZEALAND

Silvia Catalina Moreno Alfonso

2026

Whakapapa Ski Field - August 6th, 2023

“Si un volcán se apaga igual sigue siendo un volcán. Ustedes no se han apagado, siguen teniendo la fuerza de un volcán para hacer lo que quieran hacer.”

(An extinct volcano is still a volcano. You are not extinct; you still have the strength of a volcano to do whatever you want.)

Abelardo Montoya
October 10th, 2025

Abstract

Volcanoes in complex tectonic settings are natural laboratories for exploring how tectonic processes influence plumbing systems, magmatic conditions, and eruptive phases. Recent studies in tephra at the Tongariro Volcanic Centre (TgVC), New Zealand, suggest a dike-dominated plumbing system that facilitates rapid ascent of hot, anhydrous intermediate magmas. Although recent eruptions at Mount Ruapehu have been predominantly phreatic or phreatomagmatic, the processes and timescales responsible for the voluminous andesite-dacite lava flows that built its ~150 m^3 edifice over the past ~250 ka remain poorly constrained, yet critical for reconstructing the evolution of its plumbing system.

This study integrates geochemical and textural analyses, with thermodynamic modelling from samples of the Mangawhero and Whakapapa formations (<10 to 50 ka) to reconstruct the pre-eruptive magmatic conditions and transport dynamics for effusive eruptions. This provides a better understanding of differences and similarities in the magmatic conditions, timescales and rates of the plumbing system that generated effusive and explosive eruptions.

Thermobarometry, hygrometry and MELTS modelling were used to constrain the *P-T-*H_2O magmatic conditions and depths of crystallization in orthopyroxene microlites. Residence times were estimated using crystal size distribution (CSD) analyses based on 3D data, minimizing errors associated with the stereological correction of 2D datasets, in combination with a well-known growth rate. The residence times and depth of crystallization were used to determine the magma ascent rates. Magmatic processes and melt-crystal equilibrium were determined through crystal textural analysis and mapping in combination with whole rock and groundmass geochemical analyses.

The findings in this study support the hypothesis of a dike-dominated plumbing system, which facilitates the rapid transport of magma (up to 0.08 m/s), limiting crystal residence times (up to 66 days) in magma accumulation zones at variable depths within the crust (4 - 22 km). The active rifting assists the melt production through adiabatic melting, generating hot (970 - 1160 °C) and relatively undersaturated (<2.5 wt%), that maintain the trace elements patterns linked to flux-melting in arc settings. This dike-dominated plumbing system promotes crystal entrainment by ascending melts due to the reactivation of previously emplaced dikes and crystalline bodies, where crystal recycling and accumulation determine the whole-rock trend compositions.

The remarkably fast ascent rates for effusive eruptions in volcanic arc settings found at Mount Ruapehu in this study are consistent with those found in rift volcanic systems around the world, confirming the influence of the rifting processes in the magmatic activity. These results exemplify the complex tectonic interaction between an arc volcano and a rift system and indicates that variations in the shallow conduit geometry modulate gas accumulation and overpressure, ultimately influencing the eruptive style.

Acknowledgements

"다 괜찮아질 거야"
Snooze, Agust D

This thesis was possible thanks to the funding provided by the Ministry of Business, Innovation & Employment (MBIE) of New Zealand through the 2022 Endeavour Fund – Smart Ideas project "Robust volcanic eruption forecasts: leveraging magmatic speedometer into geophysical monitoring" (MAUX2202).

I thank my supervisor Georg Zellmer for accepting me as his PhD student at Massey University and giving the chance to come to such a wonderful country. His groundbreaking ideas have shaped this thesis to its current version. I am also grateful for all the collaboration opportunities that he managed to consolidate that allow me to visit Tohoku University (Japan), Academia Sinica (Taiwan) and The University of Queensland (Australia) during my PhD. Likewise, I am grateful for his enthusiasm in presenting the results of this study, pushing me to participate in three international conferences, including being a keynote speaker at IGC 2024. Thanks to Stuart Mead, my main supervisor at Massey University, who did a good job keeping in track during the last year of my PhD. Without his assistance I don't think this would have been possible. Thanks to professors Gert Lube and Gabor Kereszturi for their recommendations during my PhD confirmation that allow me to settle in the ideas towards the completion of this thesis.

To my external supervisors: Satoshi Okumura, Teresa Ubide and Geoff Kilgour. Okumura-sensei welcome me at Tohoku University. I am grateful for his support to get the funding for Synchrotron at SPring8 (Japan) analysis through proposals 2023B1698 and 2024B1705, the multiple sessions to get EPMA data and his support through the development of the manuscripts included in this thesis. 奥村先生、誠にありがとうございました。Teresa open the doors of her research group for me at The University of Queensland, giving the chance to learn about LA-ICP-MS, guiding me through the process. The meetings with her were always entertaining and productive. Gracias Teresa por ser un apoyo constante durante estos últimos meses. Geoff offer me his assistance in the moment that I needed it the most. He helped me to clarify my ideas during our zoom meeting, providing positive and very insightful feedback. Thanks for taking the time for our meetings.

I would like to thank Paul Tomascak, Michael Higgins, Dougal Jerram and three anonymous reviewers for their valuable comments and suggestions which contribute to the final versions of the manuscripts in Chapters 4 and 5.

My visit to Japan was possible thanks to the Research-Oriented Incoming Student (ROIS) Scholarship provided by JASSO and the assistance of Shinobu Okuyama at the International Joint Graduate Program in Earth and Environmental Sciences (GP-EES) at Tohoku University. Thanks to Kentaro Uesugi who manages line BL47XU at SPring-8 and Masahiro Yasutake who assisted with the FIB work and the setting up of the SR-XCT. Thanks to Masaki Kobayashi and Shifumi Watanabe who supported me in navigating life in Japan, and the analyses at SPring-8, and to Shuhei Hotta, Naoki Araya and Masanari Arao, for their support with the EPMA and SEM, and the technicians at the sample preparation lab of

Tohoku University. To all the wonderful people I meet there Natsuko, Taisei, Rikuto, Takemi, Aulia, Mujin-sensei, thank you.

To the incredible people I met at UQ: Jack, Alice, Lina, Yujin, Clint, Dani, Raiza, Igor, Sarah, Val, Julian, thanks. You have no idea how much I enjoyed your company and the little moments we shared outside the office. To Jack, Alice, Lina, Yujin and Dani, thanks for teaching me how to use other tools and answer my questions even when you were busy completing your own research.

Thanks to Yoshiyuki Iizuka and Masako Usuki, who greet me at Academia Sinica for a short visit and help me to get SEM and EPMA data. To Simon Falvard at Laboratoire Magmas et Volcans in Universit Clermont Auvergne and Akira Miyake at Kyoto University for the XCT testing that help me to define the best approach for the 3D CSD.

To all the amazing people I met in New Zealand: Nessa who travelled to Mount Ruapehu with me to find the “impossible” sample, Carlos who was my Spanish safe haven, alongside Ermanno and Steffi. Anja who solved my lab related questions. Raimundo who teach me how to use MELTS. Charline and Danny that always reply to my emails asking questions of their previous work. Dan, Sam, Jeff and Juliette, and the other PhDs at VRS, thanks. A Caro, Nat y Jess que se han convertido en un escape fuera del mundo universitario, las quiero.

To Alison and Brooke that have become my family in New Zealand for the last 3 years, thanks for making me feel at home.

A mis amigos y familia que desde la distancia me apoyan, me escuchan y me alientan. Napo, Yoha, Ligia, Dani, Paty, Leo, Ingrid, Pata, Ro, Xavi, Alex gracias!

Table of contents

List of Figures

List of Tables

List of acronyms and abbreviations

Analyses:

BS-SEM – Back scattered secondary electron microscopy

CSD – Crystal size distribution

(FE-)EPMA – (Field emission-) Electron probe micro analysis

LA-ICP-MS – Laser ablation inductively coupled plasma mass spectrometry

LOI – Loss on ignition

SR-XCT – Synchrotron radiation X-ray computational tomography

XRF – X-ray fluorescence

Mineral phases:

Aug – Augite

Cpx – Clinopyroxene

Mag – Magnetite (Fe-oxides)

Opx – Orthopyroxene

Pgt – Pigeonite

Pl – Plagioclase

Composition:

An – Anorthite number

En – Enstatite number

Wo – Wollastonite number

HREE – Heavy rare earth elements

LREE – Light rare earth elements

REE – Rare earth elements

Location:

TgVC – Tongariro Volcanic Centre

TVZ – Taupō Volcanic Zone

Age:

BP – Before Present

ka – Kilo anni

Myr(s) – Million year(s)

yr(s) – year(s)

Crystal parameters:

G – growth rate (m/s)

n – population density

S – Short axis

I – Intermediate axis

L – Long axis

Aspect ratios in Chapter 4 – determination method:

2Dc – CSDSlice

2Ds(c) – ShapeCalc

3Da – 3D average

Magmatic conditions and timescales:

P – Pressure (MPa)

τ – Residence times (days)

T – temperature (°C)

ν – Ascent rates (m/s)

Z – depth (km)

Chapter 1 Introduction

Geochemical and petrographic methods have been applied to characterise the magmatic plumbing systems and understand the processes and evolution of volcanoes through time, as well as being a key tool in monitoring volcanoes (e.g., Aiuppa et al., 2025; Wibowo et al., 2022). Textural analyses (e.g., Lormand et al., 2021; Schipper et al., 2013; Vona et al., 2020), crystal size distributions (e.g., Giuliani et al., 2020; Okumura et al., 2022) and crystallization modelling (e.g., Brookfield et al., 2023; Rooyakkers et al., 2021; Rout et al., 2021) are among the commonly used methods to infer timescales of magmatic processes and its changes through time.

Crystals are an important element to infer magmatic processes, such as magma mixing/mingling (e.g., Shane et al., 2019), degassing and/or cooling (e.g., Brugger & Hammer, 2010a; Mollo & Hammer, 2017). These crystals can also be used to provide constraints on crystal residence times (e.g., Luo et al., 2025b; Polo-Sánchez et al., 2023), magma ascent rates (e.g., Ubide et al., 2019; Wong et al., 2025), and the pre-eruptive conditions of the volcanoes (e.g., Costa et al., 2013; Degruyter et al., 2016; Phillips & Till, 2021; Ruprecht & Bachmann, 2010). While crystal residence times and magma ascent rates have been determined for tephra samples (e.g., Kilgour et al., 2014; Lormand et al., 2020), there is little information regarding the timescales of effusive eruptions responsible of building the large edifice of Mount Ruapehu. An important question is whether the plumbing system responsible for tephra generation share similarities with the system that produced voluminous lava flows at Mount Ruapehu. To identify the characteristics of the magmatic plumbing system responsible for the generation of the lava flows, and the pre- and syn-eruptive process that occurred in Mount Ruapehu, petrographic and micro-geochemical

analyses were performed in lava samples. The information obtained in this study provides valuable insights for the ultimate construction of a more comprehensive picture of the processes and timescales at the onset of effusive eruptions at Mount Ruapehu, complementing previous data obtained for explosive eruptions by Lormand (2020).

1.1 Research aims and objectives

The main aim of this study is to determine the processes that occurred during magma ascent in effusive eruptions at Mount Ruapehu, and to constrain their timescales through petrological and geochemical analyses. To achieve this, the following research questions were explored:

- Crystal residence times and rates of magma ascent for the lava flow: How did the magma ascend, and how long did it take?
- Origin of crystal cargo: Was it grown from the melt? Was it picked up?
- Plumbing system: Did the magma ascend through a complex plumbing network with storage reservoirs, or through a tectonically induced fracture? What transcrustal processes occurred?
- Lava versus tephra: How different are the timescales for effusive and explosive eruptions? How different is the plumbing system that generated the effusive eruptions compared to the one that generated the explosive eruptions?

These questions are addresses through the following specific objectives:

1. **Determine the influence of the aspect ratios used in 2D-CSD slope calculations against 3D-CSD slopes.**

Crystal size distributions (CSD) are used to infer processes occurring in the plumbing system, such as crystal residence times (Armienti et al., 1994; Cashman, 2020; Lormand et al., 2020). The crystal residence times are determined using the CSD slopes in combination with a known growth rate (Marsh, 1988, 1998). Traditionally, CSDs are determine through the outlining of crystals in 2D images (Higgins, 2000), which is not representative of the natural tridimensionality of the particles (Morgan & Jerram, 2006), requiring the measurement of a large number of crystals in order to obtain reliable results (Higgins, 2000; Mock & Jerram, 2005; Morgan & Jerram, 2006). It is more advisable to use 3D true measurements to determine the CSD if the mineral phase analysed has a high contrast (i.e., can be distinguished from other phases based on pixel values) and small crystal sizes (e.g., Gualda, 2006; Jerram et al., 2009; Okumura et al., 2022).

3D measurements avoid statistical analyses and stereological corrections to transform 2D data into true 3D using as low as ~200 crystals per sample (Mock & Jerram, 2005). The lava samples from Mount Ruapehu have small microlite crystals (<30 μm in length) and an abundance of a high contrast mineral (~20% orthopyroxene) that makes them a good candidate to test the differences between slopes calculated using 2D and 3D distributions. To determine the influence of the statistical determination of the crystal shapes on the slope determination, and consequently on the residence time, this study compares CSD slopes obtained through the analysis of both 2D and 3D data in pyroxenes.

2. **Estimate the timescales and rates of magma ascent at the onset of the effusive eruptions.**

Magma residence times and ascent rates are two of the most valuable parameters to constrain in a volcanic plumbing system towards the understanding of the volcanic processes at the onset of an eruption (Costa et al., 2020; Stix, 2018). While residence times provide

information regarding the lapse of time between injection and magma discharge (e.g., 0.4 to 9 yrs - Morgan et al., 2004; 100 to 450 yrs - Zellmer et al., 1999). The ascent rates indicate the speed of magma ascent through the volcanic conduit to the vent (e.g., 0.0001 to 0.35 m/s - Cassidy et al., 2015; ~ 0.5 m/s - Castro & Dingwell, 2009).

Crystal residence times, determined using 3D-CSD slopes from objective 1 in combination with a growth rate range for pyroxene from experimental data in Shea & Hammer (2013), and a reference growth rate for orthopyroxene from the Mangatawai Formation (Lormand et al., 2020; Zellmer et al., 2016a, 2018). The ascent rates are inferred from the residence times obtained with CSD and the depth of crystallization found through hygrothermobarometry.

3. **Compare the estimated magma ascent rates from lavas to those previously obtained from Holocene tephras.**

Previous research on tephra deposits from the last 10 ka related to the Tongariro volcanic centre (TgVC) indicates magma ascent rates of 0.03 – 0.09 m/s, where the magma crosses the upper crust in 2 to 4 days through dikes controlled by the regional tectonic setting (Lormand et al., 2020). Results obtained from lava samples of Mount Ruapehu in this study are compared to those of the tephras of the TgVC, to determine what processes influence the eruptive styles, as well as to expand the knowledge about effusive eruptions at Mount Ruapehu.

4. **Identify the origin of the crystal cargo through qualitative petrographic characterization.**

The origin of the crystal cargo has been attributed to degassing and/or cooling crystallization from the melt during ascent (Crabtree & Lange, 2011; Hammer et al., 1999; Johnson et al., 2008), crystallization in melt reservoirs (mush zones) that feed the eruption (Hobden et al., 1999; Johnson et al., 2008; Kuritani et al., 2005), and crystal uptake by aphyric melts from

previously emplaced intrusive bodies (Zellmer et al., 2013; Zellmer et al., 2016b), among other hypotheses.

To determine the origin of the crystal cargo in the Mount Ruapehu lavas, imaging of the petrography and elemental mapping analyses of minerals were used to reconstruct the origin and growth histories of the crystals based on their textural and chemical characteristics (i.e., major and trace element compositions) and their equilibrium with the melts.

5. **Infer the magmatic processes occurring in the plumbing system.**

The andesite generation in Mount Ruapehu has been described as the product of multiple events of magma mixing between stalled felsic magmas within the crust and hot mafic injections, where additional crystal fractionation and crustal contamination occur at variable levels, in a dynamic multi-level chamber system (e.g., Conway et al., 2018; Gamble et al., 1999; Kilgour et al., 2013; Price et al., 2005; Price et al., 2012; Waight et al., 1999; Waight et al., 2017).

To establish insights into magma recharge and intrusive processes, crystal texture identification and mapping were used. Additionally, analysis of the groundmass compositions to establish differences in fractionation and assimilation between the carrier melts, and the combination of thermobarometry, hygrometry, and thermodynamic crystallization modelling constrained the crystallization *P-T-*H_2O-composition conditions of the magmas at the onset of eruption.

1.2 Thesis Outline

This thesis is divided into eight chapters, organised as a thesis with publications. Chapter 1 offers an introduction to the objectives and aims of the study. Chapter 2 provides the literature review, including the notions about plumbing systems in arc volcanoes and rift

zones and how crystal cargo is related to them, as well as the geological background of Mount Ruapehu. Chapter 3 is focused on the methods used to attain the results.

Chapters 4 – 6 are presented as publications in review. Chapter 4 corresponds to the paper titled: *The influence of the aspect ratio in the determination of CSD slopes: comparing 2D versus 3D.* This paper was submitted to *American Mineralogist* and includes a comparison of CSD slopes obtained from 2D and 3D distributions, focusing on the differences in the crystal shape determination from the statistical treatment of 2D data, compared to those obtained from 3D true measurements.

Chapter 5 is the paper titled: *Short crystal residence times and fast magma ascent prior to effusive eruptions at Mount Ruapehu, New Zealand.* This paper was submitted for publication at the *Journal of Petrology* and includes the hygrothermobarometry, residence times and magma ascent rates calculations for the lava samples, comparing those to the tephra.

Chapter 6 corresponds to the paper titled: *Melt evolution and crystal cargo uptake in a dike-dominated plumbing system at Mount Ruapehu, New Zealand.* This paper will be submitted to *Contributions to Mineralogy and Petrology* and compares the textural and geochemical data obtained from the crystal cargo with the geochemical data from the whole rock and groundmasses, providing a framework towards the construction of a more comprehensive model of the plumbing system of Mount Ruapehu that produces effusive and explosive eruptions.

Chapter 7 summarises and synthesises the findings of this study, providing a comprehensive analysis of the results in the context of the unique tectonic setting in which Mount Ruapehu is located. Finally, Chapter 8 presents the conclusions and outlook of the study, including the future work opportunities. Additionally, the datasets used in the study are included in the appendices and electronic repositories.

Chapter 2 Literature Review

2.1 Volcanoes and their plumbing systems

2.1.1 Arc magmatism affected by rifting processes

Magmatism in subduction zones occurs through melting of the mantle wedge, and it is characterised by the occurrence of volcanic arcs located above the melt production zone (LaFemina, 2015). In convergent margins, the magmatism is controlled by the relative motion of the plates and the subduction angle, which deforms the overriding plate, generating fault systems along the plate boundary adjacent to or within the volcanic arcs (Aswini et al., 2024; Gazel et al., 2021; Lupi et al., 2022). These fault systems may lead to intra-arc rifting, as in the case of the Taupō Volcanic Zone (TVZ) (Villamor & Berryman, 2006a; Villamor et al., 2017).

The rifting in volcanic arcs is controlled by external factors such as the dynamics of the subduction, which control the extension rate (i.e., plate motions and slab-pull force) and the thermal and rheological structure of the overriding plate, which not only promotes the initiation of the extension but evolves over time, modifying the rifting style from wide to narrow and the location of the main volcanic arc (Balázs et al., 2022; Corradino et al., 2022; Erdős et al., 2022; Gomes et al., 2025). Here, intra-arc rifting is interpreted as the pre-stage of back-arc rifting due to melt-induced weakening in combination with slab rollback that generates arc splitting (Corradino et al., 2022). Nonetheless, although arc rifting is not unusual in subduction settings (Arai, 2021; Hilbert et al., 2024; Luo et al., 2025b), their study is scarce compared to the study of continental rifts, and there is little information regarding their influence on the products of the magmatism.

2.1.2 Melt generation processes

Melt generation in subduction zones is mainly explained by the occurrence of fluxing or wet melting, where the dehydration of minerals in the subducting slab triggers partial melting of the mantle wedge, providing the typical compositional signature that is reflected in the volcanic products (Cagnioncle et al., 2007; Cameron et al., 2003; England & Katz, 2010; Gill, 1981; Grove et al., 2002; Grove et al., 2012; Grove & Till, 2015; Iwamori, 1998; Skora & Blundy, 2010; Tatsumi, 2005; Turner & Langmuir, 2022).

In comparison, adiabatic decompression or dry melting is the main driver for melt production in rift zones due to plate spreading (Chadwick et al., 2025). Adiabatic melting, occurring concomitantly with fluxing, has also been proposed as a contributor to melt generation in subduction zones where there is little or no fluid input, and the pressure reduction occurs due to the entrainment of the mantle into the wedge corner (Cagnioncle et al., 2007; Cameron et al., 2003; Conder et al., 2002; Elkins-Tanton et al., 2001; England & Katz, 2010; Grove et al., 2012; Sisson & Bronto, 1998).

Other authors describe the melt generation by the occurrence of *mélange* diapirs generated from a mix of sediments, altered oceanic crust and serpentinised mantle that rise as cold plumes (Behn et al., 2011; Castro et al., 2010; Cruz-Uribe et al., 2018; Gerya & Yuen, 2003; Grove et al., 2012; Hall & Kincaid, 2001; Nielsen & Marschall, 2017; Vogt et al., 2013; Zhang et al., 2020). These diapirs are buoyant due to lower density and viscosity, melting during ascent through the hot mantle wedge (maximum 40 - 50 vol% melting in Zhang et al., 2020), before being emplaced in the lithosphere (Castro et al., 2010; Vogt et al., 2013; Zhang et al., 2020). Since *mélange* diapirs produce and release melts slowly during rapid bulk ascent, these will have a geochemical signature that allows for identifying the source components (e.g., Behn et al., 2011; Castro et al., 2010; Cruz-Uribe et al., 2018; Grove et al.,

2012; Hall & Kincaid, 2001; Nielsen & Marschall, 2017; Vogt et al., 2013; Zhang et al., 2020).

Lastly, some authors consider additional fluid input from mantle dehydration (Grove et al., 2009; Grove et al., 2012), and slab/sediment melting (Cameron et al., 2003; Conder, 2005; Kelemen et al., 2003; Skora & Blundy, 2010), preferentially in young and hot slabs (c. 1 Myr at T of 650 °C in Iwamori, 1998; Tatsumi, 2005).

2.1.3 Andesite generation

Although andesites are common in arc systems, the occurrence of andesitic melts is limited, creating an open discussion on their generation. The origin of the andesites has been attributed to two main processes, crystal fractionation of basaltic melts (e.g., Gill, 1981; Grove et al., 2003; Kemner et al., 2015; Lee & Bachmann, 2014; Müntener & Ulmer, 2018; Ulmer et al., 2018); and mixing/mingling of mafic and silicic magmas (Reubi & Blundy, 2009; Reubi & Müntener, 2022; Tatsumi, 2005). The felsic and mafic magmas can be the product of a bimodal magmatic system that generates basaltic and dacitic mantle melts due to slab and sediment contributions (e.g., Chen et al., 2024; Cole, 1978; Grove et al., 2002; Straub et al., 2011; Tatsumi et al., 1986). However, the silicic melts can also be derived from crustal processes such as fractionation and assimilation (Reubi & Blundy, 2009; Reubi & Müntener, 2022).

For the TgVC, the generation of andesites is mostly attributed to magma mixing/mingling of mafic and silicic magmas based on the crystal textures and compositions (Cocker et al., 2022; Price et al., 2005), where there is hybridization of stagnant felsic magma by frequent hot injections of mafic magma (Shane et al., 2008), and each magma batch has its own history of crystal fractionation, assimilation, mixing, mingling and storage (Price et al., 2012; Waight et al., 2017). The TgVC andesites have been identified as products of aphyric magmas carrying

antecrysts from mushes and/or solidified intrusive bodies affected by those injections (Kilgour et al., 2013; Shane et al., 2019; Stewart, 2010). Additionally, slab-derived contributions have been observed in the products of the TVZ (Corella Santa Cruz et al., 2023; Waight et al., 2017).

2.1.4 Transcrustal plumbing systems in subduction zone settings

Transcrustal processes have been used to describe the variation in composition observed in volcanic products and intrusive bodies through the interaction between the rising melt and crust. The most relevant models include: the assimilation and fractional crystallization model (AFC) (DePaolo, 1981), melting, assimilation, storage and homogenization (MASH) zones (Hildreth & Moorbath, 1988), deep crustal hot zones (DCHZ) (Annen et al., 2006), and transcrustal multilevel magmatic plumbing system (TCMS) (Bachmann & Bergantz, 2004; Cashman et al., 2017; Kiser et al., 2016; Marsh, 2015).

These models evolved from explaining the trace element composition and isotopic evolution of magma chambers (DePaolo, 1981), to include systems of dikes, sills, pods and chambers (Hildreth & Moorbath, 1988), and to describe reservoirs at different depths within the lower crust, where magma is stored in high-porosity layers experiencing fractional crystallization, assimilation, mixing and hybridization (Annen et al., 2006). Finally, all these models were integrated in the TCMS, including dynamic store regions denominated mushes, where the melt is distributed heterogeneously at different depths in non-eruptible crystalline frameworks (> 50 vol% crystals), that change crystallinity over time, contributing to the compositional and textural diversity of the products and mid-crust melt accumulation (Bouilhol et al., 2015; Farner & Lee, 2017; Giordano & Caricchi, 2022).

These mush zones provide an explanation for why melt proportions cannot be identified through geophysical methods in volcanic active zones, but instead, large zones with

somewhat lower seismic velocity are observed (Farrell et al., 2014; Ward et al., 2014). In TCMS, initial stages of melt fractionation and segregation occur in the mantle/crust limit, and further chemical differentiation, crustal assimilation and/or mixing/mingling processes are carried out in the mid- to upper-crustal mushes (e.g., Christopher et al., 2015; Jackson et al., 2018; Kovacs et al., 2021; Solano et al., 2014). However, it has also been advised that for more silicic magmas that magmatic differentiation may occur in the shallow crust instead of the lower crust or crust/mantle (Adam et al., 2016)

Recently, Zellmer et al. (2024) proposed the existence of transcrustal plutonic systems instead of magmatic systems in continental arcs. While in magmatic systems there is a small proportion of plutonic rocks (Cashman et al., 2017), in plutonic systems the mushes are rapidly solidified, and the melt proportion is subordinate (Zellmer et al., 2024). Transcrustal plutonic systems have been proposed to explain limited mineral phase proportions, melt-crystal disequilibrium and hydrothermally-altered crystals as the product of crystal uptake by hot aphyric melts that ascend rapidly through the crust (e.g., Coulthard Jr et al., 2024; Lormand et al., 2021; Zellmer et al., 2021).

Since the melt proportions in plutonic systems are low, these systems support the idea that melt compositional variations may be generated below the overriding crust; hence, deep crustal differentiation may not be necessary (Parolari et al., 2018; Straub et al., 2011; Zellmer et al., 2021). Here, the relamination of variable melts generated from subduction *mélanges*, instead of the delamination and fractioning of mafic melts, explains the origin, composition and characteristics of the melts (e.g., Hacker et al., 2011; Kelemen & Behn, 2016; Zellmer et al., 2021).

2.1.5 Crystal cargo and its relationship to magmatic processes in the plumbing systems

The history of crystallization and growth of mineral phases represented in their textural features can provide information on magma evolution and ascent rates (e.g., Browne & Szramek, 2015; D'Mello et al., 2023; Lormand et al., 2020; Ubide et al., 2024). The sizes, shapes and textures of crystals are related to the conditions and processes occurring in the magmatic system (Johnson et al., 2008; Sen, 2014; Toramaru et al., 2008; Zellmer et al., 2016a). The cooling rate can influence the shape and size of the crystals (e.g., Cashman, 1993; Giuliani et al., 2020; Sen, 2014), while magmatic process (*e.g.*, magma mixing, magma recharge, degassing) can lead to the development of disequilibrium textures (*i.e.,* changes in the chemical potential gradient) as a result of changes in the *P*-*T*-H_2O and composition conditions of the system (e.g., D'Mello et al., 2021; Ginibre et al., 2002b; Van Gerve et al., 2020; Welsch et al., 2016).

The crystallization of groundmass microlites (i.e., crystals with sizes between 30 – 1 μm in width as in Zellmer, 2021) usually occurs by decompression during magma ascent, due to volatiles exsolution (Browne & Szramek, 2015). However, larger microlites (i.e., up to 100 μm in length in Zellmer, 2021) might be antecrystic (*i.e.*, crystals grown from a different carrier melt in the same magmatic system) instead of autocrystic (*i.e.*, crystals grown from carrier melt), having implications in the characterization of magmatic processes for these specific plumbing systems (e.g., Lormand et al., 2020; Lormand et al., 2021).

Likewise, some phenocrysts might have different origins (*e.g.*, xenocrysts), not necessarily linked to the current carrier melt (e.g., Costa et al., 2013; D'Mello et al., 2023). The presence of glomerocrysts (*i.e.*, clustered crystals) can have many interpretations, such as a product of pre-eruptive rapid crystallization as a consequence of volatile-fluxing (McCarthy et al., 2020), the outcome of resorption and overgrowth of closely spaced crystals (Hogan, 1993), a

consequence of partial melting and the posterior recrystallization of previously formed crystals due to hot magma influx (Seaman, 2000), or a cumulate of crystals remobilized from a crystal mush (Cashman et al., 2017). In this last case, the presence of antecrysts and glomerocrysts in magmas has been interpreted as a product of magma mixing (Cashman et al., 2017). Additionally, crystal fracturing is another texture that can provide information regarding the origin of the crystals based on the location of the fracture and its relation to internal textures, which can provide information about the processes that occurred between fracture and eruption (Zellmer & Iizuka, 2025).

Similarly, the range of disequilibrium textures in the crystals helps to infer the processes that occurred in the magmas. Complex oscillatory zoning and resorption patterns in crystals have been linked to pressure fluctuations and/or multi-episodic heating-cooling events associated with new magma injections and/or remobilization (Bergantz et al., 2015; Couch et al., 2001; Zellmer et al., 2003). If these patterns are associated with groundmass crystals, it is possible that those have not been crystallized from the carrier melt, but rather picked up during ascent (Humphreys et al., 2016; Lormand et al., 2020; Zellmer et al., 2016b).

Microlites formed during magma ascent are typically euhedral and unzoned crystals or display a normal/low-oscillatory zoning (Zellmer, 2021). Autocrystic microlites provide key information regarding the conditions of the system at the time of crystallization, such as volatile (H_2O) content, temperature and pressure. This allows for determination of melt-crystal equilibrium in the system, magma ascent rates, crystallization-triggering mechanisms, depth of crystallization, and even changes in the conduit geometry that influenced the eruption style (e.g., Befus et al., 2015; Devine et al., 1998; Lormand et al., 2020; Sano et al., 2015).

The characteristics of the most common texture types are summarised in Table 2.1, including those previously described in the crystal cargo of the TgVC, such as resorption textures (Shane et al., 2008), sieve textures (Auer et al., 2015; Shane et al., 2008), oscillatory zoning (Kilgour et al., 2013), skeletal/hopper textures (Nakagawa et al., 1998) and glomerophyric texture (Auer et al., 2015; Pardo et al., 2012).

Table 2.1. Common textures in crystals.

Texture (schematic representation)	Description	Interpretations
Resorption textures 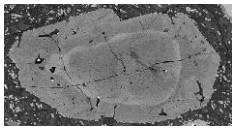	Partial dissolution of the crystal, which is observed in both core and rims, as ovoidal cores and dusty rims with wavy surfaces and mantled by overgrowing layers, which can be imposed to oscillatory or sector zoning.	High-rate decompression in volatile-rich magmas ((Viccaro et al., 2010)). Recharge of less evolved hotter, volatile-rich magmas (Ginibre et al., 2002a; Ginibre et al., 2002b; Ginibre et al., 2007).
Sieve texture 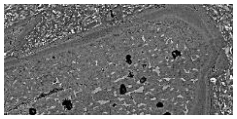	Incipient resorption (corrosion) of the crystal, usually imposed over patchy textures and oscillatory zoning. It can occur in the core and/or rims of the crystals.	Decompression (intermediate rate) triggered dissolution (Neave & Maclennan, 2020; Viccaro et al., 2010). Mixing with a less evolve magma (Tsuchiyama, 1985). H_2O-rich magma recharge (Humphreys et al., 2006).
Monotonous zonation 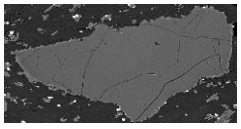	Textureless zoning. It is observed as a variation in the composition from core to rim with smooth or no changes in colour within the crystal.	Faster growth rates (Streck, 2008)
Patchy zoning 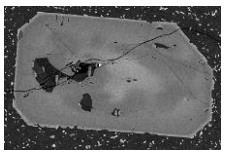	Enriched zones, which are arranged as irregular patches in the crystal. In plagioclase is observed as an abrupt transition between Ca and Na-rich zones, while in pyroxenes it is observed as an increase in the #Mg with diffuse contacts. It is commonly observed in cores.	Slow rate decompression (Humphreys et al., 2006; Viccaro et al., 2010) Reactive dissolution of the crystals (Tsuchiyama, 1985; Van Gerve et al., 2020)
Oscillatory zoning 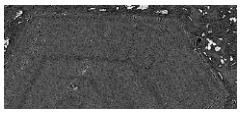	Cyclical variations in composition from core to rim, which are observed as concentric rings. That can be either Low Amplitude–High Frequency (LAHF) or High Amplitude–Low Frequency (HALF).	Dissolution/regrowth events in dynamic systems, usually HALF (Ginibre et al., 2002a; Viccaro et al., 2010). Fluctuations in the supply of cations between crystal and melt, usually LAHF (Viccaro et al., 2010; Zellmer et al., 2016b).

Sector zoning 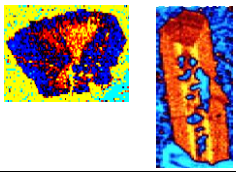	Compositional variation in the crystal due to the differential incorporation of elements along different crystallographic surfaces. These can present hourglass or prismatic shapes.	Low degrees of undercooling and supersaturation conditions (Ubide et al., 2019; Welsch et al., 2016).
Skeletal /Hopper / Swallow-tailed texture 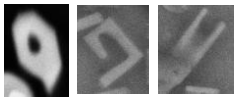	Incomplete crystals with step-like patterns resembling crystal faces. Skeletal textures have internal cavities (hollow texture), while hopper have external cavities. Swallow-tailed have forked or H-like crystal shapes.	Syn-eruptive fast decompression of degassed magma (Viccaro et al., 2010). High undercooling induced crystallization by degassing or water exsolution (Renjith, 2014; Sen, 2014)
Glomerophyric texture 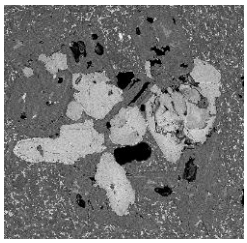	Crystals in aggregates or cloths, denominated glomerocrysts.	Suturing of spatially closer resorbed crystals (Renjith, 2014).
Broken crystal 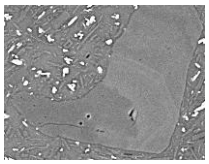	Incomplete, fractured crystals without regrowth features. It can be imposed over zoning and resorption structures.	Decompression-related forceful aerial eruption (Renjith, 2014).

2.2 Mount Ruapehu

Mount Ruapehu (39.28°S, 175.57°E) is the southernmost active volcano of the southern segment of modern TVZ (*c.* 61 ka - present) (Wilson et al., 1995; Wilson & Rowland, 2016). The TVZ is a NNE-SSW zone of hyperactive volcanism, located in the North Island of New Zealand, responsible for over 90% of the volcanic activity in the country, and a product of the Tonga-Kermadec–Hikurangi subduction system, where the Pacific plate subducts obliquely under the Australian plate (Cole & Lewis, 1981; Ewart et al., 1977; Houghton et al., 1995; Leonard et al., 2021; Milicich et al., 2020; Schellart & Spakman, 2012; Stern et al., 2006; Wilson et al., 1995).

Mount Ruapehu is an active andesite-dacite stratovolcano, part of the Tongariro Volcanic Centre (TgVC), and the highest mountain of the North Island (2797 m) (Figure 2.1) (Global Volcanism Program, 2025; GNS Science, 2025). The Ruapehu graben (Figure 2.1), located at the southern termination of the Modern Taupō Rift (*c.* 25 ka - present), is a nested structure of *c*. 40 km trending NNE (Gómez-Vasconcelos et al., 2016; Villamor & Berryman, 2006b). It was developed by a relatively younger fault system (*c*. 400 ka), which extensional rates have increased in the late Quaternary to 2.3 ± 1.2 mm/yr due to rift evolution and crust thinning (Villamor & Berryman, 2006a).

The Ruapehu Graben is filled by a thin sequence of a few tens to hundreds of meters of Cenozoic (Late Oligocene to Early Miocene) sedimentary rocks with interbedded tuffs (Cassidy et al., 2009; Price et al., 2012). This overlies a basement composed of greywackes and metamorphic rocks of the accretionary tectonostratigraphic Kaweka (Adams et al., 2009, 2011) and Waipapa (Adams et al., 2009; Price et al., 2012) terranes of the Mesozoic (Late Jurassic to Early Cretaceous) Eastern Province (Adams et al., 2007; Mortimer et al., 2014) resting on oceanic lithosphere, which have been identified as sources of meta-sedimentary xenoliths in many Mount Ruapehu andesites (Price et al., 2012).

Mount Ruapehu comprises a voluminous edifice (110 km^3) formed predominantly by lava flows surrounded by a ring plain built out of the pyroclastic deposits of the volcano and their reworked products (Hackett & Houghton, 1989). The eruptive products of the volcano over the last 250 ka have been defined as the Ruapehu Group by Hackett (1985), describing four formations, each one associated with a cone building episode, which, from oldest to youngest, are: Te Herenga (250 – 150 ka), Wahianoa (166 – 80 ka), Mangawhero (50 – 15 ka), and Whakapapa (<15 ka) formations (Figure 2.1) (Conway et al., 2016; Gamble et al., 2003; Hackett & Houghton, 1989; Leonard et al., 2021).

The oldest dated rocks of Mount Ruapehu are the lavas of the Te Herenga Formation (158.8 ± 8.2 ka in Conway, 2016; 205 ± 27 ka in Gamble et al., 2003) exposed in the northern sector of the volcano and possibly erupted from the Pinnacle Ridge (Hackett, 1985). This formation is composed of porphyritic andesites to basaltic andesites lavas, with two pyroxene and plagioclase, and glomerocrysts up to 12 mm in diameter (Conway, 2016; Hackett, 1985; Townsend et al., 2017). This formation was affected by two major glaciations, which promoted erosion of the edifice and the unconformity contact with the Whakapapa and Mangawhero formations (Conway et al., 2016; Townsend et al., 2017).

Around 160 ka, the emplacement of the Wahianoa Formation started on the southern part of the volcano, coeval with the Te Herenga Formation covering its previously emplaced flows (Conway, 2016; Hackett, 1985; Townsend et al., 2017). This period marks the beginning of the "Ruapehu geochemical trend" described by Conway (2016), characterized by the progressively increasing SiO_2 and K_2O contents in lavas erupted between c. 200 – 80 ka (Townsend et al., 2017).

The Wahianoa Formation is formed by porphyritic basaltic andesites and andesites lava flows of two pyroxenes and plagioclase, with rare occurrence of olivine, and up to 40 vol% of phenocrysts (Conway, 2016; Hackett, 1985). Lahar deposits of c. 80 – 60 ka have been recognised in the ring plain (Lecointre et al., 1998), during an apparent eruptive gap at Mount Ruapehu (c. 82 – 56 ka), in which either the volcanic activity ceased, and these events were controlled by climatic factors (i.e., temperature, precipitation) and/or slope failure of the deposits; or some sort of primary volcanic activity produced them, but the deposits of said activity were eroded and/or buried (Conway et al., 2016; Townsend et al., 2017). During the last glaciation (c. 50 – 15 ka), the products of the Mangawhero Formation were emplaced, most likely originating from glaciated vents located near the modern Summit Plateau

(northern vent) and Girdlestone Peak (southern vent) (Conway, 2016; Townsend et al., 2017). The Mangawhero Formation is an extensive, voluminous and compositionally diverse unit that forms the main cone of Mount Ruapehu (Conway, 2016; Hackett, 1985; Townsend et al., 2017). Conway (2016) reported 11 eruptive packages that exhibit clear evidence of lava-ice interaction at eruption and emplacement (Conway et al., 2015; Townsend et al., 2017). Lavas emplaced from the northern vent between c. 50 – 36 ka correspond to andesitic lavas with up to 40 vol% crystals of the Ngahuinga Member (c. 48 – 35 ka), and dacitic lavas of the Te Kohatu (c. 44 – 36 ka) and Mangaturuturu (c. 46 – 36 ka) members (Conway, 2016; Townsend et al., 2017).

The MgO relative to SiO_2 content in the members of the Mangawhero Formation, emplaced between 50 – 35 ka, presents two distinct geochemical trends: low-Mg, which heads towards a more primitive composition (Kakuki Basalt in Gamble et al., 1993) and high-Mg, which heads towards a primitive high-magnesian type (Waimarino Basalt in Gamble et al., 1993; Hackett, 1985). In the case of the Te Kohatu and Mangaturuturu members, these belong to the high- and low-Mg trends respectively (Conway, 2016; Townsend et al., 2017). A single dacitic isolated ice-dammed flow of the Mananui Member (c. 42 – 38 ka) was emplaced to the north of Mount Ruapehu around the same time, with identical composition to a flow in the southern rim of the Tama Lake crater identified by Hackett (1985) with the particularity that the MgO content is intermediate between the Mangaturuturu and Te Kohatu members (Conway, 2016; Townsend et al., 2017).

The northern vent was also active from c. 36 – 22 ka, producing the andesitic lavas of the Manganuioteao Member (c. 33 – 23 ka) and the dacitic lavas of the Whakapapaiti Member (c. 30 – 22 ka), constructing the western lava plateau, influenced by the advance (c. 31 ka) and retreat (c. 27 ka) of the Mangaturuturu and Whakapapa glaciers (Conway et al., 2015;

Townsend et al., 2017). At the same time, the andesitic lava flows of the Horonuku Member (c. 29 – 15 ka) flowed east into the Tukino ski area, interacting with the Mangatoetoenui/Whangaehu glacier system, and the andesitic lava flows of the Te Piripiri Member (c. 27 – 15 ka) flowed north, filling the Ohinepango valley (Conway et al., 2015; Conway, 2016; Townsend et al., 2017).

The emplacement of lavas erupted from the southern vent was coeval with the north, constructing the southern flank between c. 47 and 40 ka (Conway et al., 2015; Conway, 2016). These flows correspond to the Mangaehuehu Member (c. 47 – 40 ka), which is partially contemporary with the Ngahuinga Member, and is composed of voluminous andesite lava flows following the high-MgO trend (Conway, 2016; Townsend et al., 2017). The activity in the southern vent area between c. 30 – 17 ka produced the andesitic flows of the Waitonga Member (c. 31 -15 ka) that fed the south-western flank of the volcano (Conway et al., 2015; Conway, 2016; Townsend et al., 2017). Around the same time occurred the emplacement of the rootless andesitic flows of the Makotuku Member (c. 24 -16 ka) into the southern flank. These flows are inferred to be emplaced beside or beneath glaciers, tunnelling through and under the ice, or even flowed over the glacier in the Wahianoa valley (Conway et al., 2015; Conway, 2016; Townsend et al., 2017).

During the last glacial ice retreat (c. 15 – 12 ka) were emplaced the andesitic lava flows of the Paretetaitonga (c. 18 – 12 ka) and Tureiti (c. 15 – 9 ka) members of the Whakapapa Formation were emplaced, originated in the current Summit Plateau (Conway et al., 2015; Conway, 2016; Townsend et al., 2017). At the same time, in the current Crater Lake area, andesitic lava flows of the Turoa Member (c. 17 – 10 ka) flowed into the Turoa ski field area, interacting with the Mangaehuehu Glacier (Conway et al., 2015; Conway, 2016; Townsend et al., 2017). Additionally, another southern summit vent sourced the voluminous andesitic lava

flows of the Rangataua Member (c. 15 – 11 ka) (Conway, 2016; Townsend et al., 2017). During the Holocene (<12 ka), at least three cones were developed in Mount Ruapehu, which originated the extensive andesitic lava flows of the Saddle Cone Member (<11 ka in Nairn et al., 1998), the andesitic lava flows and pyroclastic deposits of the Iwikau Member (< 10 ka), and the andesitic lava flows, spatter sheets and tephra of the Crater Lake Member (< 3kyr in Donoghue et al., 1997) (Conway, 2016; Hackett, 1985; Townsend et al., 2017).

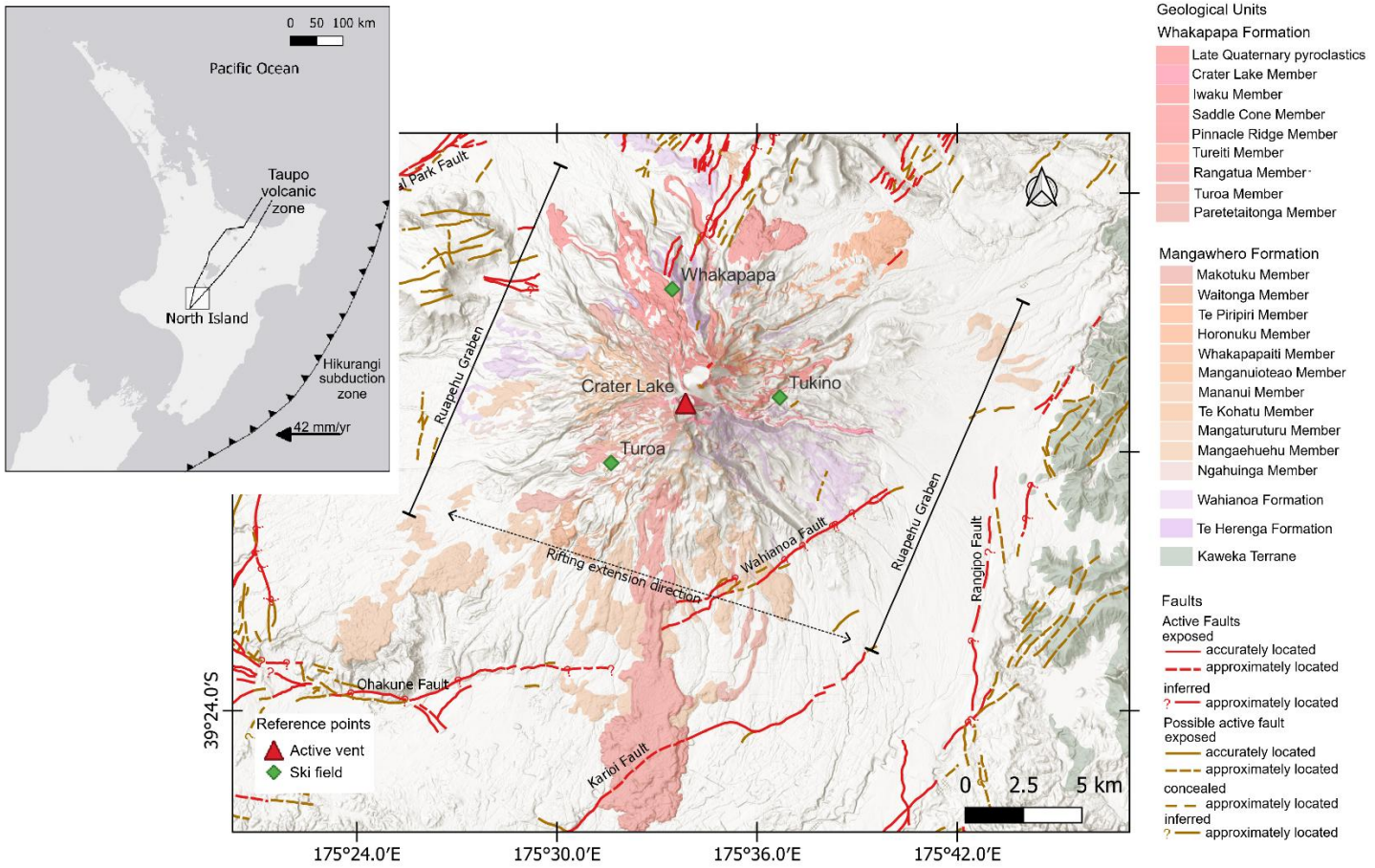

Figure 2.1. Geological map of Mount Ruapehu, showing the main units and faults around the edifice. Units from Townsend et al. (2017) after Conway (2016) and Hackett (1985)

Chapter 3 Methods

3.1 Field work and sampling

Lava flows in contact with glaciers present a rapid cooling due to heat transfer (Edwards et al., 2013; Wilson & Head, 2007), forming fractures that propagate perpendicularly away from the cooling surface (*i.e.*, glacier) due to thermal contraction (DeGraff & Aydin, 1987; Lore et al., 2000). Likewise, lava flows chilled against ice upon eruption cool rapidly enough to form a glassy matrix and preserve pre-eruptive growth structures in microlites (e.g., Owen et al., 2013).

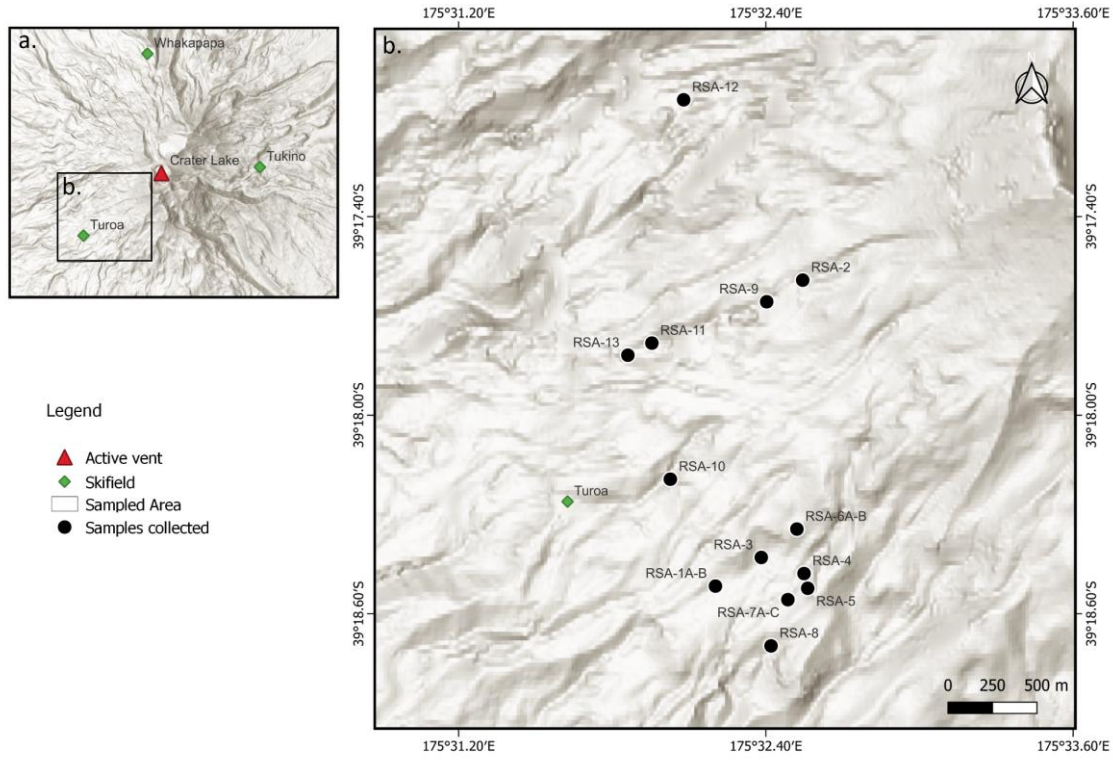

Figure 3.1. Sample locations.a. Location of the sampling area in Mount Ruapehu. b. Location of the sampling points.

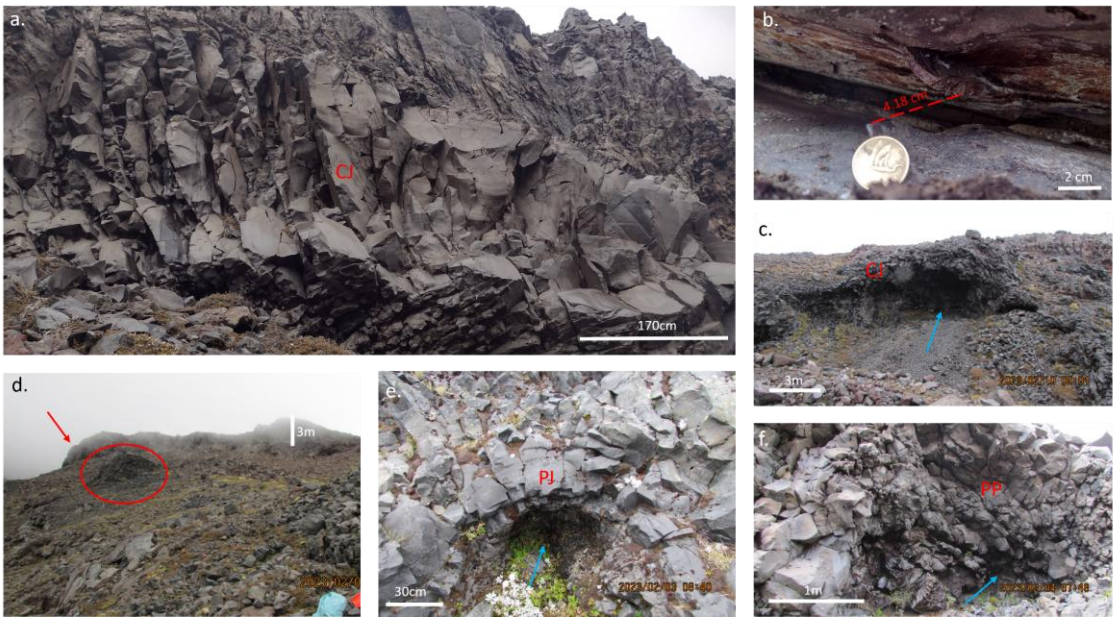

Figure 3.2. Ice/Lava interaction structures in sampled points at Mount Ruapehu.a. Column-forming joints (CJ). b. Ruptured lava bridge on crease structure. The dashed line shows the distance between the broken ends of the bridge. c. Column-forming joints (CJ). d. Ice-bounded lavas that flowed along a ridge top. Note the knuckle in a red circle and the abrupt cliff indicated by the red arrow. e. Platy joints (PJ). f. Pseudo-pillow fractures (PP). The blue arrows in photos c, e and f indicate cavities underneath the flows formed by a mass of ice/snow that melted post emplacement.Mount Ruapehu has some permanent glaciers, which during the Ōtira Glaciation (*c*. 65 – 14 ka), reached about 140 km^2 extending down to 1200 m.a.s.l. (McArthur & Shepherd, 1990), and coincided with the emplacement of the Mangawhero Formation, which shows clear signs of lava/ice interaction (Conway et al., 2015; Spörli & Rowland, 2006). For this reason, the Mount Ruapehu lava flows were suitable for the present study enabling the assessment of microlite size distributions.

Field work at Mount Ruapehu was conducted in January and February 2023. 17 samples of glassy lava were collected from 13 locations (Table 3.1) in the Turoa Ski field area on the south-western flank of the volcano (Figure 3.1).

The samples were collected from outcrops showing evidence of lava/ice interaction such as column forming and platy joints, pseudo-pillow fractures, rupture lava bridges, knuckles and cavities as described by Conway et al. (2015)(Figure 3.2) . At three locations (RSA1, 6 & 7), multiple samples were collected from different levels within the same flow (*i.e.*, top and

base) to assess possible variations in the petrography and CSD within a single flow. The samples were identified to belong to the Mangawhero (15 -50 ka) and Whakapapa (<15 ka) formations (Table 3.1), based on field observations, information from the geological map of the Tongariro National park (Townsend et al., 2017), and field confirmation by Chris Conway and Dougal Townsend in January 2023 for sampling points RSA-1 and RSA-2. The similar whole rock compositions compared to those in Conway (2016) confirmed the formation and member of each sample.

Table 3.1. Location of the lava samples collected in Mount Ruapehu.

Sample	Latitude	Longitude	Formation	Member
RSA1A	39°18'30.97"S	175°32'12.19"E	Mangawhero	Makotuku
RSA1B	39°18'30.97"S	175°32'12.19"E	Mangawhero	Makotuku
RSA2	39°17'35.52"S	175°32'32.64"E	Mangawhero	Waitonga
RSA3	39°18'25.78"S	175°32'22.93"E	Mangawhero	Makotuku
RSA4	39°18'28.70"S	175°32'32.95"E	Mangawhero	Mangaehuehu
RSA5	39°18'31.37"S	175°32'33.81"E	Mangawhero	Mangaehuehu
RSA6A	39°18'20.64"S	175°32'31.28"E	Mangawhero	Mangaehuehu
RSA6B	39°18'20.64"S	175°32'31.28"E	Mangawhero	Mangaehuehu
RSA7A	39°18'33.43"S	175°32'29.16"E	Mangawhero	Makotuku
RSA7B	39°18'33.43"S	175°32'29.16"E	Mangawhero	Makotuku
RSA7C	39°18'33.43"S	175°32'29.16"E	Mangawhero	Makotuku
RSA8	39°18'41.81"S	175°32'25.22"E	Mangawhero	Makotuku
RSA9	39°17'39.44"S	175°32'24.20"E	Mangawhero	Waitonga
RSA10	39°18'11.60"S	175°32'1.62"E	Mangawhero	Makotuku
RSA11	39°17'46.93"S	175°31'57.29"E	Whakapapa	Turoa
RSA12	39°17'2.83"S	175°32'4.74"E	Whakapapa	Turoa
RSA13	39°17'49.13"S	175°31'51.67"E	Mangawhero	Mangaehuehu

Units are inferred as described in text.

3.2 Sample preparation

Sample preparation used a variety of techniques suited to the analyses. Epoxy mounts were made at Academia Sinica (Taiwan) and Tohoku University (Japan) for backscattered scanning electron microscopy (BS-SEM), electron probe microanalysis (EPMA) and laser ablation inductively couple plasma mass spectrometry (LA-ICP-MS) analyses. Glass beads were made at Massey University, for X-ray fluorescence (XRF) analyses. For synchrotron

radiation X-ray micro-tomography (SR-XCT) two preparations were made to obtain pieces ~200 μm^3 at SPring-8 (Japan) and Tohoku University (Japan).

3.2.1 Epoxy mounts

Rock fragments from the samples were embedded in a two-component epoxy resin within 2.5 cm diameter plugs. The plugs were vacuum treated to ensure full resin impregnation. After curing, the mounts were grounded, polished and coated with a thin layer of carbon (~30 nm) for BS-SEM and EPMA analyses using vacuum evaporators Q150TE (Quorum Technologies) and IB-29510VET (JEOL) at academia Sinica and Tohoku University, respectively. The samples were repolished to remove the carbon coating using a LaboPol-30 machine equipped with a MD-Dac 1μm polishing cloth and the equivalent DiaPro all-in-one diamond solution at Massey University before performing the LA-ICP-MS analyses.

3.2.2 Glass bead preparation

Glass beads were obtained from mixing 0.8 g of heated oxidized sample powders with 8.0 g of X-Ray flux type 12:22 (35.3 vol% Lithium Tetraborate, 64.7 vol% Lithium Metaborate). The mixing was performed in glass container by shaking, and the moulding was carried out in an xrFuse2 fusion machine at Massey University using platinum crucibles.

The oxidized powders were obtained by pulverizing the samples in a tungsten carbide mill at Massey University. Subsequently, the homogeneous powders were placed in ceramic crucibles and dried in a Carbolite oven at 110 °C overnight. 2 g of dried sample were placed in ceramic crucibles in a Thermoline muffle furnace at 900 °C for 8 h. After that time the furnace was turned off and left to cool down between 200 and 100 °C. Then the oxidized samples were moved into a desiccator and weighted to determinate the loss on ignition (LOI). The LOI/volatile content calculation is included in Appendix 1 (Table S1).

3.2.3 SR-XCT sampling preparation

Rock sample RSA1A was prepared using a plasma-focused ion beam (FIB) system equipped with FE-SEM (Helios5 Hydra UX Dual Beam, Thermo Fisher Scientific) at SPring-8 by Masahiro Yasutake, to obtain a microscale specimen of 130 μm x 130 μm x 65 μm in size. The extracted micro sample was mounted on a tungsten needle for SR-XCT analysis.

The FIB method is time consuming and considering the number of samples for analysis an alternative method was implemented for all the samples including RSA1A. To obtain the micro specimens, pieces of 5 mm x 2 mm x 2 mm were cut and reduced to slices of ~200 μm in thickness by sandpaper grinding up to 1200 grit. Once the desired thickness was achieved the slices were fragmented and attached to thin rods using carbon nanotube (CNT) for SR-XCT analysis.

3.3 Laboratory Analyses

3.3.1 X-Ray fluorescence (XRF)

To determine major oxide concentrations in whole rock, XRF analyses in glass beads were performed using a Bruker S8 Tiger Series II WD-XRF spectrometer at Massey University. Oreas 24b and 24c certified reference materials served as standards, showing reproducibility values ~1 – 3%, except for the P_2O_5 which present values of ~5 – 13% (Appendix 1; Tables S2 & S3).

3.3.2 Back-scattered scanning electron microscopy (BS-SEM)

BS-SEM images for petrographic and CSD analyses were obtained at Academia Sinica by Yoshiyuki Iizuka using a JEOL thermal field emission scanning microscope (FE-SEM JSM-7100F) equipped with a Deben Centaurus scintillator detector (K.E. Developments). The

images were captured using a focused beam at working distance of 13 mm, acceleration voltage of 15 kV and beam current of 120 nA.

3.3.3 Synchrotron radiation X-ray micro-tomography (SR-XCT)

Two experimental proposals for SR-XCT using a BL47XU beam at SPring-8 were submitted and approved with assistance of Professor Satoshi Okumura from Tohoku University. The experiments were performed on November 20-21, 2023, and November 13-14, 2024. The samples were analysed for approximately 30 min using X-ray energy of 15 keV. The samples were placed between a condenser zone plate (on front) and Fresnel zone plate (behind) for the imaging capture and fixed to the rotational stage set on high-precision mode to obtain three-dimensional images with a spatial resolution (voxel sizes) of 194 and 388 nm.

Synchrotron radiation X-ray micro-tomography at SPring-8 BL47XU (Japan) uses a CMOS based detector in an ORCA Quest camera made by Hamamatsu Photonics K. K. The sample-to-detector distance is about 10 mm, taking 3600 tomographic projections over 180° scans. Neither microfocus X-ray sources nor propagation distance-based phase contrast imaging were employed in the image acquisition (e.g., Arzilli et al., 2016).

3.3.4 Electron probe microanalysis (EPMA)

Electron probe microanalyses (EPMA) were carried out at Academia Sinica and Tohoku University, to determine major element compositions, and elemental distribution mapping in crystals.

At Tohoku University were performed quantitative point analyses using a W-filament JEOL iSP100 electron microprobe with a focused beam at acceleration voltage of 15 kV and beam current of 15 nA. At Academia Sinica were performed quantitative point and transect (rim-to-rim or core-rim) analyses using a field emission electron microprobe JEOL FE-EPMA JXA-

8500F with a 2 μm defocused beam, at acceleration voltage of 12 kV and beam current of 6 nA. Five wavelength dispersive spectrometers (WDS) were fitted for both microprobes, measuring element peaks for 10 s and backgrounds for 5 s. Analyses were accepted when total major element oxides ranged between 96 to 100 wt%. X-ray intensity corrections were applied using the Oxide-ZAF method which counteract the atomic number (electron backscattering and penetration factors), absorption (reduction of the intensity of the X-ray by absorption from other elements) and fluorescence excitation (addition to the intensity of the x-ray by capturing of X-rays from other elements) effects, ensuring the characteristic X-ray intensity for a name element is corrected and comparable between standard and unknown sample (JEOL Ltd., n.d.). Detection limits for all elements were under 500 ppm, and the relative standard deviations were under 3% for secondary standard measurements. A list of standards is provided in Appendix 1 (Table S3).

Additionally, phenocryst compositional mapping was performed at Academia Sinica using a W-filament thermal emission electron micro-probe (JEOL W-EPMA JXA-8900R) equipped with four WDS. The analyses were performed at an acceleration voltage of 15 kV, beam current of 50 nA, beam size 1 μm, intervals of X-Y directions of 2 μm and dwell time of 15 ms to prevent Na migration in plagioclase.

3.3.5 Laser ablation inductively couple plasma mass spectrometry (LA-ICP-MS)

LA-ICP-MS analyses were performed at the Centre for Geoanalytical Mass Spectrometry, Radiogenic Isotope Facility of The University of Queensland (Australia) under the supervision of Professor Teresa Ubide, using an ASI RESOlution laser ablation system set up with an ArF 193 (nm) gas excimer laser controlled with GeoStar software and coupled to a Thermo Fisher iCAP RQ quadrupole inductively coupled plasma mass spectrometer (ICP-MS) operated by Qtegra software. The ablation was executed using ultrapure He (350

ml/min) combined with Ar (850 – 950 ml/min) and trace amounts of N_2 (5 ml/min) to enhance signal sensitivity, ensure efficient transport and assist with ionization (Ubide et al., 2015; Ubide et al., 2023).

LA-ICP-MS was used to determine groundmass compositions, analysing 10 raster lines of 600 μm per sample, across the microcrystalline matrix (e.g., Bennett et al., 2025; Ubide et al., 2023). The laser spot size was set up at 50 μm, with a fluence of 3 J/cm, repetition rate of 10 Hz and translation speed of 5 μm/s. Additionally, the rastering technique in Ubide et al. (2015) was applied to the analysis of mineral trace element zoning patterns by mapping (e.g., D'Mello et al., 2023; Ubide et al., 2019; Ubide et al., 2025). In this technique, the stage moves progressively and continuously under a fixed ablation site, generating an evenly ablated line using a square-shaped laser creating a map of the area from successive ablation lines. In mineral phases, particular elements were targeted such as Mg, Fe, Cr, Ni and Sc in pyroxene (Morgan et al., 2004; Ubide et al., 2019), and Sr, Ba, and Li in plagioclase (Audétat et al., 2018; Costa et al., 2003; Zellmer et al., 2003). The ablation for the maps was performed at a fluence of 3 J/cm, repetition rate of 10 Hz and translation speed of 10 or 16 μm/s defined by the spot size used (i.e., 10 or 16 μm) depending on the size of the crystal. To ensure the full coverage of the mapped area, there was set up a 1 μm overlap between lines.

3.4 Image Analyses

3.4.1 Crystal textures

The identification of textures in crystals of the lava samples of this study was carried out using BS-SEM images encompassed with EPMA and LA-ICP-MS mapping analyses. This combined approach includes a qualitative analysis of the textures through the use of images to identify common features, as those in Table 2.1, while assessing variations in composition

linked to the textures, particularly for the targeted elements in section 3.3.5, which benefited the interpretation of the structures and the processes that generated them.

3.4.2 Crystal Size Distribution (CDS)

The crystal size distribution (CSD) diagram established by Marsh (1988) works by plotting the length of the crystal *L* (i.e., the larger axis of the crystal) against the natural logarithm of the population density n (ln[n]), where n represents the number of crystals (N), per unit of length (*L*), per unit of volume (Higgins, 2000; Marsh, 1988). The CSD data interpretation resides in the recognition that for any steady or time-dependant system the slope ($1/G\tau$) is the reciprocal product of growth rate (G) and residence time (τ), where if τ is known, then, G can be found, or vice versa, and the intercept ($\ln[n^0]$) is the nucleation density (n^0) of zero-sized nuclei (Marsh, 1988).

Additionally, the shapes of the CSDs provide information about the physical process occurring in the plumbing system (e.g., crystal fractionation and accumulation, mixing of populations). Log-linear CSDs (Figure 3.3a) are associated with constant cooling and growth rates, while kinked or curved distributions (Figure 3.3b) are treated as two crystal populations of that experienced separate crystallization histories (Cashman, 2020; Marsh, 1998).

In Chapter 4, CSDs for pyroxene microlites (1 – 30 μm width in Zellmer, 2021) in groundmass of sample RSA1A were calculated using two approaches: 2D-CSDs derived from BSE-SEM images of the epoxy mount, and 3D-CSDs obtained from SR-XCT images the sample prepared with the FIB technique. These CSDs were used to assess the influence of the statistical estimation of the aspect ratio and the stereological corrections performed to transform 2D into 3D data. The influence was evaluated on CSD slopes, since this are a key parameter used in crystal residence time calculations, which are used in Chapter 5. 3D-CSDs using the same methods employed in Chapter 5 were obtained for pyroxenes in samples

RSA1B - 13 prepared using the alternative method described in section 3.2.3, to be employed in the residence time calculations. Pyroxene crystals were chosen since in lava samples the high density in microlites makes individual crystals of plagioclase almost impossible to differentiate, which can lead to significant errors in the 2D CSDs calculations (e.g., Lormand et al., 2018; Okumura et al., 2022).

For the 2D CSDs, BS-SEM images were segmented in ImageJ (Schindelin et al., 2012; Schneider et al., 2012), applying a threshold using the pixel values for pyroxene. The segmentation is possible since the samples have a limited number of mineral phases (i.e., plagioclase, pyroxene and magnetite) and the pixel values for pyroxene can be easily defined. Once the crystals were classified, the apparent length and width of the crystals was measured using the analysing tools available in ImageJ. These crystal 2D measurements were run through two database CSDSlice (Morgan & Jerram, 2006) and ShapeCalc (Mangler et al., 2022), to determine the shape factor of the crystals (i.e., long, intermediate and short axes). The conversion of 2D data into 3D was achieved through the use of the software CSDCorrections (Higgins, 2000) that can account for different crystal shapes and fabrics to obtain the CSDs. This is a well-established process which has been used to calculate almost all reported CSDs since their release (Okumura et al., 2022).

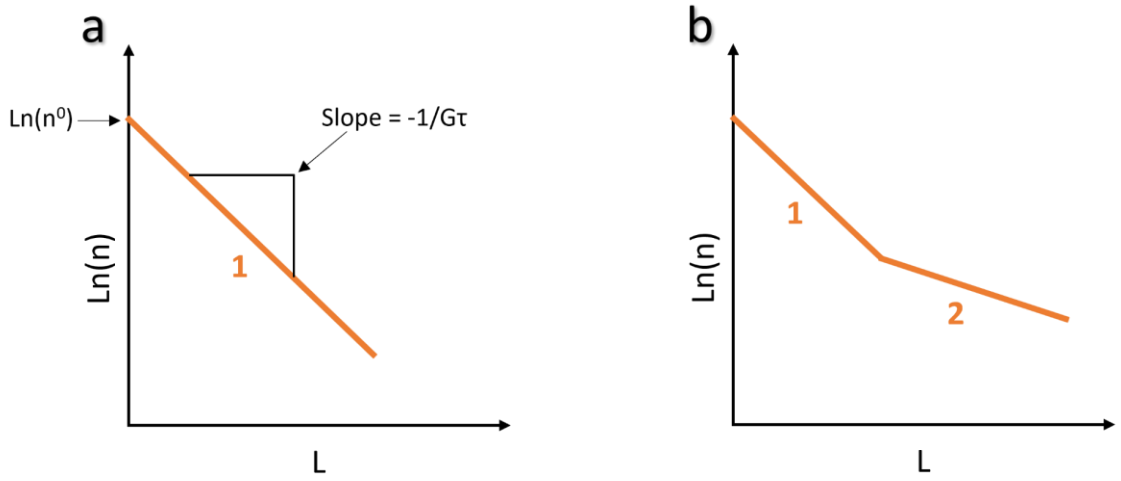

Figure 3.3. CSD schematic diagram.a. Log-linear CSD with one population (1), showing intercept (Ln[n^0]) and slope (-1/Gτ). b. Kinked or curve CSD showing two populations (1 & 2). Modified from Marsh (1988, 1998).

3D CSDs were obtained through SR-XCT images. These images were reconstructed using the free software ct-rec available at SPring8 (Uesugi, 2025), which creates computational tomography images directly from transmission image data, without intermediate files required. The images were processed using the software SLICE (Nakano et al., 2006), which allows for data reduction, image segmentation and particle measurement. The region of interest (ROI) for each sample was selected avoiding any phenocrysts (s.s., Iddings, 1892), and ensuring a sufficient number of microlites available to perform the CSD calculation (~200 crystals for 3D distributions in Mock & Jerram, 2005). The segmentation of the crystals was performed by enhancing contrast between the pyroxene crystals and the sample in ImageJ; and applying a bi-level pixel threshold manually and cleaning the resultant binary volumes using erosion and dilation filters in SLICE to improve the segmentation quality.

Since the data obtained from 3D images in SLICE represents the real dimensions (i.e., true dimensions of the axes) and volumes of the crystals, it does not require additional transformations, and the number densities can be easily calculated using the number of crystals (N) divided by the volume (V) they occupy. The CSDs were generated by plotting the long axis of the crystal against the natural logarithm of the population density (n). Further description of the image processing and segmentation, alongside with the CSDs calculation is provided in Chapter 4.

3.4.3 Crystal growth rate, magma residence times and magma ascent rates

Marsh (1988) proposed to treat the growth rate (G) as an independent variable of the crystal length (L), where the growth rate at a particular time is equal for all crystals, turning G into a constant that is also independent from time (t). Hence, any variation in G as a function of L or

t will cause a curvature in the CSDs (Marsh, 1998). Assuming constant growth has produced reliable results to obtain nucleation and grow rates from CSDs, which cannot be obtained from assuming dependant growth (Eberl et al., 2002; Marsh, 1988, 1998), extending its use for the calculation of magma residence times (e.g., Blundy & Cashman, 2008; Cashman & Marsh, 1988; Cashman, 1993; Lormand et al., 2020; Salisbury et al., 2008). For this reason considering the growth rate as a constant, the magma residence times (τ) can be constrained using the relation between G and τ with the slope of the CSD as in Marsh (1998) (Figure 3.3a).

For this study a growth rate range based on experimental data found in Shea & Hammer (2013) and Giuliani et al. (2020) was used, alongside with the well-known crystal growth rate for pyroxene used by Lormand (2020). The latter was calculated by Zellmer et al. (2016a, 2018) in orthopyroxenes of Mangatawai Formation (Sample 407-17 in Moebis, 2010) erupted from the same volcanic complex as Mount Ruapehu (i.e., TgVC), and recalculated by Lormand (2020) to match the temperature modelled by MELTS using the composition of the sample (Table 3.2).

Table 3.2. Crystal growth rates estimate for orthopyroxene of the Mangatawai Formation.

	Zellmer et al. (2016a, 2018)	**Lormand (2020)**
Temperature	1137 ± 41 ºC	1095 ± 15 ºC
Growth rate	3.7 (±2.6) × 10^{-11} m/s (2σ)	1.80 (±0.60) × 10^{-11} m/s (2σ)
***f*O₂**	QFM (quartz-fayalite-magnetite)	NNO (nickel-nickel oxide)

The magma ascent rates (*v*) were calculated dividing the residence time (τ) by the maximum depth (Z_{max}) as in Armienti et al. (2012). Here, Z_{max} was calculated using the lithostatic pressure equation, where the maximum pressure obtained through thermobarometry calculations was divided by the crust density calculated by Tenzer et al. (2011)(i.e., mean surface rock density for New Zealand = 2440 kg/m^3) and the constant for acceleration due to gravity (g = 9.81 m/s^2). Further information about the calculations is provided in Chapter 5.

3.5 Chemical thermodynamics

The influence of temperature (*T*), pressure (*P*) and source composition in magma products (*i.e.*, melts, crystals), can be interpreted through chemical thermodynamics. This involves the assessment of the energetic equilibrium of the system, using state functions with constrained parameters (*e.g.*, fixed *T*, *P* and bulk composition) in phase equilibrium calculators such as MELTS (Ghiorso & Gualda, 2015; Lesher & Spera, 2015). For this, the local equilibrium (*i.e.,* equilibrium in compositionally homogeneous regions) is assessed to determine the state of the system, evaluating the conditions required to develop a mineral assemblage and its stability, allowing the measurement of timescales and rates (Ghiorso, 1985; Ghiorso & Sack, 1995; Ghiorso et al., 2002; Ghiorso, 2013; Ghiorso & Gualda, 2015; Gualda et al., 2012; Gualda & Ghiorso, 2015).

Likewise, many thermobarometers and hygrometers use state functions derived from the Gibbs free energy (*ΔG*) functions and the ideal gas law (*PV=nRT*), to reproduce the minimum energy required at fixed conditions to reach chemical equilibrium, through the use of simple expressions (Ghiorso, 1985; Ghiorso & Gualda, 2015). One example is provided by Waters & Lange (2015) in the formulation of their hygrometer, using G as a function of *T, P* and composition (*X*), involving terms such as enthalpy (Δ*H*), entropy (Δ*S*), volume (Δ*V*), and the equilibrium constant (*K*):

$$\Delta G(T,X,P) = 0 = \Delta H°(T) - T\Delta S°(T) + RTlnK + \int_0^P \Delta V_T^{\circ}(P)dP \quad (1)$$

State functions are also applicable for equilibrium calculation of specific conditions, such as the oxygen fugacity, through the use of a fixed chemical potential for oxygen (Ghiorso, 1985; Ghiorso & Carmichael, 1985; Ghiorso & Gualda, 2015). Fixed oxygen redox states are commonly applied to the equilibrium determination in magmatic systems, through the imposition of an oxygen fugacity buffer (*e.g.*, NNO). This allows the assessment of changes

in G under the premise that the crystalline phases present in the assemblage represent the effective concentrations linked to the release or absorption of oxygen while all the other variables fixed (i.e., constant *P*, *T* and composition) (Ghiorso, 1985; Ghiorso & Carmichael, 1985; Ghiorso & Gualda, 2015).

3.5.1 Thermobarometry

Thermobarometers inform the temperature and pressure of the system at which different phases coexist (*i.e.*, magma and crystals) relying on the compositional partitioning of elements between phases in a system at equilibrium (Ghiorso & Gualda, 2015), allowing inference of magmatic processes and storage conditions (e.g., Masotta et al., 2013; Putirka & Condit, 2003). These are tested and calibrated through partial melting experiments (e.g., The library of experimental phase relations from Hirschmann et al., 2008) using global regressions to determine the minimum number of parameters (*i.e.,* significant parameters) required to reach equilibrium, minimizing the error on the dependant variable (*i.e.*, *T* or *P*) (Putirka et al., 1996; Putirka, 2008).

Four thermobarometers were used in the present study to constrain the *P-T* conditions. Two thermobarometry iterations were performed in the Python3 tool Thermobar (Wieser et al., 2022) using the orthopyroxene-liquid thermobarometer from Putirka (2008), and the clinopyroxene-liquid geothermometer from Putirka (2008) in combination with the clinopyroxene-liquid geobarometer from Neave & Putirka (2017). Pyroxene-based thermobarometers were chosen considering pyroxene is used to constrain the residence times in microlites (see 3.4.3). Likewise, thermobarometers were chosen based on the standard errors of estimate (SEE), the calibration set (*i.e.*, number of experiments used) and mineral phases available in the samples (*i.e.*, presence of ortho- or clinopyroxene).

The orthopyroxene-liquid thermometer is defined by equation 28a in Putirka (2008) which was calibrated with data from 793 experiments, with a systematic standard error (SEE) of ± 39 °C and ranges of applicability of T = 750 – 1600 °C, P = 0.0001 - 11.0 GPa, SiO_2 = 33 – 77 wt% and H_2O = 0 - 14.2 wt% (Putirka, 2008). The orthopyroxene-liquid barometer was calibrated using experimental data from 592 experiments, obtaining an SEE of ± 2.6 kbar, and is defined by equation 29a in Putirka (2008). The clinopyroxene-liquid thermometer was calibrated from 1174 experiments for P <70 kbar with an SEE of ± 45 °C, and is defined by equation 33 in Putirka (2008). Finally, the clinopyroxene-liquid barometer was calibrated from 113 experiments for ultramafic to intermediate composition in the ranges for T = 950 – 1400 °C and P = 0.001 – 20 kbar with SEE of ± 1.4 kbar, and is defined by equation 1 in Neave & Putirka (2017). The thermobarometry iterations were performed to reach a consistent solution for the *P-T* conditions of the system. Since the thermobarometers require water content input, the water content found through plagioclase hygrothermometry in section 3.5.2 was used based on the occurrence of plagioclase-pyroxene glomerocrysts in the samples as seen in Chapter 5 and Chapter 6.

Additionally, two online machine thermobarometers were used. First, the magmatic liquid-assemblage thermobarometer MagMaTab v4.0 (Weber & Blundy, 2024), and second the clinopyroxene-only thermobarometer by Ágreda-López et al. (2024), since there is no pressure, temperature or water content input requirement. MagMaTaB uses an -extremely randomized trees- random forest algorithm applied to a large experimental database (i.e., 2545 experiments), allowing the calibration of P-T regression models for magmas and increasing the predictability of these by using machine learning (Weber & Blundy, 2024). The model uses as inputs the melt compositions and mineral assemblage, providing root-mean-square-errors of P = 1.9 kbar and T = 42 °C for grouped testing data (i.e., using all the experimental data) when the results are not filtered (Weber & Blundy, 2024). The machine

learning clinopyroxene-only thermobarometer by Ágreda-López et al. (2024) uses a -extremely randomized trees- random forest algorithm applied to a data base of 1425 experiments combined with a Monte Carlo simulation to check and constrain any analytical errors associated to the model prediction, providing root-mean-square-errors of P = 2.5 kbar and T = 57 °C (Ágreda-López et al., 2024).

3.5.2 Hygrometry

Pre-eruptive information regarding the magmatic evolution, storage conditions and the ascent path can be obtained through the assessment of the solubility of H_2O in magmas, since it is directly proportional to changes in pressure (Barth & Plank, 2021; Edmonds & Wallace, 2017; Yavuz & Yıldırım, 2018). Hygrometers are used to estimate the dissolved water content of a liquid phase (*i.e.,* silica melt) in equilibrium with a coexistent solid phase (*i.e.*, crystals) relying in the compositional partitioning of elements between phases (Ghiorso & Gualda, 2015).

Although there are hygrometers based on clinopyroxenes (e.g., Perinelli et al., 2016; Plank et al., 2004) most of the pyroxenes in the samples are orthopyroxenes, reason why plagioclase, which is an abundant mineral phase in the samples, was chosen to determine the water content. Moreover, plagioclase is considered a potentially good hygrometer since it prevents water loss from the crystal lattice (i.e., resist H+ diffusion into the magma due to depressurization in Johnson & Rossman, 2013), and is sensitive to changes in pressure, temperature and water concentrations (Barth & Plank, 2021; Masotta & Mollo, 2019; Putirka, 2005; Waters & Lange, 2015).

For the water calculation, an iteration of the plagioclase-liquid hygrometer from Waters & Lange (2015) and the thermometer from equation 24a in Putirka (2008) was used in the Python3 tool Thermobar (Wieser et al., 2022). This plagioclase-liquid hygrometer was first

formulated by Lange et al. (2009) as a multiple linear regression equation with H_2O wt% as the dependent variable, allowing calculation of the H_2O wt% without information of the H_2O melt concentration. The hygrometer that was used in this study is defined by equation 14 in Waters & Lange (2015), fitted from calibration of 214 experiments on hydrous and anhydrous plagioclase-liquid equilibrium with an SEE of ±0.35 H_2O wt% and R^2 of 0.98. Since the hygrometer and thermometer required *P* input, the pressure determined with MagMaTab was used as the initial input for water calculation while the iteration in Thermobar allowed reaching a consistent solution for the *T*-H_2O conditions of the system.

3.5.3 MELTS Modelling

AlphaMELTS 2.3 (Smith & Asimow, 2005) was used to complete the thermodynamical modelling in this study, since it has the capacity of subroutine execution of the algorithms of other MELTS (Asimow & Ghiorso, 1998; Ghiorso & Sack, 1995) software versions and derivates such as rhyolite-MELTS (Gualda et al., 2012), pMELTS (Ghiorso et al., 2002) and pHMELTS (Asimow et al., 2004), using a more suitable interface. The ranges of pressure, temperature and water content were adjusted from the results obtained through the thermobarometry and thermohygrometry calculations. The modelling followed a fractional crystallization path maintaining the melt-phase equilibria under an oxygen fugacity buffered at NNO (nickel-nickel-oxide) following the parameters set in previous studies performed in the TgVC (e.g., Kilgour et al., 2013; Kilgour et al., 2014; Kilgour et al., 2016; Lormand et al., 2020; Shane et al., 2008).

The MELTS modelling was used to further constrain the P-T conditions of the melts and to determine the magma compositions that originated the crystal cargo. For this reason, the groundmass compositions, whole rock compositions of the samples in this study and TVZ whole rock compositions found in the literature were used as starting materials. The

groundmass compositions were used since those represent the carrier melts (e.g., Ubide et al., 2023) and should provide the better approximation to constrain the P-T conditions of the magmas. Meanwhile, the whole rock compositions which represent the carrier melt plus the crystal cargo (e.g., Ubide et al., 2022) were use as an approximation of the magmas that may have generated the crystals that were not in equilibria with the carrier melts.

Chapter 4 The influence of the aspect ratio in the determination of CSD slopes: comparing 2D versus 3D.

Silvia Catalina Moreno-Alfonso[1], Satoshi Okumura[2], Stuart Mead[1], Georg F. Zellmer[3], Yoshiyuki Iizuka[4], Masahiro Yasutake[5], Kentaro Uesugi[5] and Akira Miyake[6]
[1]Volcanic Risk Solutions, School of Agriculture and Environment, Massey University, Palmerston North, New Zealand.
[2]Department of Earth science, Graduate school of Science, Tohoku University, Sendai, Japan.
[3]Institute of Geosciences, University of Bonn, Bonn, Germany.
[4]Institute of Earth Sciences, Academia Sinica, Taipei, Taiwan
[5]SPring-8, JASRI, Hyogo, Japan
[6]Division of Earth and Planetary Sciences, Graduate School of Science, Kyoto University, Kyoto, Japan

This chapter was submitted as a paper to American Mineralogist for publication.

Abstract

Crystal size distribution (CSD) slopes are used to calculate magma residence times, based on the principle that the slope is inversely proportional to the product of crystal residence times and growth rate. Most CSD studies are based on two-dimensional (2D) data, relying on statistical calculations and stereological corrections of the analyzed data to estimate three-dimensional (3D) size distributions using specialized software. However, the effect of this estimation on the actual CSD distributions and their slopes remains unclear. To evaluate the effect of this CSD slope calculation/estimation on crystal residence times, we compare CSD slopes estimated from 2D and directly measured from 3D data. A 2D data set of pyroxene microlites from a glassy lava sample from Mount Ruapehu (New Zealand) was used to generate CSD (2D-CSD) applying three different aspect ratios. These aspect ratios were calculated using known databases (i.e., CSDSlice and ShapeCalc), and the average aspect ratios from a 3D dataset. The CSD slopes between 10 – 20 μm were extracted and compared

to the slope obtained from a true CSD using synchrotron radiation X-ray computational tomography (3D-CSD). Our results show differences in the shape determination by the two databases compared to the average 3D aspect ratio, mainly impacting the intermediate/long axes ratio (*I/L*) showing a *I/L* ratio difference of 0.18 between both databases, that translate in slope differences of ±0.03 μm^{-1} compared to the 3D-CSD. The slopes were applied to the determination of crystal residence times using a known growth rate (i.e., 1.80×10^{-11} m/s), finding differences of approximately 31 h between those CSD determined with the databases, and nearly 17 h comparing the 2D-CSD to the 3D-CSD. Our results contribute to the discussion about which is the best shape estimate to use for 2D stereological conversions, highlighting the uncertainties derived from the statistical calculations of the aspect ratios, and the difficulties in replicating true 3D crystal distributions. We conclude that limitations can be circumvented by using 3D datasets.

Keywords: Crystal size distributions, Aspect ratios, Microlite, 2D, 3D.

4.1 Introduction

Crystal size distributions (CSDs) describe the population density (*n*) of crystals as a function of the crystal size (Marsh, 1988). The CSD in volcanic rocks have been used to obtain information about the crystal residence times in magma using the CSDs slope data (e.g., Armienti et al., 1994; Cashman, 2020; Lormand et al., 2020; Nugroho et al., 2019; Preece et al., 2013). The slopes ($1/G\tau$), represent the reciprocal product of growth rate (G) and residence time (τ), where if τ is known, G can be calculated, or vice versa (Marsh, 1988). This method provides an easy approach to the calculation of the time between injection and eruption (e.g., Lormand et al., 2020; Preece et al., 2016) by using microlites (i.e., groundmass crystals that grow during magma ascent with size 1 - 30 μm in width in Zellmer, 2021), providing useful information for volcanic forecasting (e.g., Bonechi et al., 2024; Pappalardo

& Mastrolorenzo, 2010; Resmini & Marsh, 1995), considering a steady and time-dependent system where the growth rate is constant (Marsh, 1988, 1998).

CSD studies are mostly conducted by transforming two-dimensional (2D) data into three-dimensional (3D) data through stereological corrections to reveal the actual 3D population (e.g., Billon et al., 2025; Luo et al., 2024; Suhendro et al., 2025). These stereological corrections are typically done using the software CSDCorrections (Higgins, 2000) and crystal shape databases such as CSDSlice (Morgan & Jerram, 2006), which have been used to calculate almost all reported CSDs since their release (Fornaciai et al., 2015; Okumura et al., 2022; Wang et al., 2022). However, the stereological transformation of the data into a true 3D distribution can be complex since the measurements obtained from the crystals might not represent the crystal shapes accurately (e.g., Higgins, 2000; Mock and Jerram, 2005; Morgan and Jerram, 2006).

In 2D, the crystal shape is determined from width (w) and length (l) measurements, through a series of robust statistical calculations (e.g., Higgins, 1994; Higgins, 2000; Mangler et al., 2022; Morgan & Jerram, 2006). These calculations allow the estimation of the aspect ratio, defined as the ratio between the short (S), intermediate (I) and long (L) axes of a best fitting ellipsoid, which are used as an input for the stereological corrections that determine the CSDs (e.g., Higgins, 2000; Mangler et al., 2022; Morgan & Jerram, 2006). This means, the shape determination model used will have a direct impact on the slopes of the CSDs (Mock & Jerram, 2005). These shape determination models are able to estimate the best fitting morphology while considering the most common problems derived from small crystal populations such as cutting section and intersection effects (e.g., Higgins, 1994; Higgins, 2000, 2006; Mangler et al., 2022; Morgan & Jerram, 2006). Since the crystal population and shape is determined statistically, it is suggested that a minimum of 300 intersections (i.e., w

and *l* measurements in crystals) are required to get a ratio that can reliably approximate the actual shape of the crystals (Morgan & Jerram, 2006). However, true 3D datasets show a great variation on the crystal aspect ratios, and there is still uncertainty on which is the best shape estimate to use for the stereological conversions, since these do not account for the potential differences in the aspect ratios between crystals (e.g., Gualda & Rivers, 2006; Jerram & Higgins, 2007; Mock & Jerram, 2005). Hence, the population size and the shape model used will impact directly the calculation of the crystal residence times (Mock & Jerram, 2005).

The uncertainties of the shape determination can be solved using 3D data, which represent the real dimensions of the crystals. 3D datasets of ~200 crystals are required to reproduce CSDs (Mock & Jerram, 2005), which is slightly less than the minimum number of crystal required to constrain the 3D shapes from 2D data. Nonetheless, the 3D measurements do not require stereological correction, and any type of crystal shape can be measured directly unlike 2D, in which the sample orientation, size of the crystals and shape approximation model can influence the CSD determination (e.g., Higgins, 1994; Jerram & Higgins, 2007; Mangler et al., 2022).

2D methods are considerably more convenient since the analytical equipment required is readily accessible, relatively inexpensive, and image acquisition and processing are fast (Jerram & Higgins, 2007). Furthermore, these methods have their advantages in the size of the analyzed areas (i.e., large samples can be analyzed within a short time) and the determination of touching crystal (i.e., lattice orientations) and compositions, when the imagery is acquired with optical microscopes, electron microprobes or electron backscatter diffraction (e.g., Castro et al., 2013; Griffin et al., 2023; Suhendro et al., 2025). In contrast, high-resolution 3D equipment (i.e., synchrotron radiation X-ray micro-computational

tomography - SR-XCT), where available, can be useful for the determination of very small particles sizes and shapes, especially for high-contrast minerals where there is no crystal clustering (e.g., Okumura et al., 2022; Okumura et al., 2024). As 3D scanning is generally in-situ, the use of 3D datasets can successfully reproduce CSD distributions for different crystal sizes by adjusting the resolution and sample size without the need of a special treatment (e.g., polishing, carbon coating, impregnation) of the samples (e.g., Gualda et al., 2004; Gualda & Rivers, 2006; Pamukcu & Gualda, 2010). Although the volume size of the samples scanned by 3D methods is usually smaller than those from 2D, the measurement of the crystals is direct. With this direct measurement, it is possible to attain the same level of reliability from a smaller specimen compared to 2D as long as the minimum sample number condition is fulfilled to ensure CSD's reproducibility (i.e., ~200 crystals for 3D CSD in Mock & Jerram, 2005).

Considering the importance of crystal shape in calculating crystal residence times, we focus on comparing the CSD slopes obtained from 2D and 3D methods. To achieve this, pyroxene microlites from a glassy lava sample were analyzed using both SR-XCT to obtain true 3D crystal dimensions, and backscattered scanning electron microscopy (BSE-SEM) to generate an equivalent 2D dataset, to determine the influence of the aspect ratio determination method on the CSD slopes.

4.2 Experimental Methods

One sample of glassy andesitic lava from the Mangawhero Formation of Mount Ruapehu (New Zealand) was collected to perform the analyses. Pyroxenes microlites were selected as the target mineral phase due to their high reflectance (i.e., light grey in images) which make them easy to identify and isolate in both 2D and 3D images, facilitating the segmentation process (i.e., the definition and set up of the threshold range). The pyroxene microlites show

tabular to acicular shapes and represent about 20% of the crystals in the sample (Figure 4.1). Image acquisition was carried out by SR-XCT and BS-SEM.

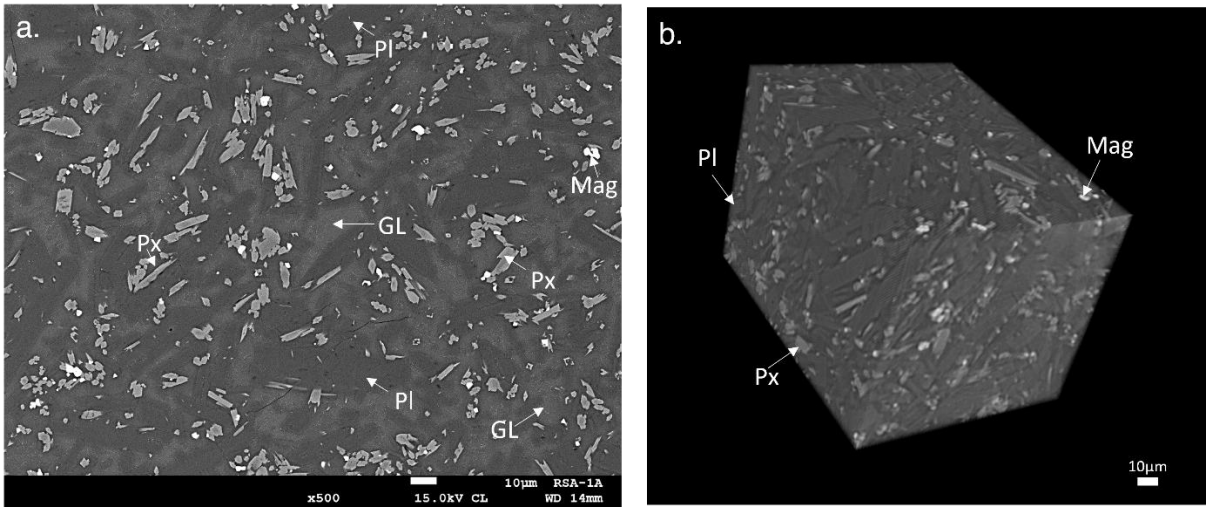

Figure 4.1. Plagioclase and two-pyroxene andesite.a. BS-SEM 2D image. b. SR-XCT 3D reconstructed model. Pl: plagioclase, Px: Pyroxene, Mag: Magnetite, GL: glass. Note the shapes of the pyroxenes which look tabular to acicular in the 2D image.

4.2.1 Image acquisition and segmentation

4.2.1.1 3D SR-XCT

For SR-XCT analysis, the sample was prepared using a plasma-focused ion beam (FIB) system equipped with FE-SEM (Helios5 Hydra UX Dual Beam, Thermo Fisher Scientific) at SPring-8, resulting in a piece of 130 µm x 130 µm x 65 µm in size, which was mounted in a titanium needle. The sample was analyzed at BL47XU of the SPring-8 facility (Japan) using an X-ray energy of 15 keV and voxel size of 194 nm.

Following image acquisition, the SR-XCT data was reconstructed to 8-bit images using the reconstruction and convert for absorption CT software (ct-rec) from SPring-8 (Uesugi, 2025), and processed to isolate the pyroxene crystals for measurement using the software series SLICE (Nakano et al., 2006), a free open-source series of software written in a C language that processes 3D data. A region of interest (ROI) was isolated using the subroutine SliceIT to obtain a sequence of 691 images of 530 x 494 pixels (102.82 µm x 95.84 µm) which was

used for the segmentation (Figure 4.2a steps 1 and 2). These images were cleaned to adjust contrast and brightness using ImageJ (Schindelin et al., 2012; Schneider et al., 2012) (Figure 4.2a step 3).

The segmentation was performed using the subroutine SlicePVR applying a manual pixel threshold (85 - 134) to isolate the pyroxene (Figure 4.2a step 4), by binarizing the image to reflect only the selected threshold. This pixel thresholding is based on the linear attenuation coefficient (LAC) distribution, where after checking the pixel value histogram, a pixel range is assigned to the target mineral (e.g., Okumura et al., 2008; Tsuchiyama et al., 2005; Tsuchiyama et al., 2013). Subsequently, the images were denoised to eliminate anomalous pixels using the erosion and dilation by 2 pixels subroutine SliceED (Figure 4.2a step 5). Finally, the data was clustered using the subroutine SliceMCL (Figure 4.2a step 6), to obtain the crystal dimensions for long (*L*), intermediate (*I*), and short (*S*) axes, determined by the best-fitted ellipsoid (e.g., Okumura et al., 2008; Okumura et al., 2022a). Measurements of the crystal axes (i.e., long, intermediate and short) can be found in an online repository (see Appendix 2).

4.2.1.2 2D BS-SEM

For BS-SEM analysis, the sample was prepared as an epoxy mount containing a 10 mm x 10 mm chip of rock, which was polished, and carbon-coated to be analyzed in a JEOL Thermal Field Emission Scanning Electron Microscope (FE-SEM) JSM7100F at Academia Sinica (Taiwan), using an acceleration voltage of 15 kV and a beam current of 0.12 nA. 10 images of 2560 x 1920 pixels (250.98 μm x 187.94 μm) were obtained from the sample to perform the segmentation.

The 2D BS-SEM images segmentation and measurement was performed in ImageJ (Schindelin et al., 2012; Schneider et al., 2012). Since pyroxene is easily identifiable after

cleaning the image (i.e., adjusting contrast and brightness - Figure 4.2b step 1), a pixel threshold was applied to isolate the pyroxenes and binarize the images. After the binarization, we applied a combination of four functions: erosion, dilation, noise reduction (i.e., despeckle) and filling holes, to eliminate isolated pixels and separate crystals (Figure 4.2b steps 2 - 3). Measurements of the crystal length (*l*) and width (*w*) was completed using the measurement tool included in ImageJ (step 4 in Figure 4.2b) using the best-fitting ellipse method for calculation. The length and width measurements can be found in an online repository (see Appendix 2).

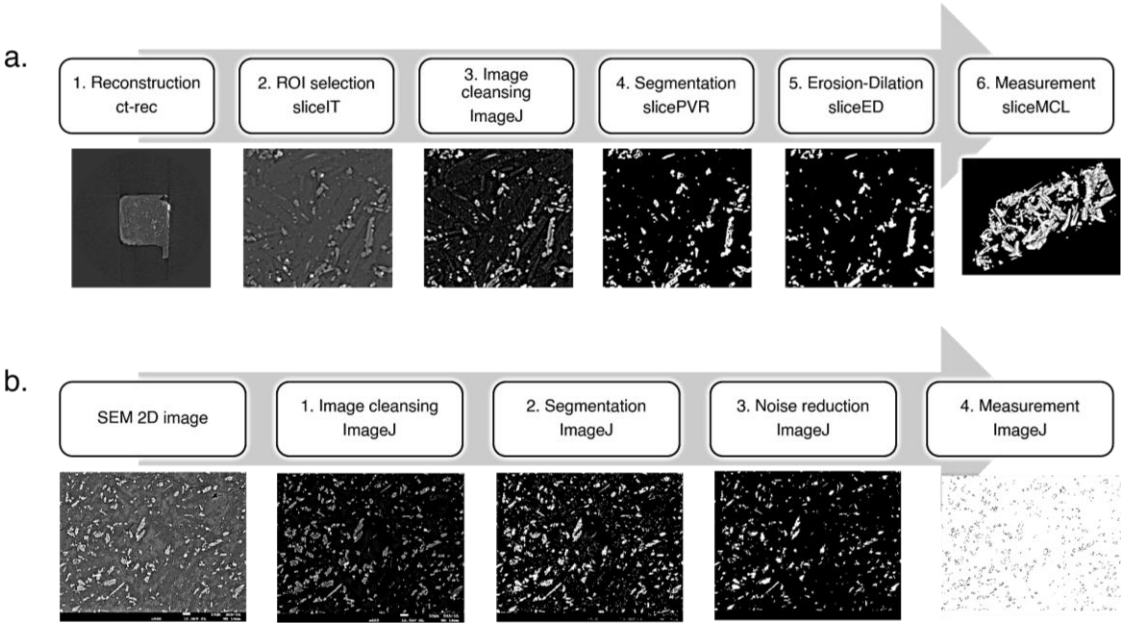

Figure 4.2. Data reduction process for crystal measurement.a. 3D data process. 1. Reconstruction of the 3D sequence. 2. Selection of the region of interest (ROI). 3. Image cleansing: adjusting of contrast and brightness. 4. Segmentation: definition of the pixel threshold for pyroxene. 5. Erosion-Dilation: erosion and dilation of pixels to eliminate isolated pixel and separate crystals. 6. Measurement: clustering of pixels and measurement using the best fitting ellipsoid method. b. 2D data process. 1. Image cleansing: contrast and brightness adjustment. 2. Segmentation: definition of the pixel threshold for pyroxene. 3. Noise reduction: holes filling, erosion and dilation to eliminate isolated pixel and separate crystals. 4. Measurement, using the best fitting ellipsoid method. Underneath every step is the tool/program used to perform the task.

4.2.2 Aspect ratios

The determination of the 2D aspect ratios has been widely performed in the literature using CSDSlice (e.g., Giuliani et al., 2020; Preece et al., 2013; Preece et al., 2016; Wang et al.,

2022). However, to assess the impact of CSDSlice on shape calculations, we compared it with ShapeCalc, a more robust database that includes a larger number of shape models (i.e., 703 in CSDSlice and 2681 in ShapeCalc), and accounts for a wider range of *S*:*I*:*L* ratios (i.e., 1:1:1 to 1:10:10 in CSDSlice and 1:1:1 to 1:20:20 in ShapeCalc).

Hence, two aspect ratios, 2Dc and 2Ds, were obtained from 2D measurements of crystal length (*l*) and width (*w*) using the databases CSDSlice v5 (Morgan & Jerram, 2006) and ShapeCalc v1.0 (Mangler et al., 2022) respectively. ShapeCalc provides uncertainties for the *S*/*I* and *I*/*L* ratios at one standard deviation (1σ), whereas CSDSlice does not. Additionally, 3D aspect ratios were determined for individual crystals in the sample. These ratios were averaged to obtain a representative 3D aspect ratio (3Da), with uncertainties calculated as the standard deviation (1σ) for the *S*/*I* and *I*/*L* ratios. Together with the two 2D-derived aspect ratios (2Dc & 2Ds) the 3Da was used in the 2D-CSD calculations.

To compare the crystal shapes estimated by each method, aspect ratios were visualized using Zingg diagrams (Zingg, 1935) which classify crystals as equant (S≈I≈L), prolate (S≈I < L), tabular (S < I≈L) and bladed (S < I < L).

4.2.3 CSD generation

The 3D-CSD derived from SR-XCT images were calculated as a function of the long (*L*) axis. For each size interval (i.e., bin), the number of crystals was normalized by the measured volume to obtain the number density, which was subsequently divided by the width of the size interval (i.e., difference between the minimum and maximum size of the bin range) to calculate the population density (*n*). The CSDs were plotted as ln(*n*) versus the average crystal size per bin. Uncertainties were calculated as twice the square root of the number of crystals per bin (e.g., Gualda, 2006; Pamukcu & Gualda, 2010). Bins containing three or

fewer intersections have been excluded from the analysis (e.g., Higgins, 2000; Okumura et al., 2022).

Binning intervals were defined using a base-10 logarithmic scale with five bins per decade (i.e., 5 bins between 1 and 10 μm and 5 bins between 10 and 100 μm) as in Higgins (2000). The analyzed crystal population includes crystals with *S*-axis dimensions between 1 – 30 μm and *L*-axis dimensions <100 μm. In 2D distributions, the *w*/*l* ratio is commonly assumed to approximate the *S/I* ratio, such that the measured width represents the short axis and the length the intermediate axis of the crystal (e.g., Higgins, 1994; Higgins, 2000; Mangler et al., 2022; Morgan & Jerram, 2006).

Using the same binning strategy, 2D-CSDs were calculated for the long (*L*) axis from BSE-SEM images using the 2D crystal measurements (i.e., *l* and *w*) and three aspect ratios (2Dc, 2Ds & 3Da), implemented in the software CSDCorrections v1.61 (Higgins, 2000), a widely use method for CSDs determination (e.g., Cashman, 2020; Lormand et al., 2020; Okumura et al., 2022).

For both 3D and 2D datasets, CSD slopes were calculated over the 10 – 20 μm size range to consistently compare distributions derived from using different aspect ratios. These slopes were then used to estimate crystal residence times using a variation of equation 68 in Marsh (1988), where the residence times (τ) is related to the slope and a known growth rate (G) accordingly to $\tau = -1/(\text{slope}*G)$. The growth rate used was 1.80 (±0.6) × 10^{-11} m/s, recalculated by Lormand (2020) from data of Zellmer et al., (2016, 2018) for orthopyroxenes of the Mangatawai Formation from Ngauruhoe volcano, which is part of the southern Taupo volcanic zone as Mount Ruapehu, and has shown similar CSDs (Lormand et al., 2020).

The resulting CSD and residence times were compared to evaluate the influence of the aspect ratio in the CSDs construction, its effect on CSDs slope determination, and the subsequent propagation of these effects into crystal residence times calculations.

4.3 Results

The segmentation results are summarized in Table 4.1 showing a larger number of crystals identified for the 2D dataset compared to the 3D dataset (i.e., 438 crystals for the 3D dataset and 3328 crystals for 2D dataset), which are expected from the image sample sizes. Nonetheless, both data sets comply with the minimum number of crystals required to perform the CSDs calculation (i.e., ~200 crystals for 3D-CSD and >300 crystals for 2D-CSD).

Table 4.1. Pyroxene microlite crystals identified by 2D and 3D.

	2D	**3D**
Sample size	4854519 μm^2	1320949 μm^3
Number of crystals	3328	438
Population density	6.86 x $10^{-4}/\mu m^2$	3.32 x $10^{-4}/\mu m^3$

4.3.1 Aspect ratios

The aspect ratios are calculated as an average for the entire crystal population based on the *w*/*l* ratio of individual crystal compared to different shape models in known databases such as CSDSlice (Morgan & Jerram, 2006) and ShapeCalc (Mangler et al., 2022). To compare these measurement to the 3D measurements we used the *S*/*I* ratio from 3D. Most of the models use the *w*/*l* ratio as an approximation to the *S*/*I* ratio (e.g., Higgins, 1994; Mangler et al., 2022; Morgan & Jerram, 2006). However, as seen in Figure 3a, the actual 3D crystal distributions are more heterogeneous and are not truthfully represented by the *w*/*l* measurements (Figure 4.3a). Here, the influence of the shape models used in the aspect ratio estimation becomes highly relevant.

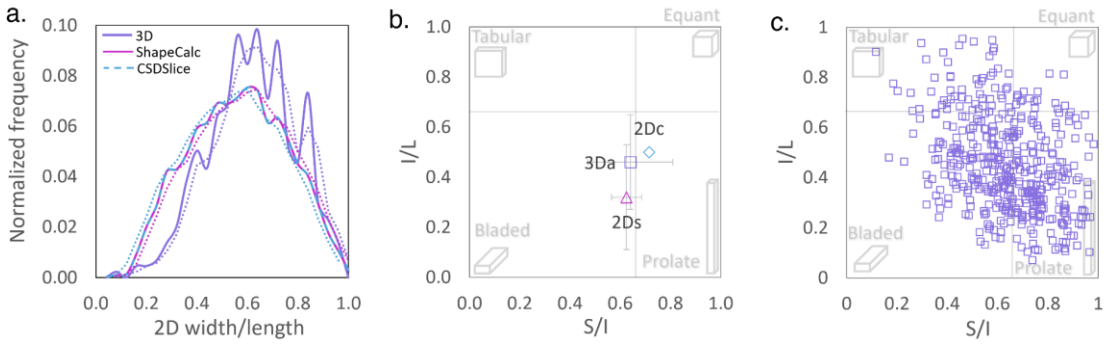

Figure 4.3. Crystal frequency distribution and Zingg diagrams. Frequency distribution of the *w/l* ratio. For the 3D measurements the ratio *S/I* was plotted since most model use the equivalence *w/l=S/I* (e.g., Higgins, 1994; Mangler et al., 2022; Morgan & Jerram, 2006). The doted lines represent the moving average of the distribution. b. Pyroxene 2D estimated ratios from CSDSlice (2Dc) and ShapeCalc (2Ds), and 3D average ratios (3Da). Note how the CSDSlice (Morgan & Jerram, 2006) and ShapeCalc (Mangler et al., 2022), estimate different aspect ratios for the same distribution. Standard deviation (1σ) uncertainties are provided for 2Ds and 3Da. c. Aspect ratios for pyroxene individual crystals measured in 3D. Zingg diagram built after Zingg (1935). The fields in panels b and c correspond to equant (S≈I≈L), prolate (S≈I<L), tabular (S<I≈L), and bladed (S<I<L) crystal shapes.

The pyroxene crystals studied show mostly tabular and prolate (i.e., acicular) shapes in 2D images (Figure 4.1a), which coincides with the location of the aspect ratios in the Zingg diagram (Figure 4.3b). Here, the data from individual pyroxene crystals is concentrated on the region between the prolate and bladed fields (Figure 4.3c), coinciding with the location of the average 3D aspect ratio (3Da). Nonetheless, there are differences between 3Da, 2Dc and 2Ds (Figure 4.3b: Table 4.2). Although 2Dc and 2Ds are within the standard deviation of the 3Da, CSDSlice (2Dc) determined a *I*/*L* ratio similar to 3Da, while ShapeCalc (2Ds) did the same with the *S*/*I* ratio, showing notable differences in the shape calculation between both data bases (Figure 4.3b). The 3Da and 2Dc *I*/*L* ratios are consistent with that from ShapeCalc within the standard deviation (i.e., *I*/*L* 2Ds: 0.32 ± 0.21; 3Da: 0.46 ± 0.19; 2Dc: 0.50 in Table 4.2; Figure 4.3). However, the *S*/*I* ratio calculated by CSDSlice is not consistent with the one calculated by ShapeCalc within the standard deviation (i.e., *S*/*I* 2Ds: 0.63 ± 0.06; 2Dc: 0.71 in Table 4.2; Figure 4.3). The impact of these shape differences on the CSD plot is described in the next section.

Table 4.2. Pyroxene microlite aspect ratios estimated through CSDSlice and ShapeCalc, and the average aspect ratio of 3D direct measurements.

Ratio	*S*	*I*	*L*	R^2	*I/L*	*S/I*
2Dc[a]	1.00	1.40	2.80	0.842	0.50	0.71
2Ds[b]	1.00	1.60	5.00	0.997	0.32 ± 0.21(1σ)	0.63 ± 0.06 (1σ)
3Da[c]	1.00	1.56	3.40	-	0.46 ± 0.19(1σ)	0.64 ± 0.17 (1σ)

Aspect ratio estimation method: [a]CSDSlice, [b] ShapeCalc & [c]3D average

4.3.2 CSD

Figure 4a shows the CSD plots generated using 2D and 3D data. Although both 3D and 2D plots describe similar shapes independent of the aspect ratio used (i.e., downturn for the smaller sizes and log-linear distributions for sizes over 10 μm), there are some evident differences between 3D and 2D plots and, between 2D plots determined using different aspect ratios (Figure 4.4a). While the 2D plots built using the aspect ratios estimated by CSDSlice (2Dc) and the average aspect ratio from 3D measurements (3Da) have almost the same trend, the CSD obtained using the aspect ratio estimated by ShapeCalc (2Ds) shows longer crystals, i.e., the 2Ds plot looks displaced toward larger sizes compared to the other 2D CSDs and shows a softer slope (Figure 4.4a - b). Evaluating the uncertainty in the *I*/*L* ratio (i.e., 1σ = ± 0.21) calculated by ShapeCalc, it is notable that *I*/*L* plus 1σ (i.e., 0.53) produces similar slopes to 2Dc and 3Da *I*/*L* ratios (Table 4.3). If this modification is used for stereological corrections, the CSD shape coincides with those obtained using the 3D average and CSDSlice estimated aspect ratios, since the length of the crystal is recalculated (See Appendix 2; Figure S1 & Tables S10 – S12). For sizes under 5 μm the 3D, 2Dc and 3Da CSDs show almost the same distribution, however, for sizes larger than 5 μm there is a notable difference in the population density, and the slope of the CSDs seems slightly more pronounced for the 2D plots (i.e., 2Dc & 3Da) between 5 – 10 μm (Figure 4.4a). Notably, the 2Ds plot approaches the population density values of the 3D plot at the larger sizes (i.e., 25 – 30 μm in Figure 4.4a).

Since, our objective is to clarify the differences in the slopes towards the determination of crystal residence times, we selected a range size between 10 – 20 μm to perform the slope calculation, avoiding the downturns for all the CSD plots, and the flattening of the curve for the larger sizes crystal in the 3D and 2Ds plots (Figure 4.4b; Table 4.3). The slopes showed R^2 >0.999 and significance <0.01 for a confidence interval of 95% (Table 4.3). From the visual inspection of the slopes, it is clear that 2Ds has a gentler slope compared to the other plots (Figure 4.4b), showing a value of -0.17 μm^{-1} (Figure 4.4c; Table 4.3). As for 2Dc and 3Da the slopes are -0.23 μm^{-1} and -0.22 μm^{-1} respectively, with the 3D slope -0.20 μm^{-1} (Figure 4.4c; Table 4.3). The differences between 3D and 2D-CSD slopes are between 0.02 – 0.03 μm^{-1}, with the 3Da CSD slope the closest to the 3D (Table 4.3).

Table 4.3. Slopes of CSD from direct measurement (3D-CSD) and estimated through stereological corrections (2D-CSD).

		Slope (μm^{-1})	Slope range (μm^{-1})		Uncertainty	R^2	p-value (α=0.05)	Confidence interval (95%)	
3D-CSD		-0.200	-0.197	-0.203	0.003	0.999	0.005	-0.18	-0.22
2D-CSD	2Dc[a]	-0.234	-0.297	-0.241	0.007	0.999	0.009	-0.19	-0.28
	2Ds[b]	-0.166	-0.163	-0.169	0.003	0.999	0.006	-0.15	-0.19
	3Da[c]	-0.220	-0.215	-0.225	0.005	0.999	0.007	-0.19	-0.25

2D CSD aspect ratio estimation method: [a]CSDSlice, [b] ShapeCalc & [c]3D average

4.3.3 Slopes applied to the calculation of the residence times

To apply the slopes to the calculation of the residence times, we used the slope calculated for the 3D and 2D CSDs in combination with an orthopyroxene growth rate ($1.80 \pm 0.6 \times 10^{-11}$ m/s) recalculated by Lormand (2020) from data of Zellmer et al., (2016, 2018). The residence time calculations are summarized in Table 4.4.

The crystal residence times present values between 66 and 93 hours, which translates into a difference of over a day (i.e., 27 h – Table 4.4), between the different slopes used (i.e., 2Dc, 2Ds and 3Da). Notably, the lowest and highest residence time values are those of the 2D CSDs calculated using the databases (i.e., 2Dc = 66 h and 2Ds = 93 h – Table 4.4). The 2D

CSD slope calculated using the 3D average ratio, provided the smallest difference compared to the 3D CSD (i.e., ~7 h). Here, 2Ds provide the largest difference between the 3D and 2D (i.e. ~16 h).

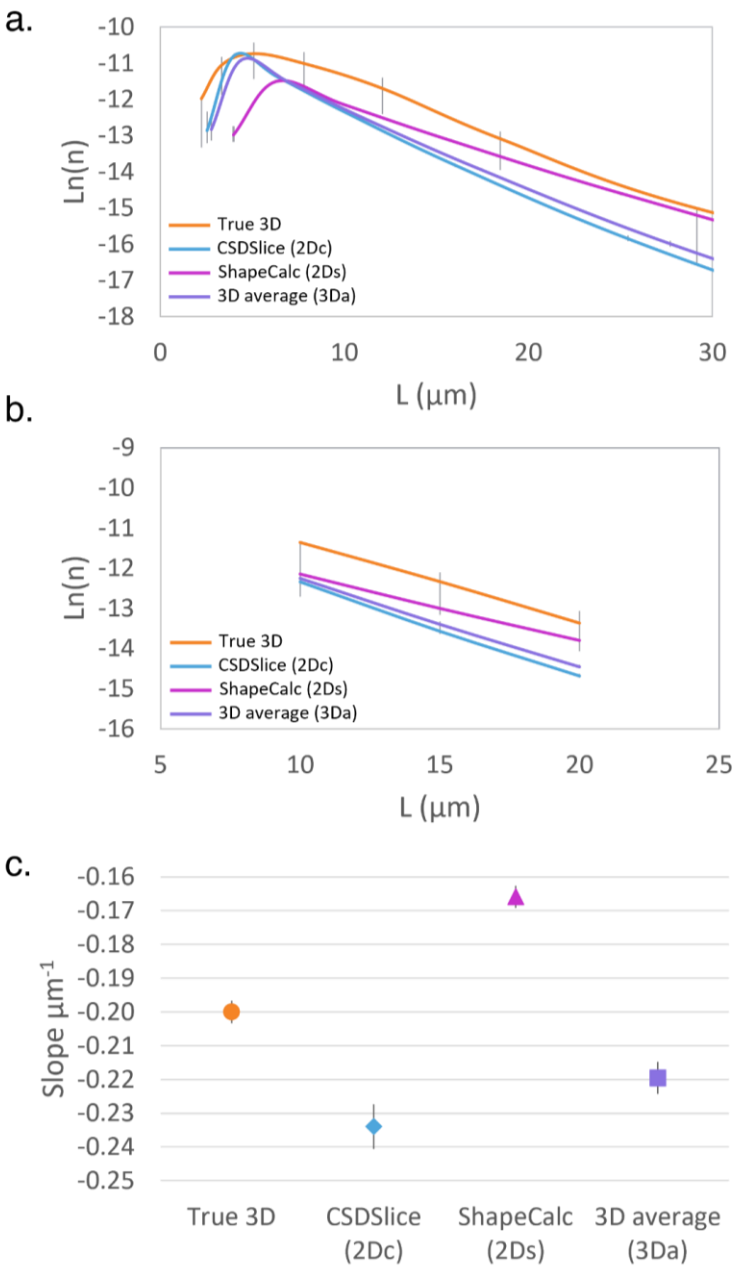

Figure 4.4. CSD plots and slopes.a. Pyroxene long axis (*L*)-plots for the range between 1 – 30 µm. Vertical error bars represent the minimum uncertainties for the population density (*n*). Horizontal bars represent the variation on the 2Ds CSD derived from the aspect ratio uncertainty provided by ShapeCalc. b. Pyroxene *L*-plots for the range between 10 – 20 µm used to calculate the slope. c. Pyroxene slopes for the range between 10 – 20 µm. The error bars represent the uncertainties in the slope calculation. 3D *L*-plot calculated using the direct measurements of the *L*-axis. 2D *L*-plots calculated using the measurements of the length (*l*) and width (*w*) of the crystal in combination with the aspect ratios in CSDCorrections (Higgins, 2000). These aspect ratios were calculated with CSDSlice (Morgan & Jerram, 2006): 2Dc, ShapeCalc (Mangler et al., 2022): 2Ds , and the average aspect ratio of the 3D measurements: 3Da.

However, the differences in the residence times are negligible when the slope (± 0.003 μm^{-1}) and growth rate (± 6 x 10^{-11} m/s) uncertainties are considered (Figure 4.5). While the uncertainties in the residence times derived from the slope are less than 2 h (Figure 4.5a), those derived from the growth rate can reach 2 days (i.e., 49 h; Figure 4.5b). The residence times derived from 3D-CSD, including the uncertainties, range from nearly 2 to 5 days (i.e., 57 - 118 h in Table 4.4; Figure 4.5b). This range covers the residence times calculated using the 2D slopes (i.e., 2Dc: 66 h, 2Ds: 93 h, and 3Da: 70 h in Table 4.4), overlapping the ranges derived from the slope and growth rate uncertainties (i.e., 2Dc: 48 - 102 h, 2Ds: 68 - 142 h, and 3Da: 52 - 108 h in Table 4.4; Figure 4.5b).

Table 4.4. Crystal residence times derived from 3D-CSD and 2D-CSD slopes in combination with a known growth rate.

		τ (hours)	min τ (hours)	max τ (hours)	slope uncertainty[d] (hours)
3D-CSD		77	57	118	±1.3
2D-CSD	2Dc[a]	66	48	102	±1.9
	2Ds[b]	93	68	142	±1.9
	3Da[c]	70	52	108	±1.6

2D CSD aspect ratio estimation method: [a]CSDSlice, [b] ShapeCalc & [c]3D average.
[d]Maximum error derived from slope uncertainties.

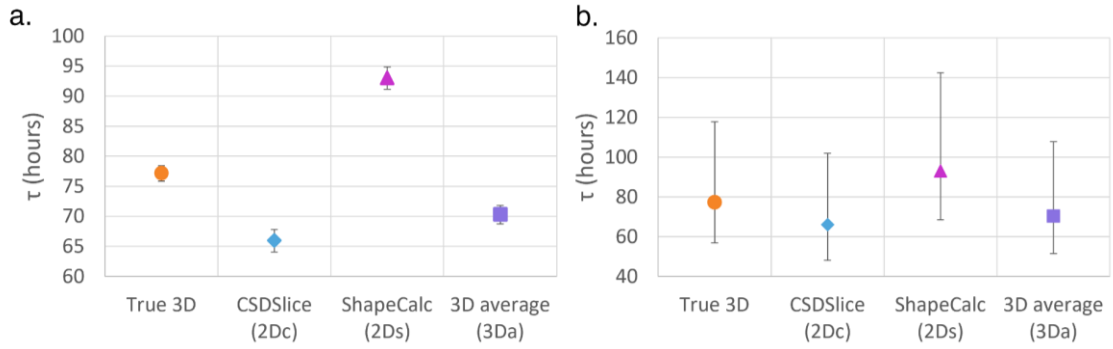

Figure 4.5. Crystal residence times. The residence times were calculated using the slopes in Table 4.3 and a well-known growth rate for orthopyroxene (1.80 × 10−11 m/s) used in Lormand et al. (2021). a. Crystal residence times including error bars for uncertainty derived from the slope calculation (Table 4.3). b. Crystal residence times including error bars for uncertainties derived from the slope (Table 4.3) and the growth rate (±0.6 m/s in Lormand, 2020). Note how the error bars overlap the residence time (τ) calculation for all the CDSs when the growth rate uncertainty is included.

4.4 Discussion

4.4.1 The influence of the aspect ratios in 2D-CSDs

It has been observed that there is a clear relation between the true shape of the crystals and the aspect ratios determined from 2D *l* and *w* measurements (Higgins, 1994; Higgins, 2000; Morgan & Jerram, 2006). For example, tabular shapes reach acceptable R^2 values (i.e., >0.8) by analyzing a lower number of crystals than cubic or acicular shapes (Higgins, 1994; Morgan and Jerram, 2006). This is explained by the sectioning of the crystals, where tabular shapes are likely to be cut showing true *S*/*I* or *S*/*L* sections, cubic shapes produce a large proportion of triangular cuts with no information, and acicular shapes have a low probability of cuts representing the length of the crystal (Morgan and Jerram, 2006). Hence, the 2D shape of the crystals produces errors in the determination of the true shape and size of the crystals, due to the cutting and intersection probability effects (Higgins, 1994). Since the shape determination is based on a statistical approach (e.g., Higgins, 1994; Higgins, 2000; Mangler et al., 2022; Morgan & Jerram, 2006), errors can be introduced by the uncertainties in databases used for shape determination (i.e., aspect ratio calculation).

Mangler et al. (2022) identified a bias in CSDSlice (Morgan & Jerram, 2006) that produces shapes with ratios S≈I for natural samples as observed in some CSDs studies (e.g., Preece et al., 2013; Preece et al., 2016), and in our results (Figure 4.3b). While CSDSlice *S*/*I* ratio (i.e., 0.71) locates in the prolate field, the ratios obtained from the 3D data (i.e., 0.64) and ShapeCalc (i.e., 0.63) are distributed in the bladed field (Figure 4.3b), showing a minimal difference in the *S*/*I* ratio value (Table 4.2). The database of ShapeCalc seems to be improved, using a more robust model that account for a larger number of shapes than CSDSlice (i.e., 1:1:1 to 1:20:20 in Mangler et al., 2022 versus 1:1:1 to 1:10:10 in Morgan and Jerram, 2006). However, in this study, ShapeCalc models did not improve CSDs

representation compared to directly measured 3D-CSDs (i.e., *L*-axis estimated size). In our sample, ShapeCalc produced *I*/*L* ratio of 0.32 is lower compared to the 3D aspect ratio (i.e., 0.46) and the one calculated by CSDSlice (i.e., 0.50). Hence, while ShapeCalc resolves the *S*/*I* bias, there is still an error in the calculation of the *I*/*L* ratio, producing a lower *I*/*L* ratio than in the directly measured shapes (Table 4.2). This error originates mainly from two factors: the difficulty of measuring the *I*/*L* ratio (e.g., Higgins, 1994; Higgins, 2000) and lack of precision on the stereological corrections made for small crystals (e.g., Higgins, 2006). Our results support the statistical limitations on the determination of the *S*/*I* and *I*/*L* ratios, caused by shape variability which fails to represent heterogeneous crystal distribution in natural samples (e.g., Mangler et al., 2022).

Since no database is infallible in the calculation of the aspect ratio based on the *l* and *w* measurements, the best approach to define the most reliable one is to test the aspect ratios for the generation of CSDs. CSDCorrections assumes that the measured *l* is the intermediate length of a parallelepiped, while the measured *w* is the short length (Higgins, 2000). Therefore, the longest dimension is calculated based on the aspect ratios, and different results for the corrected *L* axis size are yielded, depending on the aspect ratio used as seen in Figure 4.4a (i.e., 2Dc versus 2Ds). Notably, the differences in the shape between the 2Dc and 3Da are minimum compared to 2Ds which presents variation on the calculated crystal size (i.e., 2Ds plot shifted towards larger sizes compared to the other plots). Here, the miscalculation of the *L* values has caused a major effect on the CSDs determination, not only perceptible in the estimated sizes of the crystals but also in the gentler slope of the plot (Figure 4.4a - b). The steeper slope in the 2Dc and 3Da plots is determined by the *L* axis size estimated by CSDCorrections, i.e., if the program calculates a shorter *L*-axis size for the same crystal population, the slope will be steeper (e.g., 2Ds slope: -0.17 μm^{-1} versus 2Dc slope: -0.23 μm^{-1} in Figure 4.4).

Although ShapeCalc provides the uncertainty values for the *S/I* and *I/L* ratios (i.e., 1σ), without 3D data, it is not possible to know if the estimated crystal shape is accurate or not. In our case, we know that the estimated *I/L* ratio from ShapeCalc differs from the 3D average, but if only 2D data were measured, it is not possible to validate the *I/L* ratio to perform the correction (Figure S1). Even if different CSDs would be generated to account for the standard deviations of the shape model, it is not possible to determine which one is correct due to the large variations in the plots (Figure S1). Hence, although ShapeCalc provides useful information, CSDSlice offers a better approximation of the aspect ratio for 2D datasets for our results. However, we consider that the best option of approximation of the aspect ratio might be the average from the 3D measurements. If the 3D data is already available, the stereological correction of the 2D data can be bypassed, and the CSDs built from 3D true measurements that comply with the minimum number of crystals required (i.e., ~200 crystals).

4.4.2 The importance of the CSD slopes in the determination of crystal residence times.

The 3D-CSDs are assumed to be the truthful distributions of the crystals in the sample, since the measurements are performed directly in the particles (e.g., Jerram & Higgins, 2007), limiting the uncertainties derived of statistical analysis and stereological corrections applied to 2D datasets to obtain 2D-CSDs (e.g., Higgins, 2000). Furthermore, true 3D distributions are complex as observed in Figure 4.3a, meaning it is difficult to obtain an aspect ratio that comprise all the crystals shapes in one 2D sample. Since the crystal shape is fundamental for the construction of 2D-CSD, the differences on the aspect ratio impact directly on the slope determination.

In this study, the variations on the slopes between 3D and 2D are ±0.03 μm^{-1} (Table 4.3). Here, ShapeCalc (2Ds) and CSDSlice (2Dc) present the milder (i.e., 2Ds: -0.17 μm^{-1}) and

steeper (i.e., 2Dc: -0.23 μm^{-1}) slopes respectively. The slope of the CSD built using the average 3D ratio presents the smaller difference (i.e., 0.02 μm^{-1}) compared to the 3D-CSD slope (Table 4.3). The significance of the slopes under 0.01 show reliable results for each individual slope (Table 4.3). However, within the confidence interval of 95% represented by the significance values, it is notable that unlike 2Dc and 3Da which partially fall within the confidence interval of 3D, 2Ds is barely overlapping (Table 4.3). These results show that the aspect ratios failed to reproduce the 3D true CSDs. Although significant differences between 2D and 3D slopes can be bypassed by using 3D average aspect ratios (e.g., Okumura et al., 2022), it is preferable to use true 3D distributions that are not influenced by statistical calculations, if the mineral phase (i.e., minerals with high contrast clearly distinguishable in 3D datasets) and objective of the study (e.g., study of complex materials such as plutonic rocks) allows it (e.g., Cashman, 2020).

To test the influence of the slopes in the calculation of crystal residence times, we used the slopes obtained from 3D and 2D-CSDs and a known orthopyroxene growth rate (i.e., 1.80×10^{-11} m/s). Since, there is a variation in the slopes of ± 0.03 μm^{-1}, it was expected to have a variation in the residence times between those calculated from 3D-CSD and 2D-CSD slopes. It is less than 16 hours in our case (Table 4.4). Solely considering the error in CSD slopes through various methods, it leads to maximum crystal residence time differences of <2 h for each slope (e.g., 2Dc: 66 ± 1.9 h in Table 4.4), leading to differences up to 31 h between methods (i.e., 2Ds: 95 h versus 2Dc: 64 h). This is negligible when considering other uncertainties, particularly in growth rates where differences are up to 94 h (Table 4.4), as seen in Figure 4.5b, and the uncertainty ranges overlap across methods.

4.5 Implications

In this study we assessed the influence of the aspect ratios in the determination of the 2D-CSD slopes, by comparing 2D and 3D distributions of pyroxenes in a glassy lava sample from Mount Ruapehu (New Zealand). The volcanological implications of our study indicate the importance of crystal shape estimation methods in the CSD stereological corrections, their impact on the CSD shape and slope, and their influence on the residence time calculation.

CSDSlice and ShapeCalc, the two databases used for shape determination in this study fail to reproduce the aspect ratio derived from the average, directly measured, 3D data, which contains a highly heterogeneous crystal population (Figure 4.3a). Although an exact match of the crystal shapes is not expected, it is important to consider how these databases provide different results compared to each other, and the cause of disparities. Our results can be explained by the bias observed in CSDSlice by Mangler et al., (2022), in which the natural samples provide *S/I* ratios close to 1 (i.e., overestimation of the *S/I* ratio in Figure 4.3b), and the failure to reproduce the *I/L* ratio in ShapeCalc (i.e., underestimation of the *I/L* ratio in Figure 4.3b). Despite both databases relying on robust statistical analysis including numerous models, our results confirm the difficulties in determining crystal shapes out of heterogenous populations, independently of the number of intersections (i.e., over 3000 crystals) used, if the statistical models fail to estimate the *S/I* and/or *I/L* ratios. Furthermore, it is not possible to determine if the shape provided by a database is precise or not as long as only the 2D distribution is used.

The use of databases such as CSDSlice or ShapeCalc depends on the decision of the final user since the shape of the crystal may be approximated better by one or another (e.g., tabular shapes may be better approximated by ShapeCalc in Mangler et al., 2022), however, for 2D

sets where the true shape of the crystals is not known, an uniformed decision must be made. In natural samples with highly heterogeneous distributions, it may not be possible to make a precise estimation of the aspect ratio. Here, we suggest the best approach to minimize the error related to the shape determination is to use 3D distributions. This bypasses the need for statistical estimations and their derived uncertainties (e.g., Cashman, 2020; Jerram & Higgins, 2007; Mock & Jerram, 2005; Okumura et al., 2022), and appears robust even with the disparities in sample dimensions and crystal number.

The uncertainties derived from the statistical calculations of the shape are propagated into the CSD and their slopes. 2D methods fail to reproduce slopes of 3D direct measurements (Table 4.3), despite having many more crystals. This means that the miscalculation of the aspect ratios in datasets with enough crystals (i.e., over 300) is unlikely related to the dataset itself but to the statistical approach used for the shape calculation. This can be observed in the stereological correction made by CSDCorrections using the same dataset with different aspect ratios (i.e., estimation of the *L*-axis in Figure 4.4a). The underestimation of the *I/L* ratio in ShapeCalc causes the displacement of the CSD plot and their attenuation (Figure 4.4a), modifying the CSD shape and impacting directly the slope value (Table 4.3). Since most CSD studies plot the ellipse major axis or maximum length (i.e., *L*-axis) on the x-axis (e.g., Griffin et al., 2023; Lormand et al., 2020; Suhendro et al., 2025), an overestimation of the *L*-axis, will turn into a significant error on the CSDs, affecting studies that rely on the CSD shape as an indication of magmatic processes (e.g., Berger et al., 2008; Higgins, 2011; Troll & Deegan, 2023) .

However, across all methods, the uncertainty in residence times is mostly driven by crystal growth rate uncertainties, making the slope-related error relatively minor. Differences of ~31 h between minimum and maximum residence times (i.e., 2Dc: ~64 h versus 2Ds: ~95 h)

originate from variations in the slope estimate from 2D-CSD aspect ratio calculations. In contrast, the growth rate uncertainties increases these differences to ~94 h (i.e., 2Dc: 48 h versus 2Dc: 142 h). Notably, the residence times derived from 3D true data provide an intermediate range between those of 2D-CSD (i.e., 57 – 118 h in Table 4.4), which we interpret as a more truthful estimation based on the similarities of 3Da with 2Dc and 2Ds in the *I/L* and *S/I* ratios, respectively.

Although the methodology around CDS based on 2D datasets is well known and widely used, our study advocates for the use of true 3D datasets instead when possible. Our data shows that even smaller 3D samples produce comparable if not more accurate residence time results to those of 2D, without the need of statistical analyses or stereological corrections. Since 3D datasets do not require crystal shape estimations, the errors derived from the aspect ratios approximation and *L*-axis inference are minimized, limiting the error propagation into the CSD plots and slopes.

4.6 Acknowledgments

GFZ acknowledges the 2022 Endeavour Fund – Smart Ideas project "Robust volcanic eruption forecasts: leveraging magmatic speedometry into geophysical monitoring" of the Ministry of Business, Innovation & Employment (MBIE) of New Zealand (MAUX2202), which funded the present work. This study received financial support from Grants-in-aid for Scientific Research in Japan to SO (Nos. 22H00161). The SR-XCT data was acquired at SPring8 (Japan) as part of proposal 2023B1698. FIB work was supported by RIKEN. We also would like to thank Paul Tomascak, Michael Higgins, Dougal Jerram and two anonymous reviewers for their valuable comments and suggestions which contribute to the final version of this manuscript.

Chapter 5 Short crystal residence times and fast magma ascent prior to effusive eruptions at Mount Ruapehu, New Zealand.

Silvia Catalina Moreno-Alfonso[1], Satoshi Okumura[2], Geoff Kilgour[3], Teresa Ubide[4], Yoshiyuki Iizuka[5], Masahiro Yasutake[6], Kentaro Uesugi[6], Yujin Jegal[4,7], Stuart Mead[1] and Georg F. Zellmer[8].

[1]Volcanic Risk Solutions, School of Agriculture and Environment, Massey University, Palmerston North, New Zealand.
[2]Department of Earth Science, Graduate School of Science, Tohoku University, Sendai, Japan.
[3]Wairakei Research Centre. Earth Science New Zealand, Taupo, New Zealand.
[4]School of the Environment, Faculty of Science, The University of Queensland, Brisbane, Australia.
[5]Institute of Earth Sciences, Academia Sinica, Taipei, Taiwan
[6]Japan Synchroton Radiation Research Institute/SPring-8, Sayo-gun, Hyogo, Japan.
[7]GeoRessources, CNRS, Université de Lorraine, Vandoeuvre-lès-Nancy, France.
[8]Institute of Geosciences, University of Bonn, Bonn, Germany.

This chapter has been published at Journal of Petrology:
Moreno-Alfonso, S. C., Okumura, S., Kilgour, G., Ubide, T., Iizuka, Y., Yasutake, M., Uesugi, K., Jegal., J, Mead, S. & Zellmer, G. F. (2026). Short crystal residence times and fast magma ascent prior to effusive eruptions at Mount Ruapehu, New Zealand. Journal of Petrology, 67(2), egag005.

Abstract

Decoding magma evolution and transport mechanisms requires detailed examination of the groundmass glass and associated mineral phases in the eruptive products. These analyses can help determine crystal residence times and magma ascent rates prior to eruption. Magma storage and ascent rates are particularly relevant when assessing the controls on the type and style of eruptions from andesite volcanoes, which are capable of producing varied eruptive phases from highly explosive to dominantly effusive. Here, we focus on Mount Ruapehu, one of New Zealand's most active volcanoes and a significant portion of the Tongariro Volcanic

Centre, which has a rich geological history of eruptions spanning a broad range of eruptive phases from explosive to effusive. Previous analysis of crystal size distributions of microlites, <10 ka tephra showed that magma ascent occurred over a relatively short period (i.e., ~2 days at ≤0.09 m/s) immediately prior to eruption. Here, we expand this approach to include analysis of massive lava flows emplaced from 50 to <10 ka (Mangawhero and Whakapapa formations) with similar andesitic composition and mineral assemblages dominated by plagioclase and two pyroxenes. We analyze the crystal size distributions of 17 lavas and conduct bulk rock analysis, groundmass laser ablation mass spectrometry analysis, and electron probe microanalysis on plagioclase and pyroxene phenocrysts and microlites. We use the chemical data to calculate the *P-T-H_2O* conditions of crystallization. Then, we combine the derived crystal size distributions with thermobarometry and hygrometry results to determine the residence times and ascent rates of magmas that ultimately fed erupted lavas. Our data yields initial pressures up to 810 MPa, temperatures up to 1160 °C, and water contents up to ~2.7 wt% H_2O, with average crystal residence times of ~3 days (maxima of 66 days considering growth rate uncertainty) and ascent rates up to ~0.08 m/s. The similar residence times and ascent rates from effusive and explosive eruptions suggest that similar crystallization paths and undercooling conditions take place irrespective of the eventual eruption style. We propose the eruption style may be modulated by the geometry of the conduit, as observed in other volcanic centers where conduit overpressure and gas accumulation trigger explosive eruptions.

Key words: crystal size distributions, geothermobarometry, hygrometry, andesite, Ruapehu, Mangawhero Formation, Whakapapa Formation.

5.1 Introduction

Crystal size and morphology in volcanic products have been used to infer variations in magma degassing during ascent, and their potential influence on eruption style for a given bulk composition (e.g., Andrews & Befus, 2020; Befus & Andrews, 2018; Hammer, 2008; Preece et al., 2016; Shea & Hammer, 2013). Likewise, crystal size distributions (CSD) has been used to infer crystallization stages linked to changes in the P-T conditions of the system (e.g., Billon et al., 2025; Cashman, 2020; Giuliani et al., 2020; Lentze & McSween Jr., 2000). Indeed, the application of CSD in combination with thermobarometry offers an opportunity to assess magma residence times (i.e., lapse of time between injection and magma discharge) and ascent rates (i.e., speed needed to transport the magma through the volcanic conduit) (e.g., Berger et al., 2008; Bonechi et al., 2024).

Magma residence times and ascent rates, are key parameters governing magmatic processes operating at the onset of an eruption (e.g., Costa et al., 2020; Stix, 2018). Quantifying such parameters can therefore elucidate the timescales of magmatic processes (e.g., Cassidy et al., 2015; Coulthard Jr et al., 2024; Kilgour et al., 2014; Marshall & Andrews, 2023), helping to improve eruption forecasting models. A study by Lormand et al. (2020) using CSDs and P-T constrains on tephra samples of the Tongariro Volcanic Centre (TgVC) erupted in the last 10 ka revealed ascent rates between 0.02 - 0.09 m/s and crystal residence times of 3 ± 1 days, irrespective of the eruptive size (i.e., vulcanian to sub-Plinian), implying a poor correlation between these parameters and eruption explosivity at the TgVC. Different eruptive styles can yield comparable CSDs and crystal morphologies when associated with fast magma ascent, a phenomenon reported in other volcanic systems (e.g., 2021 Tajogaite eruption in Bonechi et al., 2024; 2011 Shinmoedake eruption in Okumura et al., 2024). Hence, pre-eruptive magmatic conditions might play a relatively minor role compared to in-conduit dynamics,

which are in-turn controlled by changes in the conduit geometry. Together, conduit dynamics can strongly influence magma flux rates and fragmentation (e.g., Kozono et al., 2022; Ripepe et al., 2021; Viccaro et al., 2021).

The recent eruptive activity of Mount Ruapehu, which is part of the TgVC, has been characterized by small volume eruptions (<0.01 km^3) covering a range of eruptive styles from effusive to sub-Plinian eruptions (Kilgour et al., 2010; Kilgour et al., 2013; Kilgour et al., 2014). For the 1995 and 1996 Mount Ruapehu eruptions Lormand et al. (2020) found pyroxene microlite residence times of ~3.5 and ~3.6 days and ascent rates of ~ 0.016 m/s and ~0.017 m/s respectively. For the same eruptions, diffusion chronometry in pyroxene phenocryst rims returned average residence times of 124 days (1995 eruption) and 254 days (1996 eruption) (Kilgour et al., 2014). Notably, while Lormand et al. (2020) assessed crystal residence times of the ascending melts, the data in Kilgour et al. (2014) represent storage timescales of crystals entrained by those ascending melts. Indeed, longer storage timescales in 1996 are supported by the larger crystal rims compared to those of the 1995 eruption (Kilgour et al., 2014), as well as melt inclusion data (Kilgour et al., 2013) and compositional zoning analyses in pyroxenes (Nakagawa et al., 2002).

All of the historical eruptions of Mount Ruapehu consisted of phreatic and phreatomagmatic (with minor magmatic) phases, from a vent currently occupied by Te Wai ā-Moe/Crater Lake vent (Global Volcanism Program, 2025; Scott, 2013). Extensive geological evidence shows that the volcanic edifice is mainly composed of voluminous lava flows (Leonard et al., 2021; Townsend et al., 2017). Hence, for adequate preparation during future unrest, it is imperative to assess and compare magma ascent timescales for effusive eruptions to better constrain the future style and size of eruptions. In this study, as in Lormand et al. (2020), we evaluate the crystal residence times of microlite pyroxenes (i.e., 1 - 30 μm in width; Zellmer, 2021)

grown during magma ascent, using lava samples from the Mangawhero and Whakapapa formations of Mount Ruapehu. Specifically, we combine pyroxene microlite CSDs with *P-T-H_2O* conditions derived from thermobarometry and hygrometry, to characterize the pre- and syn-eruptive conditions of effusive eruptions. The resulting magma residence times and ascent rates provide a direct comparison with previously analyzed explosive phases from the TgVC (Lormand et al., 2020).

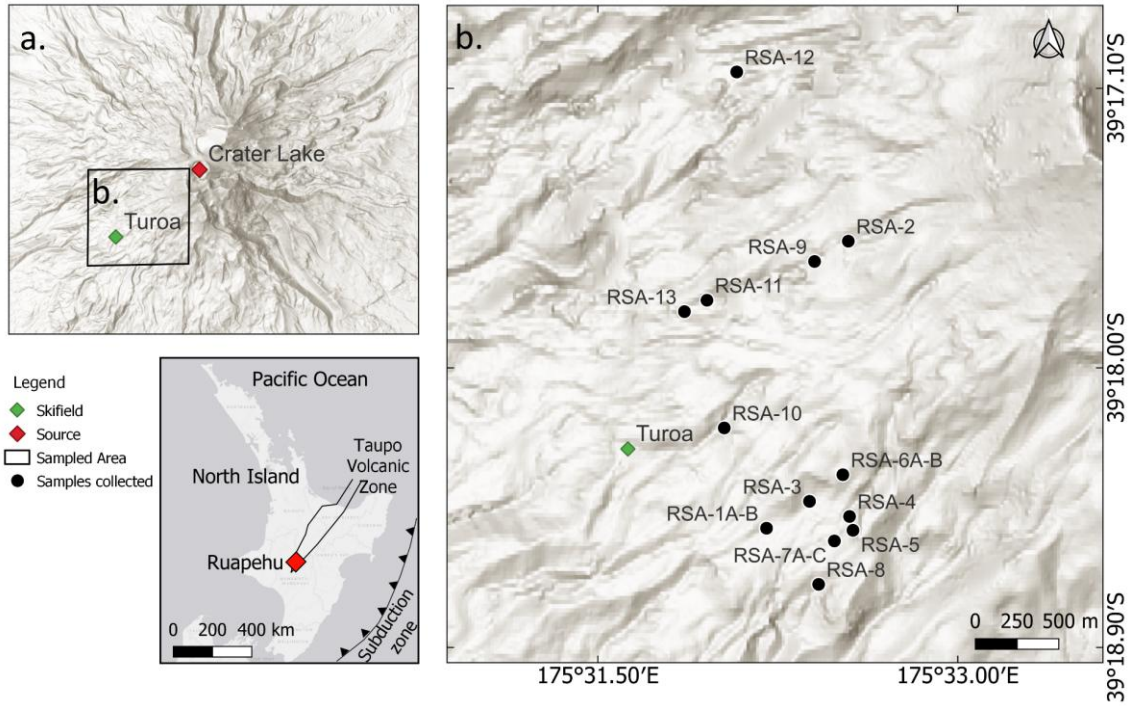

Figure 5.1. Digital terrain model of Mount Ruapehu and sample locations.a. Location of the sampling area in Mount Ruapehu (black square); inset shows location within New Zealand. b. Location of the sampling points.

5.2 Geological background and sampling

Mount Ruapehu is an active andesite-dacite stratovolcano located in the North Island of New Zealand (39.28°S, 175.57°E). It occupies the southernmost part of the Taupō Volcanic Zone (TVZ)(Wilson et al., 1995; Wilson & Rowland, 2016) (Figure 5.1). The TVZ represents a NNE-SSW zone of hyperactive volcanism, responsible for over 90% of the volcanic activity in the country (Houghton et al., 1995; Leonard et al., 2021; Wilson et al., 1995), and forms part of the broader Tonga-Kermadec–Hikurangi subduction system (Cole & Lewis, 1981;

Ewart et al., 1977; Schellart & Spakman, 2012). Mount Ruapehu is situated within a *c*. 40 km wide NNE striking nested graben (Gómez-Vasconcelos et al., 2016; Villamor & Berryman, 2006b), which is the southern termination of the Modern Taupō Rift, and has increased its extensional rate in the late Quaternary linked to changes in the evolution of the rift and the thickness of the crust (Villamor & Berryman, 2006a).

Mount Ruapehu comprises a voluminous (~150 km^3) edifice (Conway, 2016; Leonard et al., 2021) formed predominantly by lava flows surrounded by a ring plain built out of the pyroclastic deposits of the volcano and their reworked products (Hackett & Houghton, 1989; Leonard et al., 2021). The eruptive products of the volcano over the last 250 ka have been defined as the Ruapehu Group (Hackett, 1985), which includes four formations, each associated to a cone building episode, which from oldest to youngest are: Te Herenga (250–150 ka), Wahianoa (166–80 ka), Mangawhero (50–15 ka) and Whakapapa (<15 ka) (Conway et al., 2016; Gamble et al., 2003; Hackett & Houghton, 1989; Leonard et al., 2021). The lavas of Mount Ruapehu have been characterized mainly as plagioclase-pyroxene phyric calc-alkaline andesites, with minor occurrence of basalts and dacites (Graham & Hackett, 1987; Price et al., 2012). These lavas have 15 – 55 vol% phenocrysts up to 2 mm in length, where plagioclase is the dominant mineral phase, followed by roughly equal orthopyroxene and clinopyroxene contents (Graham & Hackett, 1987; Hackett, 1985; Price et al., 2012). In general, these lavas have low vesicularity (<1 %) and microcrystalline groundmasses composed of plagioclase, pyroxene and magnetite crystals (Price et al., 2012).

Table 5.1. Location of the lava samples collected in Mount Ruapehu.

Formation	Member	Whole rock compositions and classification	Sample	Latitude	Longitude
Mangawhero Formation (50 – 15 ka)	Mangaehuehu Member (47 – 40 ka)	High Magnesium Andesites SiO_2 57 - 62 wt% K_2O 1.4 – 2.3 wt% $Mg\#_{60-69}$ Possible source: Girdlestone peak.	RSA4	39°18'28.70"S	175°32'32.95"E
			RSA5	39°18'31.37"S	175°32'33.81"E
			RSA6A	39°18'20.64"S	175°32'31.28"E
			RSA6B	39°18'20.64"S	175°32'31.28"E
			RSA13	39°17'49.13"S	175°31'51.67"E
	Makotuku Member (24 – 16 ka)	Andesites SiO_2 60 - 62 wt% K_2O 1.8 – 2.1 wt% $Mg\#_{44-50}$ Possible source: Tahurangi area.	RSA1A	39°18'30.97"S	175°32'12.19"E
			RSA1B	39°18'30.97"S	175°32'12.19"E
			RSA3	39°18'25.78"S	175°32'22.93"E
			RSA7A	39°18'33.43"S	175°32'29.16"E
			RSA7B	39°18'33.43"S	175°32'29.16"E
			RSA7C	39°18'33.43"S	175°32'29.16"E
			RSA8	39°18'41.81"S	175°32'25.22"E
			RSA10	39°18'11.60"S	175°32'1.62"E
	Waitonga Member (25 – 21 ka)	High Silica Andesites SiO_2 61 - 63 wt% K_2O 1.8 – 2.0 wt% $Mg\#_{51-58}$ Possible source: Sothern summit plateau	RSA2	39°17'35.52"S	175°32'32.64"E
			RSA9	39°17'39.44"S	175°32'24.20"E
Whakapapa Formation (<15 ka)	Turoa Member (17-10 ka)	Low Silica Andesites SiO_2 59 - 60 wt% K_2O 1.5 – 2.0 wt% Mg#50 – 60 Possible source: Turoa cone in Tahurangi area.	RSA11	39°17'46.93"S	175°31'57.29"E
			RSA12	39°17'2.83"S	175°32'4.74"E

Ages, classification, whole rock compositions and possible sources taken from Conway (2016), Conway et al. (2016), Conway et al. (2018) and Townsend et al. (2017). Suffixes A, B and C in samples indicate samples collected in the same point from different levels within the same lava flow.

The Mangawhero Formation is a voluminous package of lava (~28 km^3 in Conway, 2016), forming the main cone of Mount Ruapehu, erupted from at least two vents in the south and mid-north summit areas (Conway, 2016; Hackett, 1985; Townsend et al., 2017). The Mangawhero Formation lavas are mainly andesites and dacites that display evidence of complex lava-ice interaction during eruption and emplacement (i.e., emplacement in the lateral margins of glaciers and dammed flows in Conway, 2016; Conway, 2015). The Mangawhero Formation can be subdivided into early (~50 – 35 ka), middle (~35 – 26 ka) and late (~26 – 15 ka) phases based on the ages and compositional differences constrained by Conway et al. (2016). The early Mangawhero lavas have bulk SiO_2 compositions between 57 – 65 wt% (i.e., basaltic-andesite to dacite) and present two distinct high (e.g., $Mg\#_{60-69}$ – Mangaehuehu Member) and low (e.g., $Mg\#_{48-62}$ – Ngahuinga Member) MgO versus SiO_2 trends, that are not observed in the middle and late lavas (Conway et al., 2018). The middle Mangawhero lavas show SiO_2 compositions of 60 – 63 wt% (i.e., andesites), transitional between the compositions of the dacitic and andesitic lavas of the early Mangawhero Formation (Conway et al., 2018; Townsend et al., 2017). Lastly, the late Mangawhero lavas have SiO_2 compositions of 58 – 65 wt% (i.e., basaltic-andesites to dacites) and show a reverse SiO_2 vs K/Ca trend compared to the early and middle Mangawhero lavas, overlapping in compositions with the younger Whakapapa Formation lavas (Conway et al., 2018; Townsend et al., 2017). The Whakapapa Formation is the youngest unit of the Ruapehu Group (< 15 ka) comprising mainly andesitic lava flows (~12 km^3) erupted from at least three vents aligned in a NNE direction, at the end of the last glacial period (Conway, 2016; Hackett, 1985; Leonard et al., 2021; Townsend et al., 2017). The deposits are confined to ridge tops or form lava and spatter sheets and cones near the inferred vents (Conway, 2016; Townsend et al., 2017). The Whakapapa Formation lavas are andesites to dacites (i.e., SiO_2 57 – 61 wt%) forming a continuous SiO_2 vs K/Ca trend with the lavas of the late

Mangawhero Formation. The andesites of the Mangawhero and Whakapapa formations have plagioclase as the main phenocryst phase, while the most common ferromagnesian phase is orthopyroxene. The groundmass is dominated by microcrystalline plagioclase and orthopyroxene, with abundant magnetite and small patches of microlite-free glass (5 – 10 μm) found only in samples collected in ice-bounded margins and flows cooled rapidly (Conway, 2016; Conway et al., 2018).

For this study, we collected 15 samples from the Mangawhero Formation and 2 additional samples from the Whakapapa Formation. In total, we sampled from 13 locations on the western flank of Mount Ruapehu close to the Turoa Ski field area (Figure 5.1 & Table 5.1). The samples of the Mangawhero Formation belong to 3 members; Mangaehuehu (47 – 40 ka), Waitonga (25 – 21 ka) and Makotuku (24 – 16 ka), while the samples of the Whakapapa Formation belong to the Turoa Member (17 – 10 ka). The SiO_2, K_2O and Mg# from whole rock compositions from literature along with the rock classification and member classification are provided in Table 5.1.

5.3 Methods

5.3.1 Bulk rock XRF

X-Ray Fluorescence (XRF) was performed at Massey University using a Bruker S8 Tiger Series II WD-XRF spectrometer to measure major element oxides for whole rock in glass beads of the lava samples. The reference materials Oreas 24b and 24c returned reproducibility around 1 - 3%, except for P_2O_5 which was around 5 – 13% (See Appendix 1; Tables S2 & S3). The sample preparation details can be found in Chapter 3.

5.3.2 EPMA mineral analysis

Electron probe microanalysis (EPMA) was used to determine the major element composition of microlite (i.e., small crystals embedded in the groundmass with sizes 1 - 30 μm in Zellmer, 2021) cores and rims, and phenocrysts (i.e. large crystals embedded in the groundmass with sizes ≥30 μm - s.s. Iddings, 1892) rims of plagioclase and pyroxene, using instruments at Academia Sinica (Taiwan) and Tohoku University (Japan), on carbon coated polished plugs.

At Academia Sinica, we used a field emission electron microprobe (JEOL EPMA JXA-8500F) equipped with five wave-length dispersive spectrometers (WDS), with a 2 μm beam at an acceleration voltage of 12 kV, beam current of 6 nA, and peak counting times of 10 s per element peak and 5 s for each background. The low beam current used on this probe is due to the relatively large beam power of FE-EPMA, inferred from testing at the laboratory (Y. Iizuka, personal communication, November 6, 2025). The correction of the X-ray intensities was performed through an Oxide-ZAF method (JEOL Ltd., n.d.). Relative standard deviations on secondary standard measurements were < 2% for Ti, Na and Fe, <1% for Si, Cr, Mn and K, and < 0.5% for Al and Mg.

At Tohoku University we used a JEOL iSP100 electron microprobe, with a regular tungsten filament. The accelerating voltage was 15 kV, the beam current was 15 nA, peak counting times were 10 s on peak and 5 s on each of two background positions and we used a fully focused beam (following Araya et al., 2024). Although the conditions described can impact Na results in plagioclases, the beam effect was monitored, and no significant reduction was observed in Na intensity. The Oxide-ZAF method was applied for X-ray intensity correction. The reproducibility of the analyses was better than 3% for all elements, based on measurements on secondary standards (See Appendix 1; Table S5 for information on the standard materials and Oxide-ZAF method).

Mineral compositional results were filtered to ensure total oxide content between 96 - 100 wt% and cation ratios consistent with the stoichiometry of mineral phases.

5.3.3 LA-ICP-MS groundmass analysis

Laser ablation inductively coupled plasma mass spectrometry (LA-ICP-MS) was employed to analyze major element composition of the microcrystalline matrix in resin mounts, following the rastering technique in Ubide et al. (2023), which provides equivalent results to those of EPMA in glassy groundmass (Ubide et al., 2023). Ten 50x600 μm rasters (i.e., arrays of overlapping spots) across microcrystalline matrix (including glass and microlites) were measured per sample obtaining representative melt compositions, avoiding crystal accumulation effects on whole rock (e.g., Bennett et al., 2025; Magee et al., 2021; Ubide et al., 2022).

The analyses were conducted at the Centre for Geoanalytical Mass Spectrometry, Radiogenic Isotope Facility of The University of Queensland (UQ RIFlab, Australia) using an ASI RESOlution 193-nm excimer ultraviolet ArF laser coupled with a Thermo iCap RQ quadrupole mass spectrometer. The laser was set up to 3 J/cm^2 on-sample fluence, 50 μm spot size, 10 Hz repetition rate and 5 μm/s translation speed. The ablation was undertaken in ultrapure He (350 ml/min) adding Ar (850-950 ml/min) as makeup gas and a trace amount of N_2 (5 ml/min) for efficient transport, better sensitivity and to assist with ionization. The mass spectrometer was tuned using NIST SRM 612 glass reference material, and for calibration we used BCR-2G basaltic glass standard (Jenner & O'Neill, 2012). Additional glass standards used for quality monitoring (BHVO-2G, GSD-2G, GSD-1G) achieved standard deviations (2σ precision) and accuracy better than 5% and 10%, respectively (See Appendix 1; Tables 5 & 6). Data reduction was performed in Iolite4 (Paton et al., 2011), with major oxide quantification performed following the method in Chang & Audétat (2018), normalizing the

sum of semiquantitative oxides to 100 wt% offline. Obtained Si concentrations were then used to quantify trace elements back in Iolite, and data were screened for unnoticed crystal cargo following Ubide et al. (2023).

5.3.4 SR-XCT analysis and image reconstruction

Synchrotron radiation X-ray computed tomography (SR-XCT) 3D analysis of pyroxene microlites (i.e., 1 - 30 μm in width; Zellmer, 2021) was performed at BL47XU of the SPring-8 facility (Japan), using an X-ray energy of 15 keV and voxel sizes of 194 or 388 nm (Table 5.2). The samples used in the analyses were prepared at Tohoku University (Japan), initially cutting 5 mm x 2 mm x 2 mm rock billets, which through grinding and polishing were reduced to slices of ~200 μm thickness that were finally segmented into pieces of ~200 μm. These pieces were mounted on a carbon nanotube (CNT) sheet and attached to a thin rod for analysis.

The 3D images were used to mitigate the overlapping of crystals, a common problem in 2D images due to the high crystallinity of the lava samples (>76 vol% in this study). Additionally, high resolution images aided with the distinction of closely spaced crystals. Although plagioclase is the preferred mineral phase to calculate crystal size distributions (CSD) in volcanic rocks, the high content of plagioclase microlites in the lava samples (>50 vol%), hinders outlining of individual crystals. Instead, we opted to analyze pyroxene microlites, which are comparatively less abundant (<30 vol%) but still provide the minimum number of crystals required for CSD analysis using 3D datasets (250 - 300 crystals in Mock & Jerram, 2005). Furthermore, we ensure consistency of lava results with the method used by Lormand (2020) to determine the crystal residence times of tephra, using a well constrained orthopyroxene grow rates from the same volcanic centre.

Data analysis was completed in the software SLICE (Nakano et al., 2006), using images normalized to 8-bit, which were binarized using the pixel threshold values determined for pyroxene, and processed using the erosion and dilation feature by 2 pixels. The clustered data were used to obtain measurements for the long (L), intermediate (I) and short (S) axes using the best fitted ellipsoid (e.g., Okumura et al., 2008; Okumura et al., 2022). The measurements are included in an online repository (see Appendix 2). Further description of the segmentation process and image reconstruction can be found in Chapter 4.

5.3.5 CSD generation

Since the data reduction and segmentation of the SR-XCT images provides true 3D size data, the pyroxene microlite crystal size distribution (3D-CSD) can be calculated without the need of shape (i.e., use of CSDSlice - Morgan & Jerram, 2006) and stereological corrections (i.e., use of CSDCorrections - Higgins, 2000). Hence, using the true dimensions of the long (L) axis and the sample volume, it is possible to calculate the CSD without the use of specialized software (i.e., using a calculation spreadsheet).

The CSDs were calculated as function of the L-axis, using a logarithmic (Log 10-based) scale with a maximum of five bins (intervals) per decade (e.g., Higgins, 2000) for microlite crystals (1 - 30 μm in width). To find the population density (n), the number density (i.e., number of crystals per bin by volume of analyzed sample) was divided by the width of the interval. The errors associated to n were calculated following the methodology of Higgins (2000), using the square root of the number of crystals measured per bin. The CSD plots were constructed by plotting $\ln(n)$ versus the crystal size average for the bin, ignoring bins with three or less crystals (e.g., Higgins, 2000; Okumura et al., 2022). CSD data is included in Appendix 2 (Table S13; Figure S2)

The slope calculation for the determination of crystal residence times was completed for the interval between 10 and 20 μm, to avoid the interference of syn-eruptive crystallization (e.g., steeper slopes in Melnik et al., 2011; Preece et al., 2013), and the contribution of antecrystic microlites i.e., older crystals incorporated during ascent, that show disequilibrium textures such as resorption and zonation (e.g., Lormand et al., 2020). The analytical conditions for the generation of the CSDs are summarized in Table 5.2.

Table 5.2. Analytical conditions for CSD generation.

Unit	Sample	Number of crystals		Sample volume (μm^3)	Voxel size (nm)	Number density (mm^{-3})
		Counted[a]	CSD[b]			
Mangaehuehu Member	RSA13	636	632	520186	388	1222640
	RSA6B	578	575	5646416	194	102366
	RSA6A	479	476	1767234	194	271045
	RSA5	343	343	1357882	194	252599
	RSA4	464	460	576551	194	804786
Makotuku Member	RSA8	889	886	8952939	194	99297
	RSA7C	415	411	757547	194	547821
	RSA7B	849	839	8842119	194	96018
	RSA7A	1321	1320	7149953	194	184756
	RSA10	1522	1521	814204	388	1869311
	RSA3	359	357	778878	194	460919
	RSA1B	587	586	1132318	194	518405
	RSA1A	437	436	1320949	194	330066
Waitonga Member	RSA2	1272	1270	6362244	194	199929
	RSA9	935	932	6854512	194	136406
Turoa Member	RSA11	1024	1017	5546424	194	184623
	RSA12	2944	2943	21079825	194	139660

[a] Crystals within 1μm size in width and 100μm in length.
[b] Crystals used to calculate the CSD.

5.3.6 Hygrometry and thermobarometry

Prior to applying mineral-melt thermobarometry, we assessed chemical equilibrium between crystals and melt (Figure 5.2) using mineral compositions measured by EPMA and host groundmass compositions measured by LA-ICP-MS (Appendix 3; Table S15). For plagioclase, we used the anorthite content (An = Ca/[Ca+Na]) in the plagioclase versus the content in the melt based on equilibrium experiments of Waters & Lange (2015) and

employed by other authors (e.g., D'Mello et al., 2023; Lormand et al., 2021; Zellmer et al., 2016b) (Figure 5.2a). For orthopyroxene, we used the equilibrium test of Rhodes (Rhodes et al., 1979) following the K_D (Fe-Mg) equilibrium constrains in Putirka (2008) for orthopyroxene (i.e., K_D $(Fe\text{-}Mg)^{opx\text{-}liq}$ = 0.29 ± 0.06 – Figure 5.2b). Only the crystal-melt pairs that passed all equilibrium filters were used to constrain storage *P*, *T* and H_2O. In Figure 5.2, we show how a large portion of the crystals tested are plotted outside the equilibrium fields. Plagioclase compositions extend below the equilibrium ranges, showing less mafic compositions than their carrier melts (Figure 5.2a), while orthopyroxene compositions extend below and above the equilibrium ranges (Figure 5.2b). Equilibrium testing discarded 40% of the plagioclase and 51% of the orthopyroxene compositions.

Although the samples have clinopyroxene crystals, these are less common than orthopyroxenes (i.e., 3 vol% clinopyroxene versus 16 vol% orthopyroxene on average) and have two main compositions, augite and pigeonite. Clinopyroxene calibration datasets for thermobarometry calculations are largely based on augite, with limited pigeonite, and there is no certainty in the hygrometry calculations retrieved for pigeonite as yet (Lormand et al., 2020), hence, any pigeonite compositions were discarded. We completed the crystal-melt equilibrium tests on augite and host groundmass compositions using the Rhodes test (i.e., K_D $(Fe\text{-}Mg)^{cpx\text{-}liq}$ = 0.28 ± 0.08) in Wieser et al. (2023b) which is a modification the test proposed initially by Putirka (2008). Additionally, following the recent assessments and recommendations by MacDonald et al. (2023), we performed the Di-Hd, En-Fs, CaTs and CaTi tests, modified from those by Putirka (1999) and Mollo et al. (2013). Seven samples had no augite-melt equilibrium pairs, another three samples only had 1 augite-melt equilibrium pair, and the seven remaining samples had between 3 and 5 augite-melt equilibrium pairs. For this reason, no clinopyroxene thermobarometry is included here. The equilibrium tests for the clinopyroxenes are provided in Chapter 6.

The hygrometry and thermobarometry calculations were performed using a range of recent freeware: the Python3 tool Thermobar (Wieser et al., 2022) and the online machine learning magmatic liquid-assemblage thermobarometer MagMaTab (Weber & Blundy, 2024).

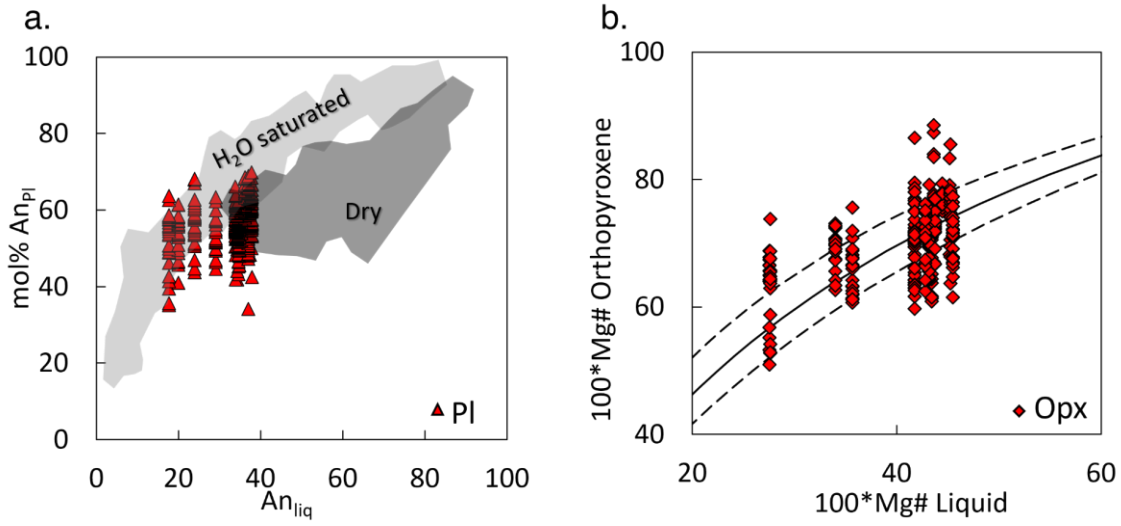

Figure 5.2. Assessment of chemical equilibrium between plagioclase-liquid and orthopyroxene-liquid, pairing mineral compositions with putative melt compositions.a. Plagioclase (Pl). Anorthite content (An) in the plagioclase versus the content in the melt. Equilibrium experiments of Waters and Lange (2015) are represented by the shaded areas: light grey water saturated and dark grey for dry experiments. Note that the equilibrium plagioclase compositions fall in both saturated and dry fields. b. Orthopyroxene (Opx). Mg# in orthopyroxene versus Mg# in melt, together with curves for the Rhodes equilibrium test (Rhodes et al., 1979) following the KD (Fe-Mg) equilibrium constrains in Putirka (2008) for orthopyroxene (i.e., KD (Fe-Mg)$^{opx\text{-}liq}$ = 0.29 ± 0.06).

We used MagMaTaB to determine pressure (*P*) and temperature (*T*) of equilibration of magmatic liquids with their mineral assemblage. We used the groundmass composition obtained via LA-ICP-MS as input, together with the equilibrium mineral assemblage based on petrographic observations (plagioclase, orthopyroxene, clinopyroxene, oxides). We used calibration experimental data with a minimum of three mineral phases, and no filtering for standard deviation.

Magmatic water (H_2O) content was calculated using an iteration between the Waters & Lange (2015) hygrometer and the thermometer from equation 24a in Putirka (2008) for plagioclase in Thermobar. Both the hygrometer and the thermometer require an input *P*, for which we used the *P* results from the MagMaTaB liquid-assemblage thermobarometer

(which does not take mineral compositions as input, and is therefore independent of plagioclase-based calibrations). Specifically, we used the maximum pressure calculated for all groundmass compositions from a given sample after removing any outlier values (i.e., any values under or over 3σ for *P* and/or *T*). The plagioclase compositions used correspond to the cores of microlites and rims of phenocrysts in equilibrium with the melt.

To further constrain *P* and *T*, we used orthopyroxene-liquid thermobarometry in Thermobar using the iteration of equations 28a and 29a from Putirka (2008). Since the thermobarometer requires H_2O content to perform the calculations, we used the one obtained from the iteration of the Waters & Lange (2015) hygrometer and the thermometer from equation 24a in Putirka (2008). The H_2O content corresponds to that constrained for the plagioclase in equilibrium with the highest anorthite content in each sample i.e., the most primitive plagioclase. The use of plagioclase-constrained H_2O values in the orthopyroxene thermobarometry is supported by the presence of glomerocrysts (i.e., coherent aggregates of coarse crystals within the groundmass, interpreted as rip-up clasts of cumulate origin) of orthopyroxene and plagioclase (see petrology below), indicating that both minerals crystallized together, under similar conditions including a similar magmatic H_2O content. Pressure values equal to or under zero and outlier values (i.e., any values under or over 3σ for *P* and/or *T*) were discarded.

5.3.7 Residence times and ascent rates

To calculate the residence times (τ), we used a variation of Equation 68 in Marsh (1988), using the slopes calculated from the CSDs and a well-known crystal growth rate:

$$\tau = -\frac{1}{[slope]G} \quad (2)$$

Where G is the crystal growth rate.

Since constraining a pyroxene growth rate directly from the Mount Ruapehu lavas was not feasible during the current study, we used the growth rate calculated for orthopyroxenes of Mangatawai Formation sample 407-17 (c. 3.4 – 2.8ka BP, Moebis, 2010) from Ngauruhoe volcano, applied here as a regional analogue within the TgVC, without implying a common magmatic reservoir (1.80×10^{-11} m/s in Lormand, 2020 recalculated from 3.7×10^{-11} m/s in Zellmer et al., 2016b; Zellmer et al., 2018). This growth rate was used to calculate a reference residence time (τ opx), based on Equation (2).

Additionally, following the approach in Cooper & Kent (2014), we compiled a range of growth rates reported for intermediate magmas in experimental studies (i.e., 1.42×10^{-9} - 9.09×10^{-11} m/s in Shea and Hammer, 2013). This range was intentionally extended to span 1×10^{-9} to 1×10^{-12} m/s, fully encompassing experimentally derived values while allowing assessment of the influence of the growth rate uncertainty on the residence time calculations. This growth rate range was used to calculate an extended range of residence times (τ).

Crystal growth rates depends on the degree of undercooling and decompression (e.g., Agostini et al., 2013; Shea & Hammer, 2013); however, they do not vary significantly depending on which of these process dominates. We therefore assume that applying the growth rate (G) calculated for explosive eruptions of the TgVC (Lormand, 2020), to effusive products does not introduce significant uncertainty over the orders of magnitude considered here. Supporting this assumption, microlite morphology is very similar in effusive (this study) and explosive (Lormand et al., 2020) products as seen in Figure 5.3, with euhedral prismatic to elongated plagioclase and pyroxenes microlites observed in both lavas and tephra, reflecting comparable undercooling conditions. Finally, maximum and minimum values for both τ (i.e., derived from the growth rate range) and τ opx (i.e., derived from the Mangatawai

Formation orthopyroxene growth rate) were calculated by propagating the uncertainties in both growth rates and CSD slope estimates.

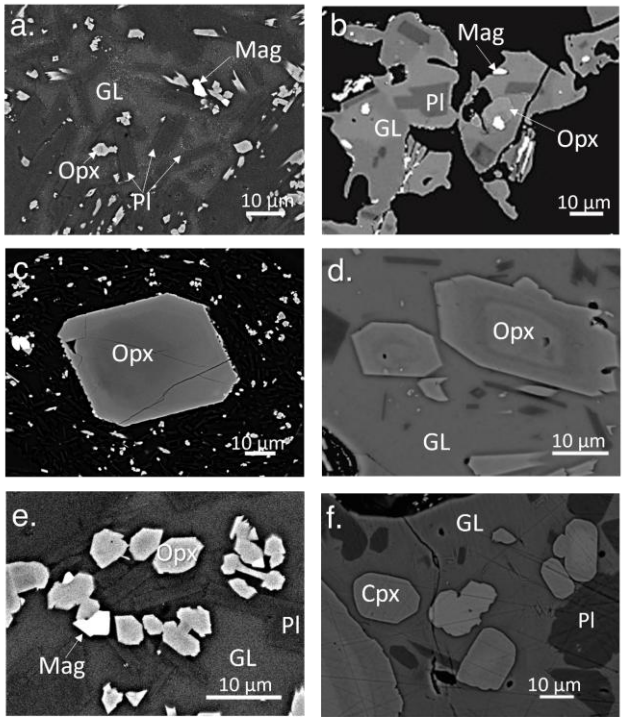

Figure 5.3. Microlite comparison between lavas (this study; left) and tephra (modified from Lormand et al., 2021; right) on back-scattered electron (BSE) images.a. RSA1A. b. Mangatawai 407-14. c. RSA2. d. Mangatawai 407-14 #41. e. RSA6B. f. Ngauruhoe 72 #26. Note how the microlites in both lavas and tephra are faceted euhedral prismatic/elongated crystals with similar appearance. Pl: plagioclase. Opx: orthopyroxene. Cpx: Clinopyroxene. Mag: Fe-oxides. GL: glass.

Once the residence times are calculated, magma ascent rates (ν) can be estimated using the following equation as reference (Armienti et al., 2012):

$$v = \frac{dZ}{dt} = \frac{Z_{max}}{\tau} \quad \textbf{(3)}$$

where dZ and dt represent changes in depth and time, respectively.

The maximum depth (Z_{max}) was determined from the maximum pressure value (Max P) obtained through thermobarometry for each sample, assuming lithostatic conditions and constant crustal density. This relationship follows the lithostatic pressure equation below:

$$Z_{max} = \frac{Max\ P}{\rho g} \quad \textbf{(4)}$$

where the crustal density (ρ) is 2560 kg/m^3, corresponding to the mean bulk density of the Torlesse Terrain in Mielke et al. (2016) which underlies Mount Ruapehu (Mortimer et al., 2023), and g is the acceleration due to gravity constant (9.81 m/s^2).

As for the residence times, ν denotes the full range of ascent rates derived from τ (i.e., residence times calculated using the compiled growth rate range), whereas ν opx specifically refers to ascent rates calculated using τ opx (i.e., residence times derived from the reference orthopyroxene growth rate from the Mangatawai Formation). Maximum and minimum values of v and v opx were calculated by propagating uncertainties associated with orthopyroxene barometry (i.e., ± 260 MPa), which affects the maximum depth (Z_{max}) calculation, as well as uncertainties in the residence time estimates arising from growth rate and CSD slope variability.

5.4 Results

5.4.1 Petrology

A brief description of the petrography and chemical composition of the lava samples of the Mangawhero and Whakapapa formations analyzed in this study is provided here to offer context to whole rock and groundmass compositions and the mineral assemblage. The samples are andesites based on whole rock compositions (Figure 5.4a) with a mineral assemblage of mainly plagioclase (50 – 70 vol%, An_{52-75}), followed by orthopyroxene (8 – 29 vol%, En_{59-74}), clinopyroxene (1 – 10 vol%, Wo_{5-42}) and minor Fe-oxides (<3 vol%) (Table 5.3).

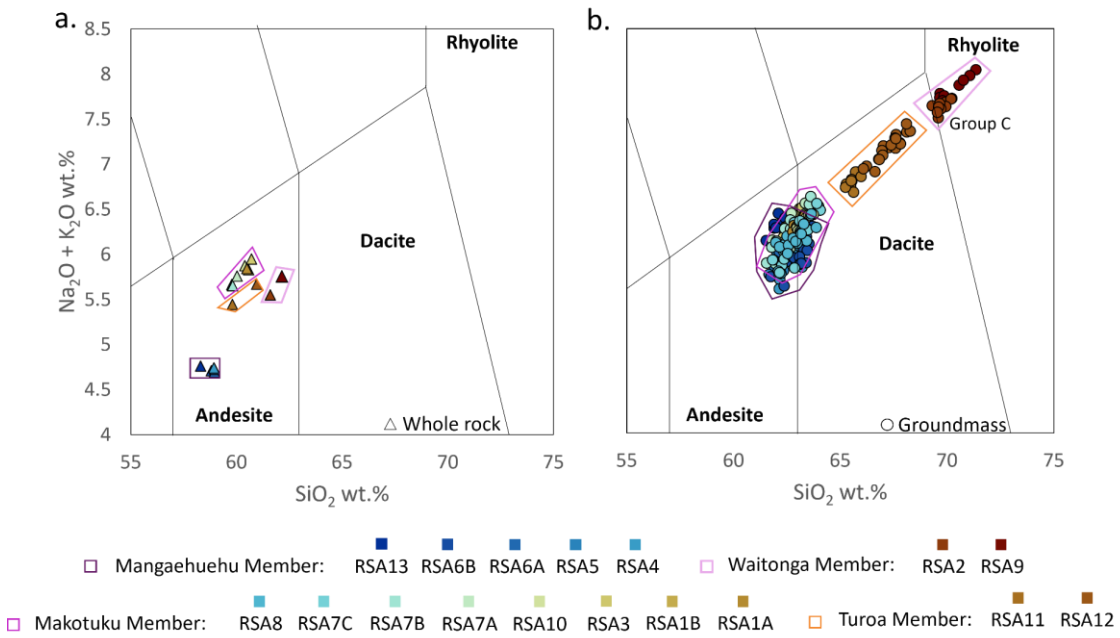

Figure 5.4. Silica (SiO_2) vs Alkalis (Na_2O+K_2O) diagram (TAS)for our Mount Ruapehu data, including a. whole rock (triangles) and b. groundmass (circles). The whole rock and groundmass compositions are color-coded following their geological units and it is notable that whole rock data are less variable than groundmass data. The Mangaehuehu Member has the most mafic whole rock compositions, the Makotuku Member has similar groundmass and less mafic whole rock compositions than the Mangaehuehu Member, and the Waitonga and Turoa members have the more silicic groundmass compositions, indicating more evolved melts compared to the other samples. The Mangaehuehu and Makotuku members, which have similar less evolved groundmass compositions, seem to prove a strong mineral composition control affecting the whole rock compositions at Mount Ruapehu.

The crystal sizes include phenocrysts (s.s., Iddings, 1892) ≥30 µm in width to 2 mm in length of plagioclase, clinopyroxene and orthopyroxene, showing resorption textures such as wavy surfaces, sieving and oscillatory zoning (Figure 5.5a - d). Large phenocrysts >1 mm make glomerocrysts/xenocrysts of pyroxene and plagioclase (Figure 5.6a) or pyroxene only (Figure 5.6b). Clinopyroxene was observed mostly as phenocrysts (Figure 5.6a – c). Xenocrysts (i.e., crystals from a foreign rock picked up by the magma in Jerram & Davidson, 2007) of orthopyroxene with olivine cores are rare but were also observed (Figure 5.6d). The phenocrysts are embedded in a hypocrystalline matrix with microlites (1 – 30 µm) of plagioclase and orthopyroxene mainly (Figure 5.5f), and minor glass (14 – 23 vol%), sometimes densely populated by nanolites of Fe-oxides (< 1 µm) (Figure 5.6d) and occasional nanolites of orthopyroxene and plagioclase (Figure 5.6e).

While most of the microlites show prismatic, tabular and blocky shapes (Figures 5.3 & 5.5), some of the smaller crystals (<10 μm) show skeletal morphologies (i.e., hollow and swallow tail textures – Figure 5.5c, and skeletal overgrowth – Figure 5.5f), and some crystals between 10 - 30 μm show resorption surfaces (Figure 5.5e), resorbed cores (Figures 5.5b & 5.5e - f), zonation (Figure 5.5f) or sieving (Figure 5.5f). Nonetheless, most of the microlite crystals have monotonous zoning (i.e., no noticeable textures - Figure 5.5). The samples show low vesicularity, based on SEM-identified void space (0 - 2 vol%) and high crystallinities (76 – 86 vol%) (Table 5.3).

Using the 3D crystal measurements obtained from SR-XCT images processed in SLICE (Nakano et al., 2006), it was possible to assess shape similarities between samples using the average aspect ratios plotted in a Zing diagram (i.e., plotting I/L versus S/I in Zingg, 1935) (Figure 5.7). We found that most of the samples are clustered between the bladed and prolate fields, with two samples isolated in the prolate field towards the equant field (i.e., samples RSA10 & 12 - Figure 5.7a). Using the aspect ratios for individual crystals from 4 samples (i.e., samples RSA2, 4, 8 & 12) we found a general trend towards the prolate field, with most of the crystals plotted between the bladed and prolate fields (Figure 5.7b), where the differences in averages are determined by crystals plotted on the edges of the clusters. For example, comparing one isolated sample (i.e., RSA12) versus samples with different locations within the cluster (i.e., RSA2, 4 & 8), a larger number of crystals towards the equant field is noticeable, dragging the average towards the 1:1 corner in sample RSA12 (Diamonds in Figure 5.7b). Likewise, sample RSA4 has more crystals plotted towards the bladed field (Circles in Figure 5.7b), while sample RSA8 has outlier crystals towards all the fields (Triangles in Figure 5.7b). Lastly, the crystal size distributions within the same sample were assessed by plotting the aspect ratios (i.e., I/L versus S/I) versus different L-axis crystal size ranges (i.e., aspect ratios for crystals with L-axis measurements of <5 μm, 5 – 10 μm, 10

– 20 µm, 20 – 30 µm & >30 µm) for sample RSA8, since this sample's average aspect ratios plot almost in the middle of all the samples (Figure 5.7a).

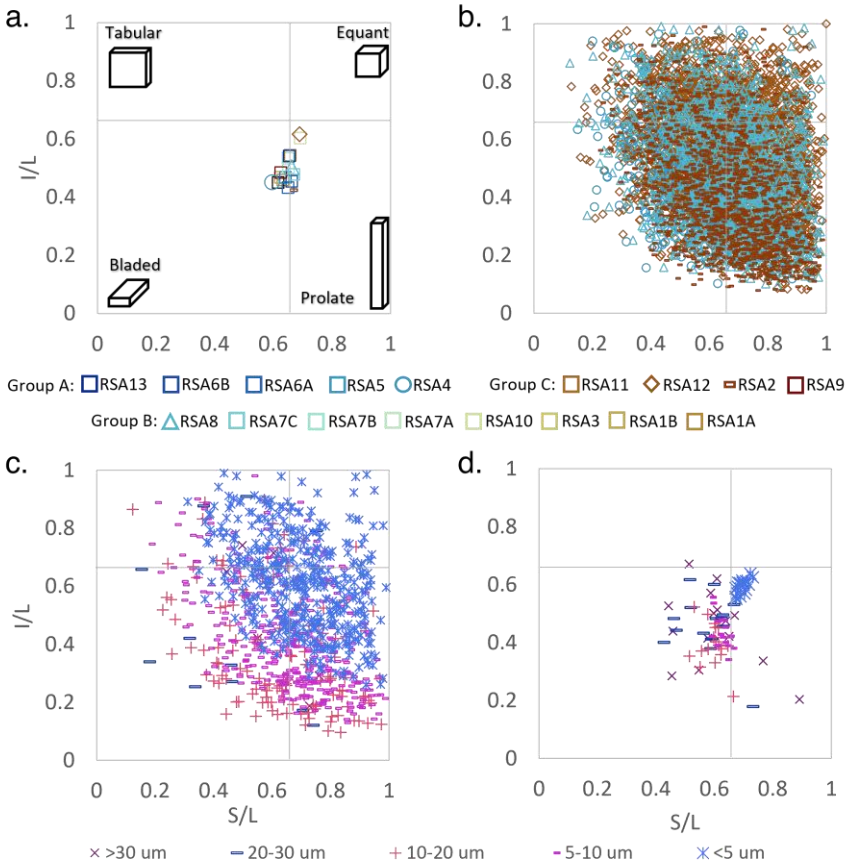

Figure 5.5. Crystal shapes based on average and measured aspect ratios.a. Pyroxene average ratios per sample. b. Pyroxene individual crystal aspect ratios for samples RSA2 (rectangle/line), RSA4 (circle), RSA8 (triangle) and RSA12 (diamond). c. Pyroxene individual crystals aspect ratios per range size for sample RSA8. d. Pyroxene average aspect ratios per sample per range size. Data obtained using the Slice Software (Nakano et al., 2006). Zingg diagram for shape classification based on axis ratios (Zingg, 1935).

Table 5.3. Petrographic description of the lava samples from count pointing in BS-SEM images.

Unit	Sample	Crystallinity (vol%)	Vesicularity (vol%)	Glass (vol%)	Plagioclase (vol%)	Average An (%)	Orthopyroxene (vol%)	Clinopyroxene* (vol%)	Average En (%)	Average Wo^{+} (%)	Fe-oxides (vol%)
Mangaehuehu Member	**RSA13**	78	0	22	50	58	20	7	73	40 (7)	1
	RSA6B	83	0	17	69	69	8	5	72	42 (5)	1
	RSA6A	78	0	22	55	60	14	8	74	42 (7)	1
	RSA5	83	0	17	67	59	10	5	73	41 (9)	1
	RSA4	81	0	19	52	59	18	10	74	42 (14)	1
Makotuku Member	**RSA8**	76	1	24	53	64	18	2	68	42 (9)	3
	RSA7C	77	1	23	56	61	15	3	67	42 (11)	3
	RSA7B	81	<2	19	60	57	16	2	69	41 (5)	3
	RSA7A	78	<1	22	53	58	22	2	66	42 (6)	1
	RSA10	80	0	20	58	73	17	2	66	42 (8)	2
	RSA3	83	0	17	50	55	29	1	67	(8)	3
	RSA1B	80	0	20	51	66	25	1	60	41 (8)	3
	RSA1A	77	0	23	54	75	21	1	65	41 (7)	1
Waitonga Member	**RSA2**	84	<1	16	70	57	10	3	59	41 (6)	1
	RSA9	86	<1	14	70	52	13	2	64	41	1
Turoa Member	**RSA11**	78	0	22	60	53	14	2	63	40 (10)	2
	RSA12	77	0	23	60	60	14	1	68	41	2

*Clinopyroxene percentages include pigeonite.

Anorthite number: An = Ca/(Ca + Na), Enstatite number: En = Mg/(Ca+Mg+Fe^{T}), Wo number: Wo = Ca/(Ca+Mg+Fe^{T})

$^{+}$Wo for pigeonite in parenthesis. Sample RSA3 did not return augite compositions, while samples RSA9 & RSA12 did not return pigeonite compositions.

The results showed that crystals over 20 µm show scattered distributions, while crystals under 5 µm plot mostly towards the equant field (Figure 5.7c). Crystals between 10 – 20 µm and 5 – 10 µm are categorized as being prolate to bladed, almost overlapping their distributions, however, displaying more scatter for the range 10 – 20 µm (Figure 5.7c). To confirm if this trend was similar for all the samples, averages per sample for the same crystal size ranges for the L-axis (i.e., <5 µm, 5 – 10 µm, 10 – 20 µm, 20 – 30 µm & >30 µm) were plotted, with similar results to those observed for sample RSA8 (Figure 5.7c & d). The averages for crystals <5 µm were generally plotted grouped in the prolate field towards the equant field. While the average sizes >20 µm are scattered between the prolate and bladed fields (Figure 5.7d). Similarly, as seen with sample RSA8, the average sizes for all samples between 5 – 10 µm and 10 – 20 µm are largely overlapping each other, with broader scatter for the size range 10 – 20 µm which trends towards the bladed field (Figure 5.7d).

As observed in Figure 5.4, the samples can be separated into 4 groups based on the content of alkalis and silica in whole rock and groundmass, which can be correlated with the geological units assigned to the samples. While in whole rock compositions, the Mangaehuehu Member is easily identifiable: alkalis ~4.8 wt% and SiO_2 ~59 wt%; the Makotuku, Waitonga and Turoa members have similar compositions: alkalis ~5.8 wt% and SiO_2 ~61 wt% (Figure 5.4a). Here, the Mangaehuehu Member whole rock compositions have higher values of MnO, $Fe_2O_3^T$ (Total iron expressed as Fe_2O_3), MgO and CaO compared to the other members ($Fe_2O_3^T$ ~7 wt%, MgO ~6 wt% and CaO ~7.2 wt%; and other members: $Fe_2O_3^T$ ~6.1 wt%, MgO ~3.3 wt% and CaO ~6 wt%) (Table 5.4).

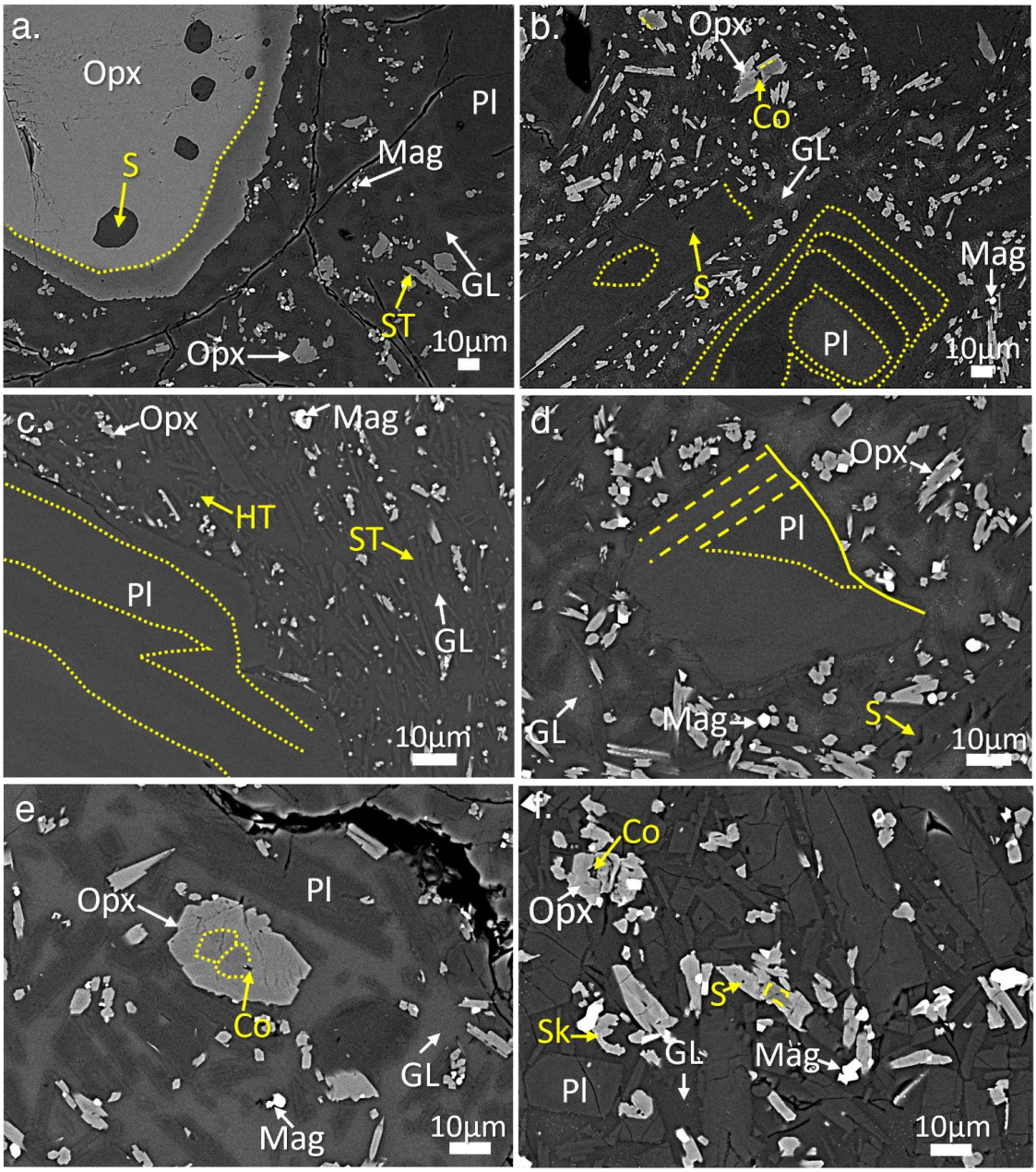

Figure 5.6. Mineral assemblage and textures in the lavas of the Mangawhero Formation, shown with backscattered electron (BSE) images.a. Orthopyroxene (Opx) phenocryst showing a coarse sieve texture (S) and a wavy resorption surface (dotted line). Note microlite orthopyroxene showing swallow tail texture (ST). b. Plagioclase (Pl) phenocrysts show zoning, which in some cases is associated to wavy resorption surfaces. Note the microlite orthopyroxene showing a resorbed core (Co) and normal zonation (dashed line). c. Plagioclase phenocryst showing oscillatory zonation with resorption wavy surfaces. Note some of the microlites show hollow textures (HT) and swallow tail textures. d. Fractured plagioclase microlite showing oscillatory zonation and resorption surface. Note also a plagioclase microlite with sieving at the bottom right corner of the image. e. Orthopyroxene microlite, with wavy resorption surfaces and incipient resorption in the core. f. Plagioclase, orthopyroxene and Fe-oxide (Mag) microlite assemblage. Some of the orthopyroxenes microlites show skeletal textures (Sk) with protruding structures, zonation and resorption features such as resorbed cores and sieving. GL: Interstitial glass. The groundmass colour varies with the presence of nanolites, with lighter grey BSE contrasts indicating a higher occurrence of nanolites in the sample compared to samples with darker groundmasses.

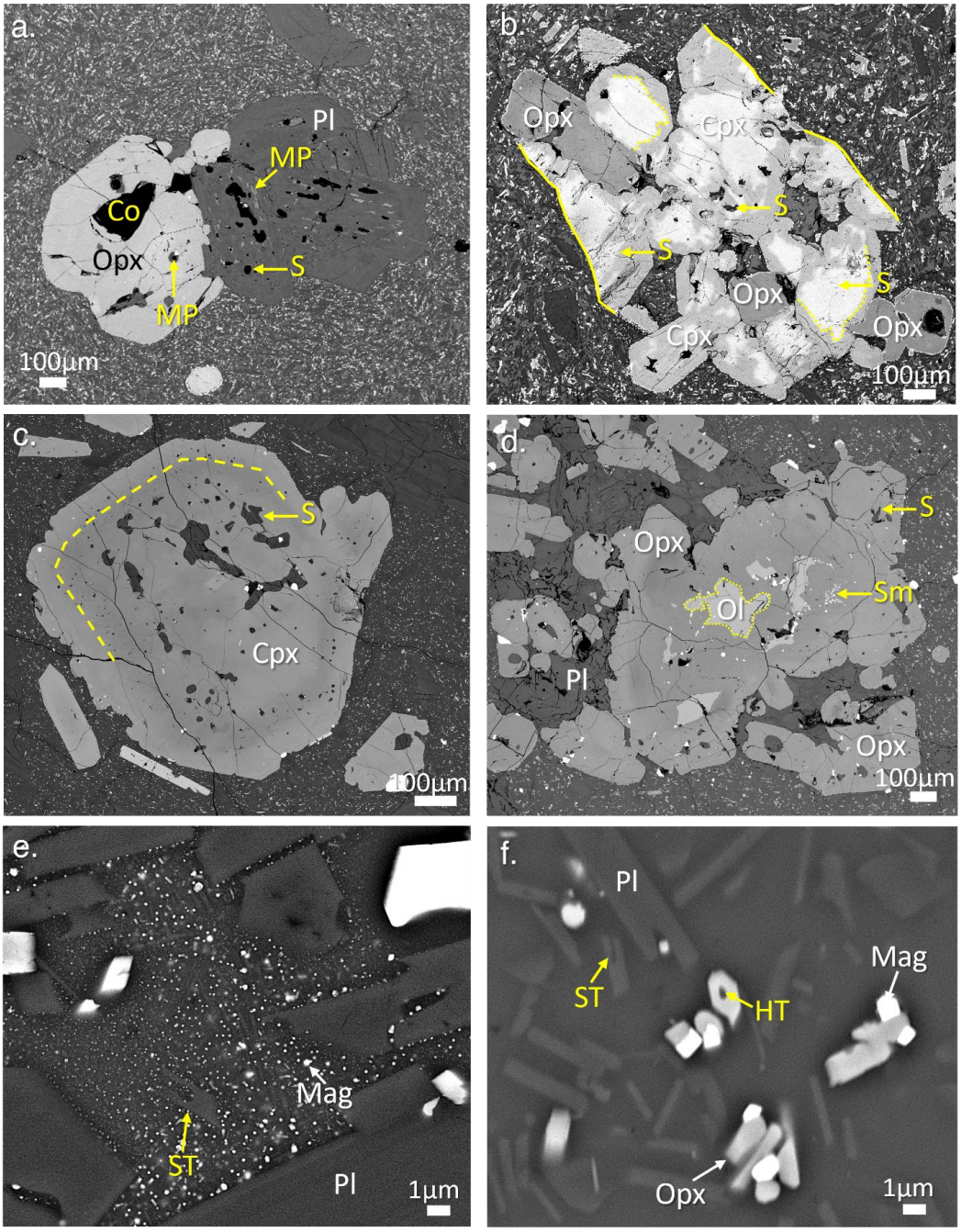

Figure 5.7. Back-scattered electron images of phenocrysts and nanolites from Mount Ruapehu. Glomerocryst of orthopyroxene (Opx) and plagioclase (Pl) from sample RSA1A. The orthopyroxene has a resorbed core (Co) and melt pockets (MP) with nanolites, while the plagioclase also shows melt pockets and sieving (S). b Glomerocryst of clinopyroxene (Cpx) and orthopyroxene from sample RSA6B. The clinopyroxene shows sieving and wavy resorbed surfaces (dotted line). Note how the crystals seem to have an abrupt stop on the continuity of the wavy surfaces suggesting a fracture plane (solid line). c. Clinopyroxene phenocryst from sample RSA2. The crystal shows sieving and oscillatory zoning (dashed line) d. Xenocryst of orthopyroxene with olivine (Ol) core from sample RSA12. The orthopyroxene shows sieving and wavy resorbed surfaces where is in contact with the olivine. Symplectite (Sm) veins of Fe-Ti oxide (magnetite) are also present in the orthopyroxene. e. Nanolite-populated glass from sample RSA3. Most of the nanolites are Fe-Oxides (Mag). Note the plagioclase nanolite exhibiting swallow tail texture (ST) f. Plagioclase, orthopyroxene and Fe-oxides nanolites in sample RSA2. Note the hollow texture (HT) in the orthopyroxene and the swallow tail texture in the plagioclase.

In contrast with the relative homogeneity of the bulk rock data, the groundmass composition ranges from andesite to rhyolite, defining a common silica and alkali differentiation trend (Figure 5.4b). The groundmass composition defines at least three different compositional groups (i.e., transitional andesite to dacite, dacite and rhyolite melts) (Figure 5.4b). The Mangaehuehu Member, which in the whole rock composition presents low alkalis and silica, has andesite-dacite groundmass compositions that overlap with the groundmass of samples of the Makotuku Member (Figure 5.4b). While the Waitonga and Turoa members, which had similar whole rock compositions to the Makotuku Member, show more evolved groundmass compositions (i.e., Waitonga Member: rhyolitic & Turoa Member: dacitic in Figure 5.4b). The groundmass groups also define a common, positive correlation between alkalis and silica, and negative correlations between silica and FeO^T, MgO and CaO contents (i.e., Mangaehuehu and Makotuku members: alkalis ~6.2 wt%, SiO_2 ~63 wt%, FeO^T ~3.7 wt%, MgO ~0.8 wt% and CaO ~2.7 wt%; Turoa Member: alkalis ~7.1 wt%, SiO_2 ~66.5 wt%, FeO^T ~4.8 wt%, MgO ~1.4 wt% and CaO ~3.8 wt%; and Waitonga Member: alkalis ~7.7 wt%, SiO_2 ~69.8 wt%, FeO^T ~6 wt%, MgO ~2.6 wt% and CaO ~5.3 wt%) (Full groundmass data can be found in an online repository, see Appendix 3).

Table 5.4. XRF whole rock normalized compositions.

Unit	Sample Name	SiO_2 (wt%)	Al_2O_3 (wt%)	TiO_2 (wt%)	MnO (wt%)	Fe_2O_3 (wt%)	MgO (wt%)	CaO (wt%)	Na_2O (wt%)	K_2O (wt%)	P_2O_5 (wt%)	Mg#	Total (wt%)	LOI*
Mangaehuehu Member	RSA13	59.19	15.50	0.71	0.12	7.01	6.72	7.25	3.20	1.63	0.19	65.50	101.52	-0.18
	RSA6B	59.61	15.62	0.69	0.12	7.10	5.96	7.32	3.23	1.55	0.18	62.46	101.36	-0.21
	RSA6A	59.83	15.59	0.70	0.12	7.06	5.96	7.29	3.19	1.57	0.18	62.55	101.49	-0.28
	RSA5	59.89	15.60	0.70	0.12	7.14	5.88	7.25	3.20	1.60	0.17	62.00	101.56	-0.03
	RSA4	59.95	15.66	0.69	0.12	7.00	5.94	7.36	3.25	1.58	0.18	62.66	101.72	-0.33
Makotuku Member	RSA8	60.53	17.89	0.76	0.10	6.40	3.10	6.55	3.83	1.91	0.20	48.93	101.26	0.23
	RSA7C	60.66	17.86	0.78	0.11	6.43	3.15	6.51	3.82	1.91	0.20	49.26	101.43	-0.04
	RSA7B	60.57	17.82	0.76	0.11	6.41	3.17	6.49	3.82	1.91	0.21	49.44	101.26	0.20
	RSA7A	60.95	17.80	0.79	0.10	6.39	3.04	6.41	3.93	1.92	0.21	48.52	101.55	-0.20
	RSA10	61.27	18.04	0.79	0.10	6.12	2.68	6.29	4.05	1.91	0.20	46.40	101.45	-0.32
	RSA3	61.61	17.52	0.81	0.10	6.41	2.74	6.04	4.01	2.03	0.21	45.86	101.48	-0.37
	RSA1B	61.28	17.87	0.79	0.10	6.16	2.65	6.23	3.95	1.95	0.20	45.98	101.18	-0.49
	RSA1A	61.54	18.02	0.79	0.10	6.18	2.70	6.24	4.01	1.93	0.21	46.34	101.73	-0.43
Waitonga Member	RSA2	62.43	16.44	0.71	0.10	6.04	4.00	5.81	3.55	2.08	0.19	56.73	101.35	-0.27
	RSA9	62.88	16.53	0.69	0.10	5.65	3.71	5.62	3.57	2.26	0.19	56.52	101.18	0.01
Turoa Member	RSA11	60.47	17.26	0.80	0.11	6.63	3.79	6.33	3.54	1.97	0.22	53.12	101.11	-0.16
	RSA12	61.91	16.95	0.76	0.10	6.24	3.67	5.97	3.86	1.90	0.20	53.80	101.56	0.10

*Loss on ignition (LOI) calculation process is available in Appendix 1, Table S1.
[T] Fe expressed as Fe_2O_3.
Mg#=100*Mg/(Mg+Fe^{+2}).

5.4.2 Crystal Size Distributions (CSD)

We obtained 17 pyroxene 3D-CSDs from the lavas of the Mangawhero and Whakapapa formations (Figure 5.8a). All CSD plots show downturns at < 5 μm (Figure 5.8a) and also show four types of trends between 5 – 30 μm with slight changes in the shapes of the plots. Type 1: almost log-linear (Figure 5.8b), type 2: concave upwards (Figure 5.8c), type 3: concave downwards (Figure 5.8d) and type 4: curved, concave downwards and upwards (Figure 5.8e). The downturns observed for the smaller sizes (< 5 μm) and the changes in the shape of the plots between 5 – 30 μm, indicate multiple populations of microlites coexisting, which may affect the slope calculations for the full microlite range (i.e., 1 – 30 μm in width). This is particularly true for samples with type 4 distributions, which showed the largest differences (Δ) in the slope calculation using the range between 5 – 30 μm versus 10 – 20 μm (i.e., Δ slope: 0.06 – 0.1 – see data comparison in Appendix 2; Table S14). Hence, the slope calculation was performed for the range between 10 – 20 μm which shows log-linear distributions for all samples (Figure 5.9a). The CSD slopes between 10 – 20 μm vary between -0.18 and -0.35 (Figure 5.9b) and are summarized in Table 5.5, alongside the intercept and R^2 and significance (i.e., p-value).

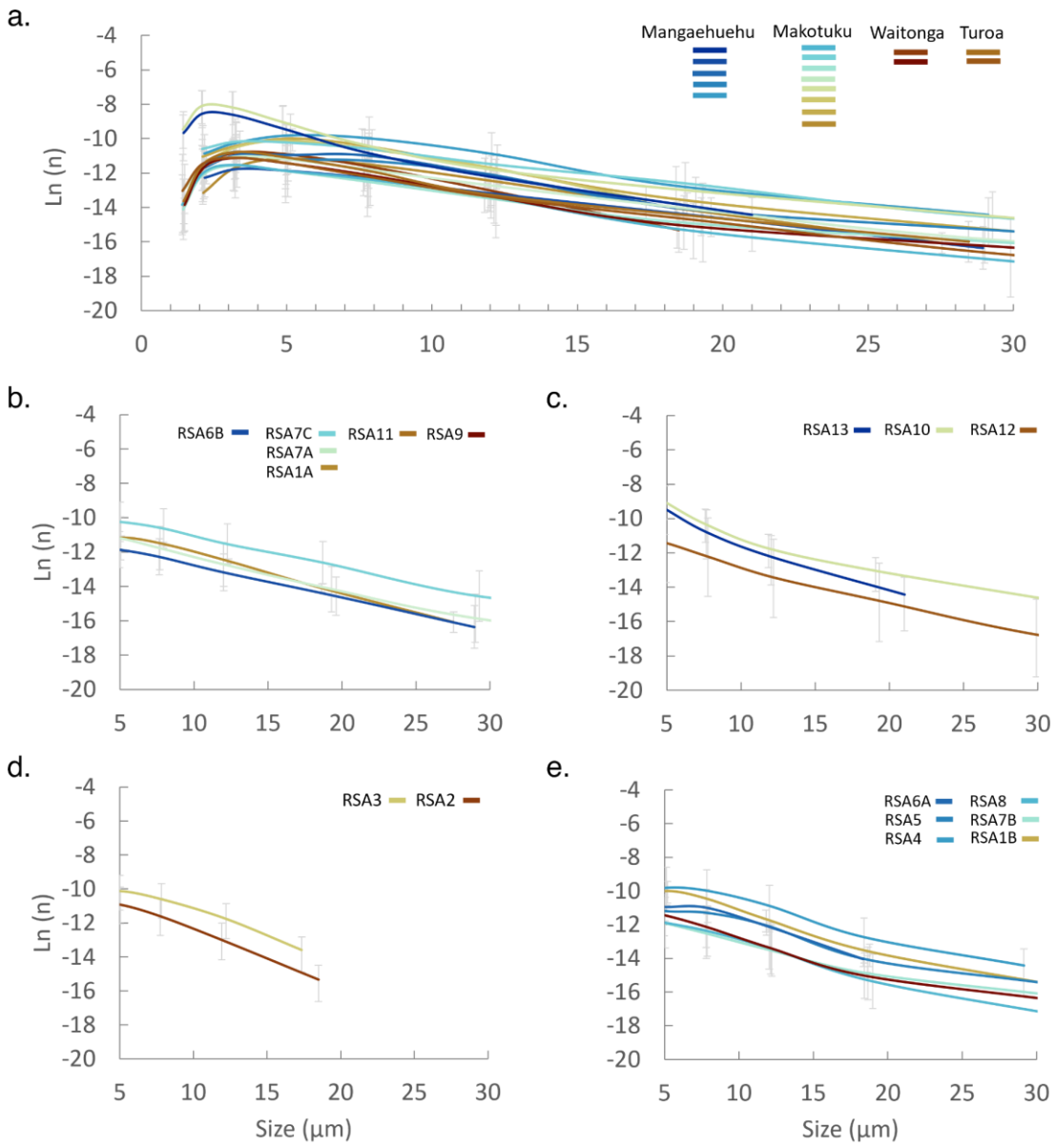

Figure 5.8. Crystal size distributions (CSD) for pyroxenes of the Mangawhero and Whakapapa formations– Mount Ruapehu, New Zealand. The bars represent the minimum error associated with population density. a. CSD Plots for all the samples. Note all the samples show a downturn for the smaller sizes, usually below 5µm. Individual plots are provided in Appendix 2. Panels b – e show detail of CSD plots trends between 5 and 30 µm. b. Trend type 1. Log-linear. c. Trend type 2. Concave upwards. d. Trend type 3. Concave downwards. e. Trend type 4. Curved (i.e., concave downwards and upwards).

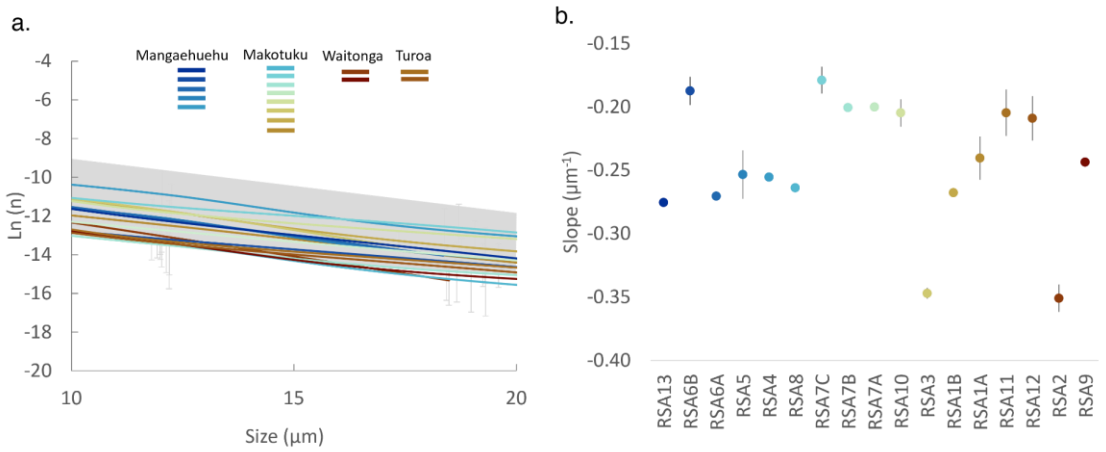

Figure 5.9. Crystal size distribution (CSD) slopes. a. Detail of CSD plots of pyroxenes between 10 and 20 µm. The area in gray represents the range covered by tephra CSDs in Lormand et al. (2020). Note how the CSD plots of the lavas almost fit the area representing the tephra, following a similar almost log-linear trend. b. CSD slopes (circles) calculated for all the samples between 10 – 20 µm, the bars represent the uncertainty of the slope. Some samples have uncertainties smaller than the symbol. The slopes data can be found in Table 5.5.

Table 5.5. Crystal size distribution (CSD) data calculated for crystals between 10 and 20 µm.

Unit	Sample	Slope	Slope Uncertainty	Intercept	R^2	p-value (α=0.05)
Mangaehuehu Member	RSA13	-0.28	0.002	-8.81	1.000	0.003
	RSA6B	-0.19	0.003	-10.90	1.000	0.005
	RSA6A	-0.27	0.011	-8.91	0.998	0.013
	RSA5	-0.25	0.003	-9.17	1.000	0.003
	RSA4	-0.26	0.003	-7.89	1.000	0.004
Makotuku Member	RSA8	-0.26	0.002	-10.26	1.000	0.003
	RSA7C	-0.18	0.004	-9.28	0.999	0.007
	RSA7B	-0.20	0.011	-11.05	0.997	0.017
	RSA7A	-0.20	0.003	-10.29	1.000	0.005
	RSA10	-0.20	0.018	-9.14	0.992	0.028
	RSA3	-0.35	0.019	-7.65	0.997	0.017
	RSA1B	-0.27	0.011	-8.48	0.998	0.013
	RSA1A	-0.20	0.003	-9.35	1.000	0.005
Waitonga Member	RSA2	-0.35	0.002	-8.84	1.000	0.002
	RSA9	-0.24	0.017	-10.39	0.995	0.022
Turoa Member	RSA11	-0.20	0.018	-10.62	0.993	0.027
	RSA12	-0.21	0.011	-9.17	0.997	0.016

5.4.3 Hygrometry and thermobarometry

The temperature (T) and pressure (P) obtained from magmatic liquid (ML) compositions and the list of minerals in the equilibrium assemblage (using the ML thermobarometer of Weber & Blundy, 2024) returned averages and standard deviations of 1015 ± 42 °C and 214 ± 190 MPa, respectively (Table 5.6 & Figure 5.10a – c). Water contents estimated from plagioclase-liquid pairs (Waters & Lange, 2015) yielded average values of 1.30 ± 0.35 wt%, in good agreement with the melt inclusion data of Kilgour et al. (2014) and Auer et al. (2016) (Figure 5.10d - f & Table 5.7). Orthopyroxene-liquid T and P conditions of crystallization (Putirka, 2008) were calculated in the ranges of 1044 ± 39 °C and 167 ± 260 MPa, respectively (Figure 5.10a - ca & Table 5.6). In sample RSA9, one orthopyroxene crystal remained within 3σ error, but results plotted notably away from the results on other crystals of the same sample. For this reason, results from the crystal are reported but the data is not considered in the results (*T*=956 °C & *P*=673 MPa – Figure 5.10c).

Notably, the orthopyroxene-melt thermobarometry calculations present the highest and lowest temperatures and pressures (Table 5.6). On the other hand, the temperature estimates for plagioclase (average of 1067 ± 36 °C) show similar values to those of orthopyroxenes-melt and liquid-assemblage estimates (Tables 5 – 6 & Figure 5.10).

Comparing the orthopyroxene-melt thermobarometry results with the geological units, we noted that the lowest average temperatures and pressures are reported for the most evolved samples (i.e., Waitonga and Turoa members: T = 936 – 1015 °C & P = 104 – 181 MPa in Table 5.6 & Figure 5.10c), where the Waitonga Member shows the lowest temperatures (i.e., RSA2: T = 940 °C & RSA9: T = 936 °C – Table 5.6). The Mangaehuehu Member samples have lower temperatures and pressures than those of the Makotuku Member (i.e., Mangaehuehu Member: T = 1042 – 1089 °C & P = 87 – 147 MPa – Figure 5.10a; Makotuku

Member: T = 1049 – 1103 °C & P = 129 – 295 MPa – Figure 5.10b; Table 5.6), overlapping the highest values of the Mangaehuehu Member with the lowest values of the Makotuku Member, similarly to the trend observed for the groundmass compositions in Figure 5.4b.

The magmatic liquid thermobarometry show similar patterns to those of the orthopyroxene-liquid thermobarometry with lowest temperature and pressure values for the Waitonga and Turoa members, and overlapping results for the Mangaehuehu and Makotuku members (i.e., Mangaehuehu Member: T = 1021 – 1036 °C & P = 187 – 223 MPa – Figure 5.10a; Makotuku Member: T = 1008 – 1038 °C & P = 192 – 257 MPa – Figure 5.10b; Waitonga Member: T = 980 – 981 °C & P = 211 – 221 MPa; Turoa Member: 977 – 1002 °C & P = 152 – 170 MPa – Figure 5.10c; Table 5.6). The hygrometry also shows correlating results with the Makotuku Member showing the lowest H_2O content, compared to the other members (i.e., Mangaehuehu Member: H_2O = 0.7 – 2.0 wt% - Figure 5.10d; Makotuku Member: H_2O = 0.2 – 1.4 wt% – Figure 5.10e; Waitonga Member: H_2O = 1.7 – 1.8 wt% – Figure 5.10f; Turoa Member: H_2O = 1.2 – 2.2 wt% – Figure 5.10f Table 5.7).

Table 5.6. Thermobarometry data.

Unit	Sample	MagMaTaB			OPX			
		Rasters analyzed	Average T (°C)	Average P (MPa)	Crystals assessed	Crystals in equilibrium	Average T (°C)	Average P (MPa)
Mangaehuehu Member	RSA13	10	1021	223	13	4	1042	115
	RSA6B	20	1027	218	16	11	1083	87
	RSA6A	10	1036	208	10	6	1080	122
	RSA5	10	1015	196	12	0		
	RSA4	10	1030	187	15	8	1089	147
Makotuku Member	RSA8	20	1038	257	15	10	1081	185
	RSA7C	20	1036	245	21	11	1103	145
	RSA7B	10	1010	205	16	14	1063	274
	RSA7A	10	1020	240	18	9	1075	295
	RSA10	20	1021	242	18	9	1049	129
	RSA3	10	1028	235	22	13	1066	184
	RSA1B	10	1008	192	13	8	1058	204
	RSA1A	10	1023	238	14	6	1060	208
Waitonga Member	RSA2	7	981	211	13	1	940	117
	RSA9	9	980	221	15	4	936	181
Turoa Member	RSA11	9	1002	170	21	13	1015	177
	RSA12	9	977	152	19	7	970	104

Thermobarometry uncertainties: MagMaTaB: T=42 °C & P=190 MPa (Weber & Blundy, 2024).
Orthopyroxene-liquid: T=39 °C & P=260 MPa (equations 28a & 29a in Putirka, 2008).

Table 5.7. Hygrometry and thermometry data from plagioclase.

Unit	Sample	Crystals assessed	Crystals in equilibrium	Melt Max P (MPa)	Average H_2O (wt.%)	Average T (°C)	Max An#	H_2O for Max An# (wt%)	T for Max An# (°C)
Mangaehuehu Member	RSA13	29	18	253	1.70	1075.94	69	1.65	1085
	RSA6B	19	19	289	0.69	1098.56	69	0.67	1106
	RSA6A	25	24	377	1.27	1099.12	70	1.21	1109
	RSA5	15	14	323	2.04	1070.49	64	2.00	1077
	RSA4	18	17	224	1.13	1087.74	68	1.11	1093
Makotuku Member	RSA8	19	3	362	0.62	1101.76	62	0.59	1106
	RSA7C	28	7	329	0.27	1110.31	62	0.24	1115
	RSA7B	21	16	243	1.40	1075.47	61	1.38	1079
	RSA7A	25	10	400	0.68	1103.69	66	0.65	1110
	RSA10	9	4	216	1.42	1071.91	62	1.42	1074
	RSA3	22	6	272	1.05	1086.97	62	1.03	1090
	RSA1B	14	4	216	1.32	1072.88	60	1.28	1077
	RSA1A	17	10	296	1.32	1083.50	64	0.97	1094
Waitonga Member	RSA11	22	7	195	1.26	1045.89	63	1.23	1050
	RSA12	21	16	165	2.22	1003.48	68	2.15	1013
Turoa Member	RSA2	22	18	239	1.72	984.67	61	1.65	993
	RSA9	26	20	245	1.92	970.54	59	1.84	978

Hygrometry uncertainties: H_2O=0.35 wt.% (Waters & Lange, 2015).
Thermometry uncertainties: T=36 °C (Putirka, 2008).
An: Anorthite number.

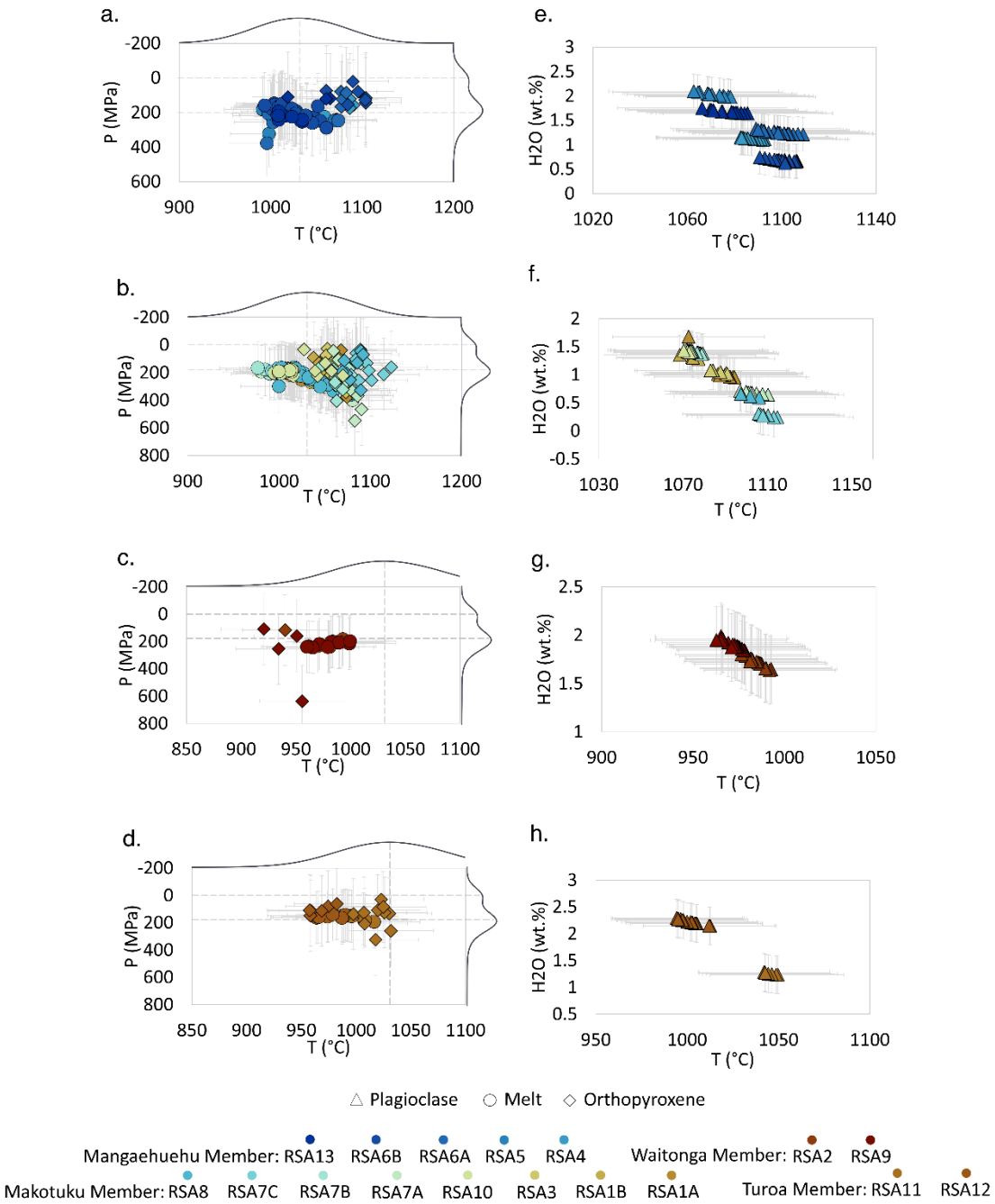

Figure 5.10. Thermobarometry and hygrometry for the studied Mount Ruapehu lavas. a – d. Temperature (*T*) versus Pressure (*P*) estimates for magmatic liquid thermobarometry (circles) and orthopyroxene-liquid (diamonds). Kernel density estimates for all the samples analyzed are included to the right and top of the diagrams to show the distribution peaks in the data. Dashed lines are included to inform peak values of the distributions (i.e., P = ~40 & ~200 MPa; T = ~1030 °C). e – h. Temperature (*T*) versus water content (H_2O) calculated in plagioclases. Note how the temperatures calculated through thermobarometry in magmatic liquids and orthopyroxenes are similar to those calculated in plagioclases. a & e. Mangaehuehu Member samples. b & f. Makotuku Member samples. c & g. Waitonga Member samples. d & h. Turoa Member samples.

5.4.4 Residence times and ascent rates

The reference crystal residence times (τ opx) for the Mangawhero and Whakapapa formations, calculated using the CSD slopes for individual samples (Table 5.5) and the reference orthopyroxene growth rate from the Mangatawai Formation (1.80×10^{-11} m/s), vary between 2 and 4 days (Table 5.8). Propagating uncertainties associated with the CSD slopes (i.e., ± 0.002 – 0.019 in Table 5.5) and the orthopyroxene growth rate (i.e., $2\sigma = \pm 0.6 \times 10^{-11}$ m/s in Lormand, 2020), extends this range from 1 to 6 days (Min & Max τ opx in Table 5.5).

When applying a broader range of growth rates to assess the impact of growth rate uncertainty on residence times, the maximum values increase substantially. Using the slowest growth rate considered (i.e. 1.00×10^{-12} m/s), the residence times increased to 66 days (Max τ for sample RSA10 in Table 5.8 & Figure 5.11a). Conversely, residence times derived from the fastest growth range (i.e., 1.00×10^{-9} m/s) yield minimum values of less than 2 hours (i.e., Min τ = 0.03 – 0.06 days in Table 5.8).

At the scale of geological units, crystal residence times show overall consistency across members, with average τ opx values under 3 days for all units (Table 5.8). The Mangaehuehu Member yields τ opx values between 2 – 5 days, the Makotuku Member 1 – 6 days, the Waitonga Member 1– 4 days, and the Turoa Member 2– 5 days. The Makotuku Member exhibits the longest crystal residence times when adopting the full growth rate range, with five samples exceeding 58 days (RSA1A, 7A, 7B, 7C & 10 – Table 5.8). In comparison, maximum residence times for the Mangaehuehu, Waitonga and Turoa members reach up to 63, 51 and 62 days, respectively (Table 5.8).

Maximum depths (Z_{max}) were calculated from the highest pressures derived from the orthopyroxene thermobarometry (Max P in Table 5.8), assuming lithostatic conditions and using the average bulk density of the Torlesse Terrain (Mielke et al., 2016). Sample RSA5

was excluded from this analysis because all analyzed orthopyroxene crystals failed the equilibrium test, preventing reliable pressure estimation (Table 5.6). Calculated Z_{max} values range from 5 to 22 km, extending to 32 km when pressure uncertainties are considered (Max Z_{max} in Table 5.8). Although uncertainties associated with EPMA analyses were propagated in the thermobarometric calculations, these remain below 50 MPa (See Appendix 3), well within the standard error of the orthopyroxene barometer (i.e., ±250 MPa in Putirka, 2008).

Depth variations broadly mirror trends observed for crystal residence times. The Makotuku Member shows the greatest depths, with an average Z_{max} of ~14 km and maximum values between 19 – 32 km (Table 5.8). In contrast, the Mangaehuehu, Waitonga and Turoa members record shallower average depths of approximately 6, 7 and 9 km, respectively, with corresponding maximum depths of 17, 20 and 23, respectively (Table 5.8).

Using τ opx and Z_{max} to calculate reference ascent rates (*v* opx), we obtained velocities between 0.02 and 0.08 m/s (Figure 5.11b & Table 5.8). When propagating uncertainties associated with both depth and residence times estimates, *v* opx increases to a maximum of 0.21 m/s (Table 5.8). Considering the full range of depths (i.e, minimum and maximum Z_{max}) in combination with the full range of residence times (i.e., minimum and maximum τ), we found magma ascent rates (*v*) up to 9 m/s (Makotuku Member: sample RSA3 – Table 5.8). Overall, the Makotuku Member exhibits the fastest ascent rates, with an average of ~0.06 m/s and a maximum *v* opx of 0.21 m/s, showing correlation with the crystal residence times and depths (Table 5.8). The Mangaehuehu, Waitonga and Turoa members show systematically lower ascent rates than the Makotuku Member. Average *v* opx values of ~0.03 m/s for the Mangaehuehu and Turoa member, and 0.04 m/s for the Waitonga Member, with maximum *v* opx values of 0.11 – 0.13 m/s and maximum *v* values of ~5 m/s (Table 5.8).

Table 5.8. Residence times, depths and ascent rates.

Unit	Sample	τ opx (days)	Min τ opx (days)	Max τ opx (days)	Min τ (days)	Max τ (days)	Max opx P(MPa)	*Zmax* (km)	Min *Zmax* (km)	Max *Zmax* (km)	v opx (m/s)	Min v opx (m/s)	Max v opx (m/s)	Min v* (m/s)	Max v (m/s)
Mangaehuehu Member	RSA13	2.3	1.7	3.5	0.04	42	120	5	0	15	0.02	0.00	0.10	0	4
	RSA6B	3.4	2.5	5.2	0.06	63	153	6	0	16	0.02	0.00	0.08	0	3
	RSA6A	2.4	1.7	3.7	0.04	45	166	7	0	17	0.03	0.00	0.11	0	5
	RSA5	2.5	1.9	3.8	0.05	46									
	RSA4	2.5	1.9	3.8	0.04	46	175	7	0	17	0.03	0.00	0.11	0	4
Makotuku Member	RSA8	2.4	1.8	3.7	0.04	44	327	13	3	23	0.06	0.01	0.15	7.0E-04	6
	RSA7C	3.6	2.6	5.5	0.06	66	257	10	0	21	0.03	0.00	0.09	0	4
	RSA7B	3.2	2.3	5.1	0.05	61	404	16	6	26	0.06	0.01	0.13	1.1E-03	6
	RSA7A	3.2	2.4	4.9	0.06	59	547	22	11	32	0.08	0.03	0.16	2.3E-03	7
	RSA10	3.1	2.2	5.2	0.05	62	225	9	0	19	0.03	0.00	0.10	0	4
	RSA3	1.9	1.3	2.9	0.03	35	342	14	3	24	0.08	0.01	0.21	1.1E-03	9
	RSA1B	2.4	1.7	3.8	0.04	45	317	13	2	23	0.06	0.01	0.15	5.8E-04	6
	RSA1A	3.2	2.4	4.9	0.06	59	377	15	5	25	0.05	0.01	0.12	9.2E-04	5
Waitonga Member	RSA2	3.1	2.2	5.2	0.03	33	117	5	0	15	0.03	0.00	0.13	0	5
	RSA9	3.1	2.2	4.9	0.04	51	254	10	0	20	0.04	0.00	0.13	0	5
Turoa Member	RSA11	1.8	1.4	2.8	0.05	62	324	13	3	23	0.05	0.01	0.12	4.8E-04	5
	RSA12	2.6	1.9	4.3	0.05	58	147	6	0	16	0.02	0.00	0.09	0	4

* Samples with ν = 0, represent samples in which ν approaches zero.
Minimum (Min) and Maximum (Max) values include uncertainties described in the text.

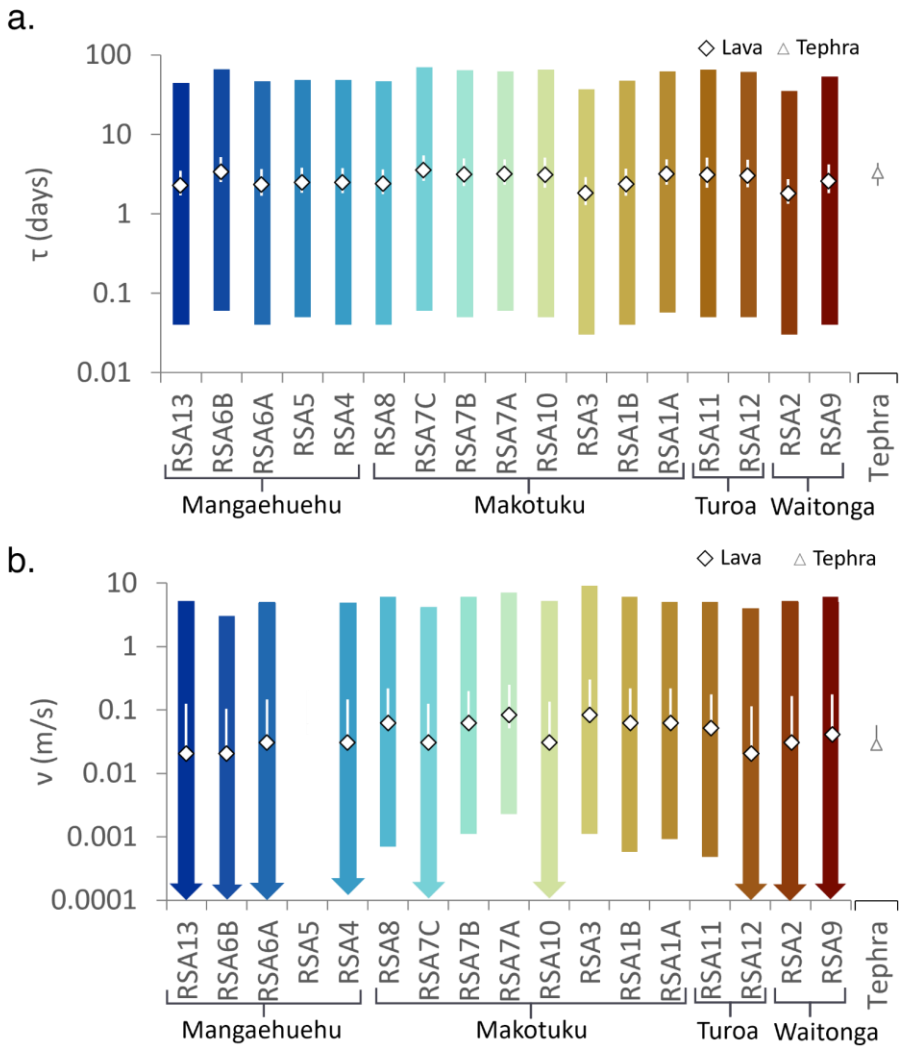

Figure 5.11. Magma residence times and ascent rates.a. Residence times (τ). Bars: τ calculated using slopes and growth rate range for pyroxene (1 x 10^{-9} to 1 x 10^{-12} m/s) including slope uncertainty (see text). Diamonds: τ opx estimated using a well-known growth rate for orthopyroxene (1.80 x 10^{-11} m/s). Slope and growth rate uncertainties are represented by white bars. b. Ascent rates (ν). Bars: calculated using the τ and depth (Z_{max}) ranges determined for each individual sample, including the uncertainties from τ and Z_{max} calculations (see text). Arrowed bars represent those samples for which ν approaches 0 m/s. Diamonds: ν opx estimated using τ opx. τ opx and Z_{max} uncertainties are represented by white bars. The missing bars indicates ν approaching 0 m/s. Tephra average data (triangles) from Lormand et al., (2020) is included for comparison with uncertainties (gray bars) indicating ±2 standard deviation of the average.

5.5 Discussion

5.5.5 Magmatic P-T-H_2O

The P-T-H_2O conditions established with the hygrometer and thermobarometers are similar to those reported previously for the TgVC, showing hot magmas with low water contents (up to 1140 °C and <2.5 wt% H_2O respectively, e.g., Auer et al., 2016; Deering et al., 2011; Kilgour et al., 2013; Kilgour et al., 2009; Lormand et al., 2020). This is in contrast to the global average H_2O content in arc volcanoes (2 - 6 wt% in Plank et al., 2013). Most of our data indicate that the 15-50 ka Mount Ruapehu lavas have relatively low water contents (average 1.36 wt%), confirming previous observations for TgVC magmas, consistent with the lack of hydrated phases in the samples.

We note that there are notable differences in the P-T-H_2O estimates for some of the samples obtained with the range of mineral and melt calibrations applied (Figure 5.10). Figure 5.10c shows that the Waitonga and Turoa members return the lowest temperatures (<1030 °C), compared to the samples of the Mangaehuehu and Makotuku members, which seem to be grouped together at T ≈ 1000-1123 °C (Figure 5.10a - b). Likewise, in Figure 5.10c, the samples of the Waitonga and Turoa members, which returned the lowest temperatures, present higher H_2O contents. This can be related to the H_2O content necessary to maintain plagioclase-melt equilibrium (Waters & Lange, 2015).

The differences in the P-T-H_2O conditions can be associated with compositional variations. The Mangawhero Formation has a wider compositional diversity compared to the older units of Mount Ruapehu, maintaining a gradual increased trend in SiO_2 and K_2O composition for the erupted lavas >26 ka (Conway, 2016; Conway et al., 2018; Townsend et al., 2017). However, for the lavas erupted <26 ka (late Mangawhero and Whakapapa formations)

Conway et al. (2018) observed a reverse SiO_2 and K_2O trend overlapping the compositions of the early and middle Mangawhero Formation. These SiO_2 and K_2O trends are reflected in the compositional differences observed for whole rock and groundmass compositions (Figure 5.4). While the groundmass shows the silica enrichment for all samples of the Mangawhero Formation, the two samples of the Whakapapa Formation (RSA11 & 12) show a regression (Figure 5.4b). Similarly, the Mangaehuehu and Makotuku members show an increasing trend in SiO_2 and K_2O in whole rock compositions, while samples of the Turoa Member show similar SiO_2 and K_2O contents to those of the Makotuku Member (i.e., SiO_2 = 60 – 62 wt% and K_2O = 1.9 – 2.0 wt% – Table 5.4). Additionally, while all of the analyzed samples exhibit the same mineral phases (i.e., plagioclase, orthopyroxene, clinopyroxene and Fe-oxides), the difference between the results of the whole rock composition and matrix geochemistry shows the influence of mineral phase proportions in the bulk chemical compositions (cf. Ubide et al., 2022; Ubide et al., 2023).

We note that different degrees of silica enrichment in the groundmass can be correlated with the temperatures and H_2O contents (also observed for historical eruptions, Kilgour et al., 2013), which appear to be independent of the age of the flows, as observed while comparing the Makotuku (24 – 16 ka) and Waitonga (25 -21 ka) members. H_2O content has been proposed to play a major role in fractionation trends for calc-alkaline magmas (e.g., Berndt et al., 2005; Lee & Bachmann, 2014; Zimmer & Plank, 2006; Zimmer et al., 2010). Fractionation leads to the depletion of FeO and MgO, and the enrichment of SiO_2 and alkalis in the residual liquids. The presence of H_2O promotes the crystallization of hydrated phases such as amphibole and biotite, hindering plagioclase formation and boosting the early appearance of Fe-oxides. However, in the absence of H_2O, plagioclase readily crystallizes, the nucleation and growth of Fe-oxides is delayed, and anhydrous phases are able to crystallize (e.g., Lee & Bachmann, 2014). By inference, the low H_2O content of the

Mangawhero Formation lavas directly influenced their limited phase assemblage. However, further analysis of the compositions and textures of the crystals, as well as crystallization modelling, will be required to constrain the influence of water in detail.

Although the thermobarometry presents challenges in terms of large errors in pressure and temperature calibrations (Humphreys et al., 2016; Wieser et al., 2023a), it is notable that the differences in pressure between samples are within the error for all the barometers, yielding similar values for crystallization of a range of minerals and independently quantified equilibration of the groundmass liquid. This provides confidence when assessing pressure results to obtain maximum depths of storage per sample, Z_{max}. Samples RSA7A (P = 547 MPa) and RSA2 (P = 117 MPa) returned the highest and lowest pressure values, which translate into a wide depth range (Z_{max} = 5 – 22 km). Although it is not surprising to observe a wide range of depths within mid-lower crust in arc systems (e.g., Dufek et al., 2022; Lucci et al., 2020; Troll & Deegan, 2023), each geological unit has more restricted ranges (i.e., Mangaehuehu Member: 5 – 7 km; Makotuku Member: 9 – 22 km; Waitonga Member: 5 – 10 km; Turoa Member: 6 – 13 km - Table 5.8). Considering that the crustal thickness in the North Island is around 25 – 35 km, thinning under the TVZ to 15 – 20 km (Eberhart-Phillips et al., 2020; Leonard et al., 2021; Stratford & Stern, 2006), it seems that samples of the Mangaehuehu, Waitonga and Turoa members were stored in the mid crust, while samples of the Makotuku Member were mainly stored on the lower crust (Table 5.8). These depths coincide with volcanic earthquake hypocenter depths prior to the 1995-1996 eruptions of Mount Ruapehu at (i.e., 10–16 km in Hurst & McGinty, 1999) and the velocity models of the lithospheric structure under the volcano that interpret zones of magma accumulation (i.e., ~4-12 km Hill et al., 2015; Leonard et al., 2021; Rowland et al., 2010; Rowlands et al., 2005), particularly for samples of the Mangaehuehu, Waitonga and Turoa members.

5.5.6 Decompression/crystallization steps

Most of the crystals in the samples are under 30 μm which is relatively small and can indicate growth just before the eruption during ascent in the shallow conduit due to decompression induced dehydration (Hammer & Rutherford, 2002; Matsumoto & Geshi, 2021), supported by microlite crystal textures that exhibit skeletal features (e.g., hollow and swallow tail textures Figures 5.5a, 5.5c & 5.6e - f).

A dominant feature observed in the CSD pyroxene plots is the downturn in the trend at crystal sizes under 5 μm. These have been attributed to multiple factors, including underestimation of the sizes of small crystals (Brugger & Hammer, 2010b; Marsh, 1998), changes in nucleation/growth rate (Marsh, 1988, 1998) and crystal coarsening (Eberl et al., 2002; Higgins, 2011; Marsh, 1998). Based on our petrological assessment of the sample CSDs, these downturns below 5 μm seem to be related to crystallization/growth processes inherent to the magma in combination with magma mixing/mingling that causes disequilibrium textures as those observed in Figure 5.5 (i.e., wavy surfaces and zonation), occurred before the eruption. Here, the smaller crystals are dissolved to favor the growth of larger ones (Ostwald ripening in Lifshitz & Slyozov, 1961; Ostwald, 1900; Wagner, 1961), causing textural re-equilibration or coarsening (i.e., decrease on the number of crystals at the smaller sizes) producing the downturn on the CSDs (Higgins, 2011; Pupier et al., 2008). Crystal coarsening due to re-equilibration after magma injection would explain observed disequilibrium textures (e.g., resorbed cores, zonation and resorption surfaces in Figure 5.5e - f) in pyroxenes under 30 μm (e.g., Eskandari & Sadeghi, 2024; Eskandari et al., 2024; Luo et al., 2024).

Changes in the shapes of CSD plots define different steps of growth/nucleation (Marsh, 1988, 1998; Pupier et al., 2008), Hence, the type 1 trends (log-linear - Figure 5.8b) describes a

constant crystal growth for the microlites. On the other hand, types 2 to 4 show variations that may be linked to physical processes such as aggregation (Cashman, 2020; Marsh, 1998; Pupier et al., 2008). This might be the case for type 2 trends (concave upwards - Figure 5.8c) which are flatter towards the larger sizes indicating the possible annexation of small crystals. This is supported by petrographic observations where the pyroxenes seem to be clustered and not evenly distributed throughout the samples (e.g., Figures 5.5f & 5.6f). Type 3 (concave downwards - Figure 5.8d), seems to be an extension of the shape determined by the coarsening of the sample, which produced a flatter top around 5μm. Lastly, type 4 (curved - Figure 5.8e), shows the combination of the crystal coarsening and annexation, with flatter CSD at the smallest (i.e. 5 – 10 μm) and largest (i.e., 20 μm) sizes. There are size-related changes in the morphology of microlites with L-axis under 20 μm, as seen in Figure 5.7, where smaller crystals trend towards the equant shape field (e.g., Figure 5.7d). This is an indication of the link between growth rate and crystal sizes, confirming the occurrence of physical processes (i.e., coarsening and aggregation) as described above (e.g., Eberl et al., 2002; Pupier et al., 2008). Nonetheless, for the size ranges between 5 – 20 μm, there is no significant difference in the shape distributions, implying that the growth rates for this size range are seemingly constant, and should not affect the calculation of the crystal residence times. Based on the CSD plots, it seems that there are at least two crystallization steps (i.e., at 10 & 20 μm), where there is interference of coarsening and/or aggregation for some of the samples. However, due to the uncertainties of the crystal population, it is not possible to define those confidently.

It has been recognized that higher undercooling rates (i.e., rate at which magma cools below its liquidus) generates ever-steeper slopes (Pupier et al., 2008; Toramaru, 2021). Hence, the difference in the slopes between the samples might be an indication of the cooling rate experienced for the analyzed size range (i.e., 10 – 20 μm). Here samples such as RSA2 & 3

that present the stepper slopes might have larger undercooling than flatter ones such as RSA6B & 7C. Nonetheless, there is no significant variation on the pyroxene crystal shapes under 20 μm from the samples in this study. The occurrence of only one type of shape at large cooling rates has been observed in pyroxenes, where the population of euhedral crystals dominate (Hammer, 2006). This seems to be the case for the samples in this study that show mainly euhedral/swallow tail shapes (e.g., Figure 5.5). This type of morphology has been related to moderate rates of undercooling (Shea & Hammer, 2013), consistent with degassing-induced crystallization (Frey & Lange, 2011). Additionally, plagioclase microlites under 10 μm in length show skeletal structures (e.g., swallow tailed and hollow texture in plagioclase in Figures 5.5c & 5.5f), which have also been linked to fast decompression (Hammer & Rutherford, 2002; Martel & Schmidt, 2003; Martel, 2012) and moderate undercooling (Shea & Hammer, 2013).

The sizes of microlites (i.e., mostly under 20 μm) in general indicate that the ascent rate was fast enough to hinder crystal growth and the curves are a true reflection of the magmatic conditions (e.g., Brugger & Hammer, 2010a; Brugger & Hammer, 2010b; Preece et al., 2013). Decompression experiments at high pressures have shown that there is no significant growth or nucleation of orthopyroxene when the pressure decreases, hence, chemical re-equilibration occurs to accommodate the pressure-induced disequilibrium (Martel & Schmidt, 2003). This coincides with the low abundance of pyroxene nanolites (Figure 5.6e - f). The sieving and resorbed cores observed in the pyroxenes (Figures 5.5b & 5.5f), may reflect the rapid decompression of the system, and mark a snapshot of the crystallization stage at the onset of eruption, which coincides with the main objective of this study to determine the magmatic timescales (i.e., crystal residence times and ascent rates) in lavas and to compare those with the ones obtained from tephra by Lormand et al. (2020) for the same magmatic centre.

5.5.7 Residences times and ascent rates

According to our results, including the uncertainties in the slopes and growth rate determination, the microlite crystals grew in the crust over a period between 1 and 66 days. However, considering τ opx, estimated using a defined growth rate previously estimated for the TgVC tephra (Lormand et al., 2020; Zellmer et al., 2016a, 2018), the upper limit is considerably reduced (i.e., 1 to 6 days). Although there is variation between members (i.e., Mangaehuehu Member: τ opx = 2 – 5 days, Max τ = 63 days; Makotuku Member: τ opx = 1 – 6 days, Max τ = 66 days; Waitonga Member: τ opx = 1 – 4 days, Max τ = 51 days; Turoa Member: τ opx = 2 – 5 days, Max τ = 62 days), the orders of magnitude for τ and τ opx remain the same, rendering the distinction between geological units insignificant. It has been established that microlite residence times can be in the order of hours to days for explosive eruptions, and days to months for effusive events (e.g., Vesuvius in Pappalardo & Mastrolorenzo, 2010). These distinctions are based on the differences related to the magma ascent histories, where shallow crystallization is assumed to be extensive for effusive eruptions, and restricted for explosive ones (Murch & Cole, 2019). Hence, while both estimations are plausible, to establish a more precise value for the residence times, it is necessary to determine a crystal growth rate for the lavas.

Similarities in the shapes of the crystals (i.e., blocky faceted crystals) in lavas from this study and tephra studied previously (Lormand, 2020; Lormand et al., 2020), indicate a similar degree of undercooling (Figure 5.4). Therefore, the similarity in microlite crystal shapes between lavas and tephra suggests broadly comparable undercooling conditions during ascent at the TgVC. This observation supports the plausibility of shorter residence times (on the order of days); however, it does not preclude longer residence times within the uncertainty range, given potential differences in ascent histories between eruptive styles. Additionally,

the full range of tephra CSD plots presented in Lormand et al. (2020) show similarities with those of the lavas (Figure 5.9a). These tephra CSDs were calculated for different types of eruption (i.e., Vulcanian to sub-Plinian eruptions), and due to the similarity of the slopes, it was considered that all tephras studied had similar crystal growth rates and population growth times (Lormand et al., 2020). In our case, the similarities observed between tephra and lava CSDs suggest that microlite populations in both products may record crystallization under comparable pressure and temperature conditions within the deeper conduit (e.g., Lormand et al., 2020; Murch & Cole, 2019). However, these similarities do not necessarily imply identical ascent histories, as differences in ascent dynamics between effusive and explosive eruptions may not be fully resolved by CSDs alone.

We obtained magma ascent rates with ν opx (i.e., determined using τ opx and Z_{max}) between 0.02 and 0.08 m/s, and maximum ν of 9 m/s, considering full variation ranges for τ and Z_{max} as well as method uncertainties. Similarly to the residence times the differences in the ascent rates for the geological units are within the same order of magnitude (i.e., Mangaehuehu Member: Max ν opx = 0.11 m/s, Max ν = 5 m/s; Makotuku Member: Max ν opx = 0.21 m/s, Max ν = 9 m/s; Waitonga Member: Max ν opx = 0.13 m/s, Max ν = 6 m/s; Turoa Member: Max ν opx = 0.12 m/s, Max ν = 5 m/s). These ν opx ascent rates fall within the upper range reported for effusive eruptions and overlap with ascent rates inferred for explosive activity.

Usual magma ascent rates in effusive eruptions are considerably slower than the ones obtained in this study (e.g., 0.0002m/s Mount Shasta - USA in Phillips & Till, 2021; 0.0009 m/s Irazú - Costa Rica in Ruprecht & Plank, 2013). However, faster rates are not unprecedented: they have been reported at extensional systems (e.g., 0.02 to 0.1 m/s Borgarhraun - Iceland in Mutch et al., 2019; 0.01 - 0.5 m/s Mid Atlantic Ridge in Paonita & Martelli, 2006) and hot spots (e.g., ~0.01 - 0.3 La Palma - Spain in Bonechi et al., 2024;

0.02–0.40 m/s Kilauea - USA in Edmonds et al., 2013). Usually ascent rates exceeding ~0.02 m/s are often associated with explosive eruptions (Browne & Szramek, 2015; Rutherford, 2008). Yet ascent rates alone are insufficient to uniquely distinguish eruptive styles. Accordingly, the ν opx velocities presented here are interpreted as effective maximum average ascent rates within the crust, rather than instantaneous ascent velocities. These velocities do not resolve temporal variations in the ascent rates, such as acceleration, deceleration, or transient stalling, which are known to differ between eruptive styles based on recent numerical modelling (e.g., Bamber et al., 2024; La Spina et al., 2021). Furthermore, it is important to clarify that the average ascent rates calculated in this study primarily represent magma transport within the deeper crustal conduits, rather than ascent rates through the shallow conduit immediately beneath the vent.

Here the fast ascent of the lavas of the Mangawhero and Whakapapa formations may be favored by the Taupō rift (Mortimer et al., 2010; Wysoczanski et al., 2010), which is considered an active contributor to the magmatic activity, because it facilitates magma ascent through NE striking faults (Bibby et al., 1995; Seebeck et al., 2014; Villamor et al., 2017; Wilson & Rowland, 2016). The increasing extensional rate and associated crustal thinning may facilitate magma transport through the crust and contribute to relatively short residence times and fast average ascent rates, possibly via fissure-type eruptions as seen in other rift systems (e.g., Ethiopian Rift in Keir et al., 2025; Wong et al., 2025).

5.5.8 Lava versus Tephra

There are clear similarities between the CSDs of Mount Ruapehu lava and TgVC tephra (Figure 5.9), and more broadly, overlap in the residence times and average ascent rates inferred from these populations (i.e., tephra: $\tau = 3\pm1$ days & $\nu = 0.02$ - 0.09 m/s in Lormand et al., 2020 and lava: τ opx $\approx$ 1 - 6 days & ν opx $\approx$ 0.02 - 0.08 m/s in this study - Figure 5.11),

highlighting comparable transport processes withing the TgVC, rather than a shared magmatic plumbing system.

In terms of residence times, similar values are consistent with comparable magmatic processes within the crust, despite these eruptions originating from distinct volcanic edifices and/or vents. For those eruptions originated at Mount Ruapehu, it is unsurprising for its products to show similar behaviors yet raises a key question about the controls on eruption style. The ascent rates calculated for the lavas fall within the upper range reported for effusive eruptions (see above), whereas those inferred for the tephra are comparatively slower than ascent rates reported for some highly explosive volcanic systems (e.g., Mount St Helens - USA: 1 - 3 m/s in Browne & Szramek, 2015; and 1- 2 m/s in Rutherford, 2008). Lormand et al. (2020) suggested conduit funneling (i.e., narrowing) in the uppermost part of the conduit, alongside gas exsolution, bubble nucleation and volume expansion, allowed the magma to achieve transiently faster velocities (3 – 13 m/s in Lormand et al., 2020), facilitating Vulcanian to sub-Plinian eruptions.

Similar magmatic conditions in volcanic systems that generate both effusive and explosive eruptions have been observed worldwide (e.g., Rabaul caldera - Papua New Guinea in Bernard et al., 2022). In most of these systems the transition between styles has been linked to volatile exsolution within a shallow storage region (e.g., Cordón Caulle - Chile in Castro et al., 2013) or conduit (e.g., Inyo volcanic chain - USA in Castro & Gardner, 2008). Moreover, shifts from effusive to explosive events have been linked to changes in conduit geometry that promotes gas accumulation and pressurization (e.g., 2021 La Palma - Spain in Bonechi et al., 2024; 1986 Izu-Oshima - Japan in Kozono et al., 2022; 2019 Stromboli - Italy in Viccaro et al., 2021), coinciding with the observations of Lormand et al. (2020) .

Here, we propose that relatively fast average ascent rates in lavas may be facilitated by the extensional regime of the Taupō Rift, where magma can exploit low resistance pathways such as faults and dike systems (e.g., Gómez-Vasconcelos et al., 2017; Magee & Jackson, 2020; Thiele et al., 2021). This is confirmed by findings of Cassidy et al. (2009) who showed that there is a potential connection between vents and fault locations for historic eruptions of TgVC, and supported by the NNE alignment of identified vents at Mount Ruapehu (Leonard et al., 2021), coinciding with the striking direction of the Taupō Rift (NNE in Villamor et al., 2017).

The magmas that generate Mount Ruapehu tephra and lava were both hot and nearly anhydrous (i.e., T = 1010 - 1130 °C & H_2O = 0 - 1.5 wt% in Lormand et al., 2020; T = 882 - 1162 °C & H_2O = 0 - 2.5 wt% in this study). Lormand et al. (2020) considered that the tephra microlites crystallized due to heat loss during magma ascent through narrow dikes, since the high temperature and low water contents are inconsistent with those observed forming during decompression-induced crystallization (e.g., H_2O = 1.26 – 1.73 wt% in Hammer et al., 1999; H_2O = 2.6 ± 2 wt% in Noguchi et al., 2006). However, in the case of the lavas these values are not inconsistent, hence decompression induced crystallization seems to be the best fitting model to the microlite crystallization in the lavas of the present study, supported also by low vesicularity (< 2), commonly associated with efficient outgassing (Lindoo et al., 2017). Furthermore, low water contents (e.g., <3.5 wt% in Popa et al., 2021a; Popa et al., 2021b; Szramek et al., 2006) and high temperatures (e.g., > 950 °C in Campagnola et al., 2016; Szramek et al., 2006) promote effusive over explosive eruptions. Hence, for the particular case of the TgVC, where low water contents appear to be characteristic (e.g., <2.5 wt% in Auer et al., 2016; Deering et al., 2011; Kilgour et al., 2013; Lormand et al., 2020), shallow conduit geometry likely represents a key contributing factor influencing the development of explosive eruptions. Here, the geometry of the conduit controls the outgassing and over

pressuring of the system (Okumura et al., 2009), allowing particle ejection at high velocities regardless of the composition and physical properties of the magmas (e.g., Ripepe et al., 2021; Schmid et al., 2022). In the narrow, long conduit, degassing is enhanced by increase magma permeability, while the explosivity is maintained in the short, wide conduit (Okumura et al., 2009; Schipper et al., 2013). The geometry of the conduit is also modified either by blockage, which reduces the size of the conduit (e.g., Kozono et al., 2022) or remobilization of material from the walls during eruption, which increases the size of the conduit (e.g., Viccaro et al., 2021), causing funnelling, which promotes the formation of gas slugs that over-pressure the systems pushing the magma column, and causing explosive eruptions (Ripepe et al., 2021), particularly in microlite-poor magmas (Pompilio et al., 2017), as those of the TgVC (i.e., 8 to 24 vol% in Lormand et al., 2020).

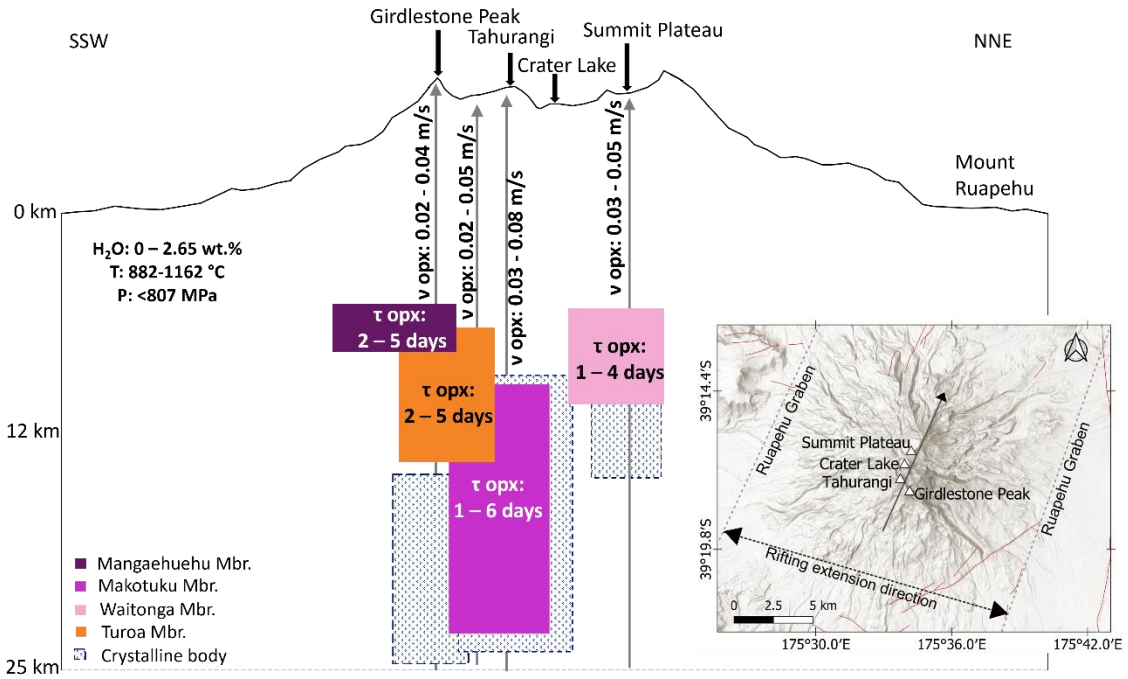

Figure 5.12. Schematic representation of the Mount Ruapehu plumbing system. Inset shows the location of Mount Ruapehu within a NNE graben structure that seems to control the position of the inferred vents (i.e., Crater Lake, Summit Plateau, Tahurangi and Girdlestone Peak – Leonard et al., 2021; Cassidy et al., 2009). Here, we infer the magma is transported by a dike-dominated plumbing system, interacting with crystalline bodies within the crust and generating magma accumulation zones at variable depth (~5 – 22 km). The residence times (τ opx) and magma ascent rates (v opx) informed are those obtained using the orthopyroxene growth rate

used in Lormand (2020) for each geological unit in Table 5.8. The size of the features is not to scale. Gray ascending arrows do not represent dikes.

Finally, we interpret the magma feeding the eruptions as dynamically ascending, interacting temporarily with crystalline bodies within the crust (i.e., dragging crystals), which likely reduced the efficient magmatic fractionation (Auer et al., 2016; Kilgour et al., 2013) (Figure 5.12). This interpretation is supported by several observations consistent with dynamic magma transport, including the high proportion of chemically disequilibrated crystal-melt pairs (> 40 % - Figure 5.2), disequilibrium textures in phenocrysts (e.g., resorption surfaces and sieving in Figure 5.5), the small size of the microlites (e.g., mostly <20 μm in Figure 5.7c) and the presence of glomerocrysts and xenocrysts (Figure 5.6a – d). Here, crystal entrainment is interpreted as a consequence of magma transport dominated by diking, in which ascending magmas interact with previously stalled magma bodies (e.g., Conway et al., 2018; Waight et al., 2017), ascending through pre-established dikes (e.g., Gómez-Vasconcelos et al., 2017; Thiele et al., 2021). These dikes are expected to crystallize upon emplacement due to conductive heat loss (e.g., Loncar & Huppert, 2022), and may be reactivated by subsequent magma injections associated with rifting-related brittle failure, promoting mechanical fracturing and partial disaggregation of the previously emplaced materials (e.g., Lormand et al., 2021; Thiele et al., 2021).

5.6 Concluding remarks

The andesitic lavas of the Mangawhero and Whakapapa formations have low water contents (averaged 1.36 and up to 2.65 wt% H_2O), alongside high temperatures (882 to 1162 °C), as indicated in previous studies on other TgVC units (e.g., Kilgour et al., 2013; Lormand et al., 2020). The relatively low water contents seems to be a signature of the products of the TgVC, related either to the melt source or transcrustal processes (Lee & Bachmann, 2014).

The maximum pressures constrained for the lava samples in this study (117 to 547 MPa) translate into crystallization depths between 5 and 22 km, locating zones of magma accumulation in the lower to middle crust coinciding with previous geophysical studies of low velocity structures and volcanic earthquake hypocenters depths in Mount Ruapehu (Hill et al., 2015; Hurst & McGinty, 1999; Leonard et al., 2021).

The residence times and magma ascent rates calculated for the lavas, suggests that the final ascent of the magma occurred between 1 – 6 days, at a speed up to 0.08 m/s, which for effusive eruptions represents a rather fast ascent through the crust, likely favored by diking (Rowland et al., 2010) enhanced in a rift setting.

The compositional groups established through whole rock and groundmass compositions for the Mangawhero Formation show slightly different behaviors, linked to specific members. While the Makotuku Member shows the longest residence times (Max τ opx = 6 days & Max τ = 66 days) and the fastest ascent rates (ν opx = 0.08 m/s), the Mangaehuehu and Turoa members present the slowest ascents rates (i.e., ν opx = 0.02 m/s), and the Waitonga Member the shortest residence times (Max τ opx = 4 days & Max τ = 51 days) (Figure 5.12).

The pyroxene microlites of Mount Ruapehu lava flows reflect the occurrence of coarsening (microlites <5 μm) and aggregation (microlites > 20 μm) framed in degassing-induced crystallization during ascent at moderate undercooling rates based on the euhedral to swallow tail textures observed (Shea & Hammer, 2013).

Lastly, since this study is based on orthopyroxene microlites, making a comparison to other systems is challenging since most studies on microlites are performed in plagioclase (e.g., Murch & Cole, 2019; Preece et al., 2013; Schiavon et al., 2023). Studies using pyroxenes usually do not discriminate between microlites and phenocrysts (e.g., Armienti et al., 2007; Jeffery et al., 2013; Suhendro et al., 2025) or focus on clinopyroxene (e.g., Giuliani et al.,

2020; Lentze & McSween Jr., 2000; Wang et al., 2022). Hence, it is of importance to expand the study of microlite CSDs towards other mineral phases as has been done for nanolites (e.g., Mujin & Nakamura, 2014; Mujin et al., 2017a; Okumura et al., 2022).

5.7 Acknowledgments

GFZ acknowledges the 2022 Endeavour Fund – Smart Ideas project "Robust volcanic eruption forecasts: leveraging magmatic speedometry into geophysical monitoring" of the Ministry of Business, Innovation & Employment (MBIE) of New Zealand (MAUX2202), which funded the present work, and the Department of Conservation of New Zealand for providing the sampling authorization to collect fresh samples from Mount Ruapehu (97663-GEO). This study received financial support from Grants-in-aid for Scientific Research in Japan to SO (Nos. 22H00161). The SR-XCT data was acquired at SPring8 (Japan) as part of proposals 2023B1698 and 2024B1705. GK is supported by the New Zealand Ministry of Business, Innovation and Employment (MBIE) through the Hazards and Risk Management Programme (Strategic Science Investment Fund, contract CO5X1702). TU is supported by the Australian Research Council (ARC Future Fellowship FT230100230). The authors acknowledge the insightful and constructive reviews provided by Michael Higgins, Dougal Jerram and an anonymous reviewer, which significantly enhanced the quality of this manuscript.

5.8 Data availability statement

The data that supports the findings of this article is available in the article; and it has also been submitted to a FAIR data repository EarthChem Library with DOI doi:10.60520/IEDA/113914.

Chapter 6 Melt evolution and crystal cargo uptake in a dike-dominated plumbing system at Mount Ruapehu, New Zealand.

Silvia Catalina Moreno-Alfonso[1], Teresa Ubide[2], Geoff Kilgour[3], Satoshi Okumura[4], Yoshiyuki Iizuka[5], Stuart Mead[1] and Georg F. Zellmer[7].

[1]Volcanic Risk Solutions, School of Agriculture and Environment, Massey University, Palmerston North, New Zealand.
[2]School of the Environment, Faculty of Science, The University of Queensland, Brisbane, Australia.
[3]Wairakei Research Centre. Earth Science New Zealand, Taupo, New Zealand.
[4]Department of Earth Science, Graduate School of Science, Tohoku University, Sendai, Japan.
[5]Institute of Earth Sciences, Academia Sinica, Taipei, Taiwan
[7]Institute of Geosciences, University of Bonn, Bonn, Germany.

This chapter will be submitted to Contributions to Mineralogy and Petrology.

Abstract

To investigate the magma plumbing architecture of Mount Ruapehu, an active stratovolcano at the Taupō Volcanic Zone (New Zealand), we combine whole rock, groundmass and crystal geochemistry of lava samples collected in the south-west flank, focusing on lava flows of the Mangawhero (50 – 15 ka) and Whakapapa (<15 ka) formations. The carrier melts have almost identical compositions, suggesting homogenous melt production and differentiation processes through this period. Whole rock compositions show MgO variations potentially linked to accumulation of mafic crystals (ortho- and clinopyroxene). The crystal cargo (plagioclase and pyroxene) is relatively small (typically <100 μm, maximum 2 mm), however variations in crystal compositions, zoning and disequilibrium with carrier liquids suggest transcrustal differentiation through variable interaction with crystalline bodies, fractional crystallization and magma mixing. In this context, ascending melts incorporate glomerocrysts

and crystal fragments through the interaction with previously emplaced crystalline bodies in dike-like structures within the crust, modulating bulk rock MgO signatures. For the most recent lavas of Mount Ruapehu (<26 ka), SiO_2 and K_2O variations had been previously described to define a reverse trend overlapping with the early and mid Mangawhero Formation. We observe this trend in whole rock and groundmass compositions, and we interpret variable crustal assimilation and fractional crystallization through time. This is consistent with previous studies that suggested crustal assimilation based on trace elements and isotope data, together with the occurrence of crustal xenoliths. We propose a dike-dominated plumbing system where rapid transport of melts and crystal cargo was favored by re-injection enhanced by rifting geodynamics.

Key words: Ruapehu, Mangawhero Formation, Whakapapa Formation, whole rock composition, groundmass composition, crystal composition.

6.1 Introduction

While continental arc magmatism is characterized by multilevel storage, where thick crust promotes extended residence times and differentiation (Cashman et al., 2017), magma plumbing architecture and processes in complex rift settings remain comparatively poorly understood. The association between the Taupō Volcanic Zone (TVZ) and the Taupō Rift turns Mount Ruapehu into a natural laboratory to study magmatic processes linked to complex volcanic systems in rift environments (e.g., Gómez-Vasconcelos et al., 2017; Lormand et al., 2021). With a relatively thin crust (25 km in Eberhart-Phillips et al., 2020) and low water contents (< 2.5 wt% in Auer et al., 2016; Kilgour et al., 2013), Mount Ruapehu may be ascribed to a rift system where dry magmas are predominant and magma influx is controlled by rift expansion (e.g., Connors et al., 2025) and adiabatic melting (e.g., Kemner et al., 2015). Given the impact of melt generation on subsequent magma history (Ubide et al.,

2024), the petrology of erupted products could shed new light into the link between transcrustal processes and tectonic environment in complex settings.

To explore intricate melt evolution and dynamic processes during magma storage, the combination of chemical and textural information in volcanic rocks is essential (e.g., Browne & Szramek, 2015; D'Mello et al., 2023; Johnson et al., 2008). Crystal-scale studies help elucidate degassing and cooling rates (e.g., Brugger & Hammer, 2010a; Cashman, 1993; Crabtree & Lange, 2011; Giuliani et al., 2020; Hammer et al., 1999; Johnson et al., 2008), as well as changes in P-T-H_2O conditions and composition of the magmatic system during crystal growth (e.g., D'Mello et al., 2021; Putirka, 2008; Ubide et al., 2019; Van Gerve et al., 2020; Welsch et al., 2016). The origin of the crystal cargo can be autocrystic i.e., related to carrier melts (e.g., Matsumoto & Geshi, 2021; Ubide et al., 2024; Zellmer et al., 2021); antecrystic i.e., from mush zones that feed the eruptions (e.g., Cashman et al., 2017; Hobden et al., 1999; Johnson et al., 2008; Kuritani et al., 2005) or previously emplaced intrusive bodies (e.g., Zellmer et al., 2013; Zellmer et al., 2016b; Zellmer et al., 2024); or xenolithic i.e., from foreign parts of the mantle and/crustal column sampled during magma ascent (e.g., Costa et al., 2013; D'Mello et al., 2023).

Meanwhile, the analysis of the melt phase provides not only an opportunity to assess equilibrium with crystal populations, but also key information on chemical differentiation due to source variations, assimilation and fractional crystallization, as well as P-T pre-eruptive conditions (e.g., Bennett et al., 2025; Longpré et al., 2025; Magee et al., 2021; Ubide et al., 2023; Weber & Blundy, 2024).

Here, we explore magma genesis and evolution in complex arc-rift systems through the study of ~ 50 – 8 ka lavas from Mount Ruapehu, an active andesite stratovolcano of the TVZ (New Zealand) linked to rifting within an overall subduction setting. To identify the characteristics

of the melts and the crystal cargo prior to and during eruption, we combine petrographic and high-resolution geochemical analyses in sub-glacial and ice-bounded lava samples, as rapid cooling against ice hinders crystal growth preserving pre-eruptive textures in microlites (e.g., Owen et al., 2013). To constrain the P-T-H_2O-X conditions of the storage system, we combine thermobarometry with thermodynamic simulations via MELTS modelling. The information obtained in this study provides valuable insights into the construction of a more comprehensive picture of the pre-eruptive processes occurring at Mount Ruapehu, contributing to our understanding of volcanism in complex tectonic environments.

6.2 Geological background

One of the most active volcanoes in New Zealand, Mount Ruapehu is the southernmost expression of the Taupō Volcanic Zone (TVZ), a NNE-SSW zone of intense volcanic activity product of the Tonga-Kermadec–Hikurangi subduction system (Cole & Lewis, 1981; Ewart et al., 1977; Houghton et al., 1995; Leonard et al., 2021; Milicich et al., 2020; Schellart & Spakman, 2012; Stern et al., 2006; Wilson et al., 1995; Wilson & Rowland, 2016).

Mount Ruapehu is situated within a *c*. 40 km wide NNE striking nested graben (Ruapehu graben), which forms the southern termination of the Modern Taupō Rift (*c.* 25ka - present) (Gómez-Vasconcelos et al., 2016; Villamor & Berryman, 2006b). The rifting process is an active contributor to the magmatic activity in the TVZ, as it facilitates magma ascent through faults (Bibby et al., 1995; Cassidy et al., 2009; Gómez-Vasconcelos et al., 2017; Seebeck et al., 2014; Villamor et al., 2017; Wilson & Rowland, 2016). The Ruapehu graben is formed by a newer, less evolved fault system (*c*. 400ka), with extensional rates of 2.3 ± 1.2mm/yr, which increased in the late Quaternary linked to changes in the evolution of the rift and the thickness of the crust (Villamor & Berryman, 2006a). The basement of the graben is composed by greywackes and metamorphic rocks of the Waipapa and Torlesse Composite

terrains, which have been identified as source of meta-sedimentary xenoliths in many Mount Ruapehu andesites (Adams et al., 2007; Mortimer et al., 2014; Price et al., 2012; Price et al., 2016). The Torlesse Composite Terraine comprises the Early Cretaceous Pahau Terrane and the Jurassic Kaweka Terraine (Adams et al., 2009, 2011), which is the most likely crustal assimilant end-member of the TVZ (Mortimer et al., 2023).

Although explosive activity has dominated the historical eruptions of Mount Ruapehu, with mid-to-moderate explosive eruptions from the Crater Lake (*Te Wai ā-Moe*) vent, the volcano has also had numerous effusive episodes in the past from vents located south and north, which emplaced voluminous lava flows between *c*. 250 and 15 ka (Kilgour et al., 2010; Leonard et al., 2021; Townsend et al., 2017). The voluminous lava flows form the volcanic edifice have been subdivided into four formations: Te Herenga (250 – 150 ka), Wahianoa (166 – 80 ka), Mangawhero (50 – 15 ka) and Whakapapa (<15 ka) (Conway et al., 2016; Gamble et al., 2003; Hackett & Houghton, 1989; Leonard et al., 2021). Plagioclase-pyroxene phyric calc-alkaline andesitic lavas dominate the eruptive products of these formations, however, there is minor occurrence of basalts and dacites (Graham & Hackett, 1987; Price et al., 2012). The phenocrysts range between 1 – 2 mm in length and are variable between 15 – 55 %, and are mainly plagioclase followed by orthopyroxene and clinopyroxene, with Fe-oxide as inclusions. The phenocrysts are embedded in a microcrystalline matrix of plagioclase and pyroxene with ubiquitous Fe-oxides and occasional patches (10 – 15 μm) of microlite free-glass in those flows cooled rapidly due to their emplacement next to glaciers (Conway, 2016; Conway et al., 2018; Graham & Hackett, 1987; Hackett, 1985; Price et al., 2012). There is also presence of <2 % crustal xenoliths, more common in younger flows, forming crystal aggregates from< 1 mm up to a few centimeters, some of those including olivine cores and symplectite veins and pools of Fe-oxides (Conway, 2016; Graham & Hackett, 1987; Hackett, 1985; Price et al., 2012).

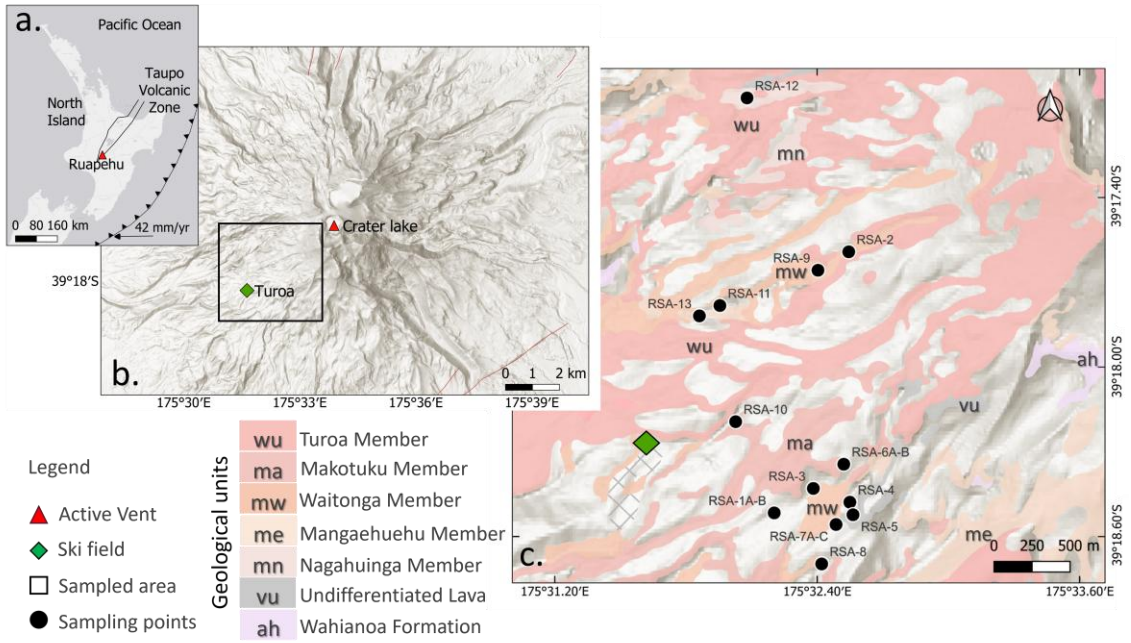

Figure 6.1. Location of Mount Ruapehu and sampling points.a. Location of Mount Ruapehu within New Zealand. b. Location of the sampling area in Mount Ruapehu (black square). c. Location of the sampling points, showing lava flows mapped in the area based on Townsend et al. (2017).

The voluminous (~28 km^3) and compositionally diverse (dacite to basaltic-andesite) lava flows of the Mangawhero Formation were erupted during the last glaciation (*c.* 50 - 15 ka) (Conway, 2016; Townsend et al., 2017). This formation is extensively exposed in the main cone of Mount Ruapehu, displaying evidence of complex ice interaction during eruption and emplacement (Conway, 2016; Hackett, 1985; Townsend et al., 2017). Notably, the lavas of the Mangawhero Formation can be grouped into three groups based on their compositional features and age (Conway, 2016; Townsend et al., 2017). The lavas emplaced *c*. 50 – 35 ka are basaltic-andesites and dacites that present two distinct bulk geochemical MgO vs SiO_2 trends; a low-Mg trend that heads towards a more primitive composition (Kakuki basalt - Gamble et al., 1993) and a high-Mg compositional group that trends towards primitive high-magnesian basalt (Waimarino basalt - Hackett, 1985). The lavas emplaced at *c*. 35 – 15 ka display intermediate compositions between andesites and dacites emplaced *c*. 50 – 35 without the distinct MgO variations of the older flows. Lastly, lavas emplaced since *c*. 26 ka define a regression to more mafic compositions (i.e., lower SiO_2 and K_2O) (Conway, 2016; Townsend

et al., 2017). The <15 ka Whakapapa Formation continues the regression towards more mafic compositions with the younger flows classified as andesites and basaltic andesites emplaced during glacial retreat (Conway, 2016; Townsend et al., 2017).

6.3 Methodology

6.3.1 Sampling

Field work was carried out on Mount Ruapehu during January and February 2023. We collected 17 samples from 13 locations of glassy lavas on the western side of the volcano close to the Turoa Ski field area, belonging to the Mangawhero and Whakapapa formations (Figure 6.1 & Table 6.1). Sample collection was carried out near structures that indicated lava/ice interaction as those described by Conway et al. (2015), since lava flows chilled against ice have rapid cooling, preserving the record of pre-eruptive phenocryst textures and compositions. Several samples were collected within the same flow at different levels (i.e., top and base) to compare potential within-flow differences.

Whole rock major element compositions were obtained through X-ray fluorescence (XRF) on glass beads obtained from melting the crushed oxidized samples mixed with X-Ray flux type 12:22 (35.3 vol% Lithium Tetraborate, 64.7 vol% Lithium Metaborate). The oxidation process of the samples determining loss on ignition (LOI) included drying the samples overnight at 110 °C and then heating the samples at 900 °C for 8 h in a muffle furnace. The samples were cooled down to 200 and 100 °C inside the closed furnace, before being taken out for weighting.

Table 6.1. Location of the lava samples used in this study.

Formation	Member	Sample	Latitude	Longitude
Mangawhero Formation (50 – 15 ka)	Mangaehuehu Member (47 – 40 ka)	RSA4	39°18'28.70"S	175°32'32.95"E
		RSA5	39°18'31.37"S	175°32'33.81"E
		RSA6A	39°18'20.64"S	175°32'31.28"E
		RSA6B	39°18'20.64"S	175°32'31.28"E
		RSA13	39°17'49.13"S	175°31'51.67"E
	Makotuku Member (24 – 16 ka)	RSA1A	39°18'30.97"S	175°32'12.19"E
		RSA1B	39°18'30.97"S	175°32'12.19"E
		RSA3	39°18'25.78"S	175°32'22.93"E
		RSA7A	39°18'33.43"S	175°32'29.16"E
		RSA7B	39°18'33.43"S	175°32'29.16"E
		RSA7C	39°18'33.43"S	175°32'29.16"E
		RSA8	39°18'41.81"S	175°32'25.22"E
		RSA10	39°18'11.60"S	175°32'1.62"E
	Waitonga Member (25 – 21 ka)	RSA2	39°17'35.52"S	175°32'32.64"E
		RSA9	39°17'39.44"S	175°32'24.20"E
Whakapapa Formation (<15 ka)	Turoa Member (17-10 ka)	RSA11	39°17'46.93"S	175°31'57.29"E
		RSA12	39°17'2.83"S	175°32'4.74"E

6.3.2 Bulk rock, matrix and mineral chemistry

For microanalytical work, small pieces of the samples were placed in 2.5 cm diameter cylinders, impregnated with a two-component epoxy resin and vacuumed. Subsequently, the resulting plugs were polished. After carbon coating, back-scattered electron microphotographs were obtained at Academia Sinica (Taiwan) using a thermal field emission scanning microscope JEOL: FE-SEM JSM-7100F with a scintillator back-scattered electron detector K.E. Developments: Deben Centaurus. For imaging, a focused beam was used at an acceleration voltage of 15 kV, a beam current of 120 nA and working distance at 13 mm.

Electron probe microanalysis (EPMA) was used to obtain major element chemical compositions of plagioclase and pyroxene crystals, and elemental distribution mapping. Mapping of plagioclase and pyroxene phenocryst (≥ 30 μm in width; s.s., Iddings, 1892) was performed at Academia Sinica using a W-filament thermal emission electron micro-probe (JEOL W-EPMA JXA-8900R) equipped with four WDS, at an acceleration voltage of 15 kV,

beam current of 50 nA, 1 μm beam size, at 2 μm intervals of X-Y directions and 15 ms dwell time. We observed no Na migration during mapping due to the short dwell time.

Quantitative EPMA point analyses in microlite (i.e., 1 - 30 μm in width; Zellmer, 2021) and phenocryst were performed at Academia Sinica (Taiwan) using a field emission electron microprobe JEOL FE-EPMA JXA-8500F at an acceleration voltage of 12 kV and beam current of 6 nA, with a 2 μm defocused beam, and at Tohoku University (Japan) using a W-filament JEOL iSP100 electron microprobe at an acceleration voltage of 15 kV and beam current of 15 nA with a focused beam, where the Na migration for the plagioclase was monitored, with no significant reduction in the Na signal observed. Additionally, transect profile lines were measured in the mapped crystals at Academia Sinica using the same conditions. The difference in the beam currents between probes lies in the internal configuration of the equipment within the laboratories for optimal quantification and does not impact inter-comparison between results. Both microprobes were equipped with five wavelength dispersive spectrometers (WDS), counting element peaks for 10 s and each background for 5 s. For X-ray intensity correction, the Oxide-ZAF method (JEOL Ltd., n.d.) was applied before the quantitative analysis, reducing the errors by increasing the counting times. Measured data were filtered based on cation ratios and total major element oxides between 96 - 100 wt %, to ensure consistent results with the stoichiometry of the mineral phases. We provide the list of standards in the Appendix 1; we obtained relative standard deviations on secondary standard measurements of <3%, with detection limits of <500 ppm for all elements.

Laser ablation inductively coupled plasma mass spectrometry (LA-ICP-MS) was used to determine the major and trace element composition of the groundmass and perform trace element crystal mapping in the same plagioclase and pyroxene phenocryst analyzed by

EPMA. The analyses were performed at the Centre for Geoanalytical Mass Spectrometry, Radiogenic Isotope Facility of The University of Queensland (UQ RIFlab, Australia). For trace element mapping, we followed the LA-ICP-MS raster technique described in Ubide et al. (2015). For high resolution matrix geochemistry, we used the LA-ICP-MS rastering method across groundmass by Ubide et al. (2023). We used an ASI RESOlution 193-nm excimer ultraviolet ArF laser with a dual-volume Laurin Technic ablation cell. Ablation took place in ultrapure He (350 ml/min) adding Ar (850-950 ml/min) as makeup gas and trace amounts of N_2 (5 ml/min) to assist ionization, get better sensitivity and effective transport. Crystal maps and groundmass rasters were programmed using GeoStar Norris software on the laser ablation system. For the maps, we used a fluence of 3 J/cm^2, repetition rate of 10 Hz, spot size of 10x10 or 16x16 μm and translation speed of 10 or 16 μm/s, respectively, with 1 μm overlap between lines. For the groundmass, we programmed ten 50x600 μm rasters per sample with a fluence of 3 J/cm^2, repetition rate of 10 Hz and translation speed of 5 μm/s. A Thermo iCap RQ quadrupole mass spectrometer, operated with Qtegra software, was used to analyze the ablated aerosol. The ICP-MS was tuned using NIST SRM 612 glass reference material.

LA-ICP-MS data reduction was performed in Iolite4 (Paton et al., 2011). For external standard calibration, we used NIS612 for maps and BCR-2G basaltic glass standard for matrix. As internal standard, we used EPMA Si content for maps and major element oxides normalization to 100 wt.% total for matrix (Chang & Audétat, 2018). Glass reference materials BHVO-2G and GSD-1G/2G were used as quality monitors returning accuracy better than 10% relative to accepted values for most elements, and relative standard deviations (2σ) <5% (Appendix 1; Tables S5 – S9). Elemental maps of plagioclase and pyroxene crystals were generated using the imaging features in the Iolite4 software, extracting compositional profiles following the same trajectories as the transect profiles

analyzed by EPMA. Further information on mapping and groundmass analytical methods and data reduction strategies can be found in Ubide et al. (2015) and in Ubide et al. (2023), respectively.

6.3.3 Melt-crystal equilibrium

Equilibrium between plagioclase and pyroxene crystals and their carrier melts was evaluated using LA-ICP-MS groundmass compositions (see Appendix 3: Table S15) and EPMA crystal compositions. We focused on microlite cores and rims, and phenocryst rims. Plagioclase-melt equilibrium was tested using the equilibrium experiments of Waters & Lange (2015) which employ the anorthite content in plagioclase and melt, and the equilibrium zone is determined by the experiment results in saturated and undersaturated conditions (e.g., D'Mello et al., 2023; Lormand et al., 2021; Zellmer et al., 2016b). Orthopyroxene-melt equilibrium was assessed using the test of Rhodes (Rhodes et al., 1979), based on the Fe-Mg exchange coefficients (i.e., K_D $[Fe\text{-}Mg]^{opx\text{-}liq} = 0.29 \pm 0.06$) as in Putirka (2008) (i.e., K_D Fe-Mg = 0.29 ± 0.06). Clinopyroxene-melt equilibrium was assessed using a combination of the traditional EnFs and DiHd equilibrium test complemented with a variation of Rhodes test (i.e., K_D $[Fe\text{-}Mg]^{cpx\text{-}liq} = 0.28 \pm 0.08$) as recommended by Wieser et al. (2023b). Additionally, following recommendations by MacDonald et al. (2023), two additional test were performed using CaTi and CaTs tests (Mollo et al., 2013; Putirka, 1999). The ranges of equilibrium were considered within 1SEE (standard error of estimate) for EnFs (± 0.05 ΔEnFs) and DiHd (± 0.1 ΔDiHd) and 2SEE for CaTi (± 0.02 ΔCaTi) and CaTs (± 0.06 ΔCaTs), following in MacDonald et al. (2023).

6.3.4 Thermodynamic modelling

We used AlphaMELTS 2.3 (Smith & Asimow, 2005) to perform thermodynamic simulations using the subroutine of rhyolite-MELTS v 1.2.0 (Gualda et al., 2012). The thermodynamic

simulations followed a fractional crystallization path, using oxygen fugacity buffered at NNO (nickel-nickel-oxide) according to previous studies performed in the Tongariro Volcanic Centre (TgVC) (Kilgour et al., 2013; Kilgour et al., 2014; Kilgour et al., 2016; Lormand et al., 2020; Shane et al., 2008), while decreasing temperature and pressure simultaneously down to 800 °C and 1 bar respectively. Our aim was to constrain the range of pressures and water contents that reproduced analyzed groundmass and mineral compositions.

Considering that the groundmass represents the erupted magmatic liquid representative groundmass analyses were used as starting compositions for the models (See Appendix 3; Table S16). Since the crystal cargo at the TgVC has been reported out of equilibrium with carrier melts (e.g., Chapter 5 in this study; Lormand et al., 2021; Zellmer et al., 2021), we also used whole rock compositions to approximate the crystallization conditions of relatively primitive plagioclase and pyroxene. Additionally, whole rock average compositions from other units within the TVZ (e.g., Ruapehu Group units from Conway, 2016; Waimarino and Kakuki basalts from Gamble et al., 1993) were used as starting compositions to model crystal compositions not achieved by groundmass and whole rock compositions from the studied units (see Appendix 3; Table S17 for average compositions used).

The initial temperatures (990 – 1123 °C), pressure (117 – 547 MPa) and water content (0.3 - 2.5 wt%) were adjusted for each individual sample based on results obtained through thermobarometry and hygrometry calculations, applying two iterations in Thermobar (Wieser et al., 2022) which are compiled in Table 6.2. The first iteration combined the Waters & Lange (2015) hygrometer and the equation 24a plagioclase thermometer from Putirka (2008) to find the H_2O content. The second iteration included equations 28a and 29a orthopyroxene-liquid thermobarometers from Putirka (2008). The water content calculated with the first (hygrometer-thermometer) iteration was used on the second (orthopyroxene)

thermobarometer. As for the initial pressure used for the plagioclase hygrothermometry, we used pressures calculated with the liquid-mineral assemblage online machine learning thermobarometer MagMaTab (Weber & Blundy, 2024), applied to matrix compositions. Average results per sample for each individual calculation (i.e., thermobarometer and hygrothermometer iterations) can be found in an online repository (Appendix 3).

Table 6.2. Hygrothermobarometry parameters used in melts calculations.

Group	Sample	T (°C)	P(MPa)	H_2O (wt%)
Mangaehuehu Member	RSA13	1065	120	1.75
	RSA6B	1104	153	0.75
	RSA6A	1105	166	1.33
	RSA5*	1039	323	2.10
	RSA4	1091	175	1.15
Makotuku Member	RSA8	1092	327	0.66
	RSA7C	1123	257	0.30
	RSA7B	1090	404	1.44
	RSA7A	1090	547	0.71
	RSA10	1070	225	1.43
	RSA3	1080	342	1.08
	RSA1B	1082	317	1.35
	RSA1A	1081	377	1.68
Waitonga Member	RSA2	993	117	1.80
	RSA9	1000	254	1.99
Turoa Member	RSA11	1032	324	1.29
	RSA12	990	147	2.30

*Temperature and pressure derived from magmatic liquid thermobarometry since the sample had no orthopyroxene in equilibrium.

Table 6.3. XRF whole rock compositions.

Unit	Sample Name	SiO_2 (wt%)	Al_2O_3 (wt%)	TiO_2 (wt%)	MnO (wt%)	$Fe_2O_3^T$ (wt%)	MgO (wt%)	CaO (wt%)	Na_2O (wt%)	K_2O (wt%)	P_2O_5 (wt%)	Mg#	LOI*
Mangaehuehu Member	RSA13	59.19	15.50	0.71	0.12	7.01	6.72	7.25	3.20	1.63	0.19	65.50	-0.18
	RSA6B	59.61	15.62	0.69	0.12	7.10	5.96	7.32	3.23	1.55	0.18	62.46	-0.21
	RSA6A	59.83	15.59	0.70	0.12	7.06	5.96	7.29	3.19	1.57	0.18	62.55	-0.28
	RSA5	59.89	15.60	0.70	0.12	7.14	5.88	7.25	3.20	1.60	0.17	62.00	-0.03
	RSA4	59.95	15.66	0.69	0.12	7.00	5.94	7.36	3.25	1.58	0.18	62.66	-0.33
Makotuku Member	RSA8	60.53	17.89	0.76	0.10	6.40	3.10	6.55	3.83	1.91	0.20	48.93	0.23
	RSA7C	60.66	17.86	0.78	0.11	6.43	3.15	6.51	3.82	1.91	0.20	49.26	-0.04
	RSA7B	60.57	17.82	0.76	0.11	6.41	3.17	6.49	3.82	1.91	0.21	49.44	0.20
	RSA7A	60.95	17.80	0.79	0.10	6.39	3.04	6.41	3.93	1.92	0.21	48.52	-0.20
	RSA10	61.27	18.04	0.79	0.10	6.12	2.68	6.29	4.05	1.91	0.20	46.40	-0.32
	RSA3	61.61	17.52	0.81	0.10	6.41	2.74	6.04	4.01	2.03	0.21	45.86	-0.37
	RSA1B	61.28	17.87	0.79	0.10	6.16	2.65	6.23	3.95	1.95	0.20	45.98	-0.49
	RSA1A	61.54	18.02	0.79	0.10	6.18	2.70	6.24	4.01	1.93	0.21	46.34	-0.43
Waitonga Member	RSA2	62.43	16.44	0.71	0.10	6.04	4.00	5.81	3.55	2.08	0.19	56.73	-0.27
	RSA9	62.88	16.53	0.69	0.10	5.65	3.71	5.62	3.57	2.26	0.19	56.52	0.01
Turoa Member	RSA11	60.47	17.26	0.80	0.11	6.63	3.79	6.33	3.54	1.97	0.22	53.12	-0.16
	RSA12	61.91	16.95	0.76	0.10	6.24	3.67	5.97	3.86	1.90	0.20	53.80	0.10

*Loss on ignition (LOI) calculation process is available in Appendix 1, Table S1.

^{T} Fe expressed as Fe_2O_3.

$Mg\#=100*Mg/(Mg+Fe^{+2})$.

6.4 Results

6.4.1 XRF whole rock compositions

All lava samples classify as andesite for whole rock compositions based on the TAS classification of Le Maitre et al. (2005) (Figure 6.2a), belonging to the calc-alkaline series (K_2O 1.53 – 2.23wt% - Table 6.3). Four analyzed geological units (Mangaehuehu Member: 47 – 40 ka, RSA4-6B & 13; Makotuku Member: 24 – 16 ka, RSA1A, 1B, 3, 7A-8 & 10; Waitonga Member: 25 – 21 ka, RSA2 & 9, and Turoa Member: 17 – 10 ka, RSA11 & 12) have slight differences in their compositions. The Mangaehuehu Member presents the lowest values of SiO_2, Na_2O, K_2O, Al_2O_3 and P_2O_5 compared with the other units, and the highest values for $Fe_2O_3^T$, MgO, CaO and MnO (Table 6.3 & Figure 6.3).

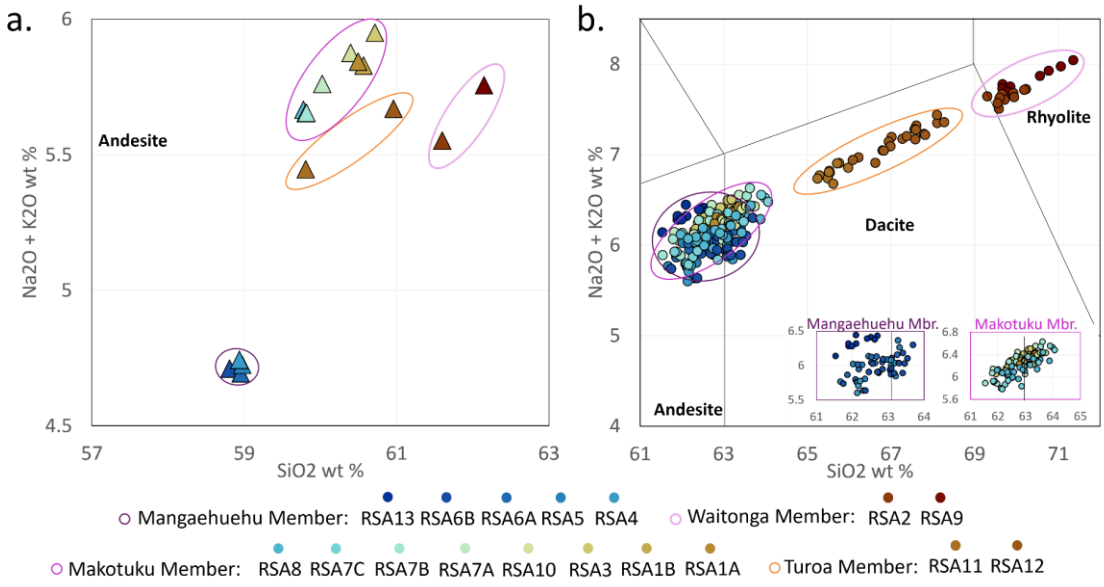

Figure 6.2. Silica (SiO_2) vs Alkalis (Na_2O+K_2O) diagram (TAS) for lava samples of Mount Ruapehu. a. XRF whole rock composition (triangles). b. LA-ICMS groundmass composition (circles). The bottom inserts show detail of Mangaehuehu and Makotuku members for groundmass compositions. Note how the groundmass compositions of Mangaehuehu Member and Makotuku Member overlap with each other while the whole rock compositions are separated. The colour scale indicates samples and members.

The Makotuku and Turoa members are compositionally closer to each other, overlapping for K_2O, CaO and $Fe_2O_3^T$, (Figure 6.3). While the Waitonga Member presents the highest SiO_2

and lowest CaO contents (Figure 6.3f). The samples of the Turoa Member show variations in Na_2O content, with sample RSA12 showing values closer to those of the Makotuku Member and sample RSA11 being similar to the Waitonga Member (Figure 6.3c).

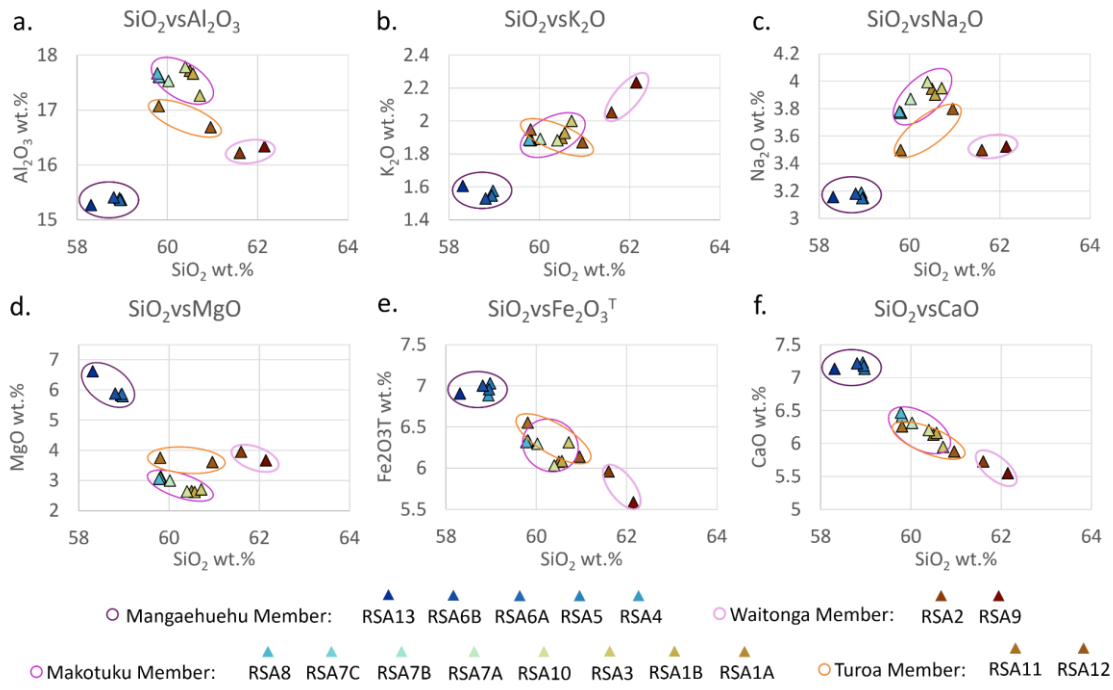

Figure 6.3. Harker diagrams for XRF whole rock composition in lava samples of Mount Ruapehu. a. SiO_2 vs Al_2O_3. b. SiO_2 vs K_2O. c. SiO_2 vs Na_2O. d. SiO_2 vs MgO. e. SiO_2 vs $Fe_2O_3^T$. f. SiO_2 vs CaO. The colour scale indicates samples and members.

6.4.2 LA-ICP-MS groundmass compositions

Volcanic matrix (groundmass) in our samples varies from andesite to rhyolite based on the TAS classification of Le Maitre et al. (2005) (Figure 6.2b). The classification of groundmass data differs from whole rock results, as expected from crystal accumulation in bulk rocks (Bennett et al., 2025; Magee et al., 2021; Ubide et al., 2022; Ubide et al., 2023). The Mangaehuehu and Makotuku members groundmass data overlap, showing lower values of SiO_2 and K_2O (Figure 6.2b) and higher values for MnO, FeO^T, MgO and CaO (Figure 6.4 & Table 6.4) compared with the Turoa and Waitonga members. The contents of Al_2O_3, Na_2O, TiO_2 and P_2O_5 are within the same ranges for all the samples (Table 6.4 & Figure 6.4).

Notably, as observed in whole rock compositions sample RSA12 has a higher Na_2O content than sample RSA 11 (Figure 6.4c).

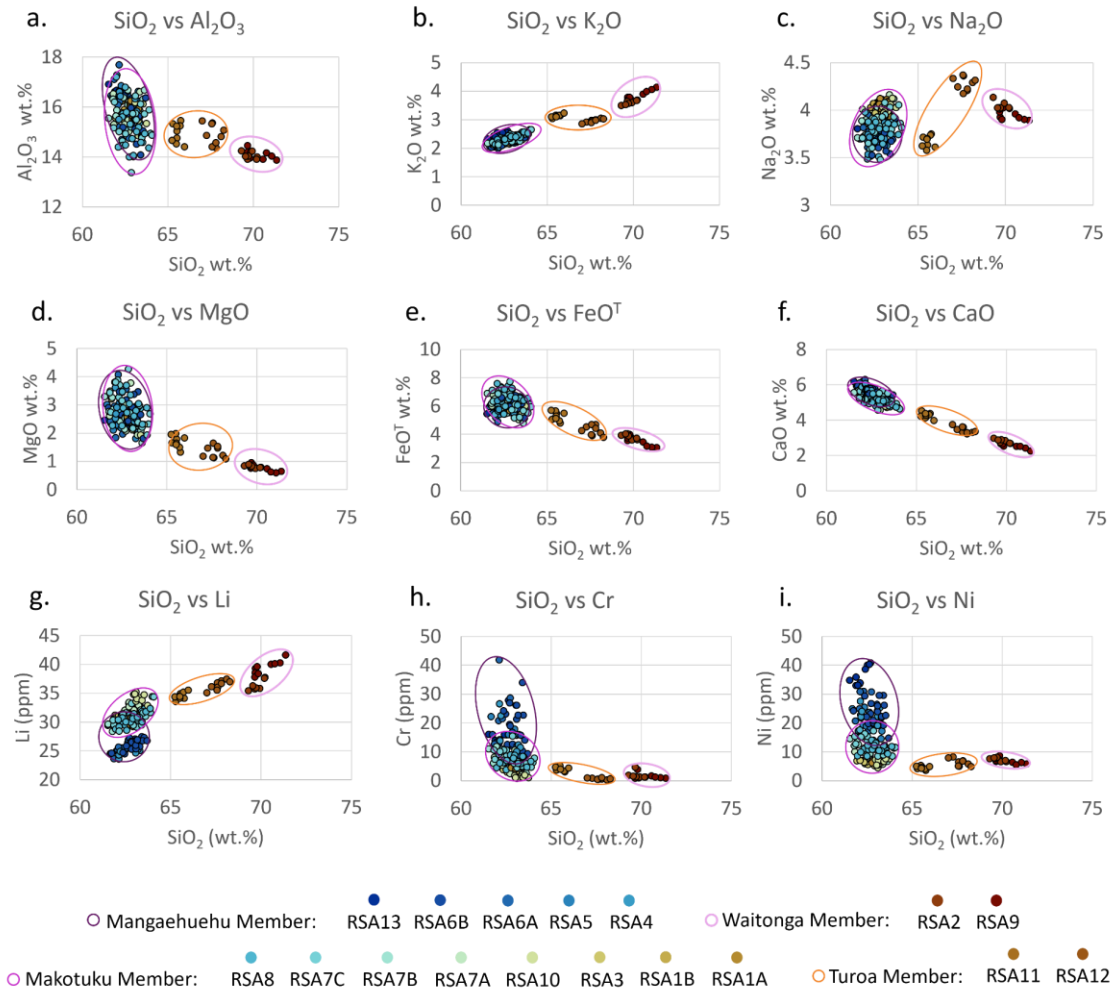

Figure 6.4. Harker diagrams for LA-ICMS groundmass major and trace elements composition in lava samples of Mount Ruapehu.a. SiO_2 vs Al_2O_3. b. SiO_2 vs K_2O. c. SiO_2 vs Na_2O. d. SiO_2 vs MgO. e. SiO_2 vs FeO^T. f. SiO_2 vs CaO. g. SiO_2 vs Li. h. SiO_2 vs Cr. i. SiO_2 vs Ni. The color scale indicates samples and members.

The trace element compositions for the Waitonga Member show lower values of compatible Sc, Cr, Ni and Sr, and higher values of incompatible Li, Zr, Ba and Th compared to the other units analyzed (Figure 6.4 & Table 6.5). The Turoa Member samples show similar behavior for Ni, Cr and Zr to those of the Waitonga Member, but lower concentrations of Li, Ba and Th, and higher contents in Sr and Sc. The Mangaehuehu Member defines two Li versus SiO_2 trends (Figure 6.4g). Sample RSA13 follows the same high Li trend as samples of the

Makotuku Member, while all other Mangaehuehu samples follow the low Li trend. the Mangaehuehu Member also shows a noticeable variation in the content of Sc, Cr and Ni compared to the Makotuku Member, with the highest values in Cr and Ni in groundmass (Table 6.5 & Figure 6.4h – i). Trace elements normalized to primitive mantle by McDonough & Sun (1995) show enrichment in Cs, Rb and Pb, and depletion in Nb and Ti for all the samples (Figure 6.5a). However, the samples from the Mangaehuehu and Makotuku members show a less marked Ti depletion and higher Sr content (Figure 6.5a).

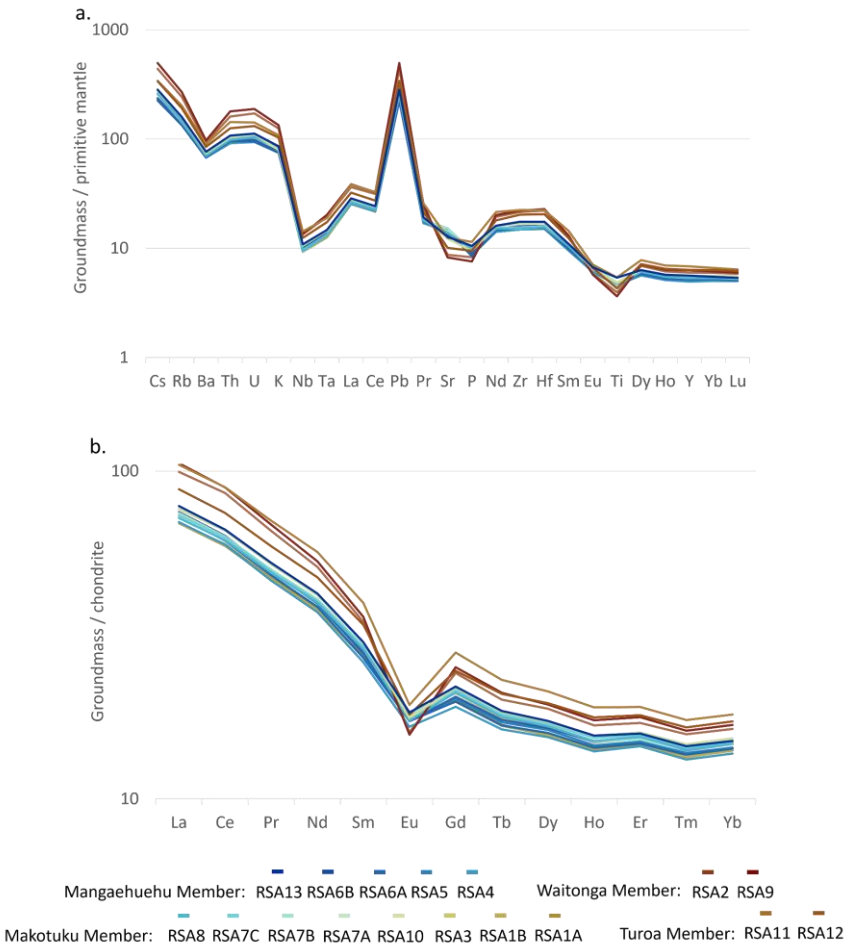

Figure 6.5. Spider diagrams for LA-ICMS groundmass composition in lava samples of Mount Ruapehu. Multi-element plot normalized to primitive mantle and b. REE normalized to chondrite, using values from McDonough & Sun (1995).

Table 6.4. LA-ICPMS major elements groundmass average compositions.

Unit	Sample	SiO_2 (wt%)	Al_2O_3 (wt%)	TiO_2 (wt%)	MnO (wt%)	FeO^T (wt%)	MgO (wt%)	CaO (wt%)	Na_2O (wt%)	K_2O (wt%)	P_2O_5 (wt%)
Mangaehuehu Member	RSA13	62.18	16.16	1.08	0.09	5.67	2.52	5.74	3.86	2.49	0.22
	RSA6B	62.97	15.61	0.98	0.10	6.02	2.72	5.43	3.72	2.26	0.19
	RSA6A	62.39	16.09	0.95	0.10	5.95	2.78	5.63	3.76	2.18	0.17
	RSA5	62.55	16.42	0.96	0.09	5.62	2.40	5.72	3.82	2.24	0.18
	RSA4	62.76	15.92	0.92	0.10	5.94	2.71	5.61	3.71	2.16	0.18
Makotuku Member	RSA8	62.88	15.22	0.95	0.12	6.45	2.87	5.15	3.78	2.38	0.20
	RSA7C	62.91	15.22	0.95	0.12	6.40	2.94	5.10	3.80	2.36	0.20
	RSA7B	62.56	16.15	0.92	0.10	5.87	2.53	5.43	3.92	2.33	0.20
	RSA7A	62.61	15.57	0.98	0.11	6.33	2.80	5.17	3.90	2.33	0.20
	RSA10	63.06	15.85	0.97	0.10	5.99	2.40	5.13	4.01	2.30	0.20
	RSA3	62.71	15.66	0.97	0.11	6.28	2.64	5.12	3.96	2.35	0.20
	RSA1B	62.72	16.02	0.97	0.10	6.03	2.46	5.20	4.07	2.24	0.19
	RSA1A	63.05	15.74	0.94	0.10	6.04	2.54	5.08	4.05	2.25	0.19
Waitonga Member	RSA2	69.79	14.06	0.79	0.06	3.83	0.82	2.82	4.05	3.61	0.17
	RSA9	70.27	14.09	0.73	0.06	3.53	0.76	2.58	3.95	3.88	0.16
Turoa Member	RSA11	65.56	14.97	1.09	0.09	5.28	1.70	4.26	3.67	3.14	0.24
	RSA12	67.67	14.92	0.86	0.08	4.26	1.32	3.44	4.28	2.97	0.20

[T] Fe expressed as FeO. Full data can be consulted in an online FAIR repository (see Appendix 3).

Table 6.5. LA-ICPMS trace elements groundmass average compositions.

Unit	Sample	Li (ppm)	Sc (ppm)	Cr (ppm)	Ni (ppm)	Rb (ppm)	Sr (ppm)	Y (ppm)	Zr (ppm)	Nb (ppm)	Cs (ppm)	Ba (ppm)	Hf (ppm)	Ta (ppm)	Pb (ppm)	Th (ppm)	U (ppm)
Mangaehuehu Member	RSA13	30.43	21.95	16.16	36.42	95.26	252.84	24.13	183.15	7.12	6.01	504.17	4.95	0.54	15.23	8.53	2.28
	RSA6B	26.25	22.47	18.90	23.29	83.87	268.90	22.82	167.01	7.05	4.98	463.61	4.55	0.52	13.90	7.83	1.99
	RSA6A	25.51	22.30	17.27	23.11	80.35	284.55	22.04	161.18	6.78	4.79	452.69	4.38	0.50	13.59	7.59	1.93
	RSA5	25.77	21.44	14.04	20.07	83.16	289.08	22.48	166.15	6.99	4.96	464.02	4.51	0.51	14.06	7.80	1.99
	RSA4	24.82	21.53	15.30	23.01	80.25	283.46	21.27	155.83	6.64	4.77	444.15	4.26	0.49	13.42	7.30	1.90
Makotuku Member	RSA8	30.59	23.55	6.59	11.21	87.81	276.23	23.02	160.10	6.19	5.52	463.09	4.42	0.48	14.50	7.82	2.11
	RSA7C	30.99	23.69	8.26	12.77	88.07	275.38	23.28	161.18	6.27	5.51	470.33	4.44	0.49	14.68	7.90	2.12
	RSA7B	30.35	22.65	6.40	10.94	86.02	303.37	22.89	159.82	6.15	5.42	473.99	4.44	0.48	14.66	7.87	2.10
	RSA7A	31.99	23.57	5.56	9.61	87.54	283.83	23.48	162.82	6.29	5.50	483.33	4.49	0.49	14.94	8.05	2.15
	RSA10	32.54	20.52	2.86	6.54	95.04	242.96	23.89	176.55	6.95	5.84	486.34	4.81	0.53	15.55	8.24	2.25
	RSA3	32.01	23.14	3.86	6.04	87.67	290.56	22.93	159.04	6.21	5.50	474.18	4.36	0.48	14.53	7.81	2.11
	RSA1B	30.67	22.23	5.04	6.71	81.71	287.16	21.79	155.96	6.07	4.96	445.69	4.24	0.46	14.19	7.24	1.95
	RSA1A	30.20	21.56	4.94	6.55	83.59	276.34	21.80	155.95	6.14	5.03	447.78	4.26	0.47	14.54	7.27	1.98
Waitonga Member	RSA2	36.37	16.89	1.89	7.36	145.48	173.24	25.69	225.34	8.86	9.32	613.02	6.26	0.71	21.47	12.76	3.47
	RSA9	39.53	17.22	1.44	6.89	161.00	163.43	27.09	231.76	8.83	10.51	638.83	6.46	0.75	22.52	14.24	3.83
Turoa Member	RSA11	34.53	21.92	4.03	4.53	121.15	248.18	29.30	235.13	9.36	7.24	589.33	6.31	0.70	18.92	11.38	2.87
	RSA12	36.43	19.02	0.62	6.35	114.41	200.31	27.16	213.14	8.18	7.15	557.47	5.79	0.64	17.77	9.98	2.67

Full data can be consulted in an online FAIR repository (see Appendix 3).

Table 6.6. LA-ICPMS REE groundmass average compositions.

Unit	Sample	La	Ce	Pr	Nd	Sm	Eu	Gd	Tb	Dy	Ho	Er	Tm	Yb	Lu
Mangaehuehu Member	RSA13	18.53	40.61	4.86	20.08	4.45	1.03	4.38	0.67	4.25	0.85	2.53	0.36	2.42	0.36
	RSA6B	17.76	38.85	4.59	18.84	4.13	0.97	4.08	0.63	4.05	0.81	2.44	0.35	2.36	0.36
	RSA6A	17.23	37.55	4.46	18.29	3.98	0.97	3.94	0.60	3.91	0.78	2.36	0.34	2.29	0.34
	RSA5	17.64	38.53	4.58	18.72	4.10	0.98	4.03	0.62	3.99	0.80	2.39	0.34	2.31	0.35
	RSA4	16.57	36.52	4.30	17.62	3.86	0.93	3.80	0.59	3.79	0.76	2.31	0.33	2.21	0.34
Makotuku Member	RSA8	17.03	37.70	4.54	18.88	4.24	0.98	4.20	0.64	4.10	0.82	2.47	0.35	2.37	0.36
	RSA7C	17.41	38.47	4.61	19.16	4.32	1.00	4.27	0.65	4.16	0.84	2.50	0.35	2.40	0.36
	RSA7B	17.27	37.85	4.56	18.88	4.24	1.02	4.20	0.64	4.10	0.82	2.43	0.35	2.36	0.35
	RSA7A	17.63	38.66	4.65	19.31	4.32	1.03	4.27	0.65	4.18	0.84	2.52	0.36	2.42	0.37
	RSA10	18.16	40.27	4.81	19.88	4.44	0.99	4.35	0.66	4.22	0.85	2.55	0.36	2.46	0.37
	RSA3	17.26	38.02	4.56	18.86	4.22	1.02	4.18	0.64	4.08	0.81	2.44	0.35	2.37	0.35
	RSA1B	16.41	36.21	4.34	17.90	3.99	0.99	3.94	0.60	3.84	0.77	2.32	0.33	2.26	0.34
	RSA1A	16.45	36.67	4.37	18.08	4.02	0.99	3.96	0.61	3.86	0.78	2.34	0.33	2.26	0.34
Waitonga Member	RSA2	23.54	52.56	6.09	24.21	5.13	0.90	4.82	0.73	4.63	0.91	2.73	0.39	2.63	0.39
	RSA9	25.02	54.58	6.36	25.17	5.31	0.88	5.01	0.76	4.77	0.95	2.84	0.40	2.71	0.40
Turoa Member	RSA11	24.75	54.69	6.55	26.87	5.86	1.09	5.56	0.83	5.23	1.04	3.05	0.43	2.91	0.43
	RSA12	20.87	45.63	5.47	22.50	5.03	1.02	4.89	0.75	4.82	0.97	2.88	0.41	2.77	0.42

Full data can be consulted in an online FAIR repository (see Appendix 3).

Rare earth element (REE) concentrations normalized to CI chondrite values by McDonough & Sun (1995) (Figure 5b) define similar patterns for all the samples. Groundmass data show elevated contents of light rare earth elements (LREE) compared with the heavy rare earth element (HREE) with LaN/LuN values of 4.92 – 6.44. The samples define negative Eu anomalies (<1 Eu/Eu* = EuN / [0.5 SmN + 0.5 GdN], where N denotes normalization to CI chondrite) of Eu/Eu* = 0.51 - 0.75, reflecting plagioclase fractionation. In this context of general REE homogeneity the Turoa Member samples show the highest contents for the REE analyzed (Sample RSA11 in Figure 6.5b & Table 6.6) and the Waitonga samples are the most depleted in Eu while also being enriched in LREE (Figure 6.5b & Table 6.6).

6.4.3 Mineralogy and crystal size

All lava samples contain plagioclase, pyroxene (ortho- and clinopyroxene) and Fe-oxides (i.e., magnetite) (Figures 6.6 - 6.8), which are representative of the dominant mineralogy of lavas at Mount Ruapehu (Conway, 2016; Graham & Hackett, 1987). Plagioclase crystals have tabular, euhedral to subhedral shapes, pyroxene crystals are acicular to tabular, euhedral to subhedral, and oxides are equant, euhedral to subhedral (Figure 6.6). Crystal size is dominantly small, mostly under 30 µm in width. According to the size classification in Zellmer (2021), all of these are classified as microlites (> 1 µm in width) (e.g., Figures 6.6 & 6.7a - f). More rarely, larger crystals (> 100 µm in length) were also identified and show sizes up to 2 mm (Figures 6.7g – i, 6.8 & 6.9). Hereby, we will be refer to crystals >30 µm in width as phenocrysts (s.s., Iddings, 1892). Lastly, we also recognized nanolites (~30 nm – 1 µm in width) (Figures 6.6 & 6.7a). The phenocrysts and microlites are predominantly plagioclase and orthopyroxene, while the nanolites are mainly Fe-oxides (Figures 6.6 - 6.8).

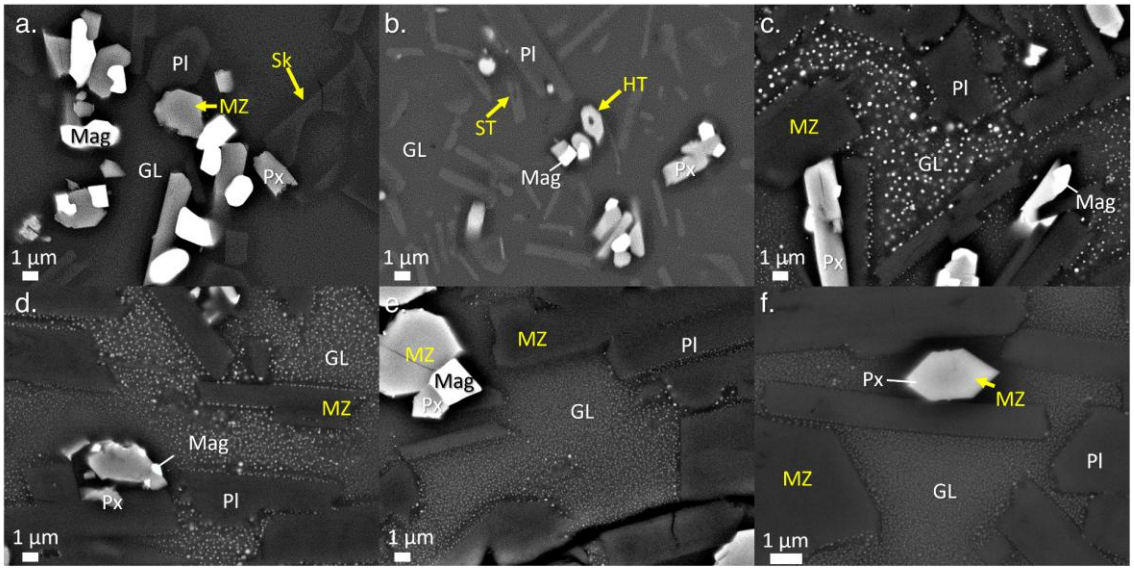

Figure 6.6. BS-SEM images of nanolites and microlites in Mount Ruapehu lava samples.a. RSA11. b. RSA2. c. RSA4. d. RSA13. e. RSA6B. f. RSA6A. The glass in samples RSA4, 6A, 6B & 13 is populated with magnetite nanolites, while the glass in samples RSA2 & 11 seems clear. Note the differences in the nanolites sizes between samples RSA6A & 6B sampled at the same point at top and mid zones of the flow respectively. Most of the microlites display monotonous zoning (MZ) and some skeletal textures such as overgrowth (Sk), swallowed tail (ST) and hollow texture (Ho). Pl: plagioclase. Px: pyroxene. Mag: magnetite. GL: glass.

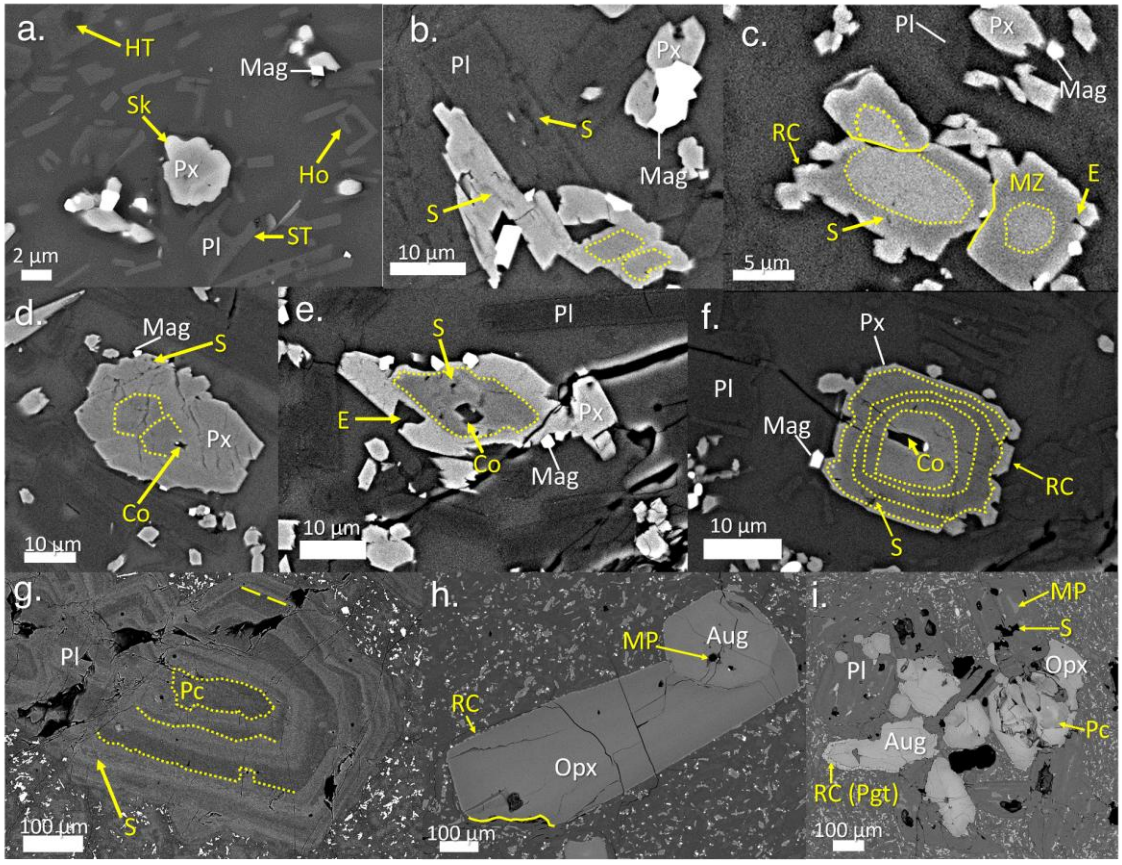

Figure 6.7. BS-SEM images of main features found in crystals.a. Microlites of pyroxene and plagioclase with magnetite nanolites. The plagioclases display various skeletal textures such as hollow (HT), hopper (Ho) and swallowed tail (ST) textures. The pyroxene shows skeletal overgrowth (Sk). b. Pyroxene, plagioclase and

magnetite micro-glomerocryst (i.e., <100 µm in length). The pyroxene and plagioclase show resorption surfaces (Dotted lines) and sieving (S). c. Pyroxene crystals with ovoidal cores. The pyroxene crystals show monotonous zoning (MZ), resorption surfaces, sieving, embayment (E) and overgrowth of smaller crystals (reaction coronas - RC). Note how the core of the crystal on top seems to stop abruptly indicating the crystal was broken (Solid line). d. Pyroxene micro-glomerocryst with ovoidal cores. The crystal also shows a resorbed core (Co) and sieving. e. Pyroxene microphenocryst showing resorption surfaces, resorbed core, sieving and embayment. f. Pyroxene microphenocryst showing wavy resorption surfaces, resorbed core, sieving and crystal overgrowth in the rims. g. Plagioclase phenocryst with patchy core (Pc), sieving, oscillatory zoning (Long dashed line) and wavy resorbed surfaces. h. Pyroxene glomerocryst of augite and orthopyroxene. Note the reaction corona of small crystals and the melt pocket (MP) in the augite crystal. The bottom left corner of the orthopyroxene shows a fracture. i. Plagioclase and pyroxene (orthopyroxene, augite and pigeonite) glomerocryst. The plagioclase shows coarse sieving and melt pockets. The orthopyroxene show patchy cores. The pigeonite is only present as a reaction corona around the augite. Pl: plagioclase. Px: pyroxene. Aug: augite. Pgt: pigeonite. Opx: orthopyroxene. Mag: magnetite. GL: glass.

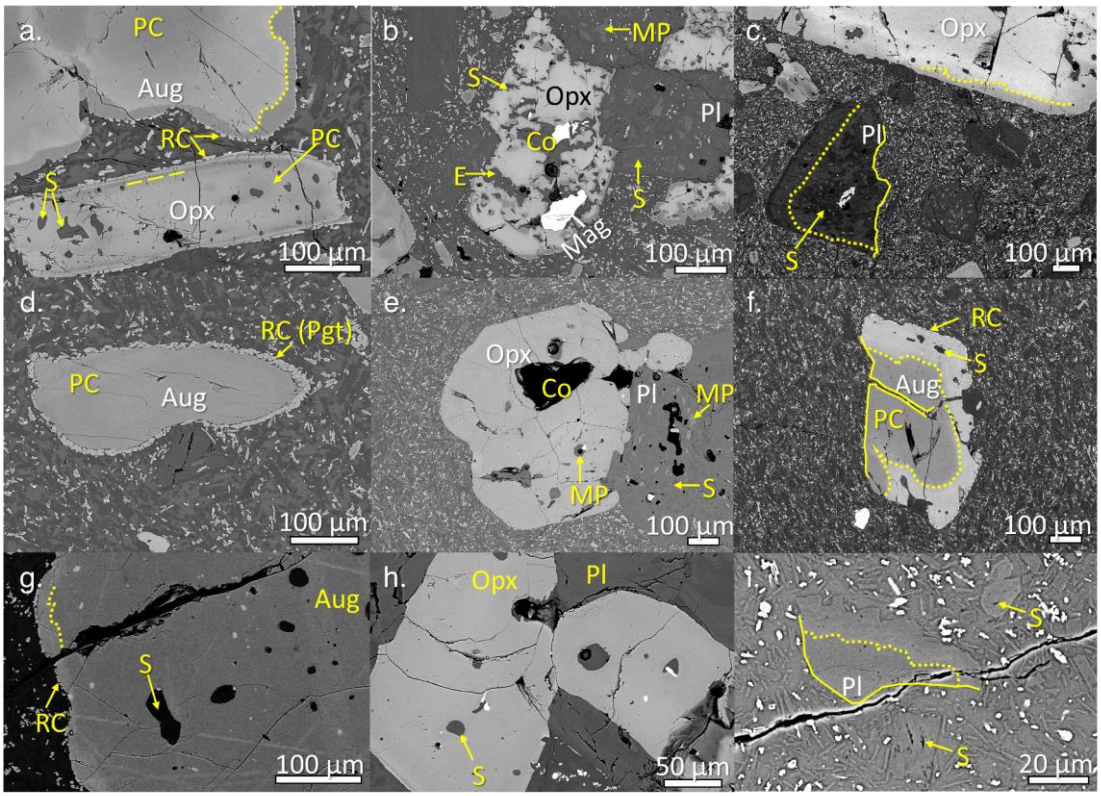

Figure 6.8. BS-SEM images of phenocrysts in Mount Ruapehu lava samples.a. RSA6B. b. RSA4. c. RSA13. d. RSA10. e. RSA1A. f. RSA1B. g. RSA11. h. RSA12. i. RSA2. The glomerocrysts (Panels b, e & h) are mainly formed by orthopyroxene and plagioclase. In panel d the reaction corona (RC) is formed by pigeonites growing around augite. These coronas are more frequent around augites, however, are also present in orthopyroxenes. Orthopyroxenes and plagioclases seem more affected that augite by resorption processes such as sieving (S) that led to the formation of resorbed cores (Co), embayment (E) and melt pockets (MP). Other features observed in phenocryst include resorption surfaces (Dotted lines), oscillatory zoning (Long dashed line), patchy cores (PC) and fractures (Solid lines) evidenced by the abrupt change in the zonation of the crystals. Pl: plagioclase. Opx: orthopyroxene. Aug: Augite. Pgt: pigeonite. Mag: magnetite.

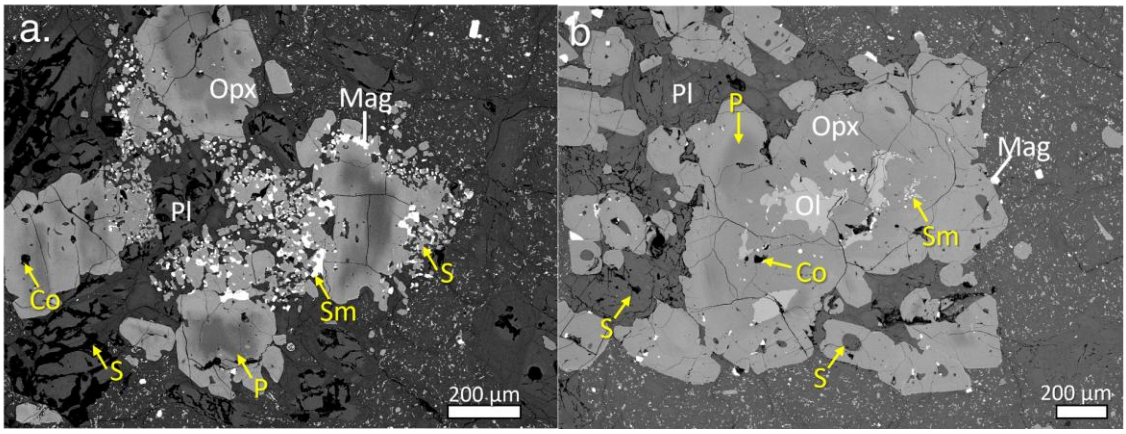

Figure 6.9. BSE images of xenocrysts in sample RSA12.a. Plagioclase (Pl) and orthopyroxene (Opx) glomerocryst with symplectitic (Sm) veins and pools of Fe-oxides (Mag). b. Plagioclase and orthopyroxene glomerocryst. The orthopyroxene has an olivine (Ol) core and symplectitic (Sm) veins of Fe-oxides (Mag). Note the patchy (P) and resorbed cores (Co) of the orthopyroxenes, and the coarse sieving (S) of the plagioclases and orthopyroxenes.

The size of the Fe-oxide nanolite crystals, as well as the number varies among samples (Figure 6.6). Some samples show nanolite-free glasses (Figure 6.6a – b), while others have nanolite-populated glasses (Figure 6.6c – f). The influence of the sample location within the flow can be observed by comparing samples collected at the same sampling points. In Figure 6.6e – f, differences within the same flow can be observed for samples RSA6A & 6B, which were collected at the top and mid regions of the flow. The same features were observed in samples RSA1A & 1B, and RSA7A, B & C, in which the nanolite sizes vary within the flow, with smaller nanolites in the samples that were the outermost part of the flow (e.g., Figure 6.6f).

6.4.4 Crystal compositions

Plagioclase crystals classify as andesine to bytownite (Figure 6.10a – b), with most of the microlites classified as labradorite (Figure 6.10a). Among the microlites, there are observable gaps in anorthite content (An = Ca [Ca+Na]) of the microlite cores at An_{70} & An_{47} (Figure 6.10a); these gaps are present in some of the samples and have been correlated with crystals that show disequilibrium textures such as coarse sieving (Figure 6.7b). The phenocryst cores

and mantles classify mostly between labradorite and bytownite, while the rims plot between the andesine and bytownite fields (Figure 6.10b). Notably, compositional gaps observed for microlites cores are also visible in the phenocrysts rims at An_{70} & An_{50} (Figure 6.10b).

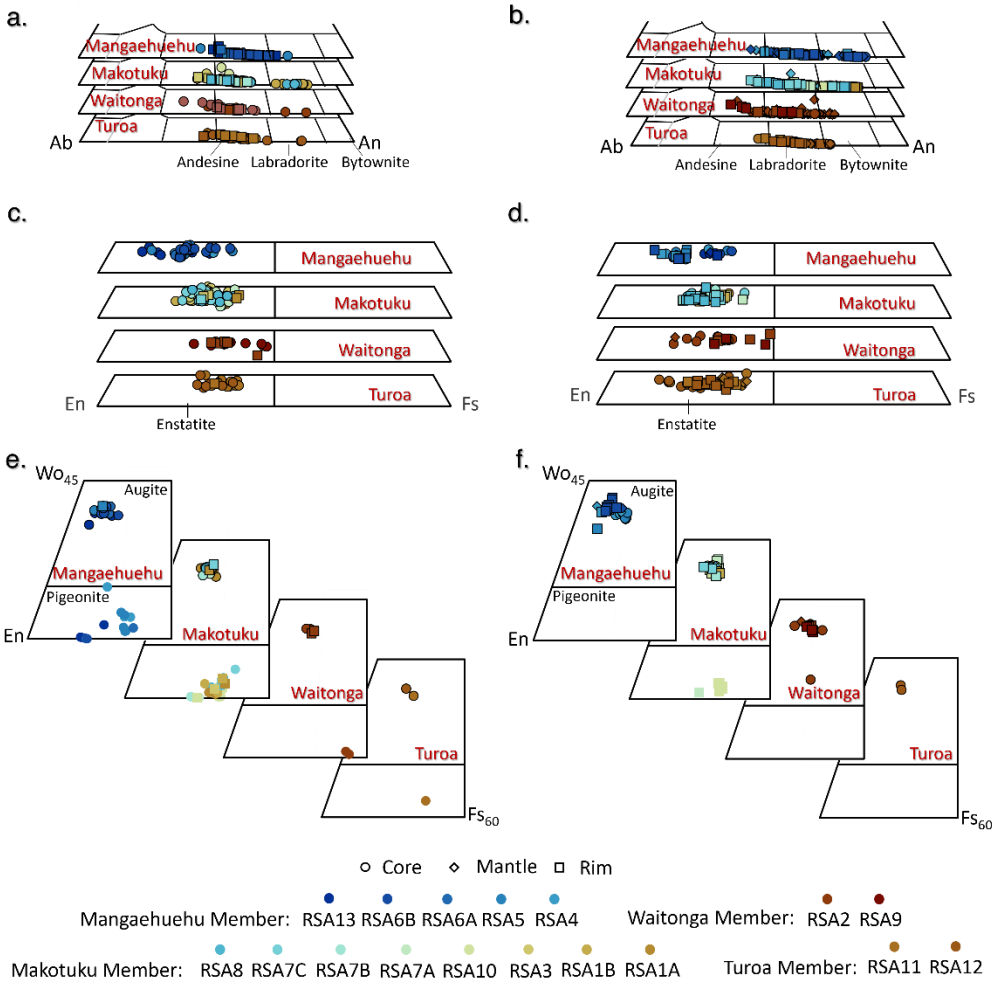

Figure 6.10. Plagioclase and pyroxene compositions based on EPMA data.a. Plagioclase microlite classification. Note there are gaps around An_{70} (bytownite) mainly in cores, and around An_{45} (Andesine) in rims which are identified as recycled microlites. b. Plagioclase phenocryst classification. Note how the rims and cores show the same gap behavior observed in the microlites. c. Orthopyroxene microlite classification. Note the gaps around En#60, En#70 and En#80. d. Orthopyroxene phenocryst classification. Note how the rims and cores show a similar gap behavior to the one observed in the microlites. e. Clinopyroxene microlite classification. f. Clinopyroxene phenocryst classification. Note the only pigeonite compositions correspond to rims in Makotuku Member. Points without a border in inserts in panels e & f are pigeonites. Circle: core measurements. Diamond: mantle measurements. Square: rim measurements. The color scale indicates the sample number.

Following the classification by Morimoto (1989), pyroxene compositions classify as enstatite orthopyroxene (Figure 6.10c – d), augite and pigeonite clinopyroxene (Figure 6.10e – f) . Most of the samples have a higher volume fraction of orthopyroxene relative to

clinopyroxene, and more augite than pigeonite (Table 6.7). Furthermore, as observed in plagioclase, the orthopyroxene crystals also define compositional gaps between distinct zones in individual crystals. In the microlites, there are gaps around enstatite (En = $Mg/[Ca+Mg+Fe^{T}]$) contents of En_{60}, En_{65}, En_{70} & En_{80} (Figure 6.10c), while in the phenocryst the gaps are around En_{55}, En_{60} & En_{70} (Figure 6.10d). These gaps are also related to the presence of complex textures such as resorbed cores and sieving (Figure 6.7b – f).

Pigeonite is present in cores and rims of microlites (Figure 6.10e), showing large compositional scatter between crystals, especially in the Mangaehuehu Member samples. Notably, pigeonite in phenocrysts is only present in rims of the Makotuku Member samples (Figure 6.10f). These phenocryst rims are associated with reaction coronas (Figures 6.7i & 6.8d). Augite is present in most of the samples, except RSA3. Augite compositions generate compositional clusters, showing consistent compositions for cores and rims within the samples, except for a few outliers (Figure 6.10e – f). The Mangaehuehu Member shows slightly higher average En contents (i.e., Mangaehuehu Member: AUG En_{46}, OPX En_{73}; Makotuku Member: AUG En_{43}, OPX En_{67}; Waitonga Member: AUG En_{42}, OPX En_{62} & Turoa Member: AUG En_{42}, OPX En_{66} -Figure 6.10e – f), and Mg number (Mg# = $Mg/[Mg+Fe^{+2}]$) (i.e., Mangaehuehu Member: AUG $Mg\#_{67}$, OPX $Mg\#_{64}$; Makotuku Member: AUG $Mg\#_{61}$, OPX $Mg\#_{57}$; Waitonga Member: AUG $Mg\#_{59}$, OPX $Mg\#_{51}$ & Turoa Member: AUG $Mg\#_{58}$, OPX $Mg\#_{55}$ - Table 6.7), for orthopyroxene and augite compared to the other members.

Lastly, the Fe-oxides include mostly Ti-magnetite (TiO_2 = ~10 – 18 wt%). Some samples contain magnetite with TiO_2 <5 wt% (i.e., RSA6A) and ilmenite with TiO_2 >40 wt% (i.e., RSA2) (see Appendix 3).

6.4.5 Crystal textures

Microlites of plagioclase and pyroxenes are divided into two populations based on the characteristics observed. The first population shows monotonous zoning (Figures 6.6a & 6.6c – f) and skeletal textures suggestive of rapid growth such as hollow (Figures 6.6b & 6.7a), swallowed tail (Figures 6.6b & 6.7a) and hopper (Figure 6.7a), as well as overgrowth (Figures 6.6a & 6.7a). The second population of microlites shows more complex textures, related to resorption processes, such as sieving in plagioclase (Figure 6.7b) and pyroxene (Figure 6.7b – f). Pyroxene microlites also show resorption surfaces (Figure 6.7b – f) that occasionally lead to ovoidal cores with monotonous (Figure 6.7c – d) and oscillatory zoning (Figure 6.7e), and resorbed cores (Figure 6.7d – f). Notably, some microlites form micro-glomerocrysts (i.e., glomerocrysts < 100 μm in length).

The phenocrysts generally show more complex structures. Plagioclases show wavy resorption surfaces and patchy cores associated with oscillatory zoning from core to rim (Figure 6.7g), while in pyroxenes the resorption surfaces and zoning are absent (Figure 6.7h – i) or located towards the rims (Figure 6.8a, c & g). Other features found in phenocrysts include: melt pockets (Figures 6.7h – i, 6.8b & 6.8e) associated to sieve textures mainly in plagioclase, patchy cores (Figures 6.7g, 6.7i, 6.8a, 6.8d & 6.8f) and sieving (Figures 6.7g, 6.7i, 6.8a – c & 6.8e – i), which is usually coarse leading to embayment (Figure 6.8b) and resorbed cores (Figures 6.8b & 6.8e). In some pyroxene phenocrysts and microlites, there are reaction coronas formed by smaller pyroxene crystals (Figures 6.7c, 6.7f, 6.7 h – i, 6.8a, 6.8d & 6.8f – g). Some of these overgrowths have been analyzed and identified as pigeonite, surrounding augite (Figures 6.7i & 6.8d). Notably, these reaction coronas have been observed in most of the samples (Figure 6.7c, 6.7f, 6.8a & 6.8f - g), not only in augite but also in some enstatite crystals (Figures 6.7h & 6.8a), although not in the abundance observed in the Makotuku

Member samples (Figure 6.10b). Some of these reaction coronas are formed by very small crystals, that cannot be resolved with EPMA spot analyses or La-ICP-MS crystal mapping.

Phenocrysts frequently form glomerocrystic associations, which can include plagioclase only (Figure 6.7g), pyroxene only (Figure 6.7h), and more frequently plagioclase and pyroxene together (Figures 6.7i, 6.8b, 6.8e, 6.8h, & 6.9). Another feature observed in glomerocrysts is the occurrence of poikilitic textures where most commonly orthopyroxene chadacrysts are enclosed by plagioclase or clinopyroxene oikocrysts (Figures 6.7i & 6.8e). However, orthopyroxene oikocrysts can also occur around clinopyroxene chadacrysts (Figure 6.7h). Glomerocrysts showing granoblastic texture (Figure 6.9a) are associated to meta-igneous granulite xenoliths interpreted as restites product of the partial melting of the Torlesse Terraine greywackes (Graham & Hackett, 1987; Graham et al., 1990). Olivine cores are rare but can be observed in some orthopyroxene associated with plagioclase in glomerocrysts (Figure 6.9b). These olivine cores have been observed mainly in lavas of the Whakapapa Formation and are interpreted as textures related to mafic nodules/xenocrysts crystallized at the base or below the crust that have been dragged by ascending melts suffering re-equilibration and crystallization of orthopyroxene (e.g., Conway, 2016; Conway et al., 2020; Graham & Hackett, 1987; Graham et al., 1990). The orthopyroxene phenocrysts show inclusions of Fe-oxides, sometimes forming symplectitic veins and pools (Figure 6.8b & 6.9), more frequent in xenocrysts. Additionally, Fe-oxides are frequently associated to pyroxene microlite (Figure 6.6 & 6.7a – f) and occasionally to phenocryst (Figure 6.8b). Lastly, broken crystals were observed in all samples, mostly in phenocrysts. These crystals are identified by discontinuities in the internal textures such as ovoidal cores (Figure 6.7c), overgrowth rims (Figure 6.7h), sieved cores (Figure 6.8c), and resorption surfaces (Figures 6.8c, 6.8f & 6.8i).

6.4.6 Crystal chemical mapping

Elemental maps allow quantification of features variably observed in BSE images (Figs. 11-12), and extraction of rim-to-core profiles that follow EPMA transects. BSE images afford highest spatial resolution, followed by EPMA major element maps and LA-ICP-MS trace element maps, which allow assessing changes at trace element level as crystals grow (Jegal et al., 2025; Ubide & Kamber, 2018). In plagioclase crystals, oscillatory zoning correlates with variations in major elements and An content (Na in Figure 6.11c). While trace element variations are unresolvable for very fine oscillations due to lower spatial resolution of the LA-ICP-MS mapping data (e.g., Ba in Figure 6.11), we find that An content (Ca over Ca+Na) typically anti-correlates with Ba, Rb and REE concentrations (see how low Na values show low Ba values in Figure 6.11b – c). Disequilibrium textures such as patchy cores, resorbed surfaces and sieve textures generate strong compositional contrasts that are detectable across our major and particularly trace element dataset (Figure 6.11), for example through low Na and Ba concentrations, lighter in BSE images, related to the sieve structures that host the melt pockets (Figures 6.11b & 6.11d).

Pyroxene maps show sharp compositional contrasts related to sector (Figure 6.12a) and oscillatory zoning (Figure 6.12a & 6.12d). As with the plagioclase, resorption features such as sieving and melt pockets are easily identified in all maps, and fine-scale zoning features are best distinguished in BSE-EPMA maps. Variations in Mg# in the patchy cores are hinted by BSE contrasts, with lighter zones having lower MgO contents, and such differences are magnified in trace elements, including the REE which allow distinguishing rim, mantle and core sections (Figure 6.12b – e). Other features such as diffusion of trace elements between oiko- and chadacryst pyroxenes are readily observable in trace element maps despite remaining almost imperceptible in profiles (Figure 6.12d - e).

Table 6.7. Crystal composition and melt-crystal equilibrium per sample.

		Melt-Crystal equilibrium				Average crystal composition per sample				Pyroxene distribution*		
Group	Sample	Pl (%)	Opx (%)	Aug (%)	Pgt (%)	An	Mg#Opx	Mg#Aug	Mg#Pgt	Opx (%)	Aug (%)	Pig (%)
Mangaehuehu Member	RSA13	66	31	40	33	58	64	71	62	68	20	12
	RSA6B	95	69	23	0	69	63	66	63	47	49	4
	RSA6A	96	60	44	0	60	65	68	53	48	43	10
	RSA5	94	0	0	0	59	64	66	45	50	36	14
	RSA4	94	53	71	33	59	65	67	49	50	42	8
Makotuku Member	RSA8	33	67	0	0	64	58	63	47	72	20	8
	RSA7C	29	52	67	0	61	57	63	45	68	21	12
	RSA7B	67	88	67	100	57	60	61	60	81	14	5
	RSA7A	24	50	57	100	58	56	59	57	63	31	6
	RSA10	65	50	100	8	73	55	62	48	51	20	29
	RSA3	29	59		0	55	57		49	96	0	4
	RSA1B	40	62	100	50	66	58	60	51	57	26	17
	RSA1A	44	43	50	0	75	53	60	48	63	26	11
Waitonga Member	RSA2	78	8	0	0	57	52	59	34	64	31	5
	RSA9	73	27	0		52	49	58		83	17	0
Turoa Member	RSA11	41	62	100	0	53	52	54	42	94	3	3
	RSA12	67	37	0		60	57	61		93	8	0

* Distribution based on the compositions of all pyroxenes analyzed per sample.
Pl: plagioclase. Opx: orthopyroxene – enstatite. Aug: augite. Pgt: pigeonite.
An: Anorthite content (An = Ca/[Ca+Na]). Mg#: Magnesium number (Mg# = 100*Mg/Mg+Fe^{+2})

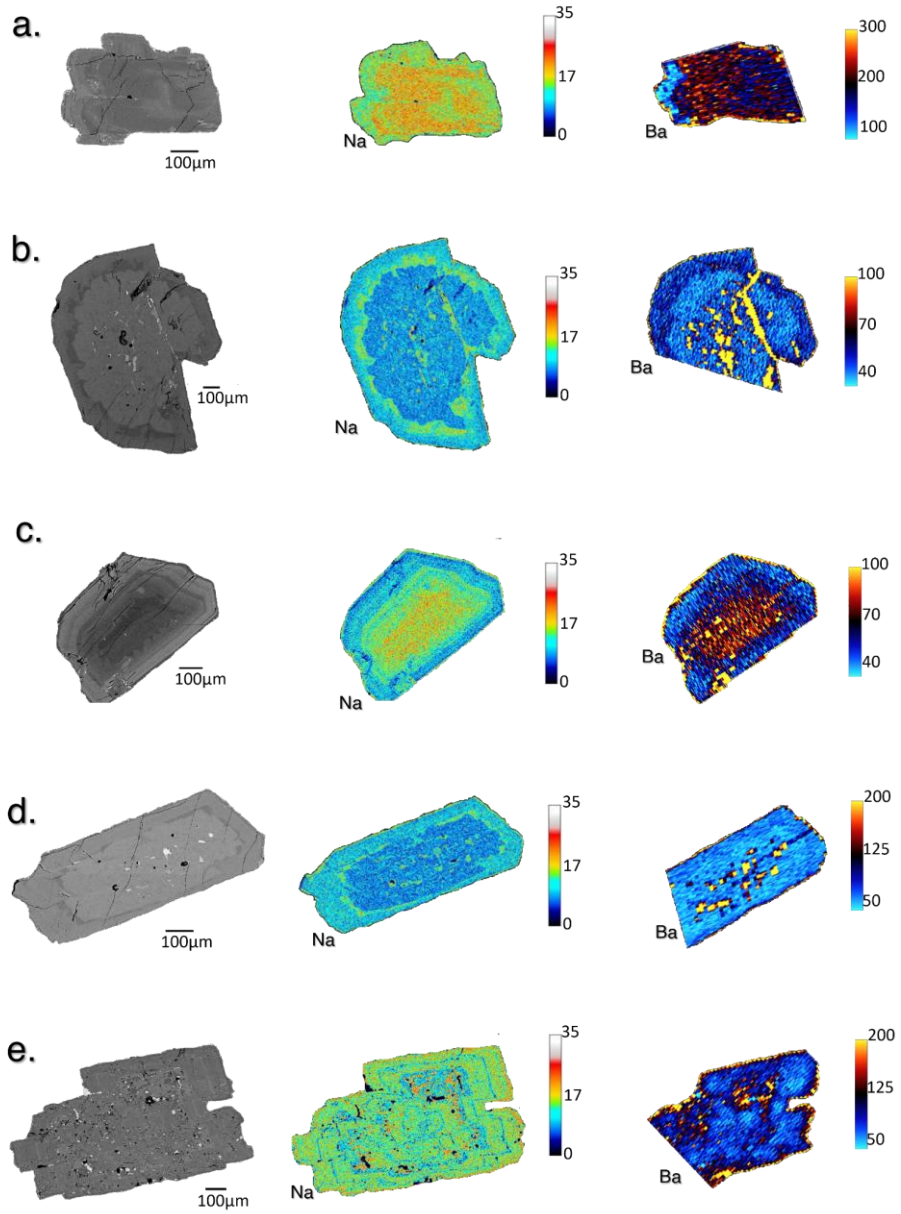

Figure 6.11. Plagioclase compositional maps.a. Crystal with patchy core, wavy resorbed surfaces and oscillatory zoning from sample RSA1B-1. b. Crystal with wavy resorbed surfaces and sieving in the core from sample RSA10. c. Crystal with patchy core, oscillatory zoning and wavy resorbed surfaces in the core of the crystal from sample RSA7A. d. Crystal with resorbed surfaces, oscillatory zoning and sieving in the core from sample RSA1B-2. e. Crystal with oscillatory zoning and coarse sieving from sample RSA13. Na: Qualitative Sodium presence from EPMA map. The calibration bar on the left indicates variations of Na within the crystal, however, does not indicate sodium content. Ba: Quantitative Barium content in the crystal from LA-ICPMS map. Scale bars indicate the content of Ba in ppm.

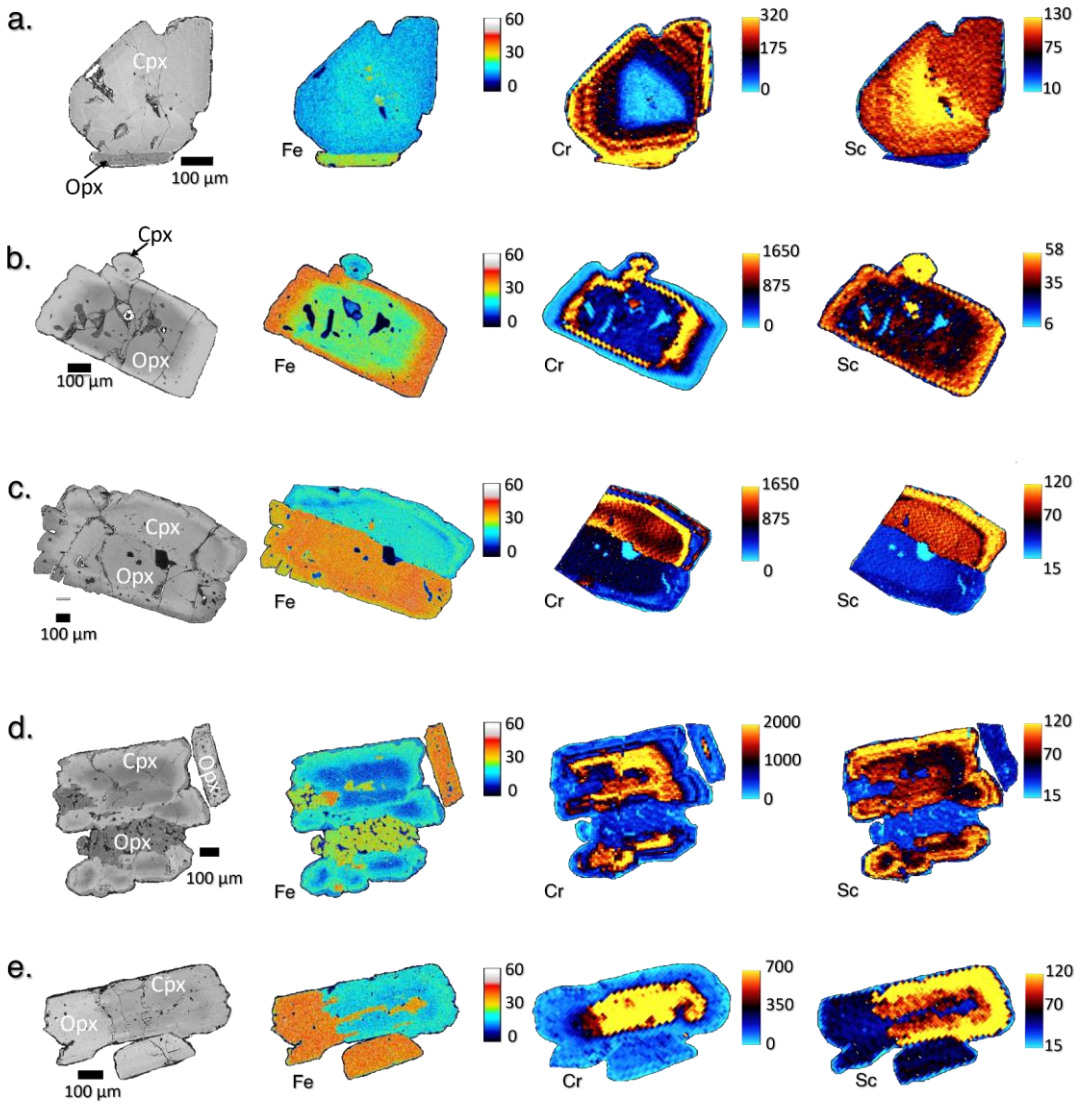

Figure 6.12. Pyroxene compositional maps.a. Clinopyroxene (Cpx) crystal with sector and oscillatory zoning from sample RSA7C. b. Orthopyroxene (Opx) crystal with oscillatory zoning and sieving in the core from sample RSA9. c. Glomerocryst of clinopyroxene (top) and orthopyroxene (bottom) with oscillatory zoning and sieving from sample RSA13. Note the sharp contact between pyroxene species. d. Glomerocryst of clinopyroxene (top and bottom) and orthopyroxene (mid) with wavy resorbed surfaces, oscillatory zoning and sieving in the core of the clinopyroxene from sample RSA6B. Note how the clinopyroxene seems to be growing around the orthopyroxenes. e. Glomerocryst of clinopyroxene (right) and orthopyroxene (left) with normal zoning and sieving from sample RSA11. Note how the clinopyroxene is engulfing the orthopyroxene. Fe: Qualitative Iron presence from EPMA map. The calibration bar on the left indicates variations of Fe within the crystal, however, does not indicate iron content. Cr: Quantitative Chromium content in the crystal from LA-ICPMS map. Scale bars indicate the content of Cr in ppm to the crystals on the right of the scale. Sc: Quantitative Scandium content in the crystal from LA-ICPMS map. Scale bars indicate the content of Sc in ppm to the crystals on the right of the scale.

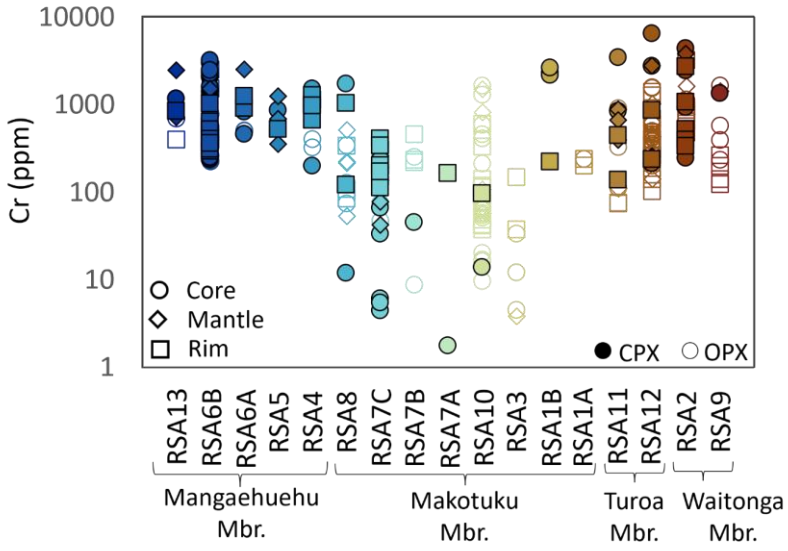

Figure 6.13. Pyroxene Cr content. Cr content in phenocrysts from LA-ICPMS data per sample. Samples RSA3 & 1A have no clinopyroxenes analyzed. Samples RSA5 & 1B have no orthopyroxenes (OPX) analyzed. Note how there is a general trend towards lower Cr concentrations from Mangaehuehu Member to Makotuku Member mainly in clinopyroxenes (CPX).

Sector zoning is strongest for Al, Zr, Ti, Sc and REE (Sc in Figure 6.12a; see Appendix 4 for other elements), while oscillatory zoning is best defined by Cr (Figure 6.12a & 6.12c - d). The Cr enriched zones are enriched in Mg and depleted in Zr in the profiles suggesting mafic recharge (e.g., Schoneveld et al., 2025; Ubide & Kamber, 2018; Ubide et al., 2025). Interestingly, the maps reveal Cr-rich zones or cores in some of the orthopyroxenes and most of the clinopyroxenes (Figure 6.12 & 6.13), the latter usually showing more than one Cr-rich zone (Figure 6.12a & 6.12c - d). These concentrations vary between samples with those of the Makotuku Member showing lowest Cr concentration (Figure 6.13).

Finally, elemental maps facilitate observation of the clino-orthopyroxene associations within glomerocrysts, also identifiable with major element abundances (e.g., Mg-Fe; Figure 6.12). Here, small orthopyroxene crystals adhered to big clinopyroxene crystals (Figure 6.12a) and vice versa (Figure 6.12b) are more distinguishable. Likewise, the poikilitic textures in glomerocrysts where clinopyroxene grows around orthopyroxene (Figure 6.12c – e), the sharp contacts between pyroxene crystals (Figure 6.12c) or the textural differences between

pyroxenes (e.g., larger resorption textures in orthopyroxenes in Figure 6.12d – e) are most clearly identified in elemental maps. Profile compositional data is provided in Appendix 4 (Figures S5 & S6).

6.4.7 Crystal melt-equilibrium

Assessment of equilibrium plagioclase, orthopyroxene and clinopyroxene and their carrier liquids (host groundmass) indicates widespread disequilibrium with mineral compositions extending above and below the equilibrium fields due to the variability in the compositions of the crystals (Figure 6.14).

In the case of plagioclase (Figure 6.14a – b), samples with lowest SiO_2 in groundmass (i.e., Mangaehuehu and Makotuku members) scatter between the dry and saturated fields, while the more silicic samples are concentrated in the H_2O-saturated conditions. Notably, some microlite cores of the Waitonga and Turoa members samples are out of equilibrium (reddish points in Figure 6.14a). The microlites core of the Mangaehuehu and Makotuku members seem to be in equilibrium, mostly at H_2O-saturated conditions (blue-green points in Figure 6.14a), however, some cores are in equilibrium at dry conditions (yellow-green points in Figure 6.14a). On the other hand, the rims seem mostly in equilibrium at dry conditions for the Waitonga and Turoa members samples (reddish squares in Figure 6.14a) and at H_2O-saturated conditions for the Mangaehuehu and Makotuku members (blue-green squares in Figure 6.14a). Plagioclase phenocryst rims show a similar behavior to microlite rims of more mafic samples (Mangaehuehu and Makotuku members), which fall in equilibrium in H_2O-saturated conditions. In the more silicic samples (Waitonga and Turoa members) equilibrium is achieved at dry conditions (Figure 6.14b). Nonetheless some of the phenocryst rims for the Mangaehuehu and Makotuku members are in equilibrium at dry conditions as was observed for some of the microlite cores (blue-green points in Figure 6.14b). The plagioclase-melt

equilibrium varies between 24% to 96%, with samples of the Makotuku Member showing the lower percentages (i.e., 41% on average) and samples in the Mangaehuehu Member showing the highest (i.e., 89% on average) (Table 6.7). The Waitonga Member samples have 75% of plagioclase compositions in equilibrium with carrier melts, while the Turoa Member has 54% (Table 6.7).

The orthopyroxene crystals from the Waitonga and Turoa members (reddish points in Figure 6.14c – d), seem to have grown from melts with more mafic compositions than the carrier melts since are located mostly above the equilibrium field. In the case of samples in the Mangaehuehu and Makotuku Members, the cores of microlites are scattered above and below the equilibrium field, meaning their origin is linked to both mafic and felsic melts, while the rims are mostly trending below the equilibrium field, with an origin linked to more silicic melts (blue-green points in Figure 6.14c). Similarly, the phenocrysts rims for the Waitonga and Turoa members have compositions that position them above the equilibrium field, while those of the Mangaehuehu and Makotuku members are positioned above and below the equilibrium fields (Figure 14d). Orthopyroxene-melt equilibrium varies between 0 - 88%, with most of the samples under 62% (Table 6.7). On average, the Makotuku Member samples have more orthopyroxene in equilibrium (i.e., 59%) than the Mangaehuehu (i.e., 43%), Waitonga (i.e., 17%) and Turoa (i.e., 49%) members (Table 6.7). However, these averages are influenced by some specific samples. The Mangaehuehu Member samples RSA5, which has no orthopyroxene in equilibrium, and RSA13, which has one of the lowest percentages of orthopyroxene crystals in equilibrium (31%), have most of the analysis performed in microlites. Sample RSA11 of the Turoa member has a 62% equilibrium, which contrasts with sample RSA12 37% (Table 6.7). In the Turoa Member there is a notable trend in which the sample with higher percentages of plagioclase in equilibrium show the lowest percentages of pyroxene in equilibrium (Table 6.7).

Clinopyroxene-melt equilibrium (Figures 14e – f & 6.15) must be analyzed carefully since the samples present two main compositions (i.e., augite and pigeonite) and the number of crystals available in the samples is low, with some samples under 10 clinopyroxene crystals (see Appendix 3 for full data). Here, the equilibrium is subjective to the pyroxene components assessed, nonetheless, the crystals need to be within equilibrium error for all the test to be considered in equilibrium with the melt.

The clinopyroxene equilibrium evaluated using a variation of Rhodes test (i.e., K_D (Fe-Mg)$^{cpx\text{-}liq}$ = 0.28 ± 0.08) as recommended by Wieser et al. (2023b) shows a 47 % of equilibrium for all the clinopyroxenes, with all the microlites and phenocrysts of the Waitonga Member out of equilibrium with the carrier melts (Figure 6.14e - f). Similarly, the Turoa Member has only one microlite core in equilibrium (Figure 6.14e). Meanwhile, the clinopyroxenes in the Mangaehuehu and Makotuku members scatter above and below of the equilibrium fields (Figure 6.14e - f), indicating variable compositions. For enstatite-ferrosilite (EnFs) and diopside-hedenbergite (DiHd) components 86% of the crystals are in equilibrium with 1 standard error of estimate (SEE) (Figure 6.15a – d). However, using the calcium-titanium (CaTi) and calcium-tschermak (CaTs) components (Figure 6.15e – h), the number of crystals in disequilibrium increases to 77%. Notably within 1SEE for the CaTi component, 60% of the clinopyroxenes are out of equilibrium (Figure 6.15e – f), while for the CaTs component 80% of the pigeonites are out of equilibrium (Figure 6.15g – h).

Examining data within permissive error constraints (i.e., 2SEE for the CaTs and CaTi components), an average 41% of augite and 17% of pigeonite crystals appear to be in equilibrium with carrier melts. Increasing the equilibrium range to 2SEE as recommended by MacDonald et al. (2023), the number of clinopyroxene crystals in equilibrium increases up to 68%, however, the distribution of the crystals is leaning towards the upper side of the 1:1 line

in the CaTi component (Figure 6.15e - f), and towards the bottom side in the CaTs component for the pigeonites (Figure 6.15g – h). These non-gaussian distributions observed in Figure 6.15 may be indication of disequilibrium. Furthermore, the combination of all the test results in a crystal-melt equilibrium of 32% even with the permissive error constraints for the CaTs and CaTi components.

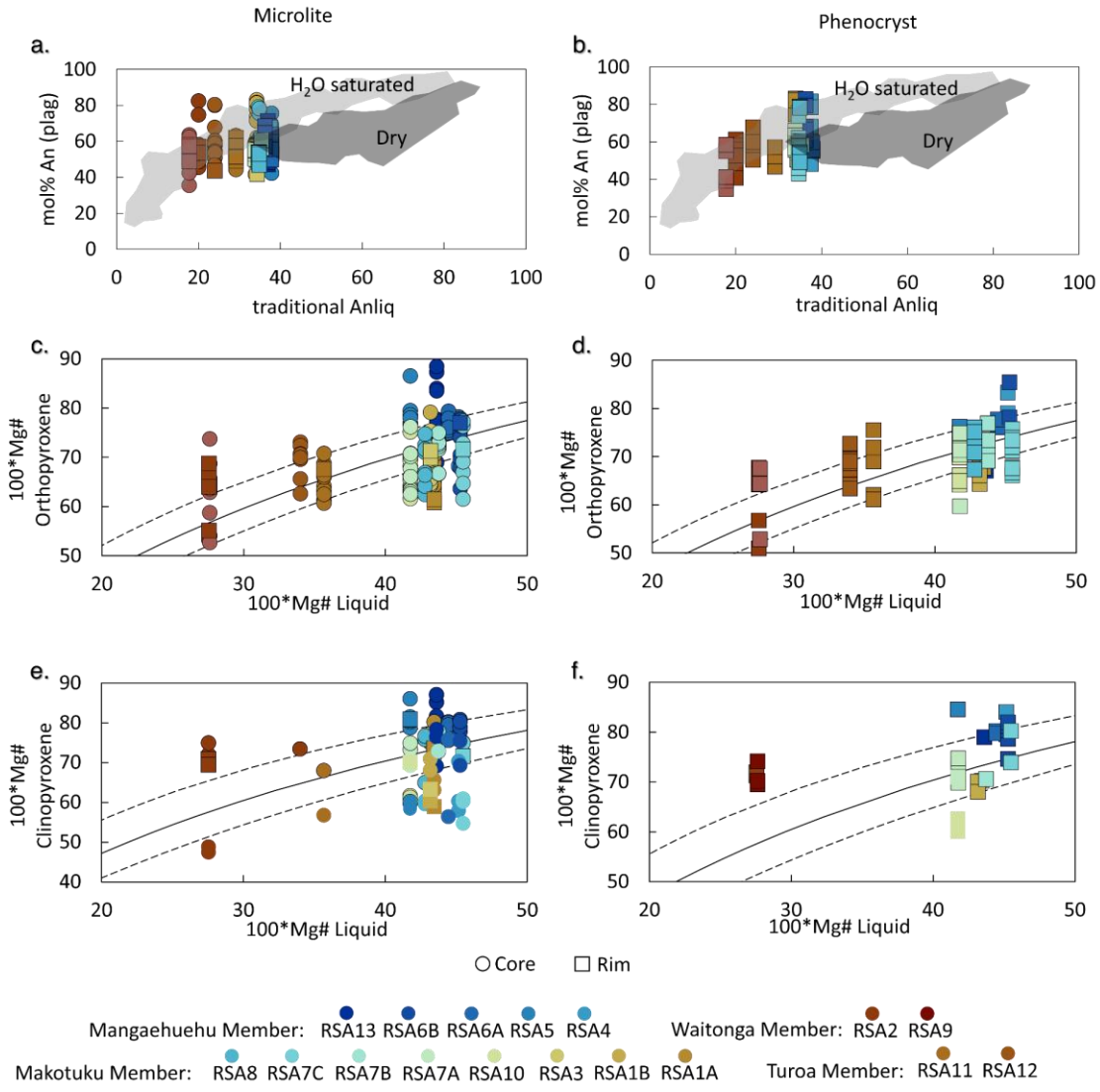

Figure 6.14. Crystal-melt equilibrium.a. & b. Plagioclase-melt equilibrium. Shaded areas represent equilibrium in dry (dark grey), and water saturated (light gray) conditions based on the experimental data from Waters & Lange (2015) as used in *Zellmer et al. (2016b)*. c. & d. Orthopyroxene-melt equilibrium using the test of Rhodes (Rhodes et al., 1979) with a range of equilibrium of K_D Fe-Mg = 0.29 ± 0.06 as in Putirka (2008). The dashed lines indicate an accepted equilibrium range of 1 SEE. e & f. Clinopyroxene-melt equilibri*um* using the test of Rhodes (Rhodes et al., 1979) with a range of equilibrium of K_D Fe-Mg = 0.2*8* ± 0.0*8* as in *Wieser et al. (2023b)*. Points without a border are classified as pigeonite. Panels on the left are equilibrium tests for microlites, while panels on the right for phenocrysts. Circle: core measurements. Square: rim measurements. The color scale indicates the sample number and member.

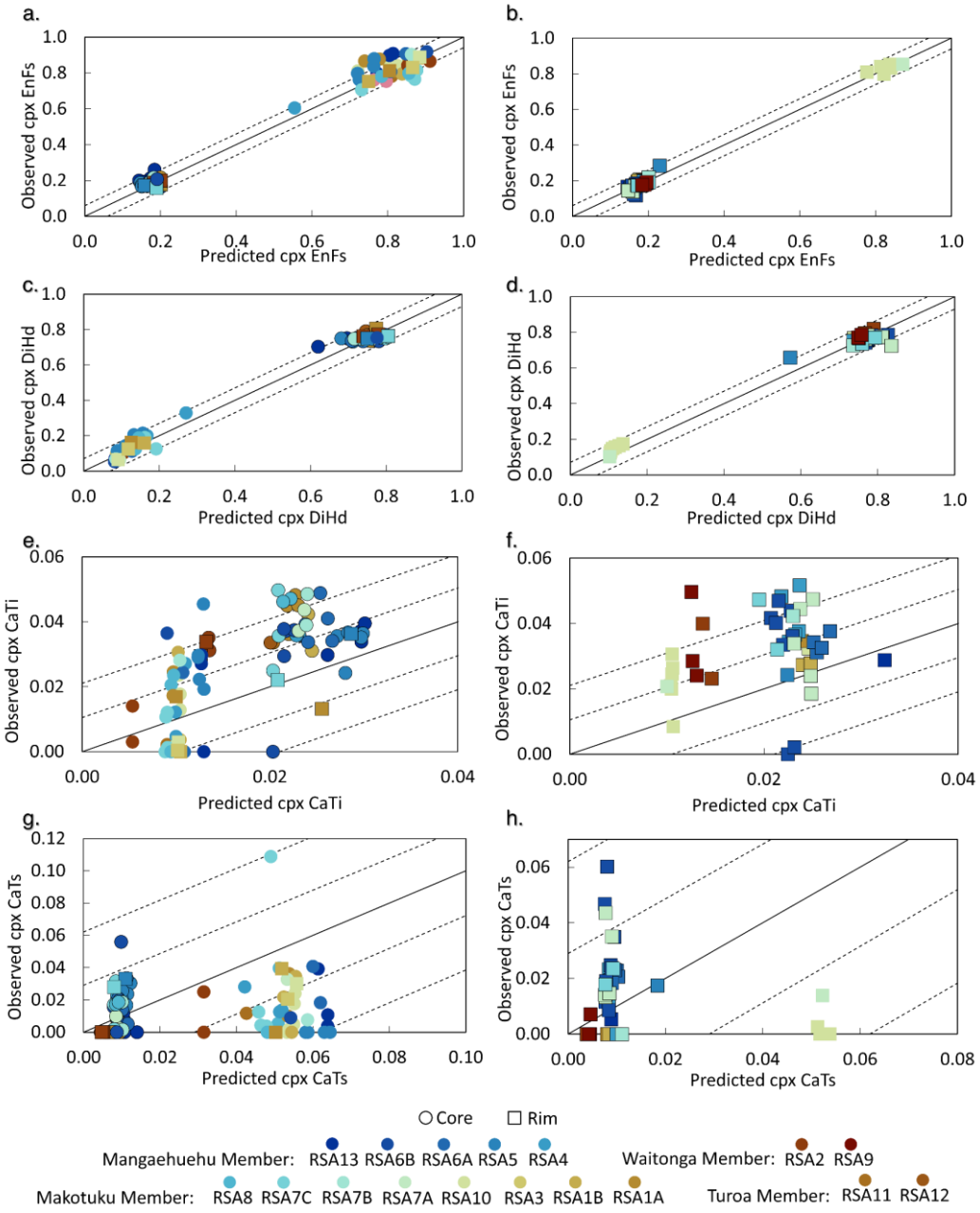

Figure 6.15. Clinopyroxene-melt equilibrium using Putirka (1999) and Mollo et al. (2013) equilibrium test after recommendation from MacDonald et al. (2023).a & b. Enstatite-Ferrosilite (EnFs) component. c & d. Diopside-Hedenbergite (DiHd) component. e & f. Calcium-Titanium (CaTi) component. g & h. Calcium-Tschermak (CaTs) component. Dashed lines indicate an accepted equilibrium range within 1SEE for EnFs (± 0.05 ΔEnFs) and DiHd (± 0.1 ΔDiHd), and 2SEE for CaTi (± 0.02 ΔCaTi) and CaTs (± 0.06 ΔCaTs) as in MacDonald et al. (2023). Points without a border are classified as pigeonite. Panels on the left are equilibrium tests for microlites, while panels on the right for phenocrysts. Circle: core measurements. Square: rim measurements. The color scale indicates the sample number and member.

6.4.8 Thermodynamic modelling

Using whole rock and groundmass data as starting compositions, we modelled a decompression-cooling fractional crystallization paths with rhyolite-MELTS (Gualda et al., 2012) thermodynamic simulations using NNO oxygen fugacity, and initial temperatures and pressures up to 1123 °C and 547 MPa respectively, derived from orthopyroxene thermobarometry, except for sample RSA5 for which we used the pressure and temperature values constrained with MagMaTaB (Weber & Blundy, 2024) for the magmatic liquids, since all the orthopyroxenes in the sample were in disequilibrium.

The modelling performed with the whole rock data reproduced the full range of carrier melt compositions (i.e., groundmass compositions) from LA-ICP-MS analyses (Figure 6.16). Modelling from the groundmass data, comparatively more evolved, reproduced the carrier melt compositions from three samples only (RSA1A, 2 & 12; e.g., Figure 6.16). The T-P results obtained by the whole rock- and groundmass-based models differ for some of the samples (Figure 6.17 & Table 6.8). The samples that show the largest differences between models are the most silicic groundmass samples (RSA2, 9 & RSA12) which are reproduced at lower P-T values in the whole rock-based model since it starts at a more mafic composition (i.e., whole rock: T = 878 – 994 °C & P = 50 – 183 MPa versus groundmass: T = 974 – 1067 °C & P = 108 – 301 MPa). Due to the same effect, some samples within the Makotuku Member (RSA7A, 7C & 8) are reproduced at higher temperatures in the groundmass-based model (i.e., whole rock: T = 1076 – 1103 °C & P = 245 – 446 MPa versus groundmass: T = 1153 – 1163 °C & P = 257 – 547 MPa).

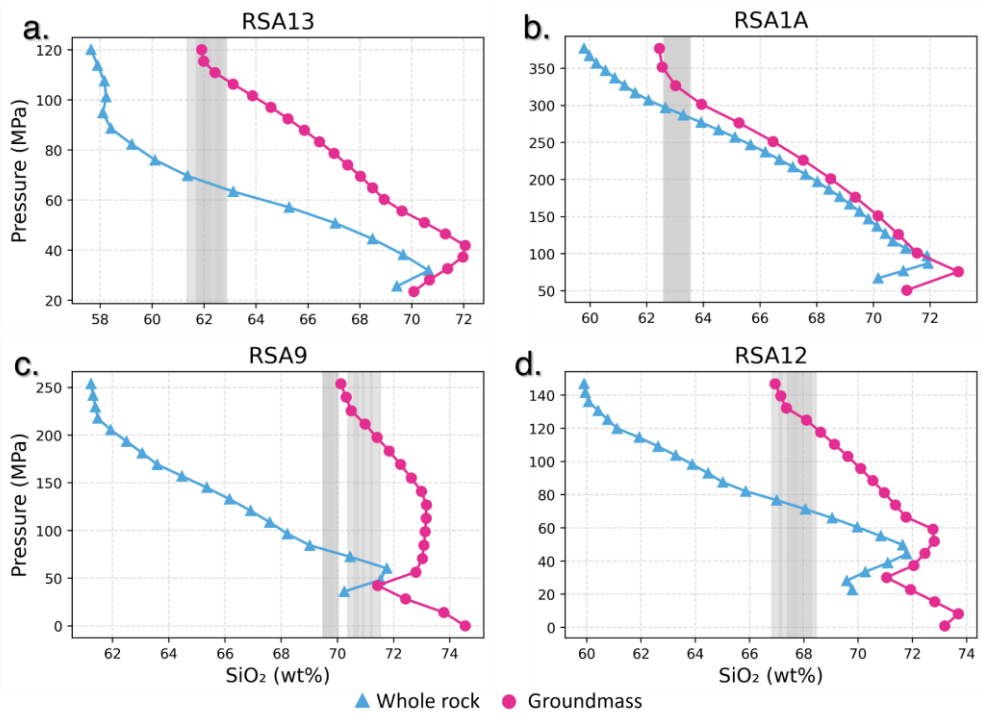

Figure 6.16. MELTS modelling pressure paths versus SiO_2.a. Mangaehuehu Member: RSA13. b. Makotuku Member: RSA1A. c. Waitonga Member: RSA9. d. Turoa Member: RSA12. The modelling of the magmatic liquid was made using whole rock (blue) and groundmass (pink) compositions to constrain the temperature and pressure (in Figure). In gray are the carrier melt compositions measured with LA-ICP-MS.

The ranges of temperature and pressure matching the groundmass compositions obtained through MELTS modelling are 1163 – 974 °C and 547 – 108 MPa, while those obtained from the whole rock-based modelling are 1105 – 878 °C and 446 – 50 MPa (Figure 6.17 & Table 6.8). These pressures translate in of depths 4 – 22 km for the groundmass models and 2 – 18 km for the whole rock models (Table 6.8). Notably, the pressure constrained with groundmass-based MELTS simulations are similar to those obtained through the thermobarometry calculations (547 – 117 MPa).

Groundmass-based models reproduced plagioclase compositions $<An_{57}$ and pyroxene $<Mg\#_{78}$ again due to their relatively evolved composition (Figure 6.18 & Table 6.9). The more primitive plagioclase and pyroxene compositions obtained through EPMA analyses can be reproduced by whole rock-based models of the studied units (i.e., Mangaehuehu, Makotuku, Waitonga and Turoa members). Some of the most primitive mineral compositions

can only be modelled using the Kakuki or Waimarino basalts as starting compositions (Figure 6.18 & Table 6.9).

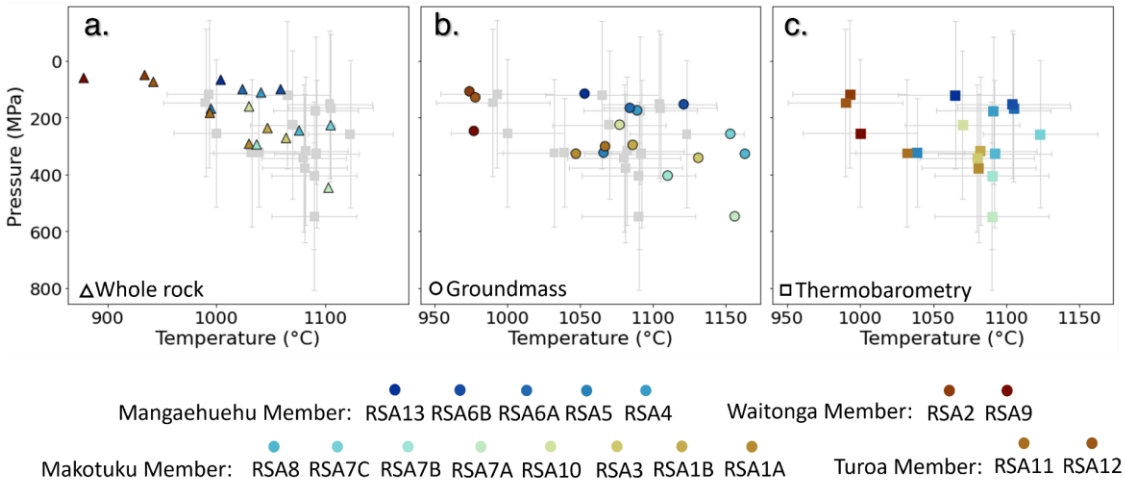

Figure 6.17. Temperature versus pressure.a. Whole rock-based MELTS modelling. b. Groundmass-based MELTS modelling. c. Thermobarometry results. The thermobarometry results are included as references in grey in panels a and b. The colour scale indicates the sample number and member.

Some samples have mineral compositions only reproduced by groundmass-based models or whole rock-based models using compositions from Mangawhero Formation members, rather than their designated units. Samples RSA13 and RSA11 have plagioclase and pyroxene compositions only reproduced by groundmass-based models at pressures <100 MPa (Figures 6.18a & 6.18e) and <200 MPa (Figure 6.18l) respectively. Sample RSA9 have plagioclase compositions only reproducible by the whole rock composition of the Whakapapaiti Member (<50 MPa in Figure 6.18c). Similarly, samples RSA1A, 7B, 9, 10 & 12 have clinopyroxene compositions reproduced by whole rock-based models using the composition of the Mangaehuehu Member (<250 MPa in Figure 6.18f – h). Lastly, orthopyroxene compositions >$Mg\#_{76}$ in the Makotuku Member samples are better reproduced by models using the composition of the Waimarino Basalt as starting material (Figure 6.18j). In the case of samples in the Mangaehuehu Member, it was necessary to increase the starting pressure about 30 MPa to model orthopyroxenes compositions > $Mg\#_{80}$. Meanwhile, plagioclase compositions >An_{85}, clinopyroxene compositions <$Mg\#_{60}$ and >$Mg\#_{83}$, and orthopyroxene

compositions <$Mg\#_{64}$ could not be reproduced by any compositions of the TVZ (Table 6.9). The overarching conclusion from these models that many mineral compositions are not in equilibrium with their host liquids, as inferred from pervious mineral-melt equilibrium tests (Figure 6.14).

Figure 6.18. MELTS modelling of mineral phases (next page).a. – d. Plagioclase: Anortithe content (An#) versus pressure. e. – h. Clinopyroxene: Magnesium number (Mg#) versus pressure. i. – l Orthopyroxene: Mg# versus pressure. The modelling of the mineral phases was made using whole rock and groundmass compositions initially, to match the plagioclase and pyroxene compositions measured with EPMA (gray bars). Since some of the compositions were not modelled by the groundmass and whole rock compositions, the compositions of some members of the Mangawhero (i.e., Mangaehuehu, Makotuku, Waitonga and Whakapapaiti) and Whakapapa (i.e., Turoa) formations were used for the modelling. The most mafic compositions were attained by the modelling of the Waimarino and Kakuki basalts, however, some compositions could not be reproduced.

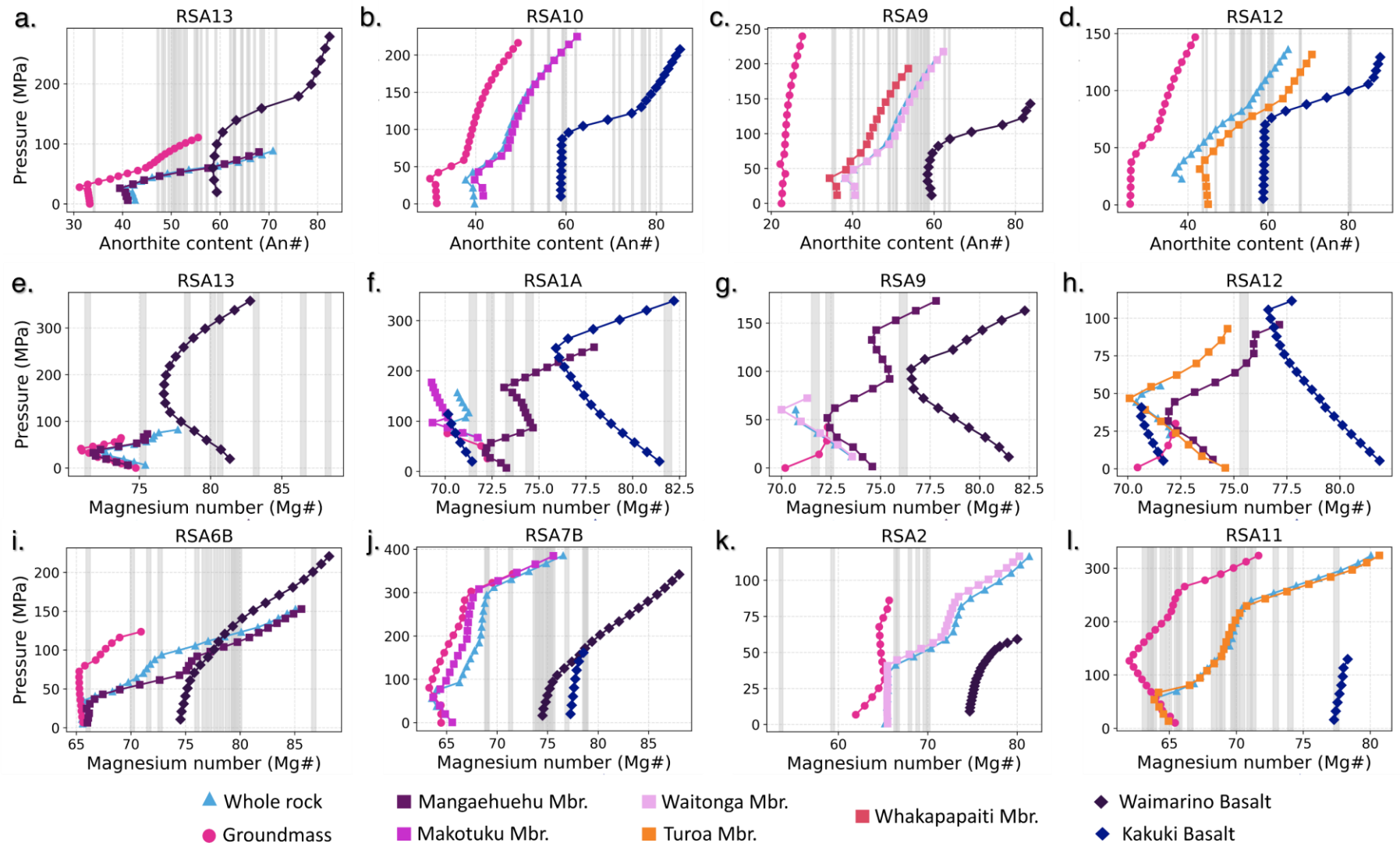
a.
RSA13
b.
RSA10
c.
RSA9
d.
RSA12
Pressure (MPa)
Anorthite content (An#)
e.
RSA13
f.
RSA1A
g.
RSA9
h.
RSA12
Magnesium number (Mg#)
i.
RSA6B
j.
RSA7B
k.
RSA2
l.
RSA11
Whole rock
Groundmass
Mangaehuehu Mbr.
Makotuku Mbr.
Waitonga Mbr.
Turoa Mbr.
Whakapapaiti Mbr.
Waimarino Basalt
Kakuki Basalt

Table 6.8. Temperature (T) and pressure (P) results from MELTS modelling.

Unit	Sample	Whole Rock			Groundmass			Thermobarometry
		T(°C)	P(MPa)	Depth (km)	T(°C)	P(MPa)	Depth (km)	Depth (km)
Mangaehuehu Member	RSA13	1004	67	3	1053	116	5	5
	RSA6B	1059	100	4	1121	153	6	6
	RSA6A	1024	100	4	1084	166	7	7
	RSA5	995	168	7	1066	323	13	*13
	RSA4	1041	112	4	1089	174	7	7
Makotuku Member	RSA8	1076	245	10	1163	327	13	13
	RSA7C	1105	226	9	1153	257	10	10
	RSA7B	1037	294	12	1110	404	16	16
	RSA7A	1103	446	18	1156	547	22	22
	RSA10	1030	161	6	1077	223	9	9
	RSA3	1064	272	11	1131	342	14	14
	RSA1B	1047	237	9	1086	296	12	13
	RSA1A	1030	292	12	1047	327	13	15
Waitonga Member	RSA2	934	50	2	974	108	4	5
	RSA9	878	60	2	977	247	10	10
Turoa Member	RSA11	994	183	7	1067	301	12	13
	RSA12	942	74	3	978	129	5	6

*The depth calculated using the pressure derived from magmatic liquid thermobarometry since the orthopyroxenes failed the equilibrium test.

Table 6.9. Mineral phase MELTS modelling results per unit.

Unit	Samples	Groundmass modelled	Whole rock modelled	Assigned unit modelled	Other units modelled	Compositions

		compositions	compositions	compositions	compositions	unable to be modelled*
Mangaehuehu Member	RSA4 – 6B & 13	An_{31} - An_{57} OPX $Mg\#_{57}$ - $Mg\#_{76}$ CPX $Mg\#_{66}$ - $Mg\#_{75}$	An_{40} - An_{71} OPX $Mg\#_{64}$ - $Mg\#_{85}$ CPX $Mg\#_{70}$ - $Mg\#_{78}$	Mangaehuehu Member: An_{38} - An_{68} OPX $Mg\#_{65}$ - $Mg\#_{86}$ CPX $Mg\#_{71}$ - $Mg\#_{79}$	Waimarino Basalt: An_{58} - An_{84} OPX $Mg\#_{74}$ - $Mg\#_{89}$ CPX $Mg\#_{76}$ - $Mg\#_{84}$	$>An_{85}$ CPX $>Mg\#_{85}$
Makotuku Member	RSA 1A, 1B, 3, 7A-8 & 10	An_{29} - An_{52} OPX $Mg\#_{57}$ - $Mg\#_{78}$ CPX $Mg\#_{54}$ - $Mg\#_{75}$	An_{36} - An_{63} OPX $Mg\#_{60}$ - $Mg\#_{79}$ CPX $Mg\#_{57}$ - $Mg\#_{75}$	Makotuku Member: An_{39} - An_{63} OPX $Mg\#_{59}$ - $Mg\#_{78}$ CPX $Mg\#_{56}$ - $Mg\#_{75}$	Kakuki Basalt: An_{58} - An_{86} CPX $Mg\#_{70}$ - $Mg\#_{83}$ Waimarino Basalt: OPX $Mg\#_{74}$ - $Mg\#_{91}$ Mangaehuehu Member: CPX $Mg\#_{68}$ - $Mg\#_{78}$	CPX $<Mg\#_{66}$
Waitonga Member	RSA2 & 9	An_{22} - An_{33} OPX $Mg\#_{60}$ - $Mg\#_{65}$ CPX $Mg\#_{70}$ - $Mg\#_{73}$	An_{37} - An_{63} OPX $Mg\#_{64}$ - $Mg\#_{82}$ CPX $Mg\#_{70}$ - $Mg\#_{75}$	Waitonga Member: An_{37} - An_{63} OPX $Mg\#_{64}$ - $Mg\#_{81}$ CPX $Mg\#_{69}$ - $Mg\#_{75}$	Waimarino Basalt: An_{58} - An_{85} CPX $Mg\#_{76}$ - $Mg\#_{83}$ Mangaehuehu Member: CPX $Mg\#_{71}$ - $Mg\#_{78}$ Whakapapaiti Member: An_{34} - An_{54} (RSA9)	OPX $<Mg\#_{60}$
Turoa Member	RSA11 & 12	An_{25} - An_{42} OPX $Mg\#_{60}$ - $Mg\#_{72}$ CPX $Mg\#_{70}$ - $Mg\#_{74}$	An_{36} - An_{66} OPX $Mg\#_{63}$ - $Mg\#_{82}$ CPX $Mg\#_{70}$ - $Mg\#_{74}$	Turoa Member: An_{42} - An_{71} OPX $Mg\#_{63}$ - $Mg\#_{81}$ CPX $Mg\#_{69}$ - $Mg\#_{75}$	Kakuki Basalt: An_{58} - An_{88} CPX $Mg\#_{70}$ - $Mg\#_{83}$ Mangaehuehu Member: CPX $Mg\#_{71}$ - $Mg\#_{78}$	CPX $<Mg\#_{60}$

*Compositions measured through EPMA that could not be modelled using whole rock compositions of the Taupō Volcanic Zone.
CPX: clinopyroxene. OPX: orthopyroxene. An: Anorthite content. Mg# Magnesium number.

6.5 Discussion

6.5.1 Crystal records of an open system magma evolution at Mount Ruapehu

The presence of phenocrysts with reverse zoning (e.g., Figure 6.11c), resorption textures (e.g., Figure 6.7g), reaction coronas (e.g., Figure 6.8d), glomerocrysts (e.g., Figure 6.9), and broken crystals (e.g., Figure 6.8c), are indication of crystal entrainment by the ascending melts as previously observed in Mount Ruapehu (e.g., Conway, 2016; Conway et al., 2018; Kilgour et al., 2013; Nakagawa et al., 2002; Price et al., 2012; Stewart, 2010). The presence of mechanically broken crystals and glomerocrysts indicates the remobilization of previously formed crystals from a crystal-rich environment by the ascending magma (e.g., Conway, 2016; Holness et al., 2019; Van Gerve et al., 2020; Zellmer & Iizuka, 2025). Meanwhile, the inverse compositional zoning reflects changes associated with the introduction of new magma via recharge and mixing (e.g., Ginibre et al., 2002a; Ginibre et al., 2007; Renjith, 2014; Viccaro et al., 2010). Hence, the crystal cargo at Mount Ruapehu was initially grown from more felsic melts that later interacted with mafic recharges (e.g., Cr enrichment in Figure 6.12a & Low Na in rim in Figure 6.11c), occasionally experiencing multiple recharge events (e.g., multiple Cr rings in Figure 6.12c), affecting the crystals throughout their grow (e.g., Cr-rich zones in core, mantle and rims in Figure 6.13 & wavy resorption surfaces linked to coarsely sieved cores in Figures 6.11b & 6.11d).

Notably, while the clinopyroxenes phenocrysts in the Mangaehuehu, Waitonga and Turoa members continue growing after the mafic recharge (i.e., Cr rings in core and mantles in Figure 6.13), those of the Makotuku Member show higher Cr concentrations in the rims of the crystals for most of the samples (Figure 6.13), indicating a mafic recharge almost at the last stage of re-equilibration before magma ascent, which may have also caused the formation of pigeonite reaction coronas (Figures 6.7i & 6.8d) (e.g., Markl & White, 1999; Villalba et

al., 2023; Wenzel et al., 2021). The presence of these reaction coronas indicates compositional re-equilibration due to changes in the magmatic conditions, caused by the interaction between the melt and stalled crystalline bodies (e.g., Masotta et al., 2018; Zierenberg et al., 2013). The cumulate nature of the recycled cargo is highlighted by the presence of poikilitic textures in clinopyroxene – orthopyroxene glomerocrysts (Figure 6.12d - e), which reflect differences in the composition of the magma injections, favoring either the growth of orthopyroxene or clinopyroxene at different times (e.g., Barnes et al., 2021; Schoneveld et al., 2025). Furthermore, the high number of crystal out of equilibrium (Table 6.7), particularly pyroxenes, serves as an additional confirmation of crystal entrainment for all the lavas (e.g., D'Mello et al., 2023; Lormand et al., 2021; Svoboda et al., 2021), where the crystals grew from more mafic magmas than the ones that carried them (e.g., Conway et al., 2018; Nakagawa et al., 2002).

MELTS modeling corroborates the complexity of the magmatic system, in which the carrier melts appear to pick up the crystal cargo from various sources while ascending through the crust. While some intermediate crystal compositions were reproduced by the composition of the Mangaehuehu Member, it is notable that the most mafic compositions are reproduced only by the Waimarino (i.e., high-MgO basalt) and Kakuki basalt (i.e., most primitive basalt of the TVZ) compositions from Hackett (1985) and Gamble et al. (1993) respectively, confirming the involvement of at least two primitive end members in the mafic injections, and the crystal uptake at Mount Ruapehu. Here, the most mafic clinopyroxene ($>Mg\#_{85}$) and plagioclase ($>An_{85}$) composition in the Mangaehuehu Member, which could not be model, may have their origin in a pure highly MgO-enriched primitive magma (e.g., similar Mg# compositions in clinopyroxenes in HMAs in Kamei et al., 2004; Luo et al., 2025a), since the clinopyroxene compositions are mainly determined by the source (e.g., Kamei et al., 2004;

Putirka et al., 1996). However, these primitive magmas never erupted on the TVZ (Conway et al., 2018; Waight et al., 2017).

Similarly, the Makotuku, Waitonga and Turoa members show non-reproducible pyroxene compositions (i.e., Makotuku Member: $<Mg\#_{66}$; Waitonga Member: $<Mg\#_{60}$; and Turoa Member: $<Mg\#_{60}$), indicating that these might have been formed from a rhyolitic melt that may have not erupted (e.g., Luo et al., 2025b; Rooyakkers et al., 2021). Notably, for sample RSA9 the plagioclases under An_{38}, could be modeled using the composition of the Whakapapaiti Member, which is slightly more silicic than the Waitonga member, confirming crystal entrainment from previously emplaced magmas and contribution from more rhyolitic sources.

The multiple resorption textures observed in the larger microlites (>20 μm) are indication of dissolution processes related to re-equilibration due to decompression or magma mixing/mingling (Renjith, 2014; Streck, 2008; Viccaro et al., 2010). In the case of the orthopyroxene microlites that show resorbed cores and fine sieving (e.g., Figures 6.7b & 6.7e), this might be the result of chemical re-equilibration to accommodate the decompression during ascent (Martel & Schmidt, 2003). In contrast, crystals showing ovoidal cores (e.g., Figure 6.7c – d) and resorption surfaces (Figure 6.7e - f) were most likely affected by magma injections that caused disequilibria and partial dissolution and are considered antecrystic in origin (e.g., Auer et al., 2015; Shane et al., 2008). On the other hand, the smaller microlites (<20 μm) show tabular and acicular shapes exhibiting hopper, swallow-tail and skeletal textures (e.g., Figures 6.6a – b & 6.7a) linked to decompression-induced crystallization at the onset of eruption (Lowrey et al., 2017; Nakagawa et al., 1998; Ohnenstetter & Brown, 1992; e.g., Shea & Hammer, 2013; e.g., Streck, 2008).

Notably, all the samples in this study have a considerable number of crystals out of chemical equilibrium meaning that these were picked up and spent a short time interacting with the carrier melts (Figure 6.13 & Table 6.7). The compositional gaps observed in plagioclases, where bytownite cores are isolated (i.e., ~An_{70} in Figure 6.10a), and the gaps for the lowest and highest En values in orthopyroxenes (i.e., ~En_{60} & ~En_{80} in Figure 6.10c), reflect the antecrystic origin of some microlites, meaning that these crystals were picked up by the melt (e.g., Lormand et al., 2021; Zellmer et al., 2013; Zellmer et al., 2016b). In contrast, the autocrystic microlites (i.e., grew from the carrier melt) have An contents between An_{47} and An_{70}, where the crystal belonging to the Mangaehuehu Member samples show the highest An contents (i.e., Mangaehuehu Member: An_{55} – An_{70}; Makotuku Member: An_{47} – An_{60}; Waitonga Member: An_{49} – An_{63} & Turoa Member: An_{50} – An_{63}), and En contents for orthopyroxene (i.e., Mangaehuehu Member: En_{71} – En_{77}; Makotuku Member: En_{58} – En_{77}; Waitonga Member: En_{57} – En_{66} & Turoa Member: En_{58} – En_{70}). Notably, the compositional gap between En_{68} - En_{71} for the Mangaehuehu Member orthopyroxenes (Figure 6.10c - d) constitute two populations of orthopyroxenes linked to different magmatic conditions (i.e., pressure and temperature), where those between En_{60} – En_{68} ($Mg\#_{49-57}$) are mostly out of equilibrium with the carrier melt , and are likely grown from a previous magma injection with lower temperature (e.g., orthopyroxene Mg# correlates positively with temperature in Kilgour et al., 2014), compared to those between En_{71} – En_{77} ($Mg\#_{62-67}$) in equilibrium with the carrier melts, providing further evidence of multiple magma injections.

6.5.2 Nanolites as record of lava/ice interaction?

Although, the nucleation of Fe-oxides in the rock groundmass is linked to fast decompression and controlled by oxygen fugacity (Hammer, 2006; Martel & Schmidt, 2003), there is an obvious link between the size and amount of the nanolites (i.e., crystals under 1µm in width

in Zellmer, 2021) and the location of the samples within the lava flow (i.e., slower cooling in the inner part of the flow; Harris & Rowland, 2015; Hon et al., 1994) and/or to the existence of lava/ice interaction that has been proven during the emplacement of the lavas at Mount Ruapehu where glassy patches in the matrix have been linked to ice-bounded margins and dammed flows (e.g., Conway et al., 2015; Stevenson et al., 2009; Tuffen & Castro, 2009).

Since rapid cooling increases nucleation of nanolites hindering their growth (e.g., Mujin et al., 2017a, b), the presence of nanolite-populated glasses (Figure 6.6c – f) may be indication of large degrees of magma undercooling (e.g., De Yoreo & Vekilov, 2003; Li & Deepak, 2022; Sen, 2014). This is particularly the case for the outermost parts of the flows, which have larger volume fractions of smaller nanolites (Figure 6.6f) compared to the inner parts of the flow which have more visible larger nanolites (Figure 6.6e). In this sense, the presence of nanolites can be linked to rapid cooling of the lava flows that were emplaced against glaciers and ice caps during the last glaciation (Conway et al., 2015; Conway, 2016; Townsend et al., 2017). Notably, the samples with fewer nanolites, (i.e., those that went through less pronounced cooling after eruption), are also those that show the most evolved melts (i.e., Waitonga and Turoa members). These samples were emplaced at <26 ka, near the end of the last glacial cycle (~ 30 – 18 ka in Eaves et al., 2016a; Eaves et al., 2016b), coinciding with the retreat of the glaciers that began at ~28 ka. To confirm the link between nanolites and emplacement of lava flows in glaciated environments further crystal size distribution analyses, experimental growth at similar undercooling conditions and crystallization modelling would be required. However, our data suggest that the flows emplaced during the glacier retreat may have had slower cooling rates leading to the growth of fewer nanolite nuclei which then developed into relatively larger nanolites.

6.5.3 Crystals influencing the whole rock composition

Whole rock vs groundmass compositions show noticeably different distributions in the TAS classification diagram (Figure 6.2). While groundmass compositions are equivalent to the carrier melt (e.g., Magee et al., 2021; Ubide et al., 2023), whole rock compositions represent the carrier melt plus the crystal cargo (e.g., Magee et al., 2021; Ubide et al., 2014; Ubide et al., 2022). In our sample set, most carrier melt compositions have similar SiO_2 versus Alkali trends (Mangaehuehu & Makotuku members) but the crystal compositions are clearly less mafic for samples of the Makotuku Member (i.e., Conway, 2016; Graham & Hackett, 1987), resulting in less mafic whole rock compositions relative to the Mangaehuehu Member (Figure 6.2a).

One of the most remarkable features observed for whole rock compositions in the lavas from Mount Ruapehu is the MgO vs. SiO2 variation for lavas emplaced between 50 – 36 ka (Conway, 2016; Conway et al., 2018; Townsend et al., 2017). Samples from the Mangaehuehu Member (47 – 40 ka) fall into the high-MgO trend and are classified as high-magnesium andesites (HMA) (Conway et al., 2018; Conway et al., 2020; Townsend et al., 2017). These samples show the highest values for Cr and Ni in the carrier melt (Figure 6.4h – i), indicating a more mafic composition than those of the younger Makotuku Member (24 – 16 ka) which align with the low-MgO trend representative of most of the products of Mount Ruapehu (Conway, 2016). Additionally, unlike other samples, the Mg# number of enstatites and augites in the Mangaehuehu Member (Table 6.7) can be correlated with the MgO content of the whole rock compositions (i.e., samples with higher MgO concentrations in whole rock have higher Mg# pyroxenes), indicating MgO enrichment due to crystal entrainment. Notably, while the Mangaehuehu Member samples have a relatively low concentration in Li, sample RSA13 has high Li content similar to samples of the Makotuku Member (Figure

6.4g). Li enrichment has been linked to intranscrustal differentiation, hence, the Li enrichment of this sample might be linked to the particular crystallization history of the magmas of this specific flow (e.g., Chen et al., 2020; Schettino et al., 2024).

The Waitonga and Turoa members samples have the most evolved groundmass compositions showing the highest concentration of incompatible elements (Figure 6.5a) and the highest SiO_2 (Figure 6.2b). These samples represent the melt evolution observed previously at Mount Ruapehu for the lavas of the Mangawhero and Whakapapa formations including the reversed SiO_2 versus K_2O trend for the lavas <26 ka (Conway et al., 2018; Price et al., 2005; Price et al., 2012; Waight et al., 1999), including the dacite groundmass compositions of the younger Turoa Member (17 – 10 ka) of the Whakapapa Formation and the rhyolite groundmasses of the Waitonga Member (25 – 21 ka) of the Mangawhero Formation (Figure 6.2b). The Turoa Member show differences in the Na_2O content in whole rock and groundmass compositions (Figures 6.3c & 6.4c), indicating a more evolved, fractionated melt in RSA12 compared to RSA11, related to different flows (RSA11: Turoa Cascades flow - 13.4±2.6 ka, and RSA12: Mangaturuturu North flow - 8.3±1.6 ka in Doll et al., 2024). Here, the slightly higher content of incompatible elements and REE in sample RSA11 compared RSA12 might be indication of crustal assimilation as has been recognized previously for Mount Ruapehu and that is supported by the presence of xenoliths in the samples of the Turoa Member as seen in Figure 6.9 (e.g., Conway et al., 2018; Price et al., 2012; Waight et al., 1999).

The lava samples in this study define homogenous REE trends of LREE enrichment, Eu negative anomalies and relatively flat HREE patterns representative of wet melting in subduction zones (Turner & Langmuir, 2022). Moreover, the REE behavior of the samples is not only similar to the behavior reported for Mount Ruapehu in the literature (e.g., Conway, 2016; Gamble et al., 1999) but also to other samples from the Southern TVZ (e.g., Corella

Santa Cruz, 2023). There, the slight variation in REE between samples has been linked with variable crustal assimilation of the basement (i.e., presence of xenoliths from the Kaweka and Waipapa terranes in Conway, 2016; Gamble et al., 1996; Gamble et al., 1999; Price et al., 2015), which coincides with the observations made for the Turoa Member samples; and slab-derived components, such as sediment recycling and tectonic erosion of the Hikurangi plateau (Corella Santa Cruz et al., 2023; Gamble et al., 1996; Timm et al., 2014; Waight et al., 2017), which require isotopic analyses, out of the scope of the present study, to determine the degree of contribution of these to the composition.

6.5.4 Inferring the plumbing system at Mount Ruapehu

Magma plumbing at Mount Ruapehu makes a complex system in which the magmas suffer different levels of mixing/mingling, fractionation, and assimilation at different depths within the crust (Conway et al., 2018; Gamble et al., 1999; Kilgour et al., 2013; Price et al., 2005; Price et al., 2012; Waight et al., 1999; Waight et al., 2017). This study agrees with many of the previous interpretations and provides further evidence about the details of the magmatic processes occurring at Mount Ruapehu in a dike-dominated rift setting.

In Figure 6.19, the changes in composition and temperature are summarized in relation to the age of the units assigned to each group. The results reflect the reverse trend in silica and K_2O content observed for the most recent products of Mount Ruapehu (<26 ka in Conway et al., 2018; Townsend et al., 2017) (Figure 6.19a - b). Additionally, the similarities in the groundmass compositions of the Mangaehuehu and Makotuku members samples, including immobile REE patterns, suggest a common initial melt for all samples, inferring that the processes leading to magmatic differentiation observed in the Waitonga and Turoa members melts (Figure 6.2b) occur within the crust due to crystal fractionation and crustal assimilation at variable depths, pressures and temperatures (Figure 6.19c). Differentiation recorded in

whole rock compositions is largely controlled by crystal accumulation, which itself is determined by interactions between the melts and previously emplaced crystalline bodies within the crust (e.g., D'Mello et al., 2023; Lormand et al., 2021; Zellmer et al., 2021; Zellmer et al., 2024). These crystalline bodies were affected by various mafic injections (i.e., MgO-rich or more primitive) reflected in the variations in Mg#, Cr and An# contents of the crystal cargo (Figure 6.19d – f), that account for the interaction between felsic magma storage in the crust and hot mafic recharges (Conway et al., 2018; Nakagawa et al., 2002).

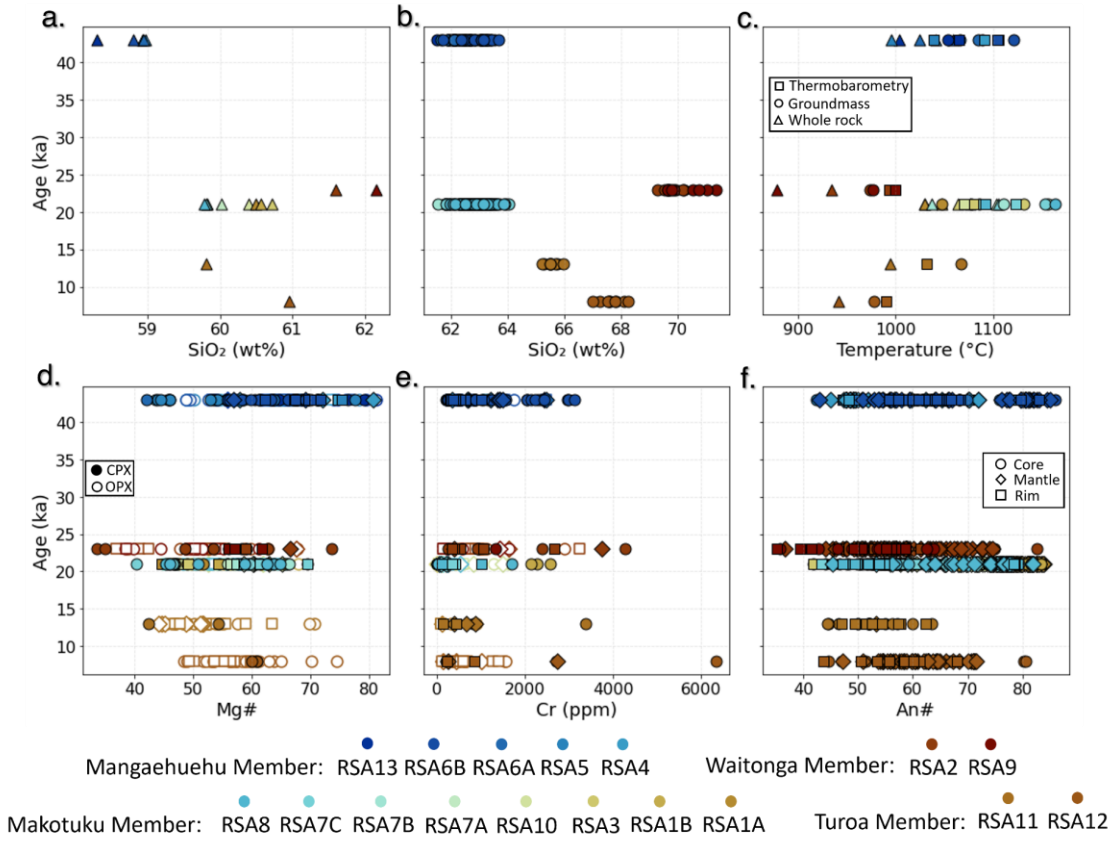

Figure 6.19. Magma evolution in terms of age. a. SiO_2 contents in whole rock compositions. b. SiO_2 contents in groundmass compositions. c. Temperature. The temperatures used are the maximum ones determined by thermobarometry (squares), and MELTS modelling of whole rock (triangles), and groundmass (circles) compositions. d. Magnesium number (Mg#) in clinopyroxenes (CPX -filled) and orthopyroxenes (OPX -outlined) in core (circles), mantle (diamonds) and rim (squares). e. Cr in pyroxene using the same conventions as in panel d. f. Anorthite content (An#) in plagioclase core (circles), mantle (diamonds) and rim (squares). The ages used are averages of those reported in Conway (2016) for the Mangaehuehu, Waitonga and Makotuku members and in Doll (2025) for the Turoa Cascades, and Mangatururu North flows of the Turoa Member.

Based on our high-resolution data from the crystal cargo and the carrier melts, we infer a plumbing system model for <50 ka lava flows at Mount Ruapehu. First, based on the

groundmass compositions and the difference in ages (i.e., ~20 ka) between the Mangaehuehu and Makotuku members, we infer a common origin of the melts at Mount Ruapehu between ~50 – 15 ka. These andesitic-dacitic melts are generated by mixing mantle-derived mafic and crustal-derived silicic melts (Cocker et al., 2022; Shane et al., 2019). The mantle melts are likely contaminated by subducting sediments, tectonically eroded material from the crust and fragments of the Hikurangi Plateau (Corella Santa Cruz et al., 2023; Waight et al., 2017), and likely produced by adiabatic melting due to low magmatic water contents (< 2.5 wt% in Table 6.2 & Auer et al., 2016; Kilgour et al., 2013) while still maintaining trace elements patterns linked to flux-melting of the mantle as typical of arcs (Turner & Langmuir, 2022). Future isotopic analyses and crustal assimilation modelling should further assess the contributions to melt generation from distinct sources.

We argue that these melts ascended through the crust and stagnated, allowing crystals to grow, forming high crystalline bodies. These bodies are repeatedly affected by mafic injections (i.e., multiple Cr rings in pyroxenes), from at least two different primitive mafic end members: basalt (Makotuku, Waitonga and Turoa members) and MgO enriched basalt (Mangaehuehu Member), which follow different paths of ascent. Later, another andesitic-dacitic melt batch interacts with these highly crystalline bodies, dragging crystal clots (i.e., glomerocrysts) that are disaggregated to form a notable portion of the crystal cargo (e.g., Shane et al., 2019; Zellmer & Iizuka, 2025). This agrees with previous interpretations regarding the interaction of felsic magmas with mafic injections, and the posterior incorporation of the crystals in the carrier melt (e.g., Conway et al., 2018; Kilgour et al., 2013; Nakagawa et al., 2002; Stewart, 2010). Lastly, these carrier melts may undergo further differentiation within the crust by crystal fractionation and/or assimilation of the basement rocks (e.g., Conway et al., 2018; Gamble et al., 1999; Price et al., 2012). However, the lack of melt-crystal equilibrium and the small sizes (i.e., <20μm) of the autocrysts (e.g.,

decompression inhibites orthopyroxene growth/ nucleation in Martel & Schmidt, 2003) imply that these magmas spend limited time within the crust.

One of the most notable characteristics of Mount Ruapehu is the emplacement of units with different geochemical signatures in close proximity and within the same period, pointing to the complexity of the plumbing system (e.g., low-MgO Andesite of Ngahuinga & high-MgO dacite of Te Kohatu members in Conway, 2016; Conway et al., 2018). Meanwhile, the relatively small size of the phenocrysts is at odds with the development of large, mush reservoirs commonly observed in arc magmas (e.g., Cashman et al., 2017; Dufek et al., 2022; Humphreys et al., 2006). The most plausible explanation for these features is the emplacement of the crystalline bodies in dike-like structures. Dikes will allow different mafic compositions (i.e., basalt and MgO enriched basalt) to affect adjacent bodies, without interacting with each other. Dykes may also lead to crystallization of relatively small crystals (i.e., microphenocrysts <500 μm in length; Zellmer, 2021) rather than larger phenocrysts typical of arc volcanoes (e.g., Cashman & McConnell, 2005; Castro & Dingwell, 2009; Neave, 2020). Additionally, it has been recognized that in rift zones, including the TVZ, diking contributes to the extension of the graben by favoring the transport of magma (e.g., Gómez-Vasconcelos et al., 2017; Keir et al., 2025; Wong et al., 2025). Moreover, dikes have been linked to magmatic differentiation, facilitating magma mobility or causing magma stalling (e.g., Piquer et al., 2023), reactivating previously emplaced bodies by recapture of newly formed dikes (e.g., Thiele et al., 2021), and causing different levels of the partial melting of host rocks (e.g., Loncar & Huppert, 2022), which explain the differences in the REE content between units (i.e., Turoa and Waitonga members slightly higher REE content compared to Mangaehuehu and Makotuku; Figure 6.5b). The rifting process would also explain the unusual occurrence of hot magmas seen in Mount Ruapehu samples (990 - 1123 °C in Table 6.2; 878 - 1163 °C in Table 6.8; and 1010 - 1130 °C in Lormand et al., 2020) and

the predominance of adiabatic melting over fluxing (e.g., Li et al., 2025; Rychert et al., 2012; Schmeling, 2010; Sola et al., 2025).

We present a schematic representation of our interpretation of the plumbing system (Figure 6.20) in which melt transport is channeled via diking through previously emplaced crystalline bodies, picking up crystals. The dikes make magmatic highways where melts can travel rapidly, creating temporary magma accumulation zones at different depths within the crust (i.e., Mangaehuehu Member: 5 – 13 km; Makotuku Member: 9 – 22 km; Waitonga Member: 4 – 10 km; Turoa Member: 5 – 12 km) for crystal fractionation and/or crustal assimilation before eruption. Inferred crystallization depths coincide with previous studies that locate volcanic earthquakes hypocenters (i.e., 10–16 km in Hurst & McGinty, 1999) and low velocity zones (i.e., ~4-12 km in Hill et al., 2015; Leonard et al., 2021; Rowland et al., 2010; Rowlands et al., 2005) under Mount Ruapehu.

6.6 Conclusions

The relatively small but compositionally complex crystal cargo at Mount Ruapehu <50 ka lava flows is mostly out of equilibrium with carrier melts, suggesting recycling during magma ascent through dikes that transect previous storage regions. These could be former plutonic bodies within the crust that re-equilibrate with ascending melts where limited growth of new crystals occurs (i.e., small autocrystic microlites <20 μm) before eruption. In the rock groundmass, microlite morphologies indicate decompression induced crystallization, whilst Fe-oxides nanolites are likely formed by rapid cooling due to lava/ice interaction.

The inferred mid-crustal plutonic bodies received multiple primitive mafic injections including basaltic and MgO-rich basaltic liquids, that produced diverse geochemical signatures as observed in the Mangaehuehu and Makotuku members. Differences in bulk

rock MgO - SiO_2 between samples are not apparent in groundmass data and are linked to incorporation of cumulate crystals. Hence, we interpret that the high-magnesium andesites of the Mangaehuehu Member were formed by the entrainment of mafic crystals into ascending melts that are equivalent to the low-MgO, aphyric bulk rock samples.

Melt source and differentiation processes between ~50 – 15 ka at Mount Ruapehu (NZ) were relatively uniform based in the similarities in groundmass compositions across all samples. We identified arc flux melting together with adiabatic melting that may explain the unusually dry and hot Mount Ruapehu magmas. Changes in the composition of the carrier melts are consistent with crustal differentiation at depths between 4 – 22 km. We conclude that the rifting dynamics at Mount Ruapehu may facilitate complex magma sourcing as well as magma transport and reinjection through diking, favoring crystal recycling and variable crystal fractionation and crustal assimilation.

6.7 Acknowledgments

GFZ acknowledges the 2022 Endeavour Fund – Smart Ideas project “Robust volcanic eruption forecasts: leveraging magmatic speedometry into geophysical monitoring” of the Ministry of Business, Innovation & Employment (MBIE) of New Zealand (MAUX2202), which funded the present work, and the Department of Conservation of New Zealand for providing the sampling authorization to collect fresh samples from Mount Ruapehu (97663-GEO). This study received financial support from Grants-in-aid for Scientific Research in Japan to SO (Nos. 22H00161). GK is supported by the New Zealand Ministry of Business, Innovation and Employment (MBIE) through the Hazards and Risk Management Programme (Strategic Science Investment Fund, contract CO5X1702). TU is supported by the Australian Research Council (ARC Future Fellowship FT230100230).

6.8 Data availability statement

The data that supports the findings of this article is available in the article, appendices and online repositories (See Appendix 3).

Figure 6.20. Model of the plumbing system under Mount Ruapehu (Next page). The plumbing system seems to be composed of a series of dikes and crystalline bodies, some of which may be fully crystallized. The dikes may experience frequent reinjections that reactivate them, generating magma accumulation zones at variable depth (~4 – 22 km). In this model are represented previously closely emplaced bodies, affected by injections of a primitive end member (right) and a high-MgO end member (left), that are crossed by dikes dragging crystal clots not only from these bodies but also from the dike itself. Likewise, the magma accumulation zones in which further crystal fractionation and crustal assimilation occur, are represented for each unit based on the maximum and minimum depths calculated for the samples in Table 6.8, indicating average temperature (T) and pressure (P). The back-scattered images insets represent crystals that were dragged by the ascending melts: a. Xenocrysts of plagioclase and orthopyroxene with Fe-oxides symplectite textures (Figure 6.9). These are meta-igneous restites product of the partial melting of the Torlesse Terrain greywackes (left) and fragments of mafic bodies (olivine cores) emplaced in the base of the crust picked up and affected for magma injections (right). b. Pyroxenes with high magnesium numbers (Mg#) rims and plagioclase with inverse zoning most likely related to a high-MgO end member mafic injection. c. Pyroxene and plagioclase glomerocrysts, orthopyroxene, clinopyroxene and plagioclase showing zonation, patchy cores and coarse sieve texture, probably dragged from a previously emplaced crystalline body. d – g. Autocrystic microlite. d. Mangaehuehu Member. e. Makotuku Member. f. Waitonga Member. g. Turoa Member. The size of the features is not on a scale. The shape and direction of the features is used to provide graphic representation of the data but does not represent the actual structure of the system since the model is limited to geochemical analyses. Toponyms in the profile (i.e., Crater Lake, Summit Plateau, Tahurangi and Girdlestone Peak) represent reference points of the inferred vents in literature for each unit (Leonard et al., 2021; Townsend et al., 2017; Cassidy et al., 2009).

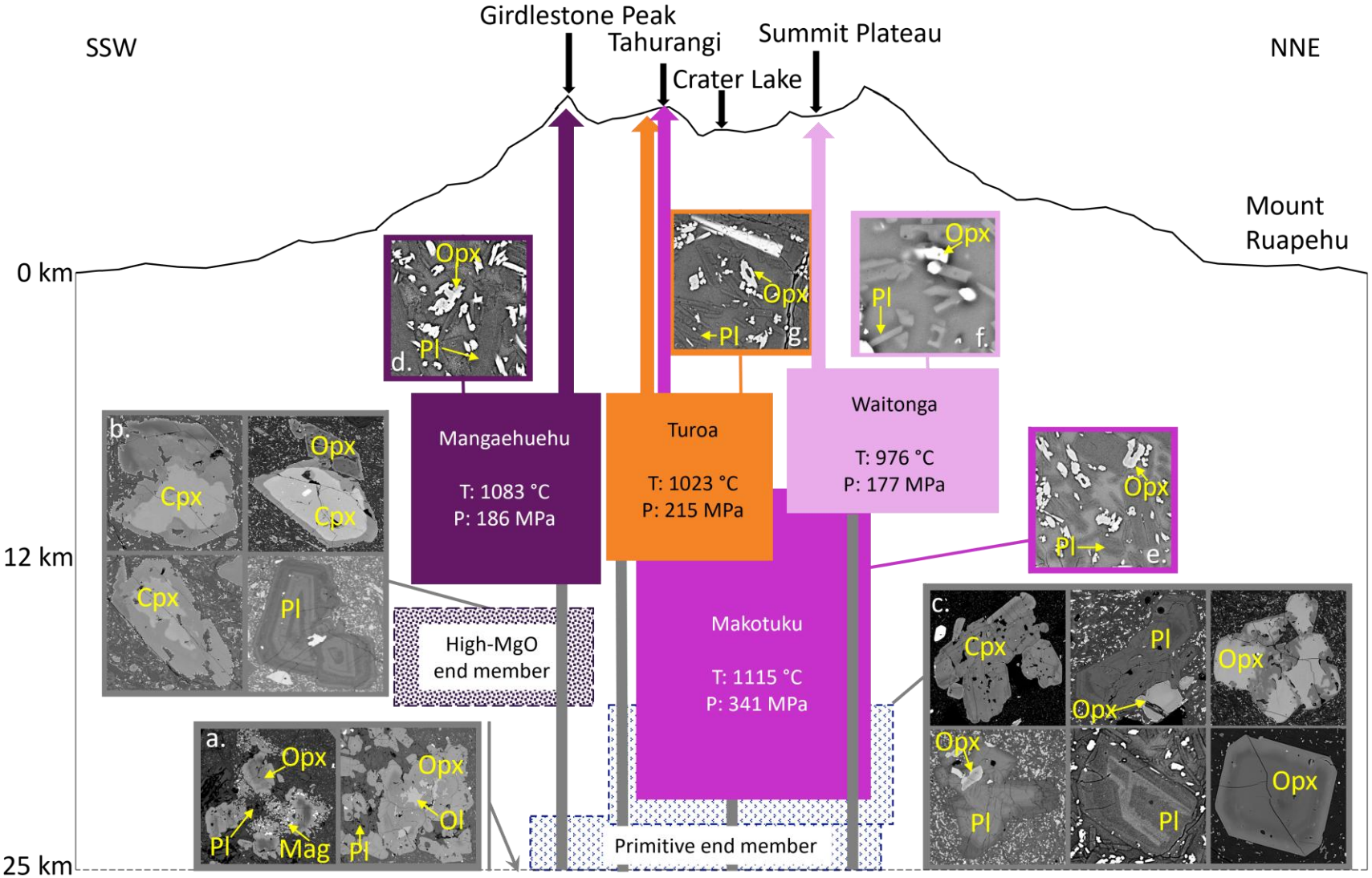
SSW
Girdlestone Peak
Tahurangi
Crater Lake
Summit Plateau
NNE
Mount
Ruapehu
0 km
12 km
25 km
Mangaehuehu
T: 1083 °C
P: 186 MPa
Turoa
T: 1023 °C
P: 215 MPa
Waitonga
T: 976 °C
P: 177 MPa
Makotuku
T: 1115 °C
P: 341 MPa
High-MgO
end member
Primitive end member
a.
b.
c.
d.
e.
f.
g.
Opx
Cpx
Pl
Mag
Ol

Chapter 7 Summary and Synthesis

This thesis investigates crystal residence times, magma ascent rates, and the P-T-H_2O-X conditions of the melts that produced voluminous lava flows at Mount Ruapehu. Previous studies on TgVC tephra revealed relatively short crystal resident times, fast magma ascent rates and an antecrystic origin of the crystal cargo (Lormand, 2020; Lormand et al., 2020; Lormand et al., 2021). This study explores whether effusive eruptions share similar conditions to those of the explosive ones to better understand the plumbing system at Mount Ruapehu.

In this chapter, the main findings from chapters 4 to 6 are first summarised (in Sections 7.1 to 7.3) before a synthesis section (Section 7.4) that summarises the findings the context of Mount Ruapehu's plumbing system.

7.1 Influence of the aspect ratios in the CSD slope determination

In Chapter 4, pyroxene 2D-CSD slopes obtained using three different aspect ratios were compared to those obtained from 3D-CSD to assess the influence of the aspect ratio calculation, and the slope equivalence between 2D and 3D-CSD data, which is crucial for calculation of residence times. Three key findings were identified in this article, related to the estimation method for the aspect ratio, the impact of this in the CSD slopes and its influence in the calculation of the residence times.

7.1.1 Key results

To determine the influence of the aspect ratio in 2D-CSDs, three aspect ratios were tested; two determined using the databases CSDSlice (2Dc) and ShapeCalc (2Ds); and one obtained

from the average aspect ratio of the 3D measurements (3Da) from the direct measurements of short (*S*), intermediate (*I*) and long (*L*) axes (Figure 4.3b). The aspect ratios determined using the data bases differed from each other and from the 3D average, showing the variability of the statistical calculations for each model (Figure 4.3b). These differences in the aspect ratio are reflected in the *L*-axis plots, which were sensitive to changes on the *I*/*L* aspect ratio (Figure 4.4a). The *L*-axis is calculated by CSDCorrections (Higgins, 2000) using the user-provided aspect ratios and dataset through stereological correction. However, if the database used to determine the crystal shape under- or overestimates the *I*/*L* ratio, the *L*-plot will be displaced compared to a 3D-CSD *L*-plot as observed in Figure 4.4a (e.g., 3D versus 2Ds). Furthermore, this miscalculation of the *L*-axis, directly affects the CSD slope. In our case ShapeCalc (2Ds) underestimated the *I*/*L* ratio producing a gentler slope compared to the 2D-CSDs determine using aspect ratios from CSDSlice (2Dc) and 3D average ratio (3Da), and the 3D-CSD (3D) (Figure 4.4b). The slope uncertainty, partially derived from the shape determination method, propagates to the crystal residence times calculation, increasing the residence time uncertainty in ±1 h, creating differences >10 h between the residence times calculated using 3D-CSD and 2D-CSD slopes (Table 4.4; Figure 4.5a). However, for crystal residence times, the uncertainty derived from the slopes calculation seems negligible compared to that of the growth rate, which causes the overlapping of the residence times (Figure 4.5b).

7.1.2 Methodological implications

In this study the *L*-axis sizes determined by CSDCorrections (i.e., stereological correction) suggest that of the two shape determination methods, CSDSlice performed a better calculation of the *I*/*L* ratio compared to the 3D average (Figure 4.4a). However, the use of 3D data avoids the stereological and statistical limitations, providing a more robust estimate of

CSD distribution. The variability of the shape calculation performed by databases such as CSDSlice and ShapeCalc (Figure 4.3b) suggest that 3D data should be used if available.

7.2 Crystal residence times and ascent rates

Chapter 5 determined the crystal residence times and magma ascent rates for the lavas, based on the 3D-CSD method developed in Chapter 4 and hygrothermobarometry. These residence times and ascent rates exhibited similar values to those of the TgVC tephras in Lormand et al. (2020), raising a question on drivers of explosive versus effusive eruptions at Mount Ruapehu. Our inference is that the shift between effusive and explosive is determined by the geometry of the shallow conduit, and that the crustal transport follows similar patterns regardless of the eruptive style.

7.2.1 Residence times

Crystal residence times (τ) for pyroxenes were calculated using equation 68 in Marsh (1988), using the slopes were derived from the 10 – 20 μm interval on 3D-CSD L-plot, and a reference growth rate of 1.80×10^{-11} m/s from Lormand (2020) calculated for the tephra of the Mangatawai Formation from Ngauruhoe volcano, used as an analogue within the TgVC. Additionally, to broaden the scope, a growth range based on experimental data in Shea & Hammer (2013) of 1×10^{-9} to 1×10^{-12} m/s was also applied.

The slope interval was applied to exclude the effects of crystal coarsening, defined as downturns ~5 μm (Figure 5.8a), and aggregation, characterized by changes in the slope ~20 μm (i.e., flatter slopes in Figure 5.8e), avoiding at the same time the recycled crystal cargo (e.g., crystals showing chemical disequilibrium textures such as resorption surfaces and zonation in Figure 6.7f). This interval includes the bulk of the microlite crystals analysed

(i.e., bins with the higher number of crystals), implying limited grow during ascent due to rapid decompression (Brugger & Hammer, 2010a, b; Matsumoto & Geshi, 2021).

The calculated residence times (up to 66 days) are consistent with other volcanoes (e.g., Metcalfe et al., 2021a, b), yet faster compared to volcanoes where a crystal mush has been identified (e.g., Polo-Sánchez et al., 2023; Rout et al., 2021). This indicates these magmas were unlikely to have been fed directly out of a mush. The timescales may therefore be representative of the final magma transport and re-equilibration within the crust before eruption (e.g., Mutch et al., 2019). Moreover, using the reference growth rate of the Mangatawai Formation, residence times drop to ~3 days, which is similar to estimates for explosive eruptions (i.e., 3±1 days in Lormand et al. 2020) (Figure 7.1). This similarity in residence times can be explained by comparable CSDs slopes (Figure 5.9a), and crystal shapes (Figure 5.3) that coincide with Lormand et al. (2020) observations, showing no significant variations in the microlite CSD shapes related to the eruptive style, indicating similar transport processes in the deeper conduits within the crust.

Similar crystal morphologies across eruption styles suggest consistent undercooling rates (e.g., Agostini et al., 2013; Shea & Hammer, 2013). The predominance of small crystals implies large to moderate undercooling rates (Sen, 2014). However, while undercooling for the tephras has been linked to the rapid heat loss during ascent through narrow dikes (Lormand, 2020; Lormand et al., 2020), it is consistent with decompression-induced crystallization (e.g., Frey & Lange, 2011; Noguchi et al., 2006) in the case of the lavas.

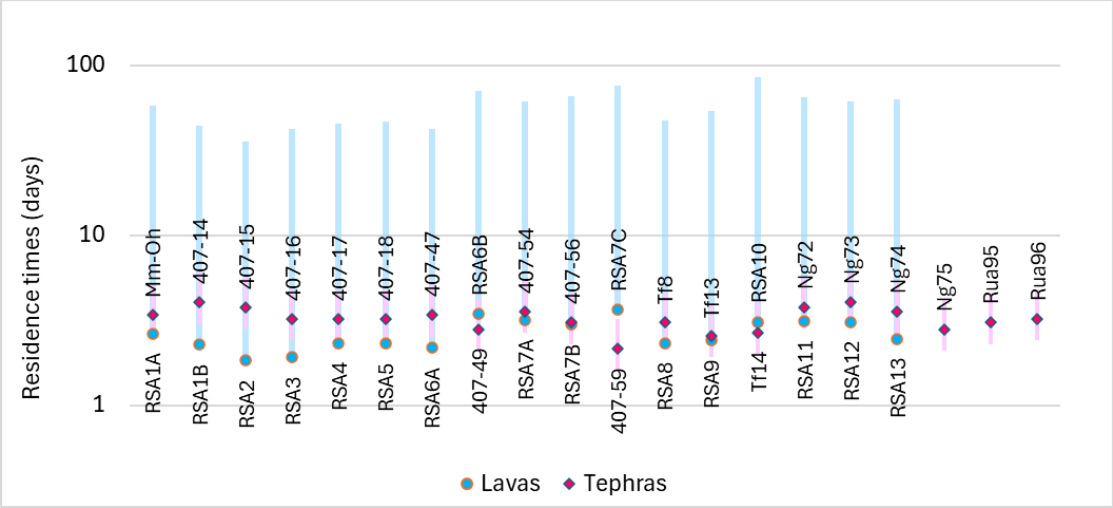

Figure 7.1. Magma residence times from TgVC tephra and Mount Ruapehu lava. The bars represent the error associated with the growth rate in tephra (i.e., $1.80 \pm 0.60 \times 10^{-11}$ m/s in Lormand, 2020), and the range of τ estimated using the growth rate range for each individual sample in lavas (Table 5.9). TgVC tephra data (diamonds) from Lormand (2020), and lava data (circles) in this study.

7.2.2 Ascent rates

Ascent rates were calculated using the maximum reservoir depths (5 and 22 km) based on geobarometry, and the crystal residence times following Armienti et al. (2012). Despite the known uncertainties in barometric calculation (Humphreys et al., 2016; Wieser et al., 2023a), the depths derived from these calculations broadly align with the volcanic earthquake hypocenter (i.e., 10–16 km in Hurst & McGinty, 1999), zones of magma accumulation (i.e., ~4-12 km Hill et al., 2015; Leonard et al., 2021; Rowland et al., 2010; Rowlands et al., 2005), and pressure-based depth calculations in other studies (~2 - 9 km in Kilgour et al., 2013; <16.5 km in Lormand et al., 2020), particularly when the results are discriminated per geological unit (i.e., Mangaehuehu Member: 5 – 7 km; Makotuku Member: 9 – 22 km; Waitonga Member: 5 – 10 km; Turoa Member: 6 – 13 km - Table 5.8).

The resulting calculated ascent rates reached up to 9m/s which are considered fast for effusive eruptions (e.g., Mutch et al., 2019; Phillips & Till, 2021; Ruprecht & Plank, 2013). More realistic ascent rates from 0.02 - 0.08 m/s, were obtained using the residence time

calculated with the reference growth rate (i.e., 1.80×10^{-11} m/s in Lormand, 2020). These ascent rates are similar to those of the tephras (i.e., 0.02 - 0.09 m/s in Lormand et al., 2020), are still fast for effusive eruptions, suggesting that a combination of the conduit geometry and shallow gas exsolution drive the transitions in eruptive style (e.g., Lormand et al., 2020).

7.3 Melt composition and crystal cargo origin

Chapter 6 examined whole rock, carrier melt and crystal compositions of the lavas, revealing the interaction between intermediate melts (i.e., transitional andesite-dacite) with crustal crystalline bodies affected by mafic recharges of at least two primitive end members with differences in MgO content. MELTS modelling further constrained P-T-X conditions and supported the antecrystic origin of the crystal cargo, discussed in the following section.

7.3.1 Whole rock and melt compositions

Mangaehuehu Member whole rock compositions show lower silica and alkalis contents (Figure 7.2a), with higher MgO (Figure 6.3d), while their groundmass compositions match the transitional andesite-dacite melts of the Makotuku Member (Figure 7.2b), indicating a shared melt origin for the lava flows emplaced on the south-west flank of Mount Ruapehu between 47 and 16 ka. These melts did not go through significant differentiation processes within the crust compared to the Waitonga and Turoa members which have rhyolite and dacite compositions respectively, due to further differentiation (Figure 7.2b).

These transitional andesite-dacite melts ascended through the crust, incorporating crystals from previously emplaced crystalline bodies. This processes influenced the whole rock compositions (Figure 7.2), as evidenced by the lack of crystal-melt equilibrium (Figure 6.14) and the complex textures found in phenocryst and antecrystic microlites (Figure 6.7), also observed previously at the volcano (e.g., Conway, 2016; Graham & Hackett, 1987). The

small size of the autocrystic microlites (Figure 6.6) suggests limited residence times as identified in Chapter 5.

In contrast, Waitonga and Turoa members samples exhibit elevated trace elements and REE patterns, indicating crustal assimilation (e.g., Conway et al., 2018; Price et al., 2012; Waight et al., 1999). These likely represent evolved versions of the transitional andesite-dacite melts, modified by crustal assimilation and crystal fractionation (e.g., Conway et al., 2018; Price et al., 2005; Price et al., 2012; Waight et al., 1999).

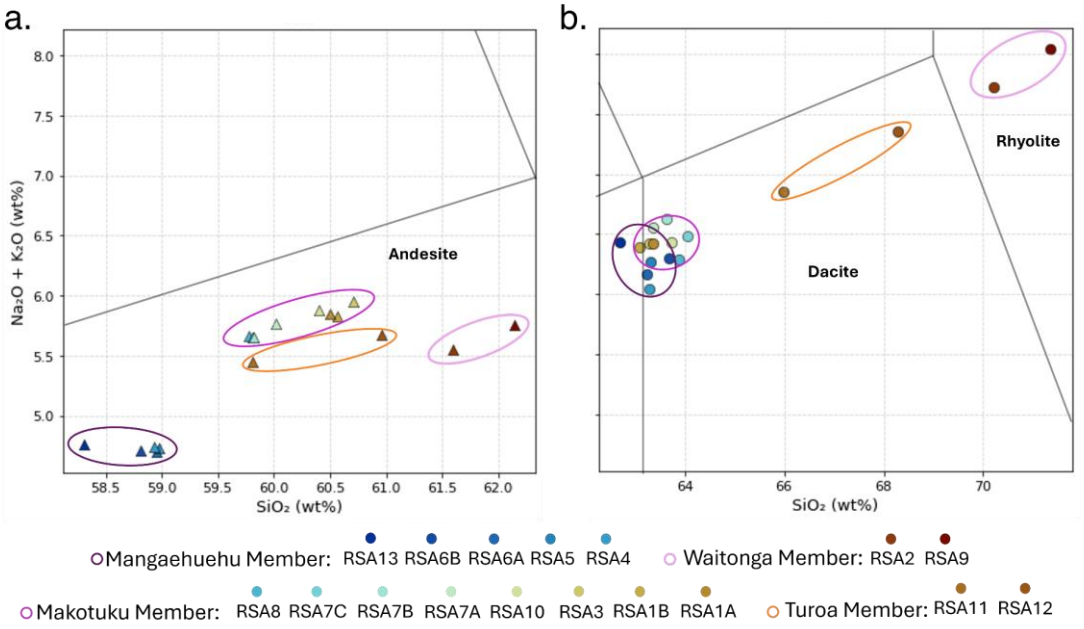

Figure 7.2. TAS diagram for lava samples of Mount Ruapehu.a. XRF whole rock composition (triangles). b. LA-ICMS groundmass average composition (circles). Group A: red circle. Group B: blue circle. Group C: purple circle. Note how the groundmass compositions of groups A and B overlap with each other while the whole rock compositions are separated.

The REE behaviour shown here aligns with other TVZ samples (e.g., Conway, 2016), and has been linked to basement assimilation, sediment recycling and/or tectonic erosion of the Hikurangi plateau (Conway et al., 2018; Corella Santa Cruz et al., 2023; Gamble et al., 1996; Timm et al., 2014; Waight et al., 2017).

7.3.2 Mafic recharges

Lavas emplaced at Mount Ruapehu between 50 and 36 ka show two distinctive MgO trends (Conway, 2016; Conway et al., 2018; Townsend et al., 2017). Despite sharing the same melt compositions (i.e., andesite-dacite), Mangaehuehu (47 – 40 ka) and Makotuku (24 – 16 ka) members show the behaviour of the high-MgO and low-MgO trends respectively, indicating that the crystal cargo controls these trends.

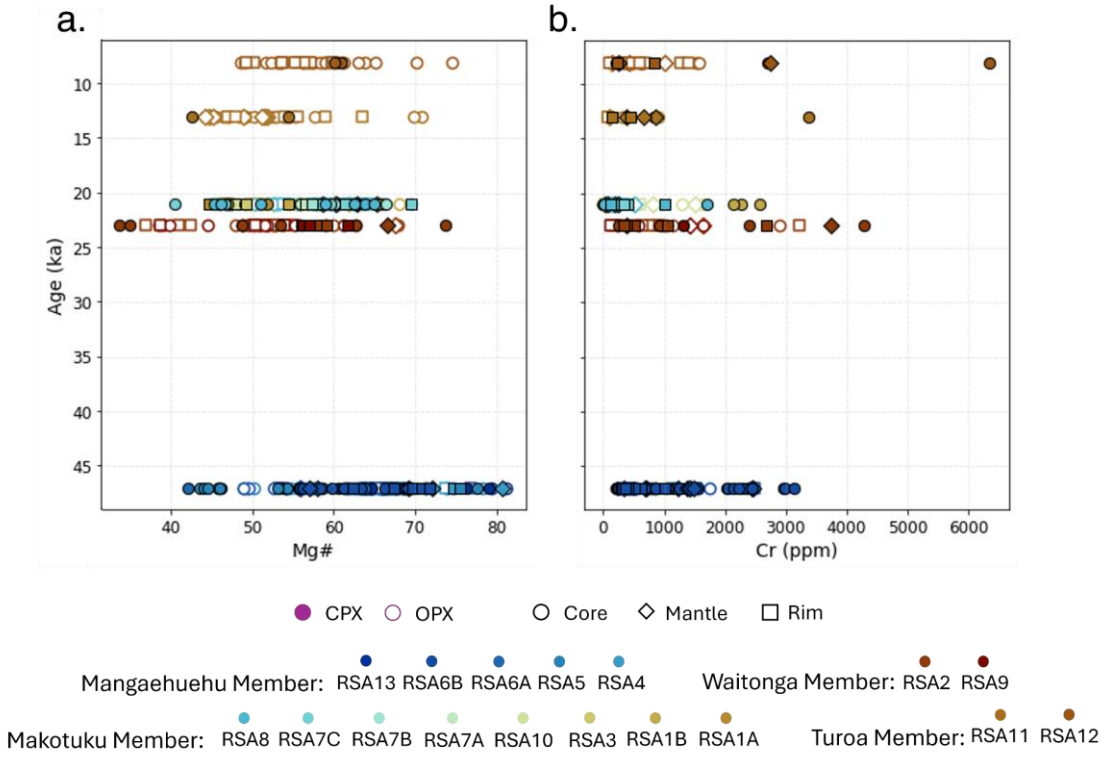

Figure 7.3. Magnesium number (Mg#) and Cr content in pyroxene crystals versus age.a. Mg#. Note how the Mg# in the Mangaehuehu Member samples (HMAs) reaches higher numbers, and most of the crystals with high Mg# are core and mantle measurements. b. Cr (ppm). Note the cores and mantles with high Cr concentrations in samples from Makotuku, Waitonga and Turoa (i.e., <25ka), these are assumed to be recycled crystals. The ages used are those of the assigned members and flows in Chapter 6.

The Mangaehuehu Member lavas are high-magnesian andesites (HMA), where the crystal cargo is the product of the interaction between hot high-MgO mafic recharges and felsic crystalline bodies within the crust (Conway et al., 2018; Nakagawa et al., 2002). This

interaction is observed in pyroxene crystals exhibiting inverse zoning (i.e., MgO enriched rims) and high Cr zonation (Cr rings in Figure 6.12c - d) indicators of mafic injections. Additionally, glomerocrysts and mechanically broken crystals further support interaction between carrier melts and highly crystalline bodies (Figures 6.7 & 6.8). The pyroxene crystals of the Mangaehuehu Member show a direct correlation between the Mg# of enstatites and augites (Table 6.7) and whole rock MgO compositions of the Mangaehuehu Member (Table 6.3) indicating a compositional control by crystal accumulation.

Similar features in the Makotuku, Waitonga and Turoa member samples (i.e., inverse zonation and Cr rings in Figures 6.12a – b & 6.12e) suggest comparable processes, where the mafic recharge was not enriched in MgO. Thus, pyroxenes with high Mg# and Cr in cores/mantles, within these samples represent recycled crystals (Figure 7.3). These trends support the interpretation of two mafic end members: an MgO-enriched basaltic primitive melt, linked to the source of the Waimarino basalt, and another basaltic primitive melt, similar to the one that sourced the Kakuki basalt (e.g., Conway, 2016).

7.3.3 Antecrystic origin of the crystal cargo

While microlites are typically considered melt-grown due to their smaller size (Zellmer, 2021), some microlites in this study show disequilibrium textures (i.e., zonation and wavy surfaces) alongside mechanically induced features (i.e., fractures and glomerocrysts) associated with re-equilibration processes and crystal recycling (e.g., Renjith, 2014; Streck, 2008; Viccaro et al., 2010) across all samples.

Hence, while small crystals (<30 μm) were grown from the melt (i.e., nanolites and autocrystic microlites in Figure 6.6), the larger ones were entrained by the melts during ascent (i.e., phenocryst and the antecrystic microlites in Figure 6.7). This is supported by the (mostly) out of equilibrium mineral assemblage (i.e., plagioclase, pyroxenes and Fe-oxides;

Figure 6.14), suggesting that these recycled crystals are transported by aphyric melts in constant motion, interacting with previously emplaced crystalline bodies (e.g., Auer et al., 2016; Kilgour et al., 2013).

While most of the previous studies linked the presence of antecrysts to the disaggregation of crustal mushes based on the studies of phenocrysts (e.g., Conway, 2016; Coote & Shane, 2016; Kilgour et al., 2013; Stewart, 2010). Lormand et al. (2021) identify antecrystic microlites in the TgVC tephra, that seem to be sourced from solidified subvolcanic intrusive bodies in dike-like structures. The existence of dike-like structures provides a plausible explanation to the proximity different geochemical compositions (e.g., Ngahuinga & Te Kohatu members, with differnt MgO trends emplaced in the northwest flank of Ruapehu in Townsend et al., 2017). Additionally, the presence of solidified intrusive bodies coincides with the observations made in other arc volcanoes by Zellmer et al. (2024). The results in this study provide evidence consistent with the hypothesis of a transcrustal plutonic system, in which subordinated magma accumulation and crystal-melt mixing replace the magma mixing typical of the canonical transcrustal magmatic systems (Zellmer et al., 2013; Zellmer et al., 2016b; Zellmer et al., 2024).

7.3.4 Fe-oxide nanolites as indication of rapid cooling against ice

While the pyroxene CSDs indicate changes in the microlite population through coarsening (microlites <5 μm) and aggregation (microlites > 20 μm) of crystals. The crystallization of these seem to be linked to degassing-induced crystallization during ascent at moderate undercooling rates based on the euhedral/swallow tail shapes (Figure 5.5) observed (Shea & Hammer, 2013). Here, some of the smaller plagioclase microlites (< 10 μm) show shapes also linked to moderate undercooling (e.g., hopper and hollow textures in Figure 6.7a), that may confirm the similar undercooling conditions at the onset of eruption.

However, in the case of the Fe-oxide nanolites, their abundance may be related to the emplacement conditions in glaciated areas (Conway, 2016), indicating nucleation-dominated crystallization after eruption (Figure 6.6). The link between the size and amount of nanolites, the location within the flow (i.e., outer or inner part of the flow) and units (i.e., Mangaehuehu, Makotuku, Waitonga or Turoa) of the samples, may reveal that the Fe-oxides are an indication of rapid undercooling due to lava/ice interactions.

Here, the samples emplaced <26 ka (i.e., Waitonga and Turoa members), near the end of the last glacial cycle (~ 30 – 18 ka in Eaves et al., 2016a; Eaves et al., 2016b), have fewer and larger nanolites (e.g., Figure 5.6a – b), implying a slower cooling due to the emplacement conditions than those of the other samples (e.g., Figure 5.6c – e). Additionally, the difference between samples collected at the same spot revealed the changes linked to location of the sample within the flow, where those located in the outermost parts have smaller nanolites (Figure 5.6f) compared to those in inner parts (Figure 5.6e), due to rapid undercooling which hinders crystal growth (e.g., Mujin et al., 2017a, b).

7.3.5 Mafic end member trends

Based on a 1:1 comparison between groundmass and whole rock compositions, it was observed the strong compositional control of the crystal cargo for some units at Mount Ruapehu (Figure 7.2). The Mangaehuehu Member HMAs crystal cargo was originated from a high-MgO end member, while the crystal cargo in Makotuku, Waitonga and Turoa trace back to a most primitive end member (e.g., Waimarino and Kakuki basalts trends in Conway, 2016; Conway et al., 2018; Townsend et al., 2017).

Figure 7.4 shows distinctive trends that complement the previous analyses. The groundmass compositions of the Mangaehuehu Member control silica and alkalis contents (Figure 7.4a & 7.4h – i), while the whole rock controls the Fe, Mg and Ca contents (Figure 7.4e – g),

reflecting the high-MgO mafic derived crystal cargo. On the other hand, the Makotuku Member has Fe and Mg contents closer to equilibrium between groundmass and whole rock (Figure 7.4e – f), although its melt composition is similar to that of the Mangaehuehu Member (Figure 7.2). Lastly, the Waitonga and Turoa members, show groundmass control over the silica and alkalis contents (Figure 7.4a & 7.4h – i), and whole rock control of Ca, Fe and Mg (Figure 7.4e – g), consistent with pyroxene uptake. The Turoa Member samples show differentiation trends in Ti (Figure 7.4c) and Na (Figure 7.4h), indicating crystal fractionation.

The behaviour showed by Makotuku Member samples, where the groundmass and whole rock have similar concentrations of $Fe_2O_3^T$ and MgO, may support a shared primitive melt origin for carrier melts and crystal cargo. Furthermore, the composition of these rocks appears to be following the compositional trend towards the Kakuki basalt (Conway et al., 2018) located North of Taupō and described as the most primitive basalt on the TVZ (Gamble et al., 1993), and hence the melt production in the south and central TVZ may be derived from the same processes.

Here, the differences in whole rock compositions between the Mangaehuehu and Makotuku member samples are determined by localized injections of an MgO-enriched source, while the enrichment in SiO_2 and K_2O showed by the Waitonga and Turoa member sample melts may be linked to further crystal fractionation and assimilation processes. The samples in this study also match the trends observed by Conway (2016) of progressive enrichment in silica and potassium, followed by a reversal around 26 ka. This can be clearly observed by comparing the samples of the Waitonga Member (25 – 21 ka) which is more silicic than those of the younger Turoa Member (15 – 10 ka).

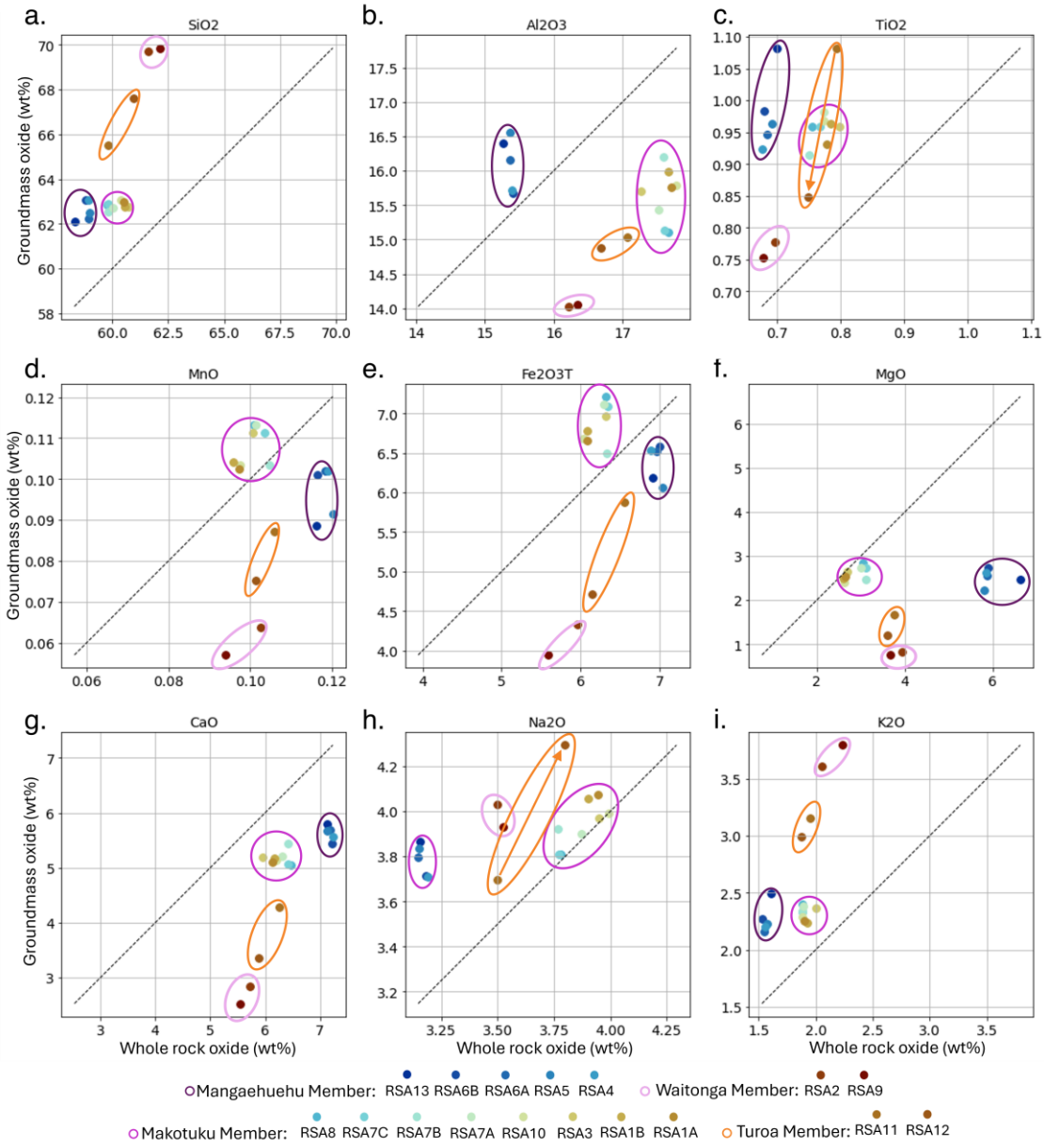

Figure 7.4. Whole rock versus groundmass 1:1 diagram for major element oxides (previous page). The diagram shows the relation of the oxides between whole rock and average groundmass compositions. a. SiO_2. b. Al_2O_3. c.TiO_2. d. MnO. e. Fe_2O_3T. f. MgO. g. CaO. h. Na_2O. i. K_2O. Note how the SiO_2, TiO_2, Na_2O and K_2O are controlled by the groundmass composition, while MgO and CaO are controlled by the whole rock composition (i.e., the crystal compositions). The color scale indicates samples and members. The orange arrows in panels c & h indicate the trend from sample RSA11 to sample RSA12.

7.3.6 Refining the magmatic conditions (MELTS Modelling)

Magmatic conditions were constrained using AlphaMELTS 2.3 (Smith & Asimow, 2005) with initial temperatures and pressures from thermobarometry (Table 6.2), which were used to estimate reservoir depths used in the ascent rate calculations.

Thermobarometers yield consistent temperature (1162 – 882 °C) and pressure (807 – 0 MPa) ranges using plagioclase, orthopyroxene, clinopyroxene and magmatic liquid models (Ágreda-López et al., 2024; Neave & Putirka, 2017; Putirka, 2008; Weber & Blundy, 2024). MELTS modelling, using most mafic groundmass compositions and water contents estimated with Waters & Lange (2015) hygrometer, produced similar results for temperature (1163 – 974 °C) and pressure (547 – 108 MPa) to those of the thermobarometry (Figure 6.17). Furthermore, reservoir depths were confirmed between 4 – 22 km (Figure 7.5a – b). Groundmass data was preferred to liquid modelling due to antecrystic influence on whole rock compositions. Differences between groundmass and whole rock derived models were under 96 °C and 101 MPa, which translates to a difference of up to 4 km in the depth estimates (Figure 7.5).

Crystal compositions were partially modelled using each sample whole rock compositions (Figure 6.18). These trends matched those produced by the modelling of the Ruapehu Group units average compositions from Conway (2016). Crystals with low Mg# and An# were modelled using groundmass compositions (e.g., samples RSA13 & 11 in Figures 6.18a & 6.18l), while some intermediate crystals required other unit compositions (e.g., Whakapapaiti Member - RSA9; Mangaehuehu Member RSA1A in Figures 6.18c & 6.18f – g). Crystals with high Mg# and An# were partially modelled by the compositions of the Waimarino and Kakuki basalts from Gamble et al. (1993), though clinopyroxenes over $Mg\#_{85}$ (e.g., sample RSA13 in Figure 6.18e) exceeded known TVZ compositions, suggesting their origin in the

high-MgO end member. Likewise, pyroxenes under $Mg\#_{65}$ (e.g., Samples RSA2 in Figure 6.18k), likely originated from a rhyolitic end member.

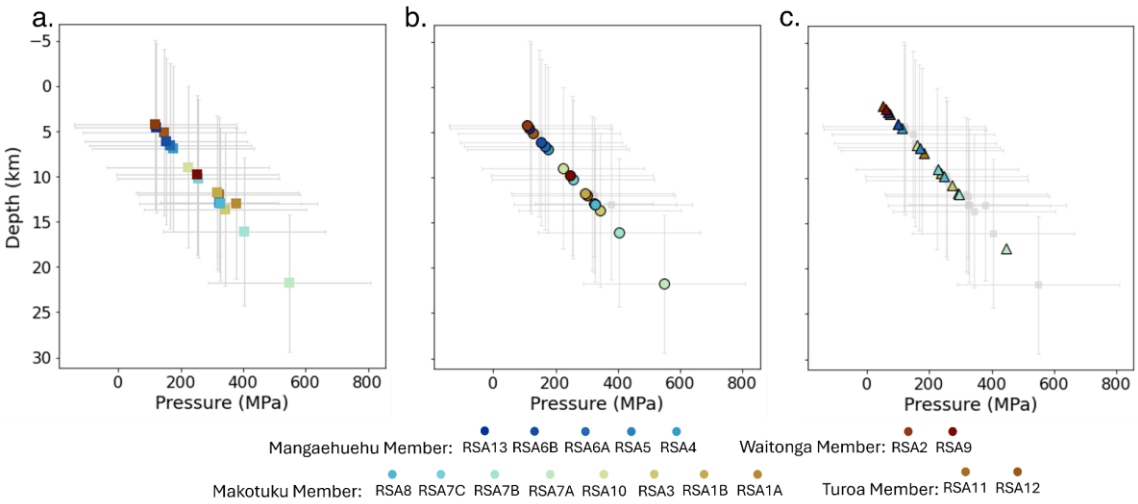

Figure 7.5. Thermobarometry and MELTS modelling pressure versus depth.a. Barometry (squares). b. MELTS modelling of the groundmass compositions (circles). Note how the pressures and depths determined by barometry are similar to those obtained from the modelling of the groundmass. C. MELTS modelling of the whole rock compositions (triangles). The barometry results were drawn in the back (gray) as reference in the groundmass (b) and whole rock (c) panels.

Clinopyroxene compositions were achieved mostly by more mafic rocks than the host in MELTS phase modelling, indicating that crystal-melts equilibrium within 1SEE (23%) may be more realistic than those within 2SEE (Figure 6.15). This supports an antecrystic origin for most crystals, suggesting the entrainment by new ascending hot magma injections (e.g., Coulthard Jr et al., 2024; D'Mello et al., 2023; Lormand et al., 2021; Zellmer et al., 2021).

7.4 Mount Ruapehu's plumbing system

The complex plumbing system identified in Chapter 6 can be used, in conjunction with conclusions from the previous chapters, to better infer and understand the main controls and processes occurring within Mount Ruapehu's pluming system. The magmatic processes are controlled by a dike-dominated transcrustal plumbing system, within an arc-rift tectonic environment.

7.4.1 Transcrustal processes

Most models describe Mount Ruapehu andesites as products of magma mixing, crystal fractionation, and crustal contamination in dynamic multi-level chamber system, with each magma batch having distinct residence times (Conway et al., 2018; Gamble et al., 1999; Kilgour et al., 2013; Lormand et al., 2021; Price et al., 2005; Price et al., 2012; Waight et al., 1999; Waight et al., 2017). Additionally, it has also been proposed that changes in the crustal contamination levels, sediment input to the mantle melts, crystal recycling and magma hybridization are directly responsible for the chemical compositions and signatures found at Mount Ruapehu (Conway et al., 2018; Kilgour et al., 2014; Lormand et al., 2021; Stewart, 2010; Waight et al., 2017).

This study supports those interpretations by adding new data. While inverse zoning and resorption textures in crystals (Figures 6.11 & 6.12) indicate mafic injection into more silicic magmas, the enrichment in REE and trace elements of the Waitonga and Turoa members samples (Figure 6.5) suggest crustal assimilation, and their more silicic groundmass composition reflect further differentiation (Figure 7.2).

The Mangaehuehu and Makotuku members share similar groundmass compositions despite erupting ~20 ka apart, suggesting a steady melt generation process, however, this process remains unresolved. The traditional interpretation of andesitic melt generation by mixing of mafic and silicic melts within the crust (Cocker et al., 2022; Shane et al., 2019; Stewart, 2010; Waight et al., 2017), or even the occurrence of melts generated from a subcrustal source (Corella Santa Cruz et al., 2023; D'Mello et al., 2023) are both possible.

Some of these melts likely underwent further fractionation and assimilation processes within the crust (Gamble et al., 1999; Price et al., 2012; Stewart, 2010; Waight et al., 2017), that lead to the more evolved compositions observed in the Waitonga Member (Figure 6.4). this

can account for a magmatic differentiation between melts emplaced during the same period (i.e., Makotuku and Waitonga members), reflecting longer crustal residence, different paths of ascent and transcrustal processes. The difference in the melts within the Waitonga and Turoa members samples also account for different levels of crustal assimilation (i.e., higher SiO_2 and K_2O in RSA2 & 9) and crystal fractionation (i.e., lower Na_2O in RSA11) (Figure 6.4).

Furthermore, the crystal cargo shows more insights into the transcrustal processes. Phenocrysts and antecrystic microlites show resorption and zoning structures (e.g., Figure 6.7f – g), indicating the interaction of two different magmas (e.g., Auer et al., 2015; Conway et al., 2018; Nakagawa et al., 2002; Price et al., 2012; Shane et al., 2008), before being entrained into the final carrier melt (e.g., Lormand et al., 2021; Stewart, 2010; Waight et al., 2017).

While the antecrystic origin of the crystal cargo is widely recognized, this study highlights their compositional differences that define the whole rock compositions at Mount Ruapehu. This is clearly seen in the comparison of samples in Mangaehuehu and Makotuku members (Figure 7.2b & 7.4). The melts of these members have low MgO contents (2.40 – 2.94 wt%; $Mg\#_{44-48}$), however, the crystal cargo in the Mangaehuehu Member samples shows higher Mg# than those of the Makotuku Member (e.g., OPX $Mg\#_{64}$ versus $Mg\#_{57}$ in Table 6.7).

The Mangaehuehu Member HMAs are interpreted as the product of the interaction between felsic crystal-rich stalled magmas and a high-MgO mafic injection that reactivated the crustal reservoir (Conway, 2016). Although the crystal cargo might be the product of mingling/mixing within the crust, the lavas erupted were the product of the interaction between ascending andesitic-dacitic aphyric melts with a crystalline body affected by the high-MgO injection (e.g., Stewart, 2010). This body may have been fully crystallized before

the interaction (e.g., Lormand et al., 2021; Zellmer et al., 2024), as indicated by the mechanically induced textures observed in the crystals (i.e., glomerocrysts and broken crystals).

On the other hand, while similar process governed the origin of the crystal cargo in the Makotuku, Waitonga and Turoa members, with stalling of magmas and reactivation by mafic injections (i.e., Cr rings and reserve zoning), these injections have their origin in the more primitive end member (i.e., Mg# of the pyroxenes; Figures 6.13 & 7.3a). This reaffirms the idea of at least two mafic primitive end members (i.e., basaltic and MgO-enriched basaltic) contributing to the differentiation of the products of the TVZ, by interacting with stalled magmas.

7.4.2 Dike-dominated plumbing system

Focusing on the plumbing system complexity (Conway et al., 2018; Waight et al., 2017), the geometry of the reservoirs and/or crystalline bodies (Lormand et al., 2021), and the likelihood that these bodies are plutonic instead of magmatic (Coulthard Jr et al., 2024; Zellmer et al., 2024), the possibility of a dike-dominated plumbing system at Mount Ruapehu seems plausible (e.g., Lormand et al., 2020; Lormand et al., 2021).

Geochemical differences in proximal/coeval volcanic units as those mentioned in section 7.3.3 between Ngahuinga and Te Kohatu members (Conway, 2016), or those observed between Makotuku and Turoa members, erupted from closer vents in the Tahurangi area (Conway, 2016), suggest individual magma batches following distinctive paths of ascent through a complex system (e.g., Gamble et al., 1999; Price et al., 2005; Price et al., 2012; Waight et al., 2017).

Piquer et al. (2023) found that magma composition is influenced by the relationship between intrusion direction and fault stress orientation. Favourable stress facilitates ascent of more primitive magmas, while misalignment traps magma, promoting differentiation or full crystallization of the intrusive bodies (Piquer et al., 2023). Hence, these closely spaced variations are easily explained by magmas travelling through nearby dikes that are not connected. Here, magmas with different compositions (e.g., primitive, high-MgO and rhyolitic end members) are stalled in the crust (e.g., Conway et al., 2018; Waight et al., 2017), and only interact with other melts that are transported through pre stablished dikes (e.g., Gómez-Vasconcelos et al., 2017; Thiele et al., 2021) (Figures 5.12 & 6.20).

The rifting process occurring in the TVZ, where magma intrusions through dikes contribute to the extension of the graben (Gómez-Vasconcelos et al., 2017), supports the existence of a dike-dominated plumbing systems. This feature has been observed in other rift systems as the Ethiopian Rift (e.g., Keir et al., 2025), where additionally, rapid transport of magmas through the crust has been linked to dike intrusions (e.g., Wong et al., 2025).

In dike-dominated plumbing systems, magma may crystallize immediately upon emplacement due to heat conduction (e.g., Loncar & Huppert, 2022). This will allow the formation of a plutonic transcrustal system in which most of the subvolcanic dike-like bodies are crystallized (e.g., Zellmer et al., 2021; Zellmer et al., 2024). These dikes reactivate via subsequent injections, which follow pre-existent paths, causing mechanical fracturing and disaggregation of the bodies explaining the presence of glomerocrysts and fractured crystals (e.g., Lormand, 2020; Thiele et al., 2021). Likewise, these injections may also induce significant partial melting of the host rock, explaining REE and trace elements variations observed in some samples (e.g., Loncar & Huppert, 2022).

The complex textures found in the phenocryst reflect a dynamic hybrid magmatic system where mafic and silicic magmas coexist within the crust mingling and/or mixing though repeated recharge events (e.g., Schaaf et al., 2022; Yamasaki, 2022). In plutonic transcrustal systems the existence of mushes is ephemeral and spatially restricted (Zellmer et al., 2024). Hence, in dike-dominated plumbing systems these textures would be the product of constant reactivation of the plutonic bodies through repeated dike re-injection, possibly linked to the active rifting process in the TVZ (Bibby et al., 1995; Seebeck et al., 2014; Villamor et al., 2017; Wilson & Rowland, 2016).

Therefore, it is proposed that aphyric andesitic melts, generated either at subcrustal or crustal levels, ascend through dike-like structures in the crust, interacting with stalled crystal bodies. Here, the interaction between the ascending melts and the crystallized bodies causes fracturing and disaggregation, explaining the presence of antecrysts, xenocrysts, glomerocrysts and fractured crystals (Figures 6.8 & 6.9). These stalled crystalline bodies have undergone repeated mafic injections and recrystallization, as shown by the multiple Cr rings in pyroxenes rims, cores and mantles (Figure 7.3b).

Meanwhile, the aphyric melts experienced varying degrees of differentiation in crustal magma accumulation zones, through crystal fractionation and/or crustal assimilation, as shown by differences in groundmass composition (Figure 7.2b). Where, the enrichment in REE and incompatible trace elements may be related to re-injection derived partial melting (e.g., Loncar & Huppert, 2022). However, these aphyric melts ascend rapidly and do not remain long enough in the crust for significant crystal grow, as confirmed by the size of the autocrystic cargo (i.e., <30 μm).

Figure 7.6 summarizes the plumbing system constrained in Figures 5.12 and 6.20 to provide a general idea of the main features of the plumbing system. This includes information on *T*-*P*-

H_2O pre-eruptive magmatic conditions, timescales of crystal residence and magma ascent rates from Chapters 5 and 6. This model represents the interaction between ascending dikes and previously emplaced crystalline bodies, which are a key factor in the whole rock compositions of the eruptive products, defining the MgO versus SiO_2 trends due to crystal accumulation (See section 7.3.5). The model also presents the tentative magma accumulation zones inferred from the calculated crystallization depths through MELTS modelling of the groundmass compositions (Table 6.8), which have been positioned considering the possible source vents informed in previous studies (e.g., Conway, 2016; Leonard et al., 2021; Townsend et al., 2017).

Figure 7.6. Model of the dike-dominated plumbing system under Mount Ruapehu (Next page). The Mount Ruapehu plumbing system consist of multi-directional dikes and crystalline bodies with variable sizes, that may be fully crystallized, and are reactivated by magma re-injections, creating magma accumulation zones at variable depth (~4 – 22 km; Table 6.8). The diagram is not to scale. The shape, position and direction of the features is used to provide graphic representation of the data but does not represent the actual structure of the system since the model is limited to geochemical analyses. Toponyms in the profile (i.e., Crater Lake, Summit Plateau, Tahurangi and Girdlestone Peak) represent reference points of the inferred vents in literature for each unit (Leonard et al., 2021; Townsend et al., 2017; Cassidy et al., 2009). The ascent rates (v) and crystal residence times (τ) are those calculated using the growth rate of the orthopyroxene of the Mangatawai Formation (Table 5.8). The temperature (T) and pressure (P) are those constrain from MELTS modelling (Table 6.8). The water content was derived from hygrometry calculations in Chapter 5 (Table 5.7). This model is a combination of those presented in Figures 5.12 & 6.

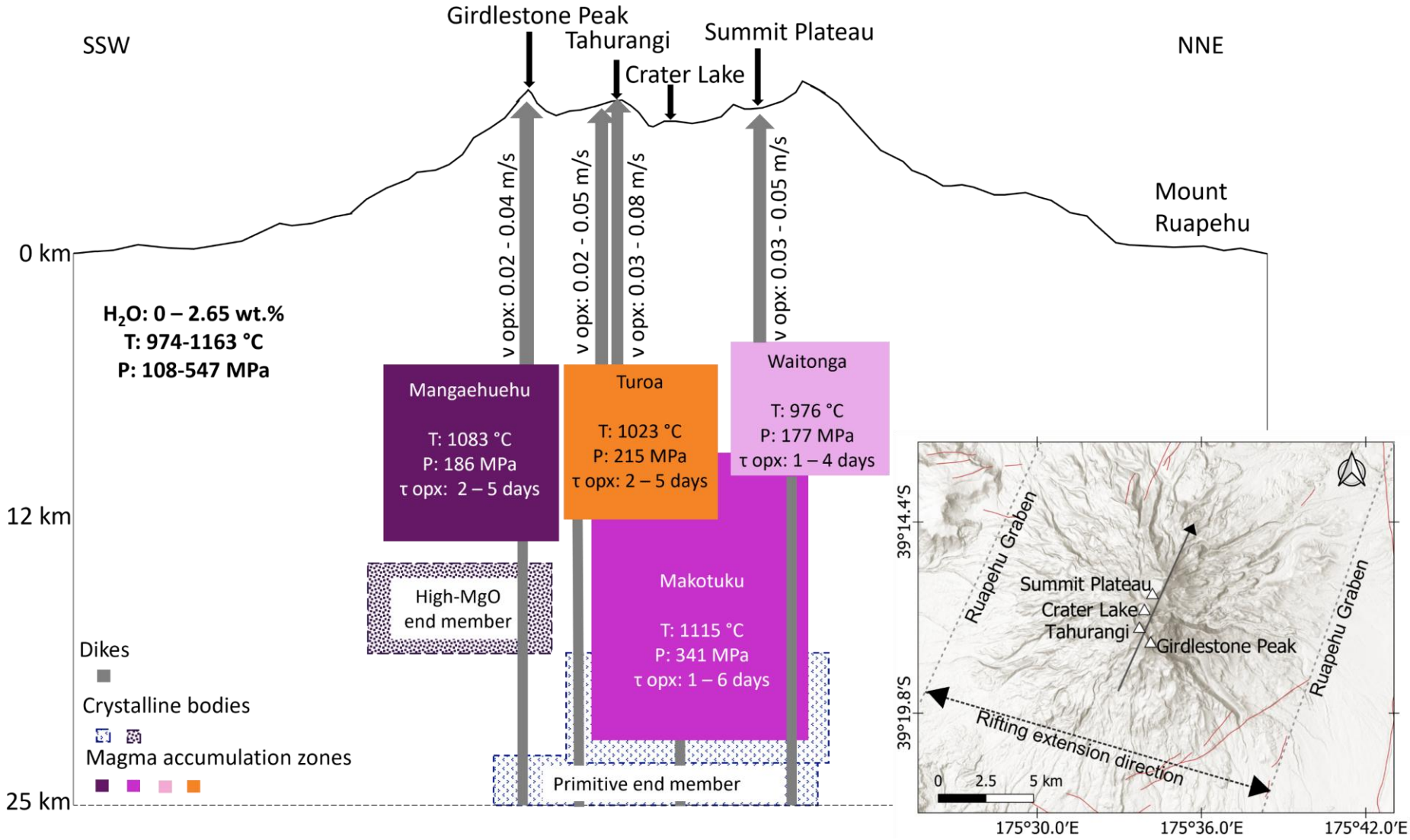
SSW
NNE
Girdlestone Peak
Tahurangi
Crater Lake
Summit Plateau
Mount Ruapehu
0 km
12 km
25 km
H2O: 0 – 2.65 wt.%
T: 974-1163 °C
P: 108-547 MPa
v opx: 0.02 - 0.04 m/s
v opx: 0.02 - 0.05 m/s
v opx: 0.03 - 0.08 m/s
v opx: 0.03 - 0.05 m/s
Mangaehuehu
T: 1083 °C
P: 186 MPa
τ opx: 2 – 5 days
Turoa
T: 1023 °C
P: 215 MPa
τ opx: 2 – 5 days
Waitonga
T: 976 °C
P: 177 MPa
τ opx: 1 – 4 days
Makotuku
T: 1115 °C
P: 341 MPa
τ opx: 1 – 6 days
High-MgO end member
Primitive end member
Dikes
Crystalline bodies
Magma accumulation zones
Ruapehu Graben
Summit Plateau
Crater Lake
Tahurangi
Girdlestone Peak
Rifting extension direction
0 2.5 5 km
39°14.4'S
39°19.8'S
175°30.0'E
175°36.0'E
175°42.0'E

7.4.3 Arc volcano controlled by rifting processes

The TVZ is located in a unique tectonic environment were the arc magmatism derived from the subduction of the Pacific plate under the Australian plate is also affected by the extensional regime of the Taupō Rift (Milicich et al., 2020; Stern et al., 2006; Wilson et al., 1995). The Taupō Rift controls the magmatism in the area, where a correlation between active faults and volcanism has been observed (Villamor et al., 2017; Wilson & Rowland, 2016). For example, the products of the TVZ have been linked to the rift extension, where the thinner crust in the central TVZ allowed the voluminous ignimbrite eruptions in Taupō (Villamor & Berryman, 2006a; Villamor et al., 2017; Wilson et al., 1995)

While arc magmatism is characterized by a thickened crust (e.g., ~60 km, Ecuadorian Andes in Iglesias et al., 2025) and high-water contents (2 - 6 wt% in Plank et al., 2013), Mount Ruapehu shows low water contents (0 - 2.7 wt% in this study) and crustal thickness of 25 km (Eberhart-Phillips et al., 2020; Leonard et al., 2021). These values seem comparable to those of the East African Rift, with crustal thickness of <16 – 38 km (Chambers et al., 2022) and water contents of ~0.3 ~ 1.6 wt% (Virunga Volcanic Province in Connors et al., 2025).

Nonetheless, the occurrence of low water contents in arc volcanoes is not unprecedented (e.g., ~1 wt% Osorno, Chile in Bechon et al., 2022), and has been suggested that it may be linked to the distance between volcano and trench (e.g., higher water content in volcanoes closer to the trench due to mantle melting at lower temperatures in Vander Auwera et al., 2025). However, the influence of the rift setting might be substantial in terms of the water content and unusual hot temperatures observed in Mount Ruapehu (e.g., <1.5 wt%; 1010 - 1130 °C in Lormand et al., 2020). This is because relatively hot/dry parental magmas are common in continental rifts environments (Collins et al., 2021; Melekhova et al., 2013).

This suggests that, the low water content and high temperatures observed in the magmas may be derived from the extensional tectonic regime, while other characteristics such as the typical magmatic arc signatures with REE and incompatible elements enrichment and depletion in Nb and Ta (Turner & Langmuir, 2022) are inherited by the subduction setting (Figure 6.5).

7.4.4 Implications for eruptive styles

A link between fault locations and vents for historic eruptions of TgVC was identified by Cassidy et al. (2009). This, in conjunction with the rift setting in which Mount Ruapehu is located (Rowland et al., 2010), provides insight into how the magma ascent at crustal depths may be favoured by diking transport through tectonically controlled structures as explained in the previous section (e.g., Gómez-Vasconcelos et al., 2017; Villamor et al., 2017; Wilson & Rowland, 2016).

While these structures offer a fast, low-resistance and effective ascent pathways at depth, they may also contribute to variations in the eruptive style through changes in the geometry of the shallow conduit (e.g., Lormand et al., 2020). Narrowing of the conduit may results in an increase of flux mass and magma compressibility, potentially favouring explosive eruptions (e.g., Brookfield et al., 2023; Kozono et al., 2022). This process can occurs due to decreasing outgassing efficiency near the surface (e.g., Yip et al., 2022), leading to higher particle ejection velocities at the vent (e.g., Schmid et al., 2022).

The potential structural influence on the eruptive styles is consistent with the water content and temperatures observed when comparing lavas and tephras. While low water content (e.g., <3.5 wt% in Popa et al., 2021a; Popa et al., 2021b), and high temperatures (e.g., 950 °C in Campagnola et al., 2016), should promote effusive eruptions, Mount Ruapehu magmas with low water contents (e.g., <2.5 wt% in Auer et al., 2016; Deering et al., 2011; Kilgour et al.,

2013; Lormand et al., 2020), and high temperatures (e.g., 1078 – 1149 °C in Lormand et al., 2020), are capable of producing explosive eruptions.

The similarities in the residence times and ascent rates between effusive and explosive eruptions are consistent with a potential structural influence on eruptive style, when considering time-averaged ascent through the deeper plumbing system. Similar residence times are found in lavas (~3 days) compared to tephra (~4 days), as well as similar average ascent rates estimated for magma transport at depth (~0.02 - 0.08 m/s in lavas and ~0.02 - 0.09 m/s in tephras) and undercooling (based on similar crystal morphologies and small sizes as described in Hammer & Rutherford, 2002; Matsumoto & Geshi, 2021). This suggests that the transition between eruptive styles is not solely controlled by outgassing and water exsolution in the deep plumbing system (e.g., Keller et al., 2023; Lindoo et al., 2017; Popa et al., 2021a; Sano et al., 2015). This observation may favour the hypothesis that differentiation can be influenced by the geometry of the shallow conduit as described by Lormand (2020).

The effect of conduit geometry in the eruptive style has been observed in other volcanoes around the world. The localized overpressurization due to changes in conduit geometry modified the magma mass flow rate, favouring the occurrence of 1986 sub-Plinian eruption at Izu-Oshima (Kozono et al., 2022). Similarly, gas accumulation and pressurization due to changes in conduit geometry has been linked to the 2019 paroxysms at Stromboli Volcano which are considered difficult to forecast (Viccaro et al., 2021). Moreover, it has also been identified that shallow conduit processes can follow broadly similar patterns across different magmas compositions and eruption scales (Ripepe et al., 2021).

Chapter 8 Conclusions and Outlook

8.1 Broader implications

This thesis focused on determining the processes occurring in the generation of the voluminous lava flows at Mount Ruapehu through petrological and geochemical analyses. Their timescales are defined and compare to those obtained for the <10 ka tephras by Lormand (2020). The following are the main findings of the present study.

8.1.1 Error propagation in the calculation of the residence times using CSD slopes and know growth rates

Testing two well-known databases (i.e., CSDSlice and ShapeCalc) for estimating crystal shapes from 2D measurements revealed substantial discrepancies in the shape determination across models for natural datasets. The uncertainties in the aspect ratio estimation propagate into errors in calculating maximum crystal sizes and the slopes of CSD plots. Using 3D data significantly minimizes these errors by eliminating the need for statistical and stereological corrections require for 2D datasets. However, when calculating the crystal residence times, the uncertainties in the growth rate exert greater influence on the results than those associated with the CSD slope determination, rendering slope-related errors comparatively negligeable when the growth rates are poorly constrained.

8.1.2 Timescales and rates of magma ascent

The crystal residence times for pyroxene determine in this study offered a maximum of 66 days using a growth range established from experimental data. Nonetheless, the similarities in the crystal shapes between tephras and lavas, suggest that the undercooling rates for the

magmas at the deeper conduit are not related to the eruptive style. Therefore, the use of a growth rate calculated for orthopyroxene of the Mangatawai Formation may provide more accurate timescales. Using this growth rate, the residence times of the lavas is shortened to a maximum of 6 days which matches those of the tephras (~3 ± 1 days), suggesting limited growth time within the crust, which is supported for the small crystal cargo (< 30 μm).

As for the magma ascent rates a maximum velocity of 9 m/s was calculated. Similarly, more realistic values lead to rates up to 0.08 m/s, which are close to those of the tephras (up to 0.09 m/s). These rates are considered rapid for effusive eruptions, yet slow for explosive eruptions, implying that conduit geometry plays a key role in the eruption style.

8.1.3 Origin of the crystal cargo

Whole rock compositions are strongly influenced by the crystal cargo. The crystal cargo is this study is mostly out of equilibrium with the carrier melt, showing disequilibrium and mechanical-induced textures, suggesting crystal recycling from previously emplaced crustal bodies, entrained during magma ascent.

On the other hand, the carrier melts seem to have a shared origin based on the similar compositions between the Mangaehuehu and Makotuku members groundmasses. These melts occasionally reached more evolved compositions as those of (e.g., Waitonga and Turoa members), via crustal assimilation and crystal fractionation. However, due to the small size of the autocrystic crystal cargo, and the calculated residence times, it is suggested that these melts spent limited time stationed within the crust.

The presence of Cr ring in cores, mantles and rims of pyroxenes suggests the mafic recharges observed in the crystal cargo are a recurrent process. Additionally, the differences in the Mg# of the pyroxenes indicate the presence of at least two mafic end members interacting with

felsic crustal bodies. These primitive mafic end members are a localized MgO-enriched magma that affected the crystal cargo in Mangaehuehu member samples and another basaltic magma that affected the crystal cargo in Makotuku, Waitonga and Turoa samples. Here, the primitive basaltic mafic magmas seem to share a common origin with the carrier melts based in the 1:1 relationship between whole rock and groundmass compositions in Makotuku Member samples (Figure 7.4).

Lastly, the presence of nanolites is an indication of post-eruption crystallization, likely due to the emplacement of the lava flows in glaciated areas, producing large undercooling and promoting the nucleation of Fe-oxide crystals over their growth.

8.1.4 Magmatic plumbing system in a complex geological context

Thermobarometry and MELTS modelling show consistent temperature (974 – 1163 °C) and pressure (108 – 545 MPa) ranges, that led to the estimation of zones of magma accumulation at depths between 4 – 22 km, where the magma was momentarily stationed before eruption.

The transcrustal processes observed include the interaction between hot mafic injections and stalled felsic magmas, crystal uptake by ascending melts and localized fractionation and crustal assimilation.

The geometry of the plumbing system seems to fit with a dike-dominated plumbing system, composed by a network of multidirectional dikes, many of which are crystallized and reactivated by new magma injections. These re-injections follow pre-existent paths causing mechanical fracturing and disaggregation of the previously emplaced bodies, explaining the presence of glomerocrysts and fractured crystals, while at the same time increasing the partial melting of the host rocks. Here, magma compositions are influenced not only by the re-

injection of magma, but also by the dike orientation, which either favours or limits the magma ascent, contributing to the compositional variation.

Mount Ruapehu's unique setting where arc magmatism is influenced by a rift-related extension favours the occurrence of a dike-dominated plumbing system controlled by fault orientations. This imposes characteristics typical of rift environments such as hotter and drier magmas generated primarily through decompression melting, while still retaining arc signatures from flux melting processes such as the REE patterns.

Lastly, the eruption styles seem to be controlled by the geometry of the shallow conduits. While diking favours magma ascent, demonstrated by the ascent rates calculated in this study, high temperatures and low water contents should favour effusive eruptions. Hence, the occurrence of explosive eruptions has been linked to changes in the geometry of the shallow conduit, leading to the alteration of the outgassing efficiency and overpressure of the system.

8.2 Future work

Three key points have been identified as possible paths for future work.

- The detailed analysis of crystal cargo: This will provide further information regarding processes and timescales. Detailed analysis of crystal mapping, linking the changes in composition with the observed textures will provide further insights into the mafic recharges and mixing events. Analysis of the crystal fractionation paths (e.g., Ubide et al., 2023), and elemental diffusion (e.g., Costa et al., 2020) will help to constrain further the composition of the melts that generated the crystal cargo and their growth rates. Additionally, the study of samples from other areas of the volcano, and different units will contribute to build a more comprehensive understanding of the origin of the crystal cargo at Mount Ruapehu.

- CSDs of Nanolites: Further analysis of the distribution of the Fe-oxide nanolites within the lavas of Mount Ruapehu can help to infer the relationship between crystal sizes and rapid undercooling in glaciated areas.

- Isotopic analyses of the carrier melts: These will help to constrain the melt sources, identifying if the carrier melts are generated from bimodal compositions within the crust (e.g., Reubi & Müntener, 2022), the product of subcrustal processes (e.g., Straub et al., 2011) or a complex mix of both.

- Experimental or analogue work: Degassing and fragmentation of hot anhydrous magmas will provide additional insights into the occurrence of explosive eruptions under dry conditions (e.g., Popa et al., 2021b). Conduit geometry modelling, in combination with geophysical monitoring information of Mount Ruapehu may assist in the determination of precursor signals to explosive eruptions (e.g., Ripepe et al., 2021), as well to create a better model of the plumbing system.

8.3 Concluding remarks

Although the influence of the Taupō rift on the volcanism of the TVZ has been recognised from a tectonic and structural point of view (Gómez-Vasconcelos et al., 2017; Villamor et al., 2017), it is important to further evaluate the effect of this tectonic setting on the magma transport, chemical differentiation and eruptive styles. While Mount Ruapehu is considered an arc volcano, there are certain characteristics that imply that the volcanoes in the TVZ should not be simply categorised as the product of a convergent margin. Differences in composition, multiple injection events and crystal recycling have been explained by individual batch of magma following particular paths, the heterogeneity of the magma reservoirs and different levels of magma storage in transcrustal magmatic systems (Conway

et al., 2018; Price et al., 2012; Svoboda et al., 2022; Waight et al., 1999; Waight et al., 2017). However, other characteristics such as the unusual hot magmas and low water contents remain somehow unexplained and may be related to the extensional regime of the area (i.e., thinning of the crust and magma transport through diking).

The present study opens the discussion to whether Mount Ruapehu, and the volcanoes in the TVZ should be studied following the same principles as other arc volcanoes, or if they should be analysed considering the complexity of the tectonic setting in which they are located. Furthermore, this study considers alternative explanations to those provided previously considering the fast ascent rates, the short residence times and the high number of crystals out of equilibrium, in which a dike-dominated plumbing system favours the transport of magma through pre-existing dikes and the crystal recycling occurs by reactivation of these already solidified paths.

The methods applied in this study to constrain magma plumbing architecture, crystal residence times and magma ascent rates are broadly transferable. These approaches can be employed to investigate magma storage and ascent dynamics in volcanic systems worldwide, regardless of the tectonic setting.

Bibliography

Adam, J., Turner, S., & Rushmer, T. (2016). The genesis of silicic arc magmas in shallow crustal cold zones. *Lithos*, *264*, 472-494. https://doi.org/10.1016/j.lithos.2016.07.036

Adams, C., Campbell, H., & Griffin, W. (2007). Provenance comparisons of Permian to Jurassic tectonostratigraphic terranes in New Zealand: perspectives from detrital zircon age patterns. *Geological Magazine*, *144*(4), 701-729. https://doi.org/10.1017/S0016756807003469

Adams, C., Mortimer, N., Campbell, H., & Griffin, W. (2009). Age and isotopic characterisation of metasedimentary rocks from the Torlesse Supergroup and Waipapa Group in the central North Island, New Zealand. *New Zealand Journal of Geology and Geophysics*, *52*(2), 149-170. https://doi.org/10.1080/00288300909509883

Adams, C., Mortimer, N., Campbell, H., & Griffin, W. (2011). Recognition of the Kaweka Terrane in northern South Island, New Zealand: preliminary evidence from Rb–Sr metamorphic and U–Pb detrital zircon ages. *New Zealand Journal of Geology and Geophysics*, *54*(3), 291-309. https://doi.org/10.1080/00288306.2011.569728

Agostini, C., Fortunati, A., Arzilli, F., Landi, P., & Carroll, M. R. (2013). Kinetics of crystal evolution as a probe to magmatism at Stromboli (Aeolian Archipelago, Italy). *Geochimica et Cosmochimica Acta*, *110*, 135-151. https://doi.org/10.1016/j.gca.2013.02.027

Ágreda-López, M., Parodi, V., Musu, A., Jorgenson, C., Carfì, A., Mastrogiovanni, F., Caricchi, L., Perugini, D., & Petrelli, M. (2024). Enhancing machine learning thermobarometry for clinopyroxene-bearing magmas. *Computers & Geosciences*, *193*, 105707. https://doi.org/10.1016/j.cageo.2024.105707

Aiuppa, A., Agusto, M., Allard, P., Carn, S., de Moor, J. M., Inguaggiato, S., Mazot, A., Moussallam, Y., & Nadeau, P. (2025). Geochemical volcano monitoring. In C. Bonadonna, L. Caricchi, A. Clarke, P. Cole, J. Lindsay, J. B. Lowenstern, R. E. A. Robertson, & V. M. L. (Eds.), *The Encyclopedia of Volcanoes, 3rd ed*. https://doi.org/10.31223/X5TT6D

Andrews, B. J., & Befus, K. S. (2020). Supersaturation nucleation and growth of plagioclase: a numerical model of decompression-induced crystallization. *Contributions to Mineralogy and Petrology*, *175*, 1-20. https://doi.org/10.1007/s00410-020-1660-9

Annen, C., Blundy, J., & Sparks, R. (2006). The genesis of intermediate and silicic magmas in deep crustal hot zones. *Journal of Petrology*, *47*(3), 505-539. https://doi.org/10.1093/petrology/egi084

Arai, R. (2021). Characteristics of seismicity in the southern Okinawa Trough and their relation to back-arc rifting processes. *Earth, Planets and Space*, *73*(1), 160. https://doi.org/10.1186/s40623-021-01491-4

Araya, N., Nakamura, M., Matsumoto, K., & Okumura, S. (2024). Time-Resolved Trigger Processes Leading to the Plinian Eruptions at Sakurajima Volcano, Japan. *Journal of Geophysical Research: Solid Earth*, *129*(9), e2023JB028558. https://doi.org/10.1029/2023JB028558

Armienti, P., Pareschi, M., Innocenti, F., & Pompilio, M. (1994). Effects of magma storage and ascent on the kinetics of crystal growth: The case of the 1991–93 Mt. Etna eruption. *Contributions to Mineralogy and Petrology*, *115*(4), 402-414. https://doi.org/10.1007/BF00320974

Armienti, P., Francalanci, L., & Landi, P. (2007). Textural effects of steady state behaviour of the Stromboli feeding system. *Journal of Volcanology and Geothermal Research*, *160*(1-2), 86-98. https://doi.org/10.1016/j.jvolgeores.2006.05.004

Armienti, P., Perinelli, C., & Putirka, K. D. (2012). A New Model to Estimate Deep-level Magma Ascent Rates, with Applications to Mt. Etna (Sicily, Italy). *Journal of Petrology*, *54*(4), 795-813. https://doi.org/10.1093/petrology/egs085

Arzilli, F., Polacci, M., Landi, P., Giordano, D., Baker, D. R., & Mancini, L. (2016). A novel protocol for resolving feldspar crystals in synchrotron X-ray microtomographic images of crystallized natural magmas and synthetic analogs. *American Mineralogist*, *101*(10), 2301-2311. https://doi.org/10.2138/am-2016-5788

Asimow, P. D., & Ghiorso, M. S. (1998). Algorithmic modifications extending MELTS to calculate subsolidus phase relations. *American Mineralogist*, *83*(9-10), 1127-1132. https://doi.org/10.2138/am-1998-9-1022

Asimow, P. D., Dixon, J. E., & Langmuir, C. H. (2004). A hydrous melting and fractionation model for mid-ocean ridge basalts: Application to the Mid-Atlantic Ridge near the Azores. *Geochemistry, Geophysics, Geosystems*, *5*(1). https://doi.org/10.1029/2003GC000568

Aswini, K., Kamesh Raju, K., Bijesh, C., Yatheesh, V., Zeba, N., & Dewangan, P. (2024). Morphotectonic characteristics of the Andaman volcanic arc and its adjoining regions, Andaman Sea. *Geo-Marine Letters*, *44*(3), 13. https://doi.org/10.1007/s00367-024-00775-4

Audétat, A., Zhang, L., & Ni, H. (2018). Copper and Li diffusion in plagioclase, pyroxenes, olivine and apatite, and consequences for the composition of melt inclusions. *Geochimica et Cosmochimica Acta*, *243*, 99-115. https://doi.org/10.1016/j.gca.2018.09.016

Auer, A., Martin, C., Palin, J., White, J., Nakagawa, M., & Stirling, C. (2015). The evolution of hydrous magmas in the Tongariro Volcanic Centre: the 10 ka Pahoka-Mangamate eruptions. *New Zealand Journal of Geology and Geophysics*, *58*(4), 364-384. https://doi.org/10.1080/00288306.2015.1089913

Auer, A., White, J. D. L., & Tobin, M. J. (2016). Variable H_2O content in magmas from the Tongariro Volcanic Centre and its relation to crustal storage and magma ascent. *Journal of Volcanology and Geothermal Research*, *325*, 203-210. https://doi.org/10.1016/j.jvolgeores.2016.06.021

Bachmann, O., & Bergantz, G. W. (2004). On the origin of crystal-poor rhyolites: extracted from batholithic crystal mushes. *Journal of Petrology*, *45*(8), 1565-1582. https://doi.org/10.1093/petrology/egh019

Balázs, A., Faccenna, C., Gerya, T., Ueda, K., & Funiciello, F. (2022). The dynamics of forearc – back - arc basin subsidence: Numerical models and observations from Mediterranean subduction zones. *Tectonics*, *41*(5), e2021TC007078. https://doi.org/10.1029/2021tc007078

Bamber, E. C., La Spina, G., Arzilli, F., Polacci, M., Mancini, L., de' Michieli Vitturi, M., Andronico, D., Corsaro, R. A., & Burton, M. R. (2024). Outgassing behaviour during highly explosive basaltic eruptions. *Communications Earth & Environment*, *5*(1), 3. https://doi.org/10.1038/s43247-023-01182-w

Barnes, S. J., Latypov, R., Chistyakova, S., Godel, B., & Schoneveld, L. E. (2021). Idiomorphic oikocrysts of clinopyroxene produced by a peritectic reaction within a solidification front of the Bushveld Complex. *Contributions to Mineralogy and Petrology*, *176*(1), 5. https://doi.org/10.1007/s00410-020-01747-4

Barrell, D. J. (2014). The Balmoral moraines near Lake Pukaki, Southern Alps: a new reference area for the early Otira Glaciation in New Zealand. *New Zealand Journal of Geology and Geophysics*, *57*(4), 442-452. https://doi.org/10.1080/00288306.2014.936473

Barth, A., & Plank, T. (2021). The ins and outs of water in olivine-hosted melt inclusions: hygrometer vs. speedometer. *Frontiers in Earth Science*, *9*, 614004. https://doi.org/10.3389/feart.2021.614004

Bechon, T., Billon, M., Namur, O., Bolle, O., Fugmann, P., Foucart, H., Devidal, J.-L., Delmelle, N., & Vander Auwera, J. (2022). Petrology of the magmatic system beneath Osorno volcano (central southern volcanic zone, Chile). *Lithos*, *426*, 106777. https://doi.org/10.1016/j.lithos.2022.106777

Befus, K. S., Manga, M., Gardner, J. E., & Williams, M. (2015). Ascent and emplacement dynamics of obsidian lavas inferred from microlite textures. *Bulletin of Volcanology*, *77*, 1-17. https://doi.org/10.1007/s00445-015-0971-6

Befus, K. S., & Andrews, B. J. (2018). Crystal nucleation and growth produced by continuous decompression of Pinatubo magma. *Contributions to Mineralogy and Petrology*, *173*, 1-20. https://doi.org/10.1007/s00410-018-1519-5

Behn, M. D., Kelemen, P. B., Hirth, G., Hacker, B. R., & Massonne, H.-J. (2011). Diapirs as the source of the sediment signature in arc lavas. *Nature Geoscience*, *4*(9), 641-646. https://doi.org/10.1038/ngeo1214

Bennett, D., Ubide, T., Ward, J. F., MacDonald, A., Rosenbaum, G., Sihombing, F. M. H., Nugroho, R. P., Jabbar, G. A., & Tapu, A.-T. (2025). Magmatic Architecture of a Potassic Arc Volcano: Batu Tara, Eastern Sunda Arc, Indonesia. *Journal of Petrology*, *66*(9). https://doi.org/10.1093/petrology/egaf071

Bergantz, G., Schleicher, J., & Burgisser, A. (2015). Open-system dynamics and mixing in magma mushes. *Nature Geoscience*, *8*(10), 793-796. https://doi.org/10.1038/ngeo2534

Berger, J., Ennih, N., Liégeois, J.-P., Nkono, C., Mercier, J.-C. C., & Demaiffe, D. (2008). A complex multi-chamber magmatic system beneath a late Cenozoic volcanic field: evidence from CSDs and thermobarometry of clinopyroxene from a single nephelinite flow (Djbel Saghro, Morocco). In N. Ennih & J.-P. Liégeois (Eds.), *The Boundaries of the West African Craton* (Vol. 297). Geological Society of London. https://doi.org/10.1144/SP297.25

Bernard, O., Li, W., Costa, F., Saunders, S., Itikarai, I., Sindang, M., & Bouvet de Maisonneuve, C. (2022). Explosive-effusive-explosive: The role of magma ascent rates and paths in modulating caldera eruptions. *Geology*, *50*(9), 1013-1017. https://doi.org/10.1130/g50023.1

Berndt, J., Koepke, J., & Holtz, F. (2005). An experimental investigation of the influence of water and oxygen fugacity on differentiation of MORB at 200 MPa. *Journal of Petrology*, *46*(1), 135-167. https://doi.org/10.1093/petrology/egh066

Bibby, H., Caldwell, T., Davey, F., & Webb, T. (1995). Geophysical evidence on the structure of the Taupo Volcanic Zone and its hydrothermal circulation. *Journal of Volcanology and Geothermal Research*, *68*(1-3), 29-58. https://doi.org/10.1016/0377-0273(95)00007-H

Billon, M., Vander Auwera, J., Namur, O., Faure, F., Holness, M. B., & Charlier, B. (2025). Plagioclase crystal size distributions, growth and nucleation rates in an anhydrous arc basaltic andesite. *Contributions to Mineralogy and Petrology*, *180*(4), 26. https://doi.org/10.1007/s00410-025-02213-9

Blundy, J., & Cashman, K. (2008). Petrologic reconstruction of magmatic system variables and processes. *Reviews in Mineralogy and Geochemistry*, *69*(1), 179-239. https://doi.org/10.2138/rmg.2008.69.6

Bonechi, B., Polacci, M., Arzilli, F., Romero, J. E., Fellowes, J., & Burton, M. (2024). Magma residence time, ascent rate and eruptive style of the November ash-laden activity during the 2021 Tajogaite eruption (La Palma, Spain). *Volcanica*, *7*(1), 51-65. https://doi.org/10.30909/vol.07.01.5165

Bouilhol, P., Schmidt, M., & Burg, J.-P. (2015). Magma transfer and evolution in channels within the arc crust: the pyroxenitic feeder pipes of Sapat (Kohistan, Pakistan). *Journal of Petrology*, *56*(7), 1309-1342. https://doi.org/10.1093/petrology/egv037

Brookfield, A., Cassidy, M., Weber, G., Popa, R.-G., Bachmann, O., & Stock, M. J. (2023). Magmatic volatile content and the overpressure 'sweet spot': Implications for volcanic eruption triggering and style. *Journal of Volcanology and Geothermal Research*, *444*, 107916. https://doi.org/10.1016/j.jvolgeores.2023.107916

Browne, B., & Szramek, L. (2015). Rates of magma ascent and storage. In H. Sigurdsson (Ed.), *The encyclopedia of volcanoes* (pp. 203-214). Elsevier. https://doi.org/10.1016/B978-0-12-385938-9.00009-2

Brugger, C. R., & Hammer, J. E. (2010a). Crystallization kinetics in continuous decompression experiments: implications for interpreting natural magma ascent processes. *Journal of Petrology*, *51*(9), 1941-1965. https://doi.org/10.1093/petrology/egq044

Brugger, C. R., & Hammer, J. E. (2010b). Crystal size distribution analysis of plagioclase in experimentally decompressed hydrous rhyodacite magma. *Earth and Planetary Science Letters*, *300*(3-4), 246-254. https://doi.org/10.1016/j.epsl.2010.09.046

Cagnioncle, A. M., Parmentier, E., & Elkins‐Tanton, L. T. (2007). Effect of solid flow above a subducting slab on water distribution and melting at convergent plate boundaries. *Journal of Geophysical Research: Solid Earth*, *112*(B9). https://doi.org/10.1029/2007JB004934

Cameron, B., Walker, J., Carr, M., Patino, L., Matıas, O., & Feigenson, M. (2003). Flux versus decompression melting at stratovolcanoes in southeastern Guatemala. *Journal of Volcanology and Geothermal Research*, *119*(1-4), 21-50. https://doi.org/10.1016/S0377-0273(02)00304-9

Campagnola, S., Romano, C., Mastin, L. G., & Vona, A. (2016). Confort 15 model of conduit dynamics: applications to Pantelleria Green Tuff and Etna 122 BC eruptions. *Contributions to Mineralogy and Petrology*, *171*(6), 60. https://doi.org/10.1007/s00410-016-1265-5

Cashman, K., & McConnell, S. (2005). Multiple levels of magma storage during the 1980 summer eruptions of Mount St. Helens, WA. *Bulletin of Volcanology*, *68*, 57-75. https://doi.org/10.1007/s00445-005-0422-x

Cashman, K. V., & Marsh, B. D. (1988). Crystal size distribution (CSD) in rocks and the kinetics and dynamics of crystallization II: Makaopuhi lava lake. *Contributions to Mineralogy and Petrology*, *99*(3), 292-305. https://doi.org/10.1007/BF00375363

Cashman, K. V. (1993). Relationship between plagioclase crystallization and cooling rate in basaltic melts. *Contributions to Mineralogy and Petrology*, *113*(1), 126-142. https://doi.org/https://doi.org/10.1007/BF00320836

Cashman, K. V., Sparks, R. S. J., & Blundy, J. D. (2017). Vertically extensive and unstable magmatic systems: a unified view of igneous processes. *Science*, *355*(6331), eaag3055. https://doi.org/10.1126/science.aag3055

Cashman, K. V. (2020). Crystal size distribution (CSD) analysis of volcanic samples: advances and challenges. *Frontiers in Earth Science*, *8*, 291. https://doi.org/10.3389/feart.2020.00291

Cassidy, J., Ingham, M., Locke, C. A., & Bibby, H. (2009). Subsurface structure across the axis of the Tongariro Volcanic Centre, New Zealand. *Journal of Volcanology and Geothermal Research*, *179*(3-4), 233-240. https://doi.org/10.1016/j.jvolgeores.2008.11.017

Cassidy, M., Cole, P. D., Hicks, K. E., Varley, N. R., Peters, N., & Lerner, A. H. (2015). Rapid and slow: Varying magma ascent rates as a mechanism for Vulcanian

explosions. *Earth and Planetary Science Letters*, *420*, 73-84. https://doi.org/10.1016/j.epsl.2015.03.025

Castro, A., Gerya, T., García-Casco, A., Fernández, C., Díaz-Alvarado, J., Moreno-Ventas, I., & Löw, I. (2010). Melting relations of MORB–sediment mélanges in underplated mantle wedge plumes; implications for the origin of Cordilleran-type batholiths. *Journal of Petrology*, *51*(6), 1267-1295. https://doi.org/10.1093/petrology/egq019

Castro, J. M., & Gardner, J. E. (2008). Did magma ascent rate control the explosive-effusive transition at the Inyo volcanic chain, California? *Geology*, *36*(4), 279-282. https://doi.org/10.1130/g24453a.1

Castro, J. M., & Dingwell, D. B. (2009). Rapid ascent of rhyolitic magma at Chaitén volcano, Chile. *Nature*, *461*(7265), 780-783. https://doi.org/10.1038/nature08458

Castro, J. M., Schipper, C. I., Mueller, S. P., Militzer, A. S., Amigo, A., Parejas, C. S., & Jacob, D. (2013). Storage and eruption of near-liquidus rhyolite magma at Cordón Caulle, Chile. *Bulletin of Volcanology*, *75*(4), 702. https://doi.org/10.1007/s00445-013-0702-9

Chadwick, W. W., Cannat, M., Eason, D., Le Saout, M., & Carey, R. (2025). Mid-Ocean Ridge Volcanism. In C. Bonadonna, L. Caricchi, A. Clarke, P. Cole, J. Lindsay, J. B. Lowenstern, R. E. A. Robertson, & V. M. L. (Eds.), *Encyclopedia of Volcanoes, 3rd Ed*. https://doi.org/10.31223/X5FH91

Chambers, E. L., Harmon, N., Rychert, C. A., Gallacher, R. J., & Keir, D. (2022). Imaging the seismic velocity structure of the crust and upper mantle in the northern East African Rift using Rayleigh wave tomography. *Geophysical Journal International*, *230*(3), 2036-2055. https://doi.org/10.1093/gji/ggac156

Chang, J., & Audétat, A. (2018). Petrogenesis and metal content of hornblende-rich xenoliths from two Laramide-age magma systems in southwestern USA: insights into the metal budget of arc magmas. *Journal of Petrology*, *59*(10), 1869-1898. https://doi.org/10.1093/petrology/egy083

Chen, C., Lee, C.-T. A., Tang, M., Biddle, K., & Sun, W. (2020). Lithium systematics in global arc magmas and the importance of crustal thickening for lithium enrichment. *Nature communications*, *11*(1), 5313. https://doi.org/10.1038/s41467-020-19106-z

Chen, L., Feng, K., Deng, J., Li, D., Li, S., & Somerville, I. (2024). Geochemical comparison between oceanic and continental arc volcanic rocks: Insights to arc magmatism. *Geological Journal*, *59*(1), 113-136. https://doi.org/10.1002/gj.4847

Christopher, T., Blundy, J., Cashman, K., Cole, P., Edmonds, M., Smith, P., Sparks, R., & Stinton, A. (2015). Crustal ‐ scale degassing due to magma system destabilization and magma ‐ gas decoupling at S oufrière H ills V olcano, M ontserrat. *Geochemistry, Geophysics, Geosystems*, *16*(9), 2797-2811. https://doi.org/10.1002/2015GC005791

Cocker, K., Shane, P., Cronin, S., Stirling, C., & Reid, M. (2022). A History of Andesite Production via Magma Mixing and Mingling Revealed Microscopically at Ngauruhoe

Volcano. *Geochemistry, Geophysics, Geosystems*, *23*(10), e2022GC010589. https://doi.org/10.1029/2022GC010589

Cole, J. (1978). Andesites of the tongariro volcanic centre, north island, New Zealand. *Journal of Volcanology and Geothermal Research*, *3*(1-2), 121-153. https://doi.org/10.1016/0377-0273(78)90007-0

Cole, J., & Lewis, K. (1981). Evolution of the Taupo-Hikurangi subduction system. *Tectonophysics*, *72*(1-2), 1-21. https://doi.org/10.1016/0040-1951(81)90084-6

Collins, W. J., Murphy, J. B., Blereau, E., & Huang, H. Q. (2021). Water availability controls crustal melting temperatures. *Lithos*, *402-403*, 106351. https://doi.org/10.1016/j.lithos.2021.106351

Conder, J. A., Wiens, D. A., & Morris, J. (2002). On the decompression melting structure at volcanic arcs and back‐arc spreading centers. *Geophysical Research Letters*, *29*(15), 17-11-17-14. https://doi.org/10.1029/2002GL015390

Conder, J. A. (2005). A case for hot slab surface temperatures in numerical viscous flow models of subduction zones with an improved fault zone parameterization. *Physics of the Earth and Planetary Interiors*, *149*(1-2), 155-164. https://doi.org/10.1016/j.pepi.2004.08.018

Connors, L., Wallace, P. J., Sims, K. W. W., Sublett, D. M., & Bodnar, R. J. (2025). Magma sources, crustal storage depths, and degassing of alkalic, CO2-rich magmas at Nyiragongo and Nyamulagira Volcanoes, Democratic Republic of the Congo. *Earth and Planetary Science Letters*, *665*, 119477. https://doi.org/10.1016/j.epsl.2025.119477

Conway, C. E., Townsend, D. B., Leonard, G. S., Wilson, C., Calvert, A., & Gamble, J. A. (2015). Lava-ice interaction on a large composite volcano: a case study from Ruapehu, New Zealand. *Bulletin of Volcanology*, *77*, 1-18. https://doi.org/10.1007/s00445-015-0906-2

Conway, C. E., Leonard, G. S., Townsend, D. B., Calvert, A. T., Wilson, C. J., Gamble, J. A., & Eaves, S. R. (2016). A high-resolution 40Ar/39Ar lava chronology and edifice construction history for Ruapehu volcano, New Zealand. *Journal of Volcanology and Geothermal Research*, *327*, 152-179. https://doi.org/10.1016/j.jvolgeores.2016.07.006

Conway, C. E. (2016). *Studies on the glaciovolcanic and magmatic evolution of Ruapehu volcano, New Zealand* Victoria University of Wellington]. Wellington, New Zealand.

Conway, C. E., Gamble, J. A., Wilson, C. J., Leonard, G. S., Townsend, D. B., & Calvert, A. T. (2018). New petrological, geochemical, and geochronological perspectives on andesite-dacite magma genesis at Ruapehu volcano, New Zealand. *American Mineralogist: Journal of Earth and Planetary Materials*, *103*(4), 565-581. https://doi.org/10.2138/am-2018-6199

Conway, C. E., Chamberlain, K. J., Harigane, Y., Morgan, D. J., & Wilson, C. J. N. (2020). Rapid assembly of high-Mg andesites and dacites by magma mixing at a continental arc stratovolcano. *Geology*, *48*(10), 1033-1037. https://doi.org/10.1130/g47614.1

Cooper, K. M., & Kent, A. J. R. (2014). Rapid remobilization of magmatic crystals kept in cold storage. *Nature*, *506*(7489), 480-483. https://doi.org/10.1038/nature12991

Coote, A. C., & Shane, P. (2016). Crystal origins and magmatic system beneath Ngauruhoe volcano (New Zealand) revealed by plagioclase textures and compositions. *Lithos*, *260*, 107-119. https://doi.org/10.1016/j.lithos.2016.05.017

Corella Santa Cruz, C. R., Zellmer, G. F., Stirling, C. H., Straub, S. M., Brenna, M., Reid, M. R., Németh, K., & Barr, D. (2023). Transcrustal and source processes affecting the chemical characteristics of magmas in a hyperactive volcanic zone. *Geochimica et Cosmochimica Acta*. https://doi.org/10.1016/j.gca.2023.05.003

Corella Santa Cruz, C. R. (2023). *Subduction cycling and its controls on hyperactive volcanism in the Taupo Volcanic Zone, New Zealand: a thesis presented in partial fulfilment of the requirements for the degree of Doctor of Philosophy in Earth Science at Massey University, Palmerston North, New Zealand* Massey University]. Palmerston North, New Zealand. http://hdl.handle.net/10179/20052

Corradino, M., Balazs, A., Faccenna, C., & Pepe, F. (2022). Arc and forearc rifting in the Tyrrhenian subduction system. *Scientific Reports*, *12*(1), 4728. https://doi.org/10.1038/s41598-022-08562-w

Costa, F., Chakraborty, S., & Dohmen, R. (2003). Diffusion coupling between trace and major elements and a model for calculation of magma residence times using plagioclase. *Geochimica et Cosmochimica Acta*, *67*(12), 2189-2200. https://doi.org/10.1016/S0016-7037(02)01345-5

Costa, F., Andreastuti, S., de Maisonneuve, C. B., & Pallister, J. S. (2013). Petrological insights into the storage conditions, and magmatic processes that yielded the centennial 2010 Merapi explosive eruption. *Journal of Volcanology and Geothermal Research*, *261*, 209-235. https://doi.org/10.1016/j.jvolgeores.2012.12.025

Costa, F., Shea, T., & Ubide, T. (2020). Diffusion chronometry and the timescales of magmatic processes. *Nature Reviews Earth & Environment*, *1*(4), 201-214. https://doi.org/10.1038/s43017-020-0038-x

Couch, S., Sparks, R., & Carroll, M. (2001). Mineral disequilibrium in lavas explained by convective self-mixing in open magma chambers. *Nature*, *411*(6841), 1037-1039. https://doi.org/10.1038/35082540

Coulthard Jr, D. A., Brahm, R., Lormand, C., Zellmer, G. F., Sakamoto, N., Iizuka, Y., & Yurimoto, H. (2024). Plutonic nature of a transcrustal magmatic system: evidence from ultrahigh resolution Sr-disequilibria in plagioclase microantecrysts from the southern Taupo volcanic zone, New Zealand. *Journal of Petrology*, *65*(1), egad087. https://doi.org/10.1093/petrology/egad087

Crabtree, S. M., & Lange, R. A. (2011). Complex phenocryst textures and zoning patterns in andesites and dacites: evidence of degassing-induced rapid crystallization? *Journal of Petrology*, *52*(1), 3-38. https://doi.org/10.1093/petrology/egq067

Cruz-Uribe, A. M., Marschall, H. R., Gaetani, G. A., & Le Roux, V. (2018). Generation of alkaline magmas in subduction zones by partial melting of mélange diapirs—An experimental study. *Geology*, *46*(4), 343-346. https://doi.org/10.1130/G39956.1

D'Mello, N., Zellmer, G., Kereszturi, G., Ubide, T., Procter, J., & Stewart, R. (2023). Crystal entrainment from cool, low-silica rocks into hot, high-silica melts: diverse primary melt compositions at Taranaki volcano, New Zealand. *Journal of the Geological Society*, jgs2022-2036. https://doi.org/10.1144/jgs2022-036

D'Mello, N. G., Zellmer, G. F., Negrini, M., Kereszturi, G., Procter, J., Stewart, R., Prior, D., Usuki, M., & Iizuka, Y. (2021). Deciphering magma storage and ascent processes of Taranaki, New Zealand, from the complexity of amphibole breakdown textures. *Lithos*, *398*, 106264. https://doi.org/10.1016/j.lithos.2021.106264

De Yoreo, J. J., & Vekilov, P. G. (2003). Principles of crystal nucleation and growth. *Reviews in Mineralogy and Geochemistry*, *54*(1), 57-93. https://doi.org/10.2113/0540057

Deering, C., Bachmann, O., Dufek, J., & Gravley, D. (2011). Rift-related transition from andesite to rhyolite volcanism in the Taupo Volcanic Zone (New Zealand) controlled by crystal–melt dynamics in mush zones with variable mineral assemblages. *Journal of Petrology*, *52*(11), 2243-2263. https://doi.org/10.1093/petrology/egr046

DeGraff, J. M., & Aydin, A. (1987). Surface morphology of columnar joints and its significance to mechanics and direction of joint growth. *Geological Society of America Bulletin*, *99*(5), 605-617. https://doi.org/10.1130/0016-7606(1987)99<605:SMOCJA>2.0.CO;2

Degruyter, W., Huber, C., Bachmann, O., Cooper, K. M., & Kent, A. J. (2016). Magma reservoir response to transient recharge events: The case of Santorini volcano (Greece). *Geology*, *44*(1), 23-26. https://doi.org/10.1130/G37333.1

DePaolo, D. J. (1981). Trace element and isotopic effects of combined wallrock assimilation and fractional crystallization. *Earth and Planetary Science Letters*, *53*(2), 189-202. https://doi.org/10.1016/0012-821X(81)90153-9

Devine, J., Rutherford, M., & Gardner, J. (1998). Petrologic determination of ascent rates for the 1995–1997 Soufriere Hills Volcano andesitic magma. *Geophysical Research Letters*, *25*(19), 3673-3676. https://doi.org/10.1029/98GL00912

Doll, P., Eaves, S. R., Kennedy, B. M., Blard, P.-h., Robert, A., Nichols, L., Leonard, G. S., Townsend, D. B., Cole, J. W., Conway, E., Baldwin, S., Fénisse, G., Zimmermann, L., & Tibari, B. (2024). Cosmogenic 3he chronology of postglacial lava flows at Mt Ruapehu , Aotearoa /New Zealand. *Geochronology*, *6*(3), pp. 365-395. https://doi.org/10.5194/gchron-6-365-2024

Donoghue, S., Neall, V., Palmer, A., & Stewart, R. (1997). The volcanic history of Ruapehu during the past 2 millennia based on the record of Tufa Trig tephras. *Bulletin of Volcanology*, *59*, 136-146. https://doi.org/10.1007/s004450050181

Dufek, J., Cashman, K., Hooft, E., & Bedrosian, P. (2022). The nature of active magma reservoirs and storage underneath Cascade volcanoes. *Elements: An International*

Magazine of Mineralogy, Geochemistry, and Petrology, *18*(4), 239-245. https://doi.org/10.2138/gselements.18.4.239

Eaves, S. R., N. Mackintosh, A., Winckler, G., Schaefer, J. M., Alloway, B. V., & Townsend, D. B. (2016a). A cosmogenic 3He chronology of late Quaternary glacier fluctuations in North Island, New Zealand (39°S). *Quaternary Science Reviews*, *132*, 40-56. https://doi.org/10.1016/j.quascirev.2015.11.004

Eaves, S. R., Mackintosh, A. N., Anderson, B. M., Doughty, A. M., Townsend, D. B., Conway, C. E., Winckler, G., Schaefer, J. M., Leonard, G. S., & Calvert, A. T. (2016b). The Last Glacial Maximum in the central North Island, New Zealand: palaeoclimate inferences from glacier modelling. *Clim. Past*, *12*(4), 943-960. https://doi.org/10.5194/cp-12-943-2016

Eberhart-Phillips, D., Bannister, S., & Reyners, M. (2020). Attenuation in the mantle wedge beneath super-volcanoes of the Taupo Volcanic Zone, New Zealand. *Geophysical Journal International*, *220*(1), 703-723. https://doi.org/10.1093/gji/ggz455

Eberl, D., Kile, D. E., & Drits, V. (2002). On geological interpretations of crystal size distributions: Constant vs. proportionate growth. *American Mineralogist*, *87*(8-9), 1235-1241. https://doi.org/10.2138/am-2002-8-923

Edmonds, M., Sides, I., Swanson, D., Werner, C., Martin, R., Mather, T., Herd, R., Jones, R., Mead, M., & Sawyer, G. (2013). Magma storage, transport and degassing during the 2008–10 summit eruption at Kīlauea Volcano, Hawai ‘i. *Geochimica et Cosmochimica Acta*, *123*, 284-301. https://doi.org/10.1016/j.gca.2013.05.038

Edmonds, M., & Wallace, P. J. (2017). Volatiles and exsolved vapor in volcanic systems. *Elements*, *13*(1), 29-34. https://doi.org/10.2113/gselements.13.1.29

Edwards, B. R., Karson, J., Wysocki, R., Lev, E., Bindeman, I., & Kueppers, U. (2013). Insights on lava–ice/snow interactions from large-scale basaltic melt experiments. *Geology*, *41*(8), 851-854. https://doi.org/10.1130/G34305.1

Elkins-Tanton, L. T., Grove, T. L., & Donnelly-Nolan, J. (2001). Hot, shallow mantle melting under the Cascades volcanic arc. *Geology*, *29*(7), 631-634. https://doi.org/10.1130/0091-7613(2001)029<0631:HSMMUT>2.0.CO;2

England, P. C., & Katz, R. F. (2010). Melting above the anhydrous solidus controls the location of volcanic arcs. *Nature*, *467*(7316), 700-703. https://doi.org/10.1038/nature09417

Erdős, Z., Huismans, R. S., & Faccenna, C. (2022). Wide versus narrow back‐arc rifting: Control of subduction velocity and convective back‐arc thinning. *Tectonics*, *41*(6), e2021TC007086. https://doi.org/10.1029/2021TC007086

Eskandari, A., & Sadeghi, B. (2024). Deciphering Igneous Rock Crystals: Unveiling Multifractal Patterns in Crystal Size Dynamics. *Minerals*, *14*(7), 660. https://doi.org/10.3390/min14070660

Eskandari, A., Amini, S., & Sadeghi, B. (2024). The dynamic of magmatic system and volcano hazard implications of the Damavand volcano (N. Iran) inferred from the textural data. *Journal of Volcanology and Geothermal Research*, *456*, 108220. https://doi.org/10.1016/j.jvolgeores.2024.108220

Ewart, A., Brothers, R., & Mateen, A. (1977). An outline of the geology and geochemistry, and the possible petrogenetic evolution of the volcanic rocks of the Tonga-Kermadec-New Zealand island arc. *Journal of Volcanology and Geothermal Research*, *2*(3), 205-250. https://doi.org/10.1016/0377-0273(77)90001-4

Farner, M. J., & Lee, C.-T. A. (2017). Effects of crustal thickness on magmatic differentiation in subduction zone volcanism: A global study. *Earth and Planetary Science Letters*, *470*, 96-107. https://doi.org/10.1016/j.epsl.2017.04.025

Farrell, J., Smith, R. B., Husen, S., & Diehl, T. (2014). Tomography from 26 years of seismicity revealing that the spatial extent of the Yellowstone crustal magma reservoir extends well beyond the Yellowstone caldera. *Geophysical Research Letters*, *41*(9), 3068-3073. https://doi.org/10.1002/2014GL059588

Fornaciai, A., Perinelli, C., Armienti, P., & Favalli, M. (2015). Crystal size distributions of plagioclase in lavas from the July–August 2001 Mount Etna eruption. *Bulletin of Volcanology*, *77*, 1-15. https://doi.org/10.1007/s00445-015-0953-8

Frey, H. M., & Lange, R. A. (2011). Phenocryst complexity in andesites and dacites from the Tequila volcanic field, Mexico: resolving the effects of degassing vs. magma mixing. *Contributions to Mineralogy and Petrology*, *162*(2), 415-445. https://doi.org/10.1007/s00410-010-0604-1

Gamble, J., Smith, I., McCulloch, M., Graham, I., & Kokelaar, B. (1993). The geochemistry and petrogenesis of basalts from the Taupo Volcanic Zone and Kermadec Island Arc, SW Pacific. *Journal of Volcanology and Geothermal Research*, *54*(3-4), 265-290. https://doi.org/10.1016/0377-0273(93)90067-2

Gamble, J., Woodhead, J., Wright, I., & Smith, I. (1996). Basalt and sediment geochemistry and magma petrogenesis in a transect from oceanic island arc to rifted continental margin arc: the Kermadec—Hikurangi Margin, SW Pacific. *Journal of Petrology*, *37*(6), 1523-1546. https://doi.org/10.1093/petrology/37.6.1523

Gamble, J. A., Wood, C. P., Price, R. C., Smith, I. E. M., Stewart, R. B., & Waight, T. (1999). A fifty year perspective of magmatic evolution on Ruapehu Volcano, New Zealand: verification of open system behaviour in an arc volcano. *Earth and Planetary Science Letters*, *170*(3), 301-314. https://doi.org/10.1016/S0012-821X(99)00106-5

Gamble, J. A., Price, R. C., Smith, I. E., McIntosh, W. C., & Dunbar, N. W. (2003). 40Ar/39Ar geochronology of magmatic activity, magma flux and hazards at Ruapehu volcano, Taupo Volcanic Zone, New Zealand. *Journal of Volcanology and Geothermal Research*, *120*(3-4), 271-287. https://doi.org/10.1016/S0377-0273(02)00407-9

Gazel, E., Flores, K. E., & Carr, M. J. (2021). Architectural and tectonic control on the segmentation of the Central American volcanic arc. *Annual Review of Earth and Planetary Sciences*, *49*(1), 495-521. https://doi.org/10.1146/annurev-earth-082420-055108

Gerya, T. V., & Yuen, D. A. (2003). Rayleigh–Taylor instabilities from hydration and melting propel 'cold plumes' at subduction zones. *Earth and Planetary Science Letters*, *212*(1-2), 47-62. https://doi.org/10.1016/S0012-821X(03)00265-6

Ghiorso, M. S. (1985). Chemical Mass transfer in magmatic processes: I. Thermodynamic relations and numerical algorithms. *Contributions to Mineralogy and Petrology*, *90*(2-3), 107-120. https://doi.org/10.1007/BF00378254

Ghiorso, M. S., & Carmichael, I. S. (1985). Chemical mass transfer in magmatic processes: II. Applications in equilibrium crystallization, fractionation and assimilation. *Contributions to Mineralogy and Petrology*, *90*(2-3), 121-141. https://doi.org/10.1007/BF00378255

Ghiorso, M. S., & Sack, R. O. (1995). Chemical mass transfer in magmatic processes IV. A revised and internally consistent thermodynamic model for the interpolation and extrapolation of liquid-solid equilibria in magmatic systems at elevated temperatures and pressures. *Contributions to Mineralogy and Petrology*, *119*, 197-212. https://doi.org/10.1007/BF00307281

Ghiorso, M. S., Hirschmann, M. M., Reiners, P. W., & Kress III, V. C. (2002). The pMELTS: A revision of MELTS for improved calculation of phase relations and major element partitioning related to partial melting of the mantle to 3 GPa. *Geochemistry, Geophysics, Geosystems*, *3*(5), 1-35. https://doi.org/10.1029/2001GC000217

Ghiorso, M. S. (2013). A globally convergent saturation state algorithm applicable to thermodynamic systems with a stable or metastable omni-component phase. *Geochimica et Cosmochimica Acta*, *103*, 295-300. https://doi.org/10.1016/j.gca.2012.11.013

Ghiorso, M. S., & Gualda, G. A. (2015). Chemical thermodynamics and the study of magmas. In H. sigurdsson (Ed.), *The encyclopedia of volcanoes, 2nd ed.* (pp. 143-161). Elsevier. https://doi.org/10.1016/B978-0-12-385938-9.00006-7

Gill, J. B. (1981). *Orogenic andesites and plate tectonics* (Vol. 16). Springer Science & Business Media.

Ginibre, C., Wörner, G., & Kronz, A. (2002a). Minor-and trace-element zoning in plagioclase: implications for magma chamber processes at Parinacota volcano, northern Chile. *Contributions to Mineralogy and Petrology*, *143*(3), 300-315. https://doi.org/10.1007/s00410-002-0351-z

Ginibre, C., Kronz, A., & WoÈrner, G. (2002b). High-resolution quantitative imaging of plagioclase composition using accumulated backscattered electron images: new constraints on oscillatory zoning. *Contributions to Mineralogy and Petrology*, *142*(4), 436-448. https://doi.org/10.1007/s004100100298

Ginibre, C., Wörner, G., & Kronz, A. (2007). Crystal zoning as an archive for magma evolution. *Elements*, *3*(4), 261-266. https://doi.org/10.2113/gselements.3.4.261

Giordano, G., & Caricchi, L. (2022). Determining the state of activity of transcrustal magmatic systems and their volcanoes. *Annual Review of Earth and Planetary Sciences*, *50*, 231-259. https://doi.org/10.1146/annurev-earth-032320-084733

Giuliani, L., Iezzi, G., Vetere, F., Behrens, H., Mollo, S., Cauti, F., Ventura, G., & Scarlato, P. (2020). Evolution of textures, crystal size distributions and growth rates of plagioclase, clinopyroxene and spinel crystallized at variable cooling rates from a mid-ocean ridge basaltic melt. *Earth-Science Reviews*, *204*, 103165. https://doi.org/10.1016/j.earscirev.2020.103165

Global Volcanism Program. (2025). *Ruapehu (241100)*. Retrieved 2025/11/05/01:48:46 from https://volcano.si.edu/volcano.cfm?vn=241100

GNS Science. (2025). *Volcano Fact Sheet Mount Ruapehu Volcano*. https://www.gns.cri.nz/assets/Our-Science/Subfiles/Natural-Hazards-and-Risks/Subfiles/Volcanoes/Volcano-Fact-Sheet-Ruapehu.pdf

Gomes, A., Balázs, A., & Gerya, T. (2025). Arc Splitting and Back‐Arc Spreading Evolution: The Control of Slab Dehydration and Melting Processes. *Geochemistry, Geophysics, Geosystems*, *26*(10), e2025GC012255. https://doi.org/10.1029/2025GC012255

Gómez-Vasconcelos, M., Villamor, P., Cronin, S., Procter, J., Kereszturi, G., Palmer, A., Townsend, D., Leonard, G., Berryman, K., & Ashraf, S. (2016). Earthquake history at the eastern boundary of the South Taupo Volcanic Zone, New Zealand. *New Zealand Journal of Geology and Geophysics*, *59*(4), 522-543. https://doi.org/10.1080/00288306.2016.1195757

Gómez-Vasconcelos, M. G., Villamor, P., Cronin, S., Procter, J., Palmer, A., Townsend, D., & Leonard, G. (2017). Crustal extension in the Tongariro graben, New Zealand: Insights into volcano-tectonic interactions and active deformation in a young continental rift. *Bulletin*, *129*(9-10), 1085-1099. https://doi.org/10.1130/B31657.1

Graham, I., & Hackett, W. (1987). Petrology of calc-alkaline lavas from Ruapehu Volcano and related vents, Taupo Volcanic Zone, New Zealand. *Journal of Petrology*, *28*(3), 531-567. https://doi.org/10.1093/petrology/28.3.531

Graham, I. J., Blattner, P., & McCulloch, M. T. (1990). Meta-igneous granulite xenoliths from Mount Ruapehu, New Zealand: fragments of altered oceanic crust? *Contributions to Mineralogy and Petrology*, *105*(6), 650-661. https://doi.org/10.1007/BF00306531

Griffin, S., Udry, A., Daly, L., Forman, L. V., Lee, M. R., & Cohen, B. E. (2023). Investigating the igneous petrogenesis of Martian volcanic rocks using augite quantitative textural analysis of the Yamato nakhlites. *Meteoritics & Planetary Science*, *58*(1), 63-84. https://doi.org/10.1111/maps.13934

Grove, T., Parman, S., Bowring, S., Price, R., & Baker, M. (2002). The role of an H 2 O-rich fluid component in the generation of primitive basaltic andesites and andesites from the Mt. Shasta region, N California. *Contributions to Mineralogy and Petrology*, *142*, 375-396. https://doi.org/10.1007/s004100100299

Grove, T., Till, C., Lev, E., Chatterjee, N., & Médard, E. (2009). Kinematic variables and water transport control the formation and location of arc volcanoes. *Nature*, *459*(7247), 694-697. https://doi.org/10.1038/nature08044

Grove, T. L., Elkins-Tanton, L. T., Parman, S. W., Chatterjee, N., Müntener, O., & Gaetani, G. A. (2003). Fractional crystallization and mantle-melting controls on calc-alkaline differentiation trends. *Contributions to Mineralogy and Petrology*, *145*, 515-533. https://doi.org/10.1007/s00410-003-0448-z

Grove, T. L., Till, C. B., & Krawczynski, M. J. (2012). The role of H_2O in subduction zone magmatism. *Annual Review of Earth and Planetary Sciences*, *40*, 413-439. https://doi.org/10.1146/annurev-earth-042711-105310

Grove, T. L., & Till, C. B. (2015). Melting the Earth's Upper Mantle. In H. Sigurdsson (Ed.), *The Encyclopedia of Volcanoes, 2nd ed.* (pp. 35-47). Elsevier. https://doi.org/10.1016/B978-0-12-385938-9.00001-8

Gualda, G. A., Cook, D. L., Chopra, R., Qin, L., Anderson, A. T., & Rivers, M. (2004). Fragmentation, nucleation and migration of crystals and bubbles in the Bishop Tuff rhyolitic magma. *Earth and Environmental Science Transactions of The Royal Society of Edinburgh*, *95*(1-2), 375-390. https://doi.org/10.1017/S0263593300001139

Gualda, G. A., & Rivers, M. (2006). Quantitative 3D petrography using X-ray tomography: Application to Bishop Tuff pumice clasts. *Journal of Volcanology and Geothermal Research*, *154*(1-2), 48-62. https://doi.org/10.1016/j.jvolgeores.2005.09.019

Gualda, G. A. (2006). Crystal size distributions derived from 3D datasets: Sample size versus uncertainties. *Journal of Petrology*, *47*(6), 1245-1254. https://doi.org/10.1093/petrology/egl010

Gualda, G. A., Ghiorso, M. S., Lemons, R. V., & Carley, T. L. (2012). Rhyolite-MELTS: a modified calibration of MELTS optimized for silica-rich, fluid-bearing magmatic systems. *Journal of Petrology*, *53*(5), 875-890. https://doi.org/10.1093/petrology/egr080

Gualda, G. A., & Ghiorso, M. S. (2015). MELTS _ E xcel: AM icrosoft E xcel ‐ based MELTS interface for research and teaching of magma properties and evolution. *Geochemistry, Geophysics, Geosystems*, *16*(1), 315-324. https://doi.org/10.1002/2014GC005545

Hacker, B. R., Kelemen, P. B., & Behn, M. D. (2011). Differentiation of the continental crust by relamination. *Earth and Planetary Science Letters*, *307*(3-4), 501-516. https://doi.org/10.1016/j.epsl.2011.05.024

Hackett, W., & Houghton, B. (1989). A facies model for a Quaternary andesitic composite volcano: Ruapehu, New Zealand. *Bulletin of Volcanology*, *51*, 51-68. https://doi.org/10.1007/BF01086761

Hackett, W. R. (1985). *Geology and petrology of Ruapehu volcano and related vents* Victoria University of Wellington]. Wellington, New Zealand.

Hall, P. S., & Kincaid, C. (2001). Diapiric flow at subduction zones: A recipe for rapid transport. *Science*, *292*(5526), 2472-2475. https://doi.org/10.1126/science.106048

Hammer, J. E., Cashman, K. V., Hoblitt, R., & Newman, S. (1999). Degassing and microlite crystallization during pre-climactic events of the 1991 eruption of Mt. Pinatubo, Philippines. *Bulletin of Volcanology*, *60*, 355-380. https://doi.org/10.1007/s004450050238

Hammer, J. E., & Rutherford, M. J. (2002). An experimental study of the kinetics of decompression - induced crystallization in silicic melt. *Journal of Geophysical Research: Solid Earth*, *107*(B1), ECV 8-1-ECV 8-24. https://doi.org/10.1029/2001JB000281

Hammer, J. E. (2006). Influence of fO2 and cooling rate on the kinetics and energetics of Fe-rich basalt crystallization. *Earth and Planetary Science Letters*, *248*(3), 618-637. https://doi.org/10.1016/j.epsl.2006.04.022

Hammer, J. E. (2008). Experimental studies of the kinetics and energetics of magma crystallization. *Reviews in Mineralogy and Geochemistry*, *69*(1), 9-59. https://doi.org/10.2138/rmg.2008.69.2

Harris, A. J., & Rowland, S. K. (2015). Lava flows and rheology. In H. Sigurdsson (Ed.), *The encyclopedia of volcanoes, 2nd ed.* (pp. 321-342). Elsevier. https://doi.org/10.1016/B978-0-12-385938-9.00017-1

Higgins, M. (1994). Determination of crystal morphology and size from bulk measurements on thin sections: numerical modelling. *American Mineralogist*, *79*, 113-119.

Higgins, M. D. (2000). Measurement of crystal size distributions. *American Mineralogist*, *85*(9), 1105-1116. https://doi.org/10.2138/am-2000-8-901

Higgins, M. D. (2006). Verification of ideal semi-logarithmic, lognormal or fractal crystal size distributions from 2D datasets. *Journal of Volcanology and Geothermal Research*, *154*(1-2), 8-16. https://doi.org/10.1016/j.jvolgeores.2005.09.015

Higgins, M. D. (2011). Textural coarsening in igneous rocks. *International Geology Review*, *53*(3-4), 354-376. https://doi.org/10.1080/00206814.2010.496177

Hilbert, H.-S., Dannowski, A., Grevemeyer, I., Berndt, C., Kodaira, S., Fujie, G., & Takahashi, N. (2024). From Symmetric Rifting to Asymmetric Spreading—Insights Into Back-Arc Formation in the Central Mariana Trough. *Geochemistry, Geophysics, Geosystems*, *25*(11), e2024GC011690. https://doi.org/10.1029/2024GC011690

Hildreth, W., & Moorbath, S. (1988). Crustal contributions to arc magmatism in the Andes of central Chile. *Contributions to Mineralogy and Petrology*, *98*, 455-489. https://doi.org/10.1007/BF00372365

Hill, G. J., Bibby, H. M., Ogawa, Y., Wallin, E. L., Bennie, S. L., Caldwell, T. G., Keys, H., Bertrand, E. A., & Heise, W. (2015). Structure of the Tongariro Volcanic system: Insights from magnetotelluric imaging. *Earth and Planetary Science Letters*, *432*, 115-125. https://doi.org/10.1016/j.epsl.2015.10.003

Hirschmann, M., Ghiorso, M., Davis, F., Gordon, S., Mukherjee, S., Grove, T., Krawczynski, M., Medard, E., & Till, C. (2008). Library of Experimental Phase Relations (LEPR): A database and Web portal for experimental magmatic phase equilibria data. *Geochemistry, Geophysics, Geosystems*, *9*(3). https://doi.org/0.1029/2007GC001894

Hobden, B., Houghton, B., Davidson, J., & Weaver, S. (1999). Small and short-lived magma batches at composite volcanoes: time windows at Tongariro volcano, New Zealand. *Journal of the Geological Society*, *156*(5), 865-868. https://doi.org/10.1144/gsjgs.156.5.0865

Hogan, J. P. (1993). Monomineralic glomerocrysts: textural evidence for mineral resorption during crystallization of igneous rocks. *The Journal of geology*, *101*(4), 531-540. https://doi.org/10.1086/648245

Holness, M. B., Stock, M. J., & Geist, D. (2019). Magma chambers versus mush zones: constraining the architecture of sub-volcanic plumbing systems from microstructural analysis of crystalline enclaves. *Philosophical Transactions of the Royal Society A*, *377*(2139), 20180006. https://doi.org/10.1098/rsta.2018.0006

Hon, K., Kauahikaua, J., Denlinger, R., & Mackay, K. (1994). Emplacement and inflation of pahoehoe sheet flows: Observations and measurements of active lava flows on Kilauea Volcano, Hawaii. *Geological Society of America Bulletin*, *106*(3), 351-370. https://doi.org/10.1130/0016-7606(1994)106<0351:EAIOPS>2.3.CO;2

Houghton, B., Wilson, C., McWilliams, M., Lanphere, M., Weaver, S., Briggs, R., & Pringle, M. (1995). Chronology and dynamics of a large silicic magmatic system: Central Taupo Volcanic Zone, New Zealand. *Geology*, *23*(1), 13-16. https://doi.org/10.1130/0091-7613(1995)023<0013:CADOAL>2.3.CO;2

Humphreys, M. C., Blundy, J. D., & Sparks, R. S. J. (2006). Magma evolution and open-system processes at Shiveluch Volcano: Insights from phenocryst zoning. *Journal of Petrology*, *47*(12), 2303-2334. https://doi.org/10.1093/petrology/egl045

Humphreys, M. C., Edmonds, M., & Klöcking, M. S. (2016). The validity of plagioclase-melt geothermometry for degassing-driven magma crystallization. *American Mineralogist*, *101*(4), 769-779. https://doi.org/10.2138/am-2016-5314

Hurst, A., & McGinty, P. (1999). Earthquake swarms to the west of Mt Ruapehu preceding its 1995 eruption. *Journal of Volcanology and Geothermal Research*, *90*(1-2), 19-28. https://doi.org/10.1016/S0377-0273(99)00019-0

Iddings, J. P. (1892). *On the crystallization of igneous rocks* (Vol. 11). The Society.

Iglesias, J., Witt, C., Poma, O., Bruguier, O., Bosch, D., Bosse, V., Zattin, M., Seyler, M., Hernández, M. J., Chanier, F., & Averbuch, O. (2025). Geochronology and geochemistry of Cenozoic magmatism in the north-western Ecuadorian Andes: the role of crustal thickness. *Lithos*, *514-515*, 108159. https://doi.org/10.1016/j.lithos.2025.108159

Iwamori, H. (1998). Transportation of H_2O and melting in subduction zones. *Earth and Planetary Science Letters*, *160*(1-2), 65-80. https://doi.org/10.1016/S0012-821X(98)00080-6

Jackson, M., Blundy, J., & Sparks, R. (2018). Chemical differentiation, cold storage and remobilization of magma in the Earth's crust. *Nature*, *564*(7736), 405-409. https://doi.org/10.1038/s41586-018-0746-2

Jeffery, A. J., Gertisser, R., Troll, V. R., Jolis, E. M., Dahren, B., Harris, C., Tindle, A. G., Preece, K., O'Driscoll, B., & Humaida, H. (2013). The pre-eruptive magma plumbing system of the 2007–2008 dome-forming eruption of Kelut volcano, East Java, Indonesia. *Contributions to Mineralogy and Petrology*, *166*, 275-308. https://doi.org/10.1007/s00410-013-0875-4

Jegal, Y., Ubide, T., Huertas, M. J., Herrera, R., Márquez, Á., Ancochea, E., & Coello-Bravo, J. J. (2025). Plagioclase antecrysts record syn-eruptive incorporation of evolved mush during the 2021 Tajogaite eruption (La Palma, Spain). *Contributions to Mineralogy and Petrology*, *180*(10), 66. https://doi.org/10.1007/s00410-025-02241-5

Jenner, F. E., & O'Neill, H. S. C. (2012). Major and trace analysis of basaltic glasses by laser - ablation ICP - MS. *Geochemistry, Geophysics, Geosystems*, *13*(3). https://doi.org/10.1029/2011GC003890

JEOL Ltd. (n.d.). *ZAF correction | Glossary | JEOL Ltd.* JEOL Ltd. . Retrieved 03/11/2025 from http://jeol.com/words/semterms/20121024.004200.php#gsc.tab=0

Jerram, D. A., & Davidson, J. P. (2007). Frontiers in Textural and Microgeochemical Analysis. *Elements*, *3*(4), 235-238. https://doi.org/10.2113/gselements.3.4.235

Jerram, D. A., & Higgins, M. D. (2007). 3D analysis of rock textures: quantifying igneous microstructures. *Elements*, *3*(4), 239-245. https://doi.org/10.2113/gselements.3.4.239

Jerram, D. A., Mock, A., Davis, G. R., Field, M., & Brown, R. J. (2009). 3D crystal size distributions: A case study on quantifying olivine populations in kimberlites. *Lithos*, *112*, 223-235. https://doi.org/10.1016/j.lithos.2009.05.042

Johnson, E. A., & Rossman, G. R. (2013). The diffusion behavior of hydrogen in plagioclase feldspar at 800–1000 C: Implications for re-equilibration of hydroxyl in volcanic phenocrysts. *American Mineralogist*, *98*(10), 1779-1787. https://doi.org/10.2138/am.2013.4521

Johnson, E. R., Wallace, P. J., Cashman, K. V., Granados, H. D., & Kent, A. J. (2008). Magmatic volatile contents and degassing-induced crystallization at Volcán Jorullo, Mexico: implications for melt evolution and the plumbing systems of monogenetic

volcanoes. *Earth and Planetary Science Letters*, *269*(3-4), 478-487. https://doi.org/10.1016/j.epsl.2008.03.004

Kamei, A., Owada, M., Nagao, T., & Shiraki, K. (2004). High-Mg diorites derived from sanukitic HMA magmas, Kyushu Island, southwest Japan arc: evidence from clinopyroxene and whole rock compositions. *Lithos*, *75*(3), 359-371. https://doi.org/10.1016/j.lithos.2004.03.006

Keir, D., La Rosa, A., Pagli, C., Wang, H., Ayele, A., Lewi, E., Monterroso, F., & Raggiunti, M. (2025). The 2024 Fentale diking episode in a slow extending continental rift. *Geophysical Research Letters*, *52*(5), e2024GL113214. https://doi.org/10.1029/2024GL113214

Kelemen, P. B., Rilling, J. L., Parmentier, E., Mehl, L., & Hacker, B. R. (2003). Thermal structure due to solid-state flow in the mantle wedge beneath arcs. *Geophysical Monograph-American Geophysical Union*, *138*, 293-311. https://doi.org/10.1029/138GM13

Kelemen, P. B., & Behn, M. D. (2016). Formation of lower continental crust by relamination of buoyant arc lavas and plutons. *Nature Geoscience*, *9*(3), 197-205. https://doi.org/10.1038/ngeo2662

Keller, F., Popa, R. G., Allaz, J., Bovay, T., Bouvier, A. S., Geshi, N., Miyakawa, A., & Bachmann, O. (2023). Variations in water saturation states and their impact on eruption size and frequency at the Aso supervolcano, Japan. *Earth and Planetary Science Letters*, *622*, 118400. https://doi.org/10.1016/j.epsl.2023.118400

Kemner, F., Haase, K. M., Beier, C., Krumm, S., & Brandl, P. A. (2015). Formation of andesite melts and Ca-rich plagioclase in the submarine Monowai volcanic system, Kermadec arc. *Geochemistry, Geophysics, Geosystems*, *16*(12), 4130-4152. https://doi.org/10.1002/2015GC005884

Kilgour, G., Manville, V., Della Pasqua, F., Graettinger, A., Hodgson, K., & Jolly, G. (2010). The 25 September 2007 eruption of Mount Ruapehu, New Zealand: directed ballistics, surtseyan jets, and ice-slurry lahars. *Journal of Volcanology and Geothermal Research*, *191*(1-2), 1-14. https://doi.org/10.1016/j.jvolgeores.2009.10.015

Kilgour, G., Blundy, J., Cashman, K., & Mader, H. M. (2013). Small volume andesite magmas and melt–mush interactions at Ruapehu, New Zealand: evidence from melt inclusions. *Contributions to Mineralogy and Petrology*, *166*, 371-392. https://doi.org/10.1007/s00410-013-0880-7

Kilgour, G., Saunders, K., Blundy, J., Cashman, K., Scott, B., & Miller, C. (2014). Timescales of magmatic processes at Ruapehu volcano from diffusion chronometry and their comparison to monitoring data. *Journal of Volcanology and Geothermal Research*, *288*, 62-75. https://doi.org/10.1016/j.jvolgeores.2014.09.010

Kilgour, G. N., Della Pasqua, F., & Jolly, G. E. (2009). *Magma ascent during eruptions at Mt. Ngauruhoe: insight from xenolith fluid inclusions* (GNS Science Consultancy Report, Issue. https://www.naturalhazards.govt.nz/resilience-and-

research/research/search-all-research-reports/magma-ascent-during-eruptions-at-mt-ngauruhoe-insights-from-xenolith-fluid-inclusions/

Kilgour, G. N., Mader, H. M., Blundy, J. D., & Brooker, R. A. (2016). Rheological controls on the eruption potential and style of an andesite volcano: A case study from Mt. Ruapehu, New Zealand. *Journal of Volcanology and Geothermal Research*, *327*, 273-287. https://doi.org/10.1016/j.jvolgeores.2016.08.001

Kiser, E., Palomeras, I., Levander, A., Zelt, C., Harder, S., Schmandt, B., Hansen, S., Creager, K., & Ulberg, C. (2016). Magma reservoirs from the upper crust to the Moho inferred from high-resolution Vp and Vs models beneath Mount St. Helens, Washington State, USA. *Geology*, *44*(6), 411-414. https://doi.org/10.1130/G37591.1

Kovacs, M., Fülöp, A., Seghedi, I., & Pécskay, Z. (2021). Architecture of volcanic plumbing systems inferred from thermobarometry: A case study from the Miocene Gutâi Volcanic Zone in the Eastern Carpathians, Romania. *Lithos*, *396*, 106191. https://doi.org/10.1016/j.lithos.2021.106191

Kozono, T., Ishibashi, H., Okumura, S., & Miwa, T. (2022). Conduit flow dynamics during the 1986 sub-Plinian eruption at Izu-Oshima volcano. *Journal of Disaster Research*, *17*(5), 754-767. https://doi.org/10.20965/jdr.2022.p0754

Kuritani, T., Kitagawa, H., & Nakamura, E. (2005). Assimilation and fractional crystallization controlled by transport process of crustal melt: Implications from an alkali basalt–dacite suite from Rishiri Volcano, Japan. *Journal of Petrology*, *46*(7), 1421-1442. https://doi.org/10.1093/petrology/egi021

La Spina, G., Arzilli, F., Llewellin, E. W., Burton, M. R., Clarke, A. B., de' Michieli Vitturi, M., Polacci, M., Hartley, M. E., Di Genova, D., & Mader, H. M. (2021). Explosivity of basaltic lava fountains is controlled by magma rheology, ascent rate and outgassing. *Earth and Planetary Science Letters*, *553*, 116658. https://doi.org/10.1016/j.epsl.2020.116658

LaFemina, P. C. (2015). Plate tectonics and volcanism. In H. Sigurdsson (Ed.), *The encyclopedia of volcanoes, 2nd ed,* (pp. 65-92). Elsevier. https://doi.org/10.1016/B978-0-12-385938-9.00003-1

Lange, R. A., Frey, H. M., & Hector, J. (2009). A thermodynamic model for the plagioclase-liquid hygrometer/thermometer. *American Mineralogist*, *94*(4), 494-506. https://doi.org/10.2138/am.2009.3011

Le Maitre, R., Streckeisen, A., Zanettin, B., Le Bas, M., Bonin, B., Bateman, P., Bellieni, G., Dudek, A., Efremova, S., & Keller, J. (2005). *Igneous rocks: a classification and glossary of terms: recommendations of the International Union of Geological Sciences Subcommission on the Systematics of Igneous Rocks* (2 ed.). Cambridge University Press.

Lecointre, J. A., Neall, V. E., & Palmer, A. S. (1998). Quaternary lahar stratigraphy of the western Ruapehu ring plain, New Zealand. *New Zealand Journal of Geology and Geophysics*, *41*(3), 225-245. https://doi.org/10.1080/00288306.1998.9514807

Lee, C.-T. A., & Bachmann, O. (2014). How important is the role of crystal fractionation in making intermediate magmas? Insights from Zr and P systematics. *Earth and Planetary Science Letters*, *393*, 266-274. https://doi.org/10.1016/j.epsl.2014.02.044

Lentze, R. C. F., & McSween Jr., H. Y. (2000). Crystallization of the basaltic shergottites: Insights from crystal size distribution (CSD) analysis of pyroxenes. *Meteoritics & Planetary Science*, *35*(5), 919-927. https://doi.org/10.1111/j.1945-5100.2000.tb01481.x

Leonard, G. S., Cole, R. P., Christenson, B. W., Conway, C. E., Cronin, S. J., Gamble, J. A., Hurst, T., Kennedy, B. M., Miller, C. A., & Procter, J. N. (2021). Ruapehu and Tongariro stratovolcanoes: a review of current understanding. *New Zealand Journal of Geology and Geophysics*, *64*(2-3), 389-420. https://doi.org/10.1080/00288306.2021.1909080

Lesher, C. E., & Spera, F. J. (2015). Thermodynamic and transport properties of silicate melts and magma. In H. Sigurdsson (Ed.), *The encyclopedia of volcanoes, 2nd ed.* (pp. 113-141). Elsevier. https://doi.org/10.1016/B978-0-12-385938-9.00005-5

Li, F., Sun, Z., Yang, H., Zhang, Y., Xu, Z., & Wang, L. (2025). Crustal Melting Events During the Late Stage of Syn‐Rift at the Magma‐Intermediate Continental Margin: A Numerical Study From the Northern South China Sea Margin. *Basin Research*, *37*(3), e70035. https://doi.org/10.1111/bre.70035

Li, J., & Deepak, F. L. (2022). In situ kinetic observations on crystal nucleation and growth. *Chemical reviews*, *122*(23), 16911-16982. https://doi.org/10.1021/acs.chemrev.1c01067

Lifshitz, I. M., & Slyozov, V. V. (1961). The kinetics of precipitation from supersaturated solid solutions. *Journal of Physics and Chemistry of Solids*, *19*(1), 35-50. https://doi.org/10.1016/0022-3697(61)90054-3

Lindoo, A., Larsen, J., Cashman, K., & Oppenheimer, J. (2017). Crystal controls on permeability development and degassing in basaltic andesite magma. *Geology*, *45*(9), 831-834. https://doi.org/https://doi.org/10.1130/G39157.1

Loncar, M., & Huppert, H. E. (2022). Dyke cooling upon intrusion: Subsequent shape change, cooling regimes and the effect of further magma input. *Earth and Planetary Science Letters*, *593*, 117687. https://doi.org/10.1016/j.epsl.2022.117687

Longpré, M.-A., Tramontano, S., Pankhurst, M. J., Roman, D. C., Reiss, M. C., Cortese, F., James, M. R., Spina, L., Rodríguez, F., Coldwell, B., Martín-Lorenzo, A., Barbee, O., D'Auria, L., Chamberlain, K. J., & Scarrow, J. H. (2025). Shifting melt composition linked to volcanic tremor at Cumbre Vieja volcano. *Nature Geoscience*, *18*(2), 175-183. https://doi.org/10.1038/s41561-024-01623-x

Lore, J., Gao, H., & Aydin, A. (2000). Viscoelastic thermal stress in cooling basalt flows. *Journal of Geophysical Research: Solid Earth*, *105*(B10), 23695-23709. https://doi.org/10.1029/2000JB900226

Lormand, C., Zellmer, G. F., Németh, K., Kilgour, G., Mead, S., Palmer, A. S., Sakamoto, N., Yurimoto, H., & Moebis, A. (2018). Weka trainable segmentation plugin in imagej: A semi-automatic tool applied to crystal size distributions of microlites in volcanic rocks. *Microscopy and Microanalysis*, *24*(6), 667-675. https://doi.org/10.1017/S1431927618015428

Lormand, C. (2020). *Understanding magmatic processes and their timescales beneath the Tongariro Volcanic Centre through microanalytical investigations of the tephra record* Massey University]. Palmerston North, New Zealand. http://hdl.handle.net/10179/15790

Lormand, C., Zellmer, G. F., Kilgour, G., Németh, K., Palmer, A. S., Sakamoto, N., Yurimoto, H., Kuritani, T., Iizuka, Y., & Moebis, A. (2020). Slow ascent of unusually hot intermediate magmas triggering Strombolian to sub-Plinian eruptions. *Journal of Petrology*, *61*(10), egaa077. https://doi.org/10.1093/petrology/egaa077

Lormand, C., Zellmer, G. F., Sakamoto, N., Ubide, T., Kilgour, G., Yurimoto, H., Palmer, A., Németh, K., Iizuka, Y., & Moebis, A. (2021). Shallow magmatic processes revealed by cryptic microantecrysts: a case study from the Taupo Volcanic Zone. *Contributions to Mineralogy and Petrology*, *176*(11), 97. https://doi.org/10.1007/s00410-021-01857-7

Lowrey, J. R., Ivanic, T. J., Wyman, D. A., & Roberts, M. P. (2017). Platy pyroxene: new insights into spinifex texture. *Journal of Petrology*, *58*(9), 1671-1700. https://doi.org/10.1093/petrology/egx069

Lucci, F., Carrasco-Núñez, G., Rossetti, F., Theye, T., White, J. C., Urbani, S., Azizi, H., Asahara, Y., & Giordano, G. (2020). Anatomy of the magmatic plumbing system of Los Humeros Caldera (Mexico): implications for geothermal systems. *Solid Earth*, *11*(1), 125-159. https://doi.org/10.5194/se-11-125-2020

Luo, Q., Gong, X., Xu, J., Yang, Z., Dong, Z., & Xiong, F. (2025a). A burst of middle-late Jurassic high-Mg andesitic magmatism in central Tibet: types, magmatic process, and subduction dynamics. *International Geology Review*, 1-22. https://doi.org/10.1080/00206814.2025.2560955

Luo, X., Zeng, Z., Chen, Z., Zhang, Y., Du, X., & Qi, H. (2024). The evolution of crystal-poor rhyolite in the middle Okinawa Trough and its implications for the state of magma chamber. *Geological Journal*, *59*(6), 1812-1827. https://doi.org/10.1002/gj.4971

Luo, X., Zeng, Z., Zhang, Y., & Chen, Z. (2025b). Pre-eruptive processes and timescales of shallow silicic magma reservoir beneath the Iheya Graben in the middle Okinawa Trough. *Lithos*, *514-515*, 108222. https://doi.org/10.1016/j.lithos.2025.108222

Lupi, M., De Gori, P., Valoroso, L., Baccheschi, P., Minetto, R., & Mazzini, A. (2022). Northward migration of the Javanese volcanic arc along thrust faults. *Earth and Planetary Science Letters*, *577*, 117258. https://doi.org/10.1016/j.epsl.2021.117258

MacDonald, A., Ubide, T., Mollo, S., Pontesilli, A., & Masotta, M. (2023). The Influence of Undercooling and Sector Zoning on Clinopyroxene–Melt Equilibrium and

Thermobarometry. *Journal of Petrology*, *64*(10). https://doi.org/10.1093/petrology/egad074

Magee, C., & Jackson, C. A.-L. (2020). Can we relate the surface expression of dike-induced normal faults to subsurface dike geometry? *Geology*, *49*(4), 366-371. https://doi.org/10.1130/g48171.1

Magee, R., Ubide, T., & Caulfield, J. (2021). Days to weeks of syn-eruptive magma interaction: High-resolution geochemistry of the 2002-03 branched eruption at Mount Etna. *Earth and Planetary Science Letters*, *565*, 116904. https://doi.org/10.1016/j.epsl.2021.116904

Mangler, M. F., Humphreys, M. C. S., Wadsworth, F. B., Iveson, A. A., & Higgins, M. D. (2022). Variation of plagioclase shape with size in intermediate magmas: a window into incipient plagioclase crystallisation. *Contributions to Mineralogy and Petrology*, *177*(6), 64. https://doi.org/10.1007/s00410-022-01922-9

Markl, G., & White, C. (1999). Complex zoning between super-calcic pigeonite and augite from the Graveyard Point sill, Oregon: a record of the interplay between bulk and interstitial liquid fractionation. *Contributions to Mineralogy and Petrology*, *137*(1), 170-183. https://doi.org/10.1007/s004100050589

Marsh, B. D. (1988). Crystal size distribution (CSD) in rocks and the kinetics and dynamics of crystallization: I. Theory. *Contributions to Mineralogy and Petrology*, *99*, 277-291. https://doi.org/10.1007/BF00375362

Marsh, B. D. (1998). On the interpretation of crystal size distributions in magmatic systems. *Journal of Petrology*, *39*(4), 553-599. https://doi.org/10.1093/petroj/39.4.553

Marsh, B. D. (2015). Magma chambers. In H. Sigurdsson (Ed.), *The encyclopedia of volcanoes, 2nd ed.* (pp. 185-201). Elsevier. https://doi.org/10.1016/B978-0-12-385938-9.00008-0

Marshall, A. A., & Andrews, B. J. (2023). Modeling decompression paths in a basaltic andesite magma using the nucleation and growth of plagioclase microlites. *Contributions to Mineralogy and Petrology*, *178*(9), 62. https://doi.org/10.1007/s00410-023-02030-y

Martel, C., & Schmidt, B. C. (2003). Decompression experiments as an insight into ascent rates of silicic magmas. *Contributions to Mineralogy and Petrology*, *144*(4), 397-415. https://doi.org/10.1007/s00410-002-0404-3

Martel, C. (2012). Eruption dynamics inferred from microlite crystallization experiments: application to Plinian and dome-forming eruptions of Mt. Pelée (Martinique, Lesser Antilles). *Journal of Petrology*, *53*(4), 699-725. https://doi.org/10.1093/petrology/egr076

Masotta, M., Mollo, S., Freda, C., Gaeta, M., & Moore, G. (2013). Clinopyroxene–liquid thermometers and barometers specific to alkaline differentiated magmas. *Contributions to Mineralogy and Petrology*, *166*, 1545-1561. https://doi.org/10.1007/s00410-013-0927-9

Masotta, M., Mollo, S., Nazzari, M., Tecchiato, V., Scarlato, P., Papale, P., & Bachmann, O. (2018). Crystallization and partial melting of rhyolite and felsite rocks at Krafla volcano: A comparative approach based on mineral and glass chemistry of natural and experimental products. *Chemical Geology*, *483*, 603-618. https://doi.org/10.1016/j.chemgeo.2018.03.031

Masotta, M., & Mollo, S. (2019). A new plagioclase-liquid hygrometer specific to trachytic systems. *Minerals*, *9*(6), 375. https://doi.org/10.3390/min9060375

Matsumoto, K., & Geshi, N. (2021). Shallow crystallization of eruptive magma inferred from volcanic ash microtextures: a case study of the 2018 eruption of Shinmoedake volcano, Japan. *Bulletin of Volcanology*, *83*(5), 31. https://doi.org/10.1007/s00445-021-01451-6

McArthur, J., & Shepherd, M. (1990). Late Quaternary glaciation of Mt Ruapehu, North Island, New Zealand. *Journal of the Royal Society of New Zealand*, *20*(3), 287-296. https://doi.org/10.1080/03036758.1990.10416823

McCarthy, A., Chelle-Michou, C., Blundy, J. D., Vonlanthen, P., Meibom, A., & Escrig, S. (2020). Taking the pulse of volcanic eruptions using plagioclase glomerocrysts. *Earth and Planetary Science Letters*, *552*, 116596. https://doi.org/10.1016/j.epsl.2020.116596

McDonough, W. F., & Sun, S. s. (1995). The composition of the Earth. *Chemical Geology*, *120*(3), 223-253. https://doi.org/10.1016/0009-2541(94)00140-4

Melekhova, E., Annen, C., & Blundy, J. (2013). Compositional gaps in igneous rock suites controlled by magma system heat and water content. *Nature Geoscience*, *6*(5), 385-390. https://doi.org/10.1038/ngeo1781

Melnik, O. E., Blundy, J. D., Rust, A. C., & Muir, D. D. (2011). Subvolcanic plumbing systems imaged through crystal size distributions. *Geology*, *39*(4), 403-406. https://doi.org/10.1130/g31691.1

Metcalfe, A., Moune, S., Komorowski, J.-C., Kilgour, G., Jessop, D. E., Moretti, R., & Legendre, Y. (2021a). Corrigendum: Magmatic Processes at La Soufrière de Guadeloupe: Insights From Crystal Studies and Diffusion Timescales for Eruption Onset [Correction]. *Frontiers in Earth Science*, *Volume 9 - 2021*. https://doi.org/10.3389/feart.2021.723763

Metcalfe, A., Moune, S., Komorowski, J.-C., Kilgour, G., Jessop, D. E., Moretti, R., & Legendre, Y. (2021b). Magmatic Processes at La Soufrière de Guadeloupe: Insights From Crystal Studies and Diffusion Timescales for Eruption Onset [Original Research]. *Frontiers in Earth Science*, *Volume 9 - 2021*. https://doi.org/10.3389/feart.2021.617294

Mielke, P., Weinert, S., Bignall, G., & Sass, I. (2016). Thermo-physical rock properties of greywacke basement rock and intrusive lavas from the Taupo Volcanic Zone, New Zealand. *Journal of Volcanology and Geothermal Research*, *324*, 179-189. https://doi.org/10.1016/j.jvolgeores.2016.06.002

Milicich, S., Chambefort, I., Wilson, C., Alcaraz, S., Ireland, T., Bardsley, C., & Simpson, M. (2020). A zircon U-Pb geochronology for the Rotokawa geothermal system, New Zealand, with implications for Taupō Volcanic Zone evolution. *Journal of Volcanology and Geothermal Research*, *389*, 106729. https://doi.org/10.1016/j.jvolgeores.2019.106729

Mock, A., & Jerram, D. (2005). Crystal size distributions (CSD) in three dimensions: insights from the 3D reconstruction of a highly porphyritic rhyolite. *Journal of Petrology*, *46*(8), 1525-1541. https://doi.org/10.1093/petrology/egi024

Moebis, A. (2010). *Understanding the Holocene explosive eruption record of the Tongariro Volcanic Centre* Massey University]. Palmerston North, New Zealand. http://hdl.handle.net/10179/2200

Mollo, S., Putirka, K., Misiti, V., Soligo, M., & Scarlato, P. (2013). A new test for equilibrium based on clinopyroxene–melt pairs: Clues on the solidification temperatures of Etnean alkaline melts at post-eruptive conditions. *Chemical Geology*, *352*, 92-100. https://doi.org/10.1016/j.chemgeo.2013.05.026

Mollo, S., & Hammer, J. E. (2017). Dynamic crystallization in magmas. In W. Heinrich & R. Abart (Eds.), *Mineral reaction kinetics: Microstructures, textures, chemical and isotopic signatures* (Vol. 16). European Mineralogical Union and Mineralogical Society of Great Britain and Ireland. https://doi.org/10.1180/EMU-notes.16

Morgan, D., Blake, S., Rogers, N., DeVivo, B., Rolandi, G., Macdonald, R., & Hawkesworth, C. (2004). Time scales of crystal residence and magma chamber volume from modelling of diffusion profiles in phenocrysts: Vesuvius 1944. *Earth and Planetary Science Letters*, *222*(3-4), 933-946. https://doi.org/10.1016/j.epsl.2004.03.030

Morgan, D. J., & Jerram, D. A. (2006). On estimating crystal shape for crystal size distribution analysis. *Journal of Volcanology and Geothermal Research*, *154*(1-2), 1-7. https://doi.org/10.1016/j.jvolgeores.2005.09.016

Morimoto, N. (1989). Nomenclature of pyroxenes. *Mineralogical Journal*, *14*(5), 198-221. https://doi.org/10.2465/minerj.14.198

Mortimer, N., Gans, P., Palin, J., Meffre, S., Herzer, R., & Skinner, D. (2010). Location and migration of Miocene–Quaternary volcanic arcs in the SW Pacific region. *Journal of Volcanology and Geothermal Research*, *190*(1-2), 1-10. https://doi.org/10.1016/j.jvolgeores.2009.02.017

Mortimer, N., Rattenbury, M., King, P., Bland, K., Barrell, D., Bache, F., Begg, J., Campbell, H., Cox, S., & Crampton, J. (2014). High-level stratigraphic scheme for New Zealand rocks. *New Zealand Journal of Geology and Geophysics*, *57*(4), 402-419. https://doi.org/10.1080/00288306.2014.946062

Mortimer, N., Charlier, B. L. A., Rooyakkers, S. M., Turnbull, R. E., Wilson, C. J. N., Negrini, M., Bannister, S., Milicich, S. D., Chambefort, I., Miller, C. A., & Kilgour, G. (2023). Crustal basement terranes under the Taupō Volcanic Zone, New Zealand: Context for hydrothermal and magmatic processes. *Journal of Volcanology and Geothermal Research*, *440*, 107855. https://doi.org/10.1016/j.jvolgeores.2023.107855

Mujin, M., & Nakamura, M. (2014). A nanolite record of eruption style transition. *Geology*, *42*(7), 611-614. https://doi.org/10.1130/g35553.1

Mujin, M., Nakamura, M., & Miyake, A. (2017a). Eruption style and crystal size distributions: Crystallization of groundmass nanolites in the 2011 Shinmoedake eruption. *American Mineralogist: Journal of Earth and Planetary Materials*, *102*(12), 2367-2380. https://doi.org/0.2138/am-2017-6052CCBYNCND

Mujin, M., Nakamura, M., & Miyake, A. (2017b). *Characteristics of nanolite crystallization in volcanic pyroclasts* AGU Fall Meeting Abstracts, New Orleans. https://ui.adsabs.harvard.edu/abs/2017AGUFM.V32A..06M/abstract

Müntener, O., & Ulmer, P. (2018). Arc crust formation and differentiation constrained by experimental petrology. *American Journal of Science*, *318*(1), 64-89. https://doi.org/10.2475/01.2018.04

Murch, A. P., & Cole, P. D. (2019). Using microlites to gain insights into ascent conditions of differing styles of volcanism at Soufrière Hills Volcano. *Journal of Volcanology and Geothermal Research*, *384*, 221-231. https://doi.org/10.1016/j.jvolgeores.2019.07.022

Mutch, E. J. F., Maclennan, J., Shorttle, O., Edmonds, M., & Rudge, J. F. (2019). Rapid transcrustal magma movement under Iceland. *Nature Geoscience*, *12*(7), 569-574. https://doi.org/10.1038/s41561-019-0376-9

Nairn, I. A., Kobayashi, T., & Nakagawa, M. (1998). The~ 10 ka multiple vent pyroclastic eruption sequence at Tongariro Volcanic Centre, Taupo Volcanic Zone, New Zealand:: Part 1. Eruptive processes during regional extension. *Journal of Volcanology and Geothermal Research*, *86*(1-4), 19-44. https://doi.org/10.1016/S0377-0273(98)00085-7

Nakagawa, M., Nairn, I. A., & Kobayashi, T. (1998). The~ 10 ka multiple vent pyroclastic eruption sequence at Tongariro Volcanic Centre, Taupo Volcanic Zone, New Zealand: Part 2. Petrological insights into magma storage and transport during regional extension. *Journal of Volcanology and Geothermal Research*, *86*(1-4), 45-65. https://doi.org/10.1016/S0377-0273(98)00086-9

Nakagawa, M., Wada, K., & Wood, C. P. (2002). Mixed magmas, mush chambers and eruption triggers: Evidence from zoned clinopyroxene phenocrysts in Andesitic Scoria from the 1995 eruptions of Ruapehu volcano, New Zealand [Article]. *Journal of Petrology*, *43*(12), 2279-2303. https://doi.org/10.1093/petrology/43.12.2279

Nakano, T., Tsuchiyama, A., Uesugi, K., Uesugi, M., & Shinohara, K. (2006). *"Slice" - Softwares for basic 3-D analysis-*. In Japan Synchrotron Radiation Research Institute (JASRI). http://www-bl20.spring8.or.jp/slice/

Neave, D. A., & Putirka, K. D. (2017). A new clinopyroxene-liquid barometer, and implications for magma storage pressures under Icelandic rift zones. *American Mineralogist*, *102*(4), 777-794. https://doi.org/10.2138/am-2017-5968

Neave, D. A., & Maclennan, J. (2020). Clinopyroxene dissolution records rapid magma ascent. *Frontiers in Earth Science*, *8*, 188. https://doi.org/10.3389/feart.2020.00188

Neave, D. A. (2020). Chemical variability in peralkaline magmas and magma reservoirs: insights from the Khaggiar lava flow, Pantelleria, Italy. *Contributions to Mineralogy and Petrology*, *175*(4), 39. https://doi.org/10.1007/s00410-020-01678-0

Nielsen, S. G., & Marschall, H. R. (2017). Geochemical evidence for mélange melting in global arcs. *Science advances*, *3*(4), e1602402. https://doi.org/10.1126/sciadv.1602402

Noguchi, S., Toramaru, A., & Shimano, T. (2006). Crystallization of microlites and degassing during magma ascent: Constraints on the fluid mechanical behavior of magma during the Tenjo Eruption on Kozu Island, Japan. *Bulletin of Volcanology*, *68*(5), 432-449. https://doi.org/10.1007/s00445-005-0019-4

Nugroho, R., Disando, T., Kurniawan, I., & Abdurrachman, M. (2019). Crystal size distribution (CSD) of plagioclase phenocryst-microphenocryst and the calculation of crystal resident times in the continuous central eruption sequences of Mount Lasem, Central Java, Indonesia. *Journal of Physics: Conference Series*, *1363*(1), 012041. https://doi.org/10.1088/1742-6596/1363/1/012041

Ohnenstetter, D., & Brown, W. L. (1992). Overgrowth textures, disequilibrium zoning, and cooling history of a glassy four-pyroxene boninite dyke from New Caledonia. *Journal of Petrology*, *33*(1), 231-271. https://doi.org/10.1093/petrology/33.1.231

Okumura, S., Nakamura, M., Tsuchiyama, A., Nakano, T., & Uesugi, K. (2008). Evolution of bubble microstructure in sheared rhyolite: Formation of a channel ‐ like bubble network. *Journal of Geophysical Research: Solid Earth*, *113*(B7). https://doi.org/10.1029/2007JB005362

Okumura, S., Nakamura, M., Takeuchi, S., Tsuchiyama, A., Nakano, T., & Uesugi, K. (2009). Magma deformation may induce non-explosive volcanism via degassing through bubble networks. *Earth and Planetary Science Letters*, *281*(3-4), 267-274. https://doi.org/10.1016/j.epsl.2009.02.036

Okumura, S. H., Mujin, M., Tsuchiyama, A., & Miyake, A. (2022). 3D crystal size distributions of pyroxene nanolites from nano X-ray computed tomography: Improved correction of crystal size distributions from CSDCorrections for magma ascent dynamics in conduits. *American Mineralogist*, *107*(9), 1766-1778. https://doi.org/10.2138/am-2022-8039

Okumura, S. H., Mujin, M., Tsuchiyama, A., & Miyake, A. (2024). Crystal habit (tracht) of groundmass pyroxene crystals recorded magma ascent paths during the 2011 Shinmoedake eruption. *American Mineralogist*, *109*(2), 325-338. https://doi.org/10.2138/am-2022-8765

Ostwald, W. (1900). Über die vermeintliche Isomerie des roten und gelben Quecksilberoxyds und die Oberflächenspannung fester Körper. *Zeitschrift für Physikalische Chemie*, *34U*(1), 495-503. https://doi.org/10.1515/zpch-1900-3431

Owen, J., Tuffen, H., & McGarvie, D. W. (2013). Pre-eruptive volatile content, degassing paths and depressurisation explaining the transition in style at the subglacial rhyolitic eruption of Dalakvísl, South Iceland. *Journal of Volcanology and Geothermal Research*, *258*, 143-162. https://doi.org/0.1016/j.jvolgeores.2013.03.021

Pamukcu, A. S., & Gualda, G. A. (2010). Quantitative 3D petrography using X-ray tomography 2: Combining information at various resolutions. *Geosphere*, *6*(6), 775-781. https://doi.org/10.1130/GES00565.1

Paonita, A., & Martelli, M. (2006). Magma dynamics at mid-ocean ridges by noble gas kinetic fractionation: Assessment of magmatic ascent rates. *Earth and Planetary Science Letters*, *241*(1), 138-158. https://doi.org/10.1016/j.epsl.2005.10.018

Pappalardo, L., & Mastrolorenzo, G. (2010). Short residence times for alkaline Vesuvius magmas in a multi-depth supply system: Evidence from geochemical and textural studies. *Earth and Planetary Science Letters*, *296*(1), 133-143. https://doi.org/10.1016/j.epsl.2010.05.010

Pardo, N., Cronin, S., Palmer, A., Procter, J., & Smith, I. (2012). Andesitic Plinian eruptions at Mt. Ruapehu: quantifying the uppermost limits of eruptive parameters. *Bulletin of Volcanology*, *74*, 1161-1185. https://doi.org/10.1007/s00445-012-0588-y

Parolari, M., Gómez-Tuena, A., Cavazos-Tovar, J. G., & Hernández-Quevedo, G. (2018). A balancing act of crust creation and destruction along the western Mexican convergent margin. *Geology*, *46*(5), 455-458. https://doi.org/10.1130/G39972.1

Paton, C., Hellstrom, J., Paul, B., Woodhead, J., & Hergt, J. (2011). Iolite: Freeware for the visualisation and processing of mass spectrometric data [10.1039/C1JA10172B]. *Journal of Analytical Atomic Spectrometry*, *26*(12), 2508-2518. https://doi.org/10.1039/C1JA10172B

Perinelli, C., Mollo, S., Gaeta, M., De Cristofaro, S. P., Palladino, D. M., Armienti, P., Scarlato, P., & Putirka, K. D. (2016). An improved clinopyroxene-based hygrometer for Etnean magmas and implications for eruption triggering mechanisms. *American Mineralogist*, *101*(12), 2774-2777. https://doi.org/10.2138/am-2016-5916

Phillips, M., & Till, C. B. (2021). Crustal storage and ascent history of the Mt. Shasta primitive magnesian andesite: implications for arc magma crustal flux rates. *Contributions to Mineralogy and Petrology*, *177*(1), 9. https://doi.org/10.1007/s00410-021-01853-x

Piquer, J., Fischer, T., Torres, F., & Plissart, G. (2023). Spatiotemporal variability of magmatic products under a changing structural and tectonic context: a case study in the Andes of southern Central Chile [Original Research]. *Frontiers in Earth Science*, *Volume 11 - 2023*. https://doi.org/10.3389/feart.2023.1064209

Plank, T., Benjamin, E., Wade, J., & Grove, T. (2004). *A new hygrometer based on the europium anomaly in clinopyroxene phenocrysts in arc volcanic rocks* AGU Fall Meeting Abstracts, San Francisco. https://ui.adsabs.harvard.edu/abs/2004AGUFM.V12A..05P/abstract

Plank, T., Kelley, K. A., Zimmer, M. M., Hauri, E. H., & Wallace, P. J. (2013). Why do mafic arc magmas contain ~4wt% water on average? *Earth and Planetary Science Letters*, *364*, 168-179. https://doi.org/10.1016/j.epsl.2012.11.044

Polo-Sánchez, A., Flaherty, T., Hervé, G., Druitt, T., Fabbro, G. N., Nomikou, P., & Balcone-Boissard, H. (2023). Tracking timescales of magma reservoir recharge through caldera cycles at Santorini (Greece). Emphasis on an explosive eruption of Kameni Volcano [Original Research]. *Frontiers in Earth Science*, *Volume 11 - 2023*. https://doi.org/10.3389/feart.2023.1128083

Pompilio, M., Bertagnini, A., Del Carlo, P., & Di Roberto, A. (2017). Magma dynamics within a basaltic conduit revealed by textural and compositional features of erupted ash: the December 2015 Mt. Etna paroxysms. *Scientific Reports*, *7*(1), 4805. https://doi.org/10.1038/s41598-017-05065-x

Popa, R.-G., Tollan, P., Bachmann, O., Schenker, V., Ellis, B., & Allaz, J. M. (2021a). Water exsolution in the magma chamber favors effusive eruptions: Application of Cl-F partitioning behavior at the Nisyros-Yali volcanic area. *Chemical Geology*, *570*, 120170. https://doi.org/10.1016/j.chemgeo.2021.120170

Popa, R.-G., Bachmann, O., & Huber, C. (2021b). Explosive or effusive style of volcanic eruption determined by magma storage conditions. *Nature Geoscience*, *14*(10), 781-786. https://doi.org/10.1038/s41561-021-00827-9

Preece, K., Barclay, J., Gertisser, R., & Herd, R. A. (2013). Textural and micro-petrological variations in the eruptive products of the 2006 dome-forming eruption of Merapi volcano, Indonesia: Implications for sub-surface processes. *Journal of Volcanology and Geothermal Research*, *261*, 98-120. https://doi.org/10.1016/j.jvolgeores.2013.02.006

Preece, K., Gertisser, R., Barclay, J., Charbonnier, S. J., Komorowski, J.-C., & Herd, R. A. (2016). Transitions between explosive and effusive phases during the cataclysmic 2010 eruption of Merapi volcano, Java, Indonesia. *Bulletin of Volcanology*, *78*, 1-16. https://doi.org/10.1007/s00445-016-1046-z

Price, R., Mortimer, N., Smith, I., & Maas, R. (2015). Whole-rock geochemical reference data for Torlesse and Waipapa terranes, North Island, New Zealand. *New Zealand Journal of Geology and Geophysics*, *58*(3), 213-228. https://doi.org/10.1080/00288306.2015.1026832

Price, R. C., Gamble, J. A., Smith, I. E., Stewart, R. B., Eggins, S., & Wright, I. C. (2005). An integrated model for the temporal evolution of andesites and rhyolites and crustal development in New Zealand's North Island. *Journal of Volcanology and Geothermal Research*, *140*(1-3), 1-24. https://doi.org/10.1016/j.jvolgeores.2004.07.013

Price, R. C., Gamble, J. A., Smith, I. E., Maas, R., Waight, T., Stewart, R. B., & Woodhead, J. (2012). The anatomy of an andesite volcano: a time–stratigraphic study of andesite petrogenesis and crustal evolution at Ruapehu Volcano, New Zealand. *Journal of Petrology*, *53*(10), 2139-2189. https://doi.org/0.1093/petrology/egs050

Price, R. C., Smith, I. E., Stewart, R. B., Gamble, J. A., Gruender, K., & Maas, R. (2016). High-K andesite petrogenesis and crustal evolution: Evidence from mafic and ultramafic xenoliths, Egmont Volcano (Mt. Taranaki) and comparisons with Ruapehu Volcano, North Island, New Zealand. *Geochimica et Cosmochimica Acta*, *185*, 328-357. https://doi.org/10.1016/j.gca.2015.12.009

Pupier, E., Duchene, S., & Toplis, M. J. (2008). Experimental quantification of plagioclase crystal size distribution during cooling of a basaltic liquid. *Contributions to Mineralogy and Petrology*, *155*(5), 555-570. https://doi.org/10.1007/s00410-007-0258-9

Putirka, K., Johnson, M., Kinzler, R., Longhi, J., & Walker, D. (1996). Thermobarometry of mafic igneous rocks based on clinopyroxene-liquid equilibria, 0–30 kbar. *Contributions to Mineralogy and Petrology*, *123*, 92-108. https://doi.org/10.1007/s004100050145

Putirka, K. (1999). Clinopyroxene + liquid equilibria to 100 kbar and 2450 K. *Contributions to Mineralogy and Petrology*, *135*(2), 151-163. https://doi.org/10.1007/s004100050503

Putirka, K., & Condit, C. D. (2003). Cross section of a magma conduit system at the margin of the Colorado Plateau. *Geology*, *31*(8), 701-704. https://doi.org/10.1130/G19550.1

Putirka, K. D. (2005). Igneous thermometers and barometers based on plagioclase+ liquid equilibria: Tests of some existing models and new calibrations. *American Mineralogist*, *90*(2-3), 336-346. https://doi.org/10.2138/am.2005.1449

Putirka, K. D. (2008). Thermometers and barometers for volcanic systems. *Reviews in Mineralogy and Geochemistry*, *69*(1), 61-120. https://doi.org/10.2138/rmg.2008.69.3

Renjith, M. L. (2014). Micro-textures in plagioclase from 1994–1995 eruption, Barren Island Volcano: Evidence of dynamic magma plumbing system in the Andaman subduction zone. *Geoscience Frontiers*, *5*(1), 113-126. https://doi.org/10.1016/j.gsf.2013.03.006

Resmini, R. G., & Marsh, B. D. (1995). Steady-state volcanism, paleoeffusion rates, and magma system volume inferred from plagioclase crystal size distributions in mafic lavas: Dome Mountain, Nevada. *Journal of Volcanology and Geothermal Research*, *68*(4), 273-296. https://doi.org/10.1016/0377-0273(95)00003-5

Reubi, O., & Blundy, J. (2009). A dearth of intermediate melts at subduction zone volcanoes and the petrogenesis of arc andesites. *Nature*, *461*(7268), 1269-1273. https://doi.org/10.1038/nature08510

Reubi, O., & Müntener, O. (2022). Making Andesites and the Continental Crust: Mind the Step When Wet. *Journal of Petrology*, *63*(6). https://doi.org/10.1093/petrology/egac044

Rhodes, J., Dungan, M., Blanchard, D., & Long, P. (1979). Magma mixing at mid-ocean ridges: evidence from basalts drilled near 22 N on the Mid-Atlantic Ridge. *Tectonophysics*, *55*(1-2), 35-61. https://doi.org/10.1016/0040-1951(79)90334-2

Ripepe, M., Lacanna, G., Pistolesi, M., Silengo, M. C., Aiuppa, A., Laiolo, M., Massimetti, F., Innocenti, L., Della Schiava, M., Bitetto, M., La Monica, F. P., Nishimura, T., Rosi, M., Mangione, D., Ricciardi, A., Genco, R., Coppola, D., Marchetti, E., & Delle Donne, D. (2021). Ground deformation reveals the scale-invariant conduit dynamics driving explosive basaltic eruptions. *Nature communications*, *12*(1), 1683. https://doi.org/10.1038/s41467-021-21722-2

Rooyakkers, S. M., Stix, J., Berlo, K., Petrelli, M., Hampton, R. L., Barker, S. J., & Morgavi, D. (2021). The Origin of Rhyolitic Magmas at Krafla Central Volcano (Iceland). *Journal of Petrology*, *62*(8). https://doi.org/10.1093/petrology/egab064

Rout, S. S., Blum-Oeste, M., & Wörner, G. (2021). Long-Term Temperature Cycling in a Shallow Magma Reservoir: Insights from Sanidine Megacrysts at Taápaca Volcano, Central Andes. *Journal of Petrology*, *62*(9). https://doi.org/10.1093/petrology/egab010

Rowland, J. V., Wilson, C. J. N., & Gravley, D. M. (2010). Spatial and temporal variations in magma-assisted rifting, Taupo Volcanic Zone, New Zealand. *Journal of Volcanology and Geothermal Research*, *190*(1), 89-108. https://doi.org/10.1016/j.jvolgeores.2009.05.004

Rowlands, D. P., White, R. S., & Haines, A. J. (2005). Seismic tomography of the Tongariro Volcanic Centre, New Zealand. *Geophysical Journal International*, *163*(3), 1180-1194. https://doi.org/10.1111/j.1365-246X.2005.02716.x

Ruprecht, P., & Bachmann, O. (2010). Pre-eruptive reheating during magma mixing at Quizapu volcano and the implications for the explosiveness of silicic arc volcanoes. *Geology*, *38*(10), 919-922. https://doi.org/10.1130/G31110.1

Ruprecht, P., & Plank, T. (2013). Feeding andesitic eruptions with a high-speed connection from the mantle. *Nature*, *500*(7460), 68-72. https://doi.org/10.1038/nature12342

Rutherford, M. J. (2008). Magma Ascent Rates. *Reviews in Mineralogy and Geochemistry*, *69*(1), 241-271. https://doi.org/10.2138/rmg.2008.69.7

Rychert, C. A., Hammond, J. O. S., Harmon, N., Michael Kendall, J., Keir, D., Ebinger, C., Bastow, I. D., Ayele, A., Belachew, M., & Stuart, G. (2012). Volcanism in the Afar Rift sustained by decompression melting with minimal plume influence. *Nature Geoscience*, *5*(6), 406-409. https://doi.org/10.1038/ngeo1455

Salisbury, M. J., Bohrson, W. A., Clynne, M. A., Ramos, F. C., & Hoskin, P. (2008). Multiple plagioclase crystal populations identified by crystal size distribution and in situ chemical data: implications for timescales of magma chamber processes associated with the 1915 eruption of Lassen Peak, CA. *Journal of Petrology*, *49*(10), 1755-1780. https://doi.org/10.1093/petrology/egn045

Sano, K., Wada, K., & Sato, E. (2015). Rates of water exsolution and magma ascent inferred from microstructures and chemical analyses of the Tokachi–Ishizawa obsidian lava, Shirataki, northern Hokkaido, Japan. *Journal of Volcanology and Geothermal Research*, *292*, 29-40. https://doi.org/10.1016/j.jvolgeores.2014.11.015

Schaaf, P., Corona-Chávez, P., Ortiz Joya, G., Solís-Pichardo, G., Arrieta García, G., Hernández Treviño, T., & Poli, S. (2022). Magma hybridization, mingling, and recycling in the Manzanillo plutonic complex, Mexican Cordillera. *International Geology Review*, *64*(9), 1248-1269. https://doi.org/10.1080/00206814.2021.1919931

Schellart, W. P., & Spakman, W. (2012). Mantle constraints on the plate tectonic evolution of the Tonga–Kermadec–Hikurangi subduction zone and the South Fiji Basin region. *Australian Journal of Earth Sciences*, *59*(6), 933-952. https://doi.org/10.1080/08120099.2012.679692

Schettino, E., González-Pérez, I., Marchesi, C., González-Jiménez, J. M., Grégoire, M., Tilhac, R., Gervilla, F., Blanco-Quintero, I. F., Corgne, A., & Schilling, M. E. (2024). Slab melting boosts the mantle wedge contribution to Li-rich magmas. *Scientific Reports*, *14*(1), 15168. https://doi.org/10.1038/s41598-024-66174-y

Schiavon, B., Mollo, S., Pontesilli, A., Del Bello, E., Nazzari, M., & Scarlato, P. (2023). Plagioclase crystal size distribution parameterization: A tool for tracking magma dynamics at Stromboli. *Lithos*, *446-447*, 107143. https://doi.org/10.1016/j.lithos.2023.107143

Schindelin, J., Arganda-Carreras, I., Frise, E., Kaynig, V., Longair, M., Pietzsch, T., Preibisch, S., Rueden, C., Saalfeld, S., & Schmid, B. (2012). Fiji: an open-source platform for biological-image analysis. *Nature methods*, *9*(7), 676-682. https://doi.org/10.1038/nmeth.2019

Schipper, C. I., Castro, J. M., Tuffen, H., James, M. R., & How, P. (2013). Shallow vent architecture during hybrid explosive–effusive activity at Cordón Caulle (Chile, 2011–12): evidence from direct observations and pyroclast textures. *Journal of Volcanology and Geothermal Research*, *262*, 25-37. https://doi.org/10.1016/j.jvolgeores.2013.06.005

Schmeling, H. (2010). Dynamic models of continental rifting with melt generation. *Tectonophysics*, *480*(1), 33-47. https://doi.org/10.1016/j.tecto.2009.09.005

Schmid, M., Kueppers, U., Cigala, V., & Dingwell, D. B. (2022). Complex geometry of volcanic vents and asymmetric particle ejection: experimental insights. *Bulletin of Volcanology*, *84*(8), 71. https://doi.org/10.1007/s00445-022-01580-6

Schneider, C. A., Rasband, W. S., & Eliceiri, K. W. (2012). NIH Image to ImageJ: 25 years of image analysis. *Nature methods*, *9*(7), 671-675. https://doi.org/10.1038/nmeth.2089

Schoneveld, L., Barnes, S. J., Luolavirta, K., Hu, S., Verrall, M., & Le Vaillant, M. (2025). Extent and survival of zoned pyroxene within intrusions hosting magmatic sulfides: Implications for zoned pyroxene as a prospectivity indicator. *Mineralium Deposita*, *60*(2), 533-549. https://doi.org/10.1007/s00126-024-01292-1

Scott, B. (2013). *A revised catalogue of Ruapehu volcano eruptive activity: 1830-2012*. GNS Science.

Seaman, S. (2000). Crystal clusters, feldspar glomerocrysts, and magma envelopes in the Atascosa Lookout lava flow, southern Arizona, USA: recorders of magmatic events. *Journal of Petrology*, *41*(5), 693-716. https://doi.org/10.1093/petrology/41.5.693

Seebeck, H., Nicol, A., Giba, M., Pettinga, J., & Walsh, J. (2014). Geometry of the subducting Pacific plate since 20 Ma, Hikurangi margin, New Zealand. *Journal of the Geological Society*, *171*(1), 131-143. https://doi.org/10.1144/jgs2012-14

Sen, G. (2014). *Petrology: Principles and Practice*. Springer Berlin, Heidelberg. https://doi.org/10.1007/978-3-642-38800-2

Shane, P., Doyle, L. R., & Nairn, I. A. (2008). Heterogeneous andesite–dacite ejecta in 26–16.6 ka pyroclastic deposits of Tongariro Volcano, New Zealand: the product of multiple magma-mixing events. *Bulletin of Volcanology*, *70*, 517-536. https://doi.org/10.1007/s00445-007-0152-3

Shane, P., Cocker, K., Coote, A., Stirling, C. H., & Reid, M. R. (2019). The prevalence of plagioclase antecrysts and xenocrysts in andesite magma, exemplified by lavas of the Tongariro volcanic complex, New Zealand. *Contributions to Mineralogy and Petrology*, *174*, 1-18. https://doi.org/10.1007/s00410-019-1626-y

Shea, T., & Hammer, J. E. (2013). Kinetics of cooling- and decompression-induced crystallization in hydrous mafic-intermediate magmas. *Journal of Volcanology and Geothermal Research*, *260*, 127-145. https://doi.org/10.1016/j.jvolgeores.2013.04.018

Sisson, T., & Bronto, S. (1998). Evidence for pressure-release melting beneath magmatic arcs from basalt at Galunggung, Indonesia. *Nature*, *391*(6670), 883-886. https://doi.org/10.1038/36087

Skora, S., & Blundy, J. (2010). High-pressure hydrous phase relations of radiolarian clay and implications for the involvement of subducted sediment in arc magmatism. *Journal of Petrology*, *51*(11), 2211-2243. https://doi.org/10.1093/petrology/egq054

Smith, P. M., & Asimow, P. D. (2005). Adiabat_1ph: A new public front-end to the MELTS, pMELTS, and pHMELTS models. *Geochemistry, Geophysics, Geosystems*, *6*(2). https://doi.org/10.1029/2004GC000816

Sola, A. M., Morfulis, M., Weinberg, R. F., & Maro, G. (2025). Thermal Structure and Melting Conditions of the Mantle Beneath Salta Rift, NW Argentina: A Combined Empirical and Forward Petrological Approach. *Journal of Petrology*, *66*(9). https://doi.org/10.1093/petrology/egaf080

Solano, J., Jackson, M., Sparks, R., & Blundy, J. (2014). Evolution of major and trace element composition during melt migration through crystalline mush: implications for chemical differentiation in the crust. *American Journal of Science*, *314*(5), 895-939. https://doi.org/10.2475/05.2014.01

Spörli, K., & Rowland, J. (2006). 'Column on column'structures as indicators of lava/ice interaction, Ruapehu andesite volcano, New Zealand. *Journal of Volcanology and Geothermal Research*, *157*(4), 294-310. https://doi.org/10.1016/j.jvolgeores.2006.04.004

Stern, T., Stratford, W., & Salmon, M. (2006). Subduction evolution and mantle dynamics at a continental margin: Central North Island, New Zealand. *Reviews of geophysics*, *44*(4). https://doi.org/10.1029/2005RG000171

Stevenson, J. A., Smellie, J. L., McGarvie, D. W., Gilbert, J. S., & Cameron, B. I. (2009). Subglacial intermediate volcanism at Kerlingarfjöll, Iceland: magma–water interactions beneath thick ice. *Journal of Volcanology and Geothermal Research*, *185*(4), 337-351. https://doi.org/10.1016/j.jvolgeores.2008.12.016

Stewart, R. B. (2010). Andesites as Magmatic Liquids or Liquid-crystal Mixtures; Insights from Egmont and Ruapehu Volcanoes, New Zealand Research Article. *Central European Journal of Geosciences*, *2*, 329-338. https://doi.org/10.2478/v10085-010-0022-7

Stix, J. (2018). Understanding fast and slow unrest at volcanoes and implications for eruption forecasting. *Frontiers in Earth Science*, *6*, 56. https://doi.org/10.3389/feart.2018.00056

Stratford, W. R., & Stern, T. A. (2006). Crust and upper mantle structure of a continental backarc: Central North Island, New Zealand [Article]. *Geophysical Journal International*, *166*(1), 469-484. https://doi.org/10.1111/j.1365-246X.2006.02967.x

Straub, S. M., Gomez-Tuena, A., Stuart, F. M., Zellmer, G. F., Espinasa-Perena, R., Cai, Y., & Iizuka, Y. (2011). Formation of hybrid arc andesites beneath thick continental crust. *Earth and Planetary Science Letters*, *303*(3-4), 337-347. https://doi.org/10.1016/j.epsl.2011.01.013

Streck, M. J. (2008). Mineral textures and zoning as evidence for open system processes. *Reviews in Mineralogy and Geochemistry*, *69*(1), 595-622. https://doi.org/10.2138/rmg.2008.69.15

Suhendro, I., Harijoko, A., Wibowo, H. E., Naen, G. N. R. B., Agroli, G., Nurfiani, D., Mutaqin, B. W., & Sobaruddin, D. P. (2025). Timing, process, and origin of the alkaline magmas beneath Satonda volcano (Lesser Sunda Arc, Indonesia): evidence of magma mush disruption and mobilization. *Bulletin of Volcanology*, *87*(3), 25. https://doi.org/10.1007/s00445-025-01811-6

Svoboda, C., Rooney, T. O., Girard, G., & Deering, C. (2021). Transcrustal magmatic systems: evidence from andesites of the southern Taupo Volcanic Zone. *Journal of the Geological Society*, *179*(1). https://doi.org/10.1144/jgs2020-204

Svoboda, C., Rooney, T. O., Girard, G., & Deering, C. (2022). Transcrustal magmatic systems: evidence from andesites of the southern Taupo Volcanic Zone. *Journal of the Geological Society*, *179*(1), jgs2020-2204. https://doi.org/10.1144/jgs2020-204

Szramek, L., Gardner, J. E., & Larsen, J. (2006). Degassing and microlite crystallization of basaltic andesite magma erupting at Arenal Volcano, Costa Rica. *Journal of Volcanology and Geothermal Research*, *157*(1), 182-201. https://doi.org/10.1016/j.jvolgeores.2006.03.039

Tatsumi, Y., Hamilton, D., & Nesbitt, R. (1986). Chemical characteristics of fluid phase released from a subducted lithosphere and origin of arc magmas: evidence from high-pressure experiments and natural rocks. *Journal of Volcanology and Geothermal Research*, *29*(1-4), 293-309. https://doi.org/10.1016/0377-0273(86)90049-1

Tatsumi, Y. (2005). The subduction factory: How it operates in the evolving Earth. *GSA today*, *15*(7), 4. https://doi.org/10:1130/1052-5173(2005)015<4:TSFHIO>2.0.CO;2

Tenzer, R., Sirguey, P., Rattenbury, M., & Nicolson, J. (2011). A digital rock density map of New Zealand. *Computers & Geosciences*, *37*(8), 1181-1191. https://doi.org/10.1016/j.cageo.2010.07.010

Thiele, S. T., Cruden, A. R., Zhang, X., Micklethwaite, S., & Matchan, E. L. (2021). Reactivation of Magma Pathways: Insights From Field Observations, Geochronology, Geomechanical Tests, and Numerical Models. *Journal of Geophysical Research: Solid Earth*, *126*(5), e2020JB021477. https://doi.org/10.1029/2020JB021477

Timm, C., Davy, B., Haase, K., Hoernle, K. A., Graham, I. J., De Ronde, C. E., Woodhead, J., Bassett, D., Hauff, F., & Mortimer, N. (2014). Subduction of the oceanic Hikurangi Plateau and its impact on the Kermadec arc. *Nature communications*, *5*(1), 4923. https://doi.org/10.1038/ncomms5923

Toramaru, A., Noguchi, S., Oyoshihara, S., & Tsune, A. (2008). MND (microlite number density) water exsolution rate meter. *Journal of Volcanology and Geothermal Research*, *175*(1-2), 156-167. https://doi.org/10.1016/j.jvolgeores.2008.03.035

Toramaru, A. (2021). CSD (crystal size distribution). In *Vesiculation and Crystallization of Magma: Fundamentals of the Volcanic Eruption Process* (pp. 301-347). Springer. https://doi.org/10.1007/978-981-16-4209-8

Townsend, D., Leonard, G., Conway, C., Eaves, S., & Wilson, C. (2017). *Geology of the Tongariro National Park area, scale 1 :60 000*. Lower Hutt, New Zealand, GNS Science.

Troll, V. R., & Deegan, F. M. (2023). The magma plumbing system of Merapi: The petrological perspective. In R. Gertisser, V. R. Troll, T. R. Walter, I. G. M. A. Nandaka, & A. Ratdomopurbo (Eds.), *Merapi Volcano: Geology, Eruptive Activity, and Monitoring of a High-Risk Volcano* (pp. 233-263). Springer. https://doi.org/10.1007/978-3-031-15040-1_8

Tsuchiyama, A. (1985). Dissolution kinetics of plagioclase in the melt of the system diopside-albite-anorthite, and origin of dusty plagioclase in andesites. *Contributions to Mineralogy and Petrology*, *89*(1), 1-16. https://doi.org/10.1007/BF01177585

Tsuchiyama, A., Uesugi, K., Nakano, T., & Ikeda, S. (2005). Quantitative evaluation of attenuation contrast of X-ray computed tomography images using monochromatized beams. *American Mineralogist*, *90*(1), 132-142. https://doi.org/10.2138/am.2005.1552

Tsuchiyama, A., Nakano, T., Uesugi, K., Uesugi, M., Takeuchi, A., Suzuki, Y., Noguchi, R., Matsumoto, T., Matsuno, J., & Nagano, T. (2013). Analytical dual-energy microtomography: A new method for obtaining three-dimensional mineral phase images and its application to Hayabusa samples. *Geochimica et Cosmochimica Acta*, *116*, 5-16. https://doi.org/10.1016/j.gca.2012.11.036

Tuffen, H., & Castro, J. M. (2009). The emplacement of an obsidian dyke through thin ice: Hrafntinnuhryggur, Krafla Iceland. *Journal of Volcanology and Geothermal Research*, *185*(4), 352-366. https://doi.org/10.1016/j.jvolgeores.2008.10.021

Turner, S. J., & Langmuir, C. H. (2022). A quantitative framework for global variations in arc geochemistry. *Earth and Planetary Science Letters*, *584*, 117411. https://doi.org/10.1016/j.epsl.2022.117411

Ubide, T., Galé, C., Larrea, P., Arranz, E., & Lago, M. (2014). Antecrysts and their effect on rock compositions: The Cretaceous lamprophyre suite in the Catalonian Coastal Ranges (NE Spain). *Lithos*, *206-207*, 214-233. https://doi.org/10.1016/j.lithos.2014.07.029

Ubide, T., McKenna, C. A., Chew, D. M., & Kamber, B. S. (2015). High-resolution LA-ICP-MS trace element mapping of igneous minerals: In search of magma histories. *Chemical Geology*, *409*, 157-168. https://doi.org/10.1016/j.chemgeo.2015.05.020

Ubide, T., & Kamber, B. S. (2018). Volcanic crystals as time capsules of eruption history. *Nature communications*, *9*(1), 326. https://doi.org/10.1038/s41467-017-02274-w

Ubide, T., Mollo, S., Zhao, J.-x., Nazzari, M., & Scarlato, P. (2019). Sector-zoned clinopyroxene as a recorder of magma history, eruption triggers, and ascent rates. *Geochimica et Cosmochimica Acta*, *251*, 265-283. https://doi.org/10.1016/j.gca.2019.02.021

Ubide, T., Larrea, P., Becerril, L., & Galé, C. (2022). Volcanic plumbing filters on ocean-island basalt geochemistry. *Geology*, *50*(1), 26-31. https://doi.org/10.1130/g49224.1

Ubide, T., Márquez, Á., Ancochea, E., Huertas, M. J., Herrera, R., Coello-Bravo, J. J., Sanz-Mangas, D., Mulder, J., MacDonald, A., & Galindo, I. (2023). Discrete magma injections drive the 2021 La Palma eruption. *Science advances*, *9*(27), eadg4813. https://doi.org/10.1126/sciadv.adg4813

Ubide, T., Wieser, P. E., Bachmann, O., Gualda, G. A. R., Neave, D. A., Samaniego, P., & Kent, A. (2024). Petrological characterisation of magma storage. In C. Bonadonna, L. Caricchi, A. Clarke, P. Cole, J. Lindsay, J. B. Lowenstern, R. E. A. Robertson, & V. M. L. (Eds.), *Encyclopedia of Volcanoes, 3rd Ed*. https://doi.org/10.31223/X5NX44

Ubide, T., Murphy, D. T., Emo, R. B., Jones, M. W. M., Acevedo Zamora, M. A., & Kamber, B. S. (2025). Early pyroxene crystallisation deep below mid-ocean ridges. *Earth and Planetary Science Letters*, *663*, 119423. https://doi.org/10.1016/j.epsl.2025.119423

Uesugi, K. (2025). *Reconstruction and convert for absorption CT*. In *Reconstruction and convert for absorption CT (CUDA 12.2)* (Version 1.2) Japan Synchrotron Radiation Research Institute (JASRI). http://www-bl20.spring8.or.jp/xct/index-e.html

Ulmer, P., Kaegi, R., & Müntener, O. (2018). Experimentally derived intermediate to silica-rich arc magmas by fractional and equilibrium crystallization at 1· 0 GPa: an evaluation of phase relationships, compositions, liquid lines of descent and oxygen fugacity. *Journal of Petrology*, *59*(1), 11-58. https://doi.org/10.1093/petrology/egy017

Van Gerve, T., Neave, D., Almeev, R., Holtz, F., & Namur, O. (2020). Zoned crystal records of transcrustal magma transport, storage and differentiation: insights from the Shatsky Rise oceanic plateau. *Journal of Petrology*, *61*(8), egaa080. https://doi.org/10.1093/petrology/egaa080

Vander Auwera, J., Bechon, T., Montalbano, S., Bolle, O., Schiano, P., Cluzel, N., Devidal, J.-L., Ottolini, L., Lara, L. E., & Namur, O. (2025). *So close, so different: Calbuco and Osorno volcanoes (Central Southern Volcanic Zone, Chile) tap into mantle sources that diverge only in their volatile content* Goldschmidt Conference, Prague. https://goldschmidtabstracts.info/2025/29590.pdf

Viccaro, M., Giacomoni, P. P., Ferlito, C., & Cristofolini, R. (2010). Dynamics of magma supply at Mt. Etna volcano (Southern Italy) as revealed by textural and compositional features of plagioclase phenocrysts. *Lithos*, *116*(1-2), 77-91. https://doi.org/10.1016/j.lithos.2009.12.012

Viccaro, M., Cannata, A., Cannavò, F., De Rosa, R., Giuffrida, M., Nicotra, E., Petrelli, M., & Sacco, G. (2021). Shallow conduit dynamics fuel the unexpected paroxysms of Stromboli volcano during the summer 2019. *Scientific Reports*, *11*(1), 266. https://doi.org/10.1038/s41598-020-79558-7

Villalba, N., Murcia, H., Jerez, E., Piedrahita, D., Schonwalder-Ángel, D., Pardo-Trujillo, A., & Echeverri, S. (2023). Compositional and geothermobarometric analysis of the Upper Miocene tholeiitic volcanic products in the northern Andes at 5-6° N latitude: The Combia Volcanic Province. *Andean geology*, *50*(2), 181-200. https://doi.org/10.5027/andgeov50n2-3503

Villamor, P., & Berryman, K. (2006a). Evolution of the southern termination of the Taupo Rift, New Zealand. *New Zealand Journal of Geology and Geophysics*, *49*(1), 23-37. https://doi.org/10.1080/00288306.2006.9515145

Villamor, P., & Berryman, K. (2006b). Late Quaternary geometry and kinematics of faults at the southern termination of the Taupo Volcanic Zone, New Zealand. *New Zealand Journal of Geology and Geophysics*, *49*(1), 1-21. https://doi.org/10.1080/00288306.2006.9515144

Villamor, P., Berryman, K., Ellis, S., Schreurs, G., Wallace, L., Leonard, G., Langridge, R., & Ries, W. (2017). Rapid evolution of subduction ‐ related continental intraarc rifts: The Taupo Rift, New Zealand. *Tectonics*, *36*(10), 2250-2272. https://doi.org/10.1002/2017TC004715

Vogt, K., Castro, A., & Gerya, T. (2013). Numerical modeling of geochemical variations caused by crustal relamination. *Geochemistry, Geophysics, Geosystems*, *14*(2), 470-487. https://doi.org/10.1002/ggge.20072

Vona, A., Romano, C., Giordano, G., & Sulpizio, R. (2020). Linking magma texture, rheology and eruptive style during the 472 AD Pollena Subplinian eruption (Somma-Vesuvius). *Lithos*, *370*, 105658. https://doi.org/10.1016/j.lithos.2020.105658

Wagner, C. (1961). Theorie der alterung von niederschlägen durch umlösen (Ostwald ‐ reifung). *Zeitschrift für Elektrochemie, Berichte der Bunsengesellschaft für physikalische Chemie*, *65*(7 ‐ 8), 581-591. https://doi.org/10.1002/bbpc.19610650704

Waight, T., Price, R., Stewart, R., Smith, I., & Gamble, J. (1999). Stratigraphy and geochemistry of the Turoa area, with implications for andesite petrogenesis at Mt

Ruapehu, Taupo Volcanic Zone, New Zealand. *New Zealand Journal of Geology and Geophysics*, *42*(4), 513-532. https://doi.org/10.1080/00288306.1999.9514858

Waight, T. E., Troll, V. R., Gamble, J. A., Price, R. C., & Chadwick, J. P. (2017). Hf isotope evidence for variable slab input and crustal addition in basalts and andesites of the Taupo Volcanic Zone, New Zealand. *Lithos*, *284-285*, 222-236. https://doi.org/10.1016/j.lithos.2017.04.009

Wang, M., Wang, C. Y., & Tan, W. (2022). Compositional Evolution of Interstitial Liquid After Onset of Abundant Fe–Ti Oxide Crystallization in Crystal Mush: Insights from Late-Stage Microstructures and Mineral Compositions of the Bijigou Layered Intrusion, Central China. *Journal of Petrology*, *63*(4), egac025. https://doi.org/10.1093/petrology/egac025

Ward, K. M., Zandt, G., Beck, S. L., Christensen, D. H., & McFarlin, H. (2014). Seismic imaging of the magmatic underpinnings beneath the Altiplano-Puna volcanic complex from the joint inversion of surface wave dispersion and receiver functions. *Earth and Planetary Science Letters*, *404*, 43-53. https://doi.org/10.1016/j.epsl.2014.07.022

Waters, L. E., & Lange, R. A. (2015). An updated calibration of the plagioclase-liquid hygrometer-thermometer applicable to basalts through rhyolites. *American Mineralogist*, *100*(10), 2172-2184. https://doi.org/10.2138/am-2015-5232

Weber, G., & Blundy, J. (2024). A Machine Learning-Based Thermobarometer for Magmatic Liquids. *Journal of Petrology*, *65*(4). https://doi.org/10.1093/petrology/egae020

Welsch, B., Hammer, J., Baronnet, A., Jacob, S., Hellebrand, E., & Sinton, J. (2016). Clinopyroxene in postshield Haleakala ankaramite: 2. Texture, compositional zoning and supersaturation in the magma. *Contributions to Mineralogy and Petrology*, *171*, 1-19. https://doi.org/10.1007/s00410-015-1213-9

Wenzel, A., Filiberto, J., Stephen, N., Schwenzer, S. P., & Hammond, S. J. (2021). Constraints on the petrologic history of gabbroic shergottite Northwest Africa 6963 from pyroxene zoning profiles and electron backscattered diffraction. *Meteoritics & Planetary Science*, *56*(9), 1744-1757. https://doi.org/10.1111/maps.13737

Wibowo, H. E., Nakagawa, M., Kuritani, T., Furukawa, R., Prambada, O., & Harijoko, A. (2022). Petrological and geochemical study of Sundoro Volcano, Central Java, Indonesia: Temporal variations in differentiation and source processes during the growth of an individual volcano. *Journal of Petrology*, *63*(9), egac083. https://doi.org/10.1093/petrology/egac083

Wieser, P., Petrelli, M., Lubbers, J., Wieser, E., Ozaydin, S., Kent, A., & Till, C. (2022). Thermobar: An open-source Python3 tool for thermobarometry and hygrometry. *Volcanica*, *5*(2), 349 - 384. https://doi.org/10.30909/vol.05.02.349384

Wieser, P. E., Kent, A. J., Till, C. B., Donovan, J., Neave, D. A., Blatter, D. L., & Krawczynski, M. J. (2023a). Barometers behaving badly I: Assessing the influence of analytical and experimental uncertainty on clinopyroxene thermobarometry calculations at crustal conditions. *Journal of Petrology*, *64*(2), egac126. https://doi.org/10.1093/petrology/egac126

Wieser, P. E., Kent, A. J. R., & Till, C. B. (2023b). Barometers Behaving Badly II: a Critical Evaluation of Cpx-Only and Cpx-Liq Thermobarometry in Variably-Hydrous Arc Magmas. *Journal of Petrology*, *64*(8). https://doi.org/10.1093/petrology/egad050

Wilson, C., Houghton, B., McWilliams, M., Lanphere, M., Weaver, S., & Briggs, R. (1995). Volcanic and structural evolution of Taupo Volcanic Zone, New Zealand: a review. *Journal of Volcanology and Geothermal Research*, *68*(1-3), 1-28. https://doi.org/10.1016/0377-0273(95)00006-G

Wilson, C. J., & Rowland, J. V. (2016). The volcanic, magmatic and tectonic setting of the Taupo Volcanic Zone, New Zealand, reviewed from a geothermal perspective. *Geothermics*, *59*, 168-187. https://doi.org/10.1016/j.geothermics.2015.06.013

Wilson, L., & Head, J. W. (2007). Heat transfer in volcano–ice interactions on Earth. *Annals of Glaciology*, *45*, 83-86. https://doi.org/10.3189/172756407782282507

Wong, K., Morgan, D., Ferguson, D., Edmonds, M., Tadesse, A. Z., Murphy Quinlan, M., Yirgu, G., & Wright, T. (2025). Rapid crustal transit of magmas beneath the Main Ethiopian Rift. *Nature Geoscience*, *18*(9), 916-922. https://doi.org/10.1038/s41561-025-01770-9

Wysoczanski, R., Todd, E., Wright, I., Leybourne, M., Hergt, J., Adam, C., & Mackay, K. (2010). Backarc rifting, constructional volcanism and nascent disorganised spreading in the southern Havre Trough backarc rifts (SW Pacific). *Journal of Volcanology and Geothermal Research*, *190*(1-2), 39-57. https://doi.org/10.1016/j.jvolgeores.2009.04.004

Yamasaki, T. (2022). Magma hybridization and crystallization in coexisting gabbroic and granitic bodies in the mid-crust, Akechi district, central Japan. *Mineralogy and Petrology*, *116*(3), 189-228. https://doi.org/10.1007/s00710-022-00775-1

Yavuz, F., & Yıldırım, D. K. (2018). A Windows program for pyroxene-liquid thermobarometry. *Periodico di Mineralogia*, *87*(2). https://doi.org/10.2451/2018PM787

Yip, S. T. H., Biggs, J., Edmonds, M., Liggins, P., & Shorttle, O. (2022). Contrasting Volcanic Deformation in Arc and Ocean Island Settings Due To Exsolution of Magmatic Water. *Geochemistry, Geophysics, Geosystems*, *23*(7), e2022GC010387. https://doi.org/10.1029/2022GC010387

Zellmer, G., Sparks, R., Hawkesworth, C., & Wiedenbeck, M. (2003). Magma emplacement and remobilization timescales beneath Montserrat: insights from Sr and Ba zonation in plagioclase phenocrysts. *Journal of Petrology*, *44*(8), 1413-1431. https://doi.org/10.1093/petrology/44.8.1413

Zellmer, G. F., Blake, S., Vance, D., Hawkesworth, C., & Turner, S. (1999). Plagioclase residence times at two island arc volcanoes (Kameni Islands, Santorini, and Soufriere, St. Vincent) determined by Sr diffusion systematics. *Contributions to Mineralogy and Petrology*, *136*, 345-357. https://doi.org/10.1007/s004100050543

Zellmer, G. F., Sakamoto, N., Iizuka, Y., Miyoshi, M., Tamura, Y., Hsieh, H.-H., & Yurimoto, H. (2013). Crystal uptake into aphyric arc melts: insights from two-

pyroxene pseudo-decompression paths, plagioclase hygrometry, and measurement of hydrogen in olivines from mafic volcanics of SW Japan. *Geological Society, London, Special Publications*, *385*(1), 161-184. https://doi.org/10.1144/SP385.3

Zellmer, G. F., Sakamoto, N., Matsuda, N., Iizuka, Y., Moebis, A., & Yurimoto, H. (2016a). On progress and rate of the peritectic reaction Fo+ SiO_2→ En in natural andesitic arc magmas. *Geochimica et Cosmochimica Acta*, *185*, 383-393. https://doi.org/10.1016/j.gca.2016.01.005

Zellmer, G. F., Pistone, M., Iizuka, Y., Andrews, B., Gomez-Tuena, A., Straub, S. M., & Cottrell, E. (2016b). Petrogenesis of antecryst-bearing arc basalts from the Trans-Mexican Volcanic Belt: Insights into along-arc variations in magma-mush ponding depths, H_2O contents, and surface heat flux. *American Mineralogist*, *101*(11), 2405-2422. https://doi.org/10.2138/am-2016-5701

Zellmer, G. F., Sakamoto, N., Matsuda, N., Iizuka, Y., Moebis, A., & Yurimoto, H. (2018). Corrigendum to; On progress and rate of the peritectic reaction Fo+ SiO_2→ En in natural andesitic arc magmas;[Geochim. Cosmochim. Acta 185 (2016) 383-393]. *Geochimica et Cosmochimica Acta*, *220*, 552-553. https://doi.org/10.1016/j.gca.2017.09.043

Zellmer, G. F., Iizuka, Y., Lormand, C., & Moebis, A. (2021). Beyond crystal mushes: evidence for uptake of high-T pyroxene antecrysts from mid-to upper crustal andesites into tephras from the Central Plateau, New Zealand. *New Zealand Journal of Geology and Geophysics*, *64*(2-3), 443-455. https://doi.org/10.1080/00288306.2020.1848883

Zellmer, G. F. (2021). Gaining acuity on crystal terminology in volcanic rocks. *Bulletin of Volcanology*, *83*(11), 78. https://doi.org/10.1007/s00445-021-01505-9

Zellmer, G. F., Iizuka, Y., & Straub, S. M. (2024). Origin of Crystals in Mafic to Intermediate Magmas from Circum-Pacific Continental Arcs: Transcrustal Magmatic Systems Versus Transcrustal Plutonic Systems. *Journal of Petrology*, *65*(3). https://doi.org/10.1093/petrology/egae013

Zellmer, G. F., & Iizuka, Y. (2025). Crystal Fragmentation Inducing Euhedral Crystal Habits in Volcanic Rocks: Fracture Histories of Crystals from Various Tectonomagmatic Settings and Implications for Plumbing System Processes. *The Canadian Journal of Mineralogy and Petrology*, *63*(3), 207-216. https://doi.org/10.3749/2400041

Zhang, N., Behn, M. D., Parmentier, E. M., & Kincaid, C. (2020). Melt segregation and depletion during ascent of buoyant diapirs in subduction zones. *Journal of Geophysical Research: Solid Earth*, *125*(2), e2019JB018203. https://doi.org/10.1029/2019JB018203

Zierenberg, R. A., Schiffman, P., Barfod, G. H., Lesher, C. E., Marks, N. E., Lowenstern, J. B., Mortensen, A. K., Pope, E. C., Bird, D. K., Reed, M. H., Friðleifsson, G. Ó., & Elders, W. A. (2013). Composition and origin of rhyolite melt intersected by drilling in the Krafla geothermal field, Iceland. *Contributions to Mineralogy and Petrology*, *165*(2), 327-347. https://doi.org/10.1007/s00410-012-0811-z

Zimmer, M. M., & Plank, T. (2006, December 01, 2006). *The role of water in generating Fe-depletion and the calc-alkaline trend* AGU Fall Meeting Abstracts, San Francisco. https://ui.adsabs.harvard.edu/abs/2006AGUFM.V23C0636Z

Zimmer, M. M., Plank, T., Hauri, E. H., Yogodzinski, G. M., Stelling, P., Larsen, J., Singer, B., Jicha, B., Mandeville, C., & Nye, C. J. (2010). The Role of Water in Generating the Calc-alkaline Trend: New Volatile Data for Aleutian Magmas and a New Tholeiitic Index. *Journal of Petrology*, *51*(12), 2411-2444. https://doi.org/10.1093/petrology/egq062

Zingg, T. (1935). *Beitrag zur schotteranalyse* [Doctoral dissetation, ETH Zurich].

Appendix 1 Loss on ignition and quality standards data

Loss on ignition (LOI)

LOI was found using the following calculation:

$$LOI\ (wt\%) = 100 \times ((n2-n3)/(n2-n1))$$

Where: n1 is the empty crucible, n2 is the crucible plus dried at 110°C sample powder, and n3 is the crucible plus sample powder after heating in the 900°C furnace.

Table S1. LOI (loss on ignition) data and calculation

Sample Name	n1	n2	n3	LOI
RSA-1A	28.2774	30.2793	30.288	-0.435
RSA-1B	26.9718	28.973	28.9828	-0.49
RSA-2	28.07	30.1825	30.1882	-0.27
RSA-3	27.667	29.6636	29.671	-0.371
RSA-4	16.6835	18.9235	18.9308	-0.326
RSA-5	18.9635	21.1119	21.1125	-0.028
RSA-6A	18.6185	20.9774	20.984	-0.28
RSA-6B	17.4999	19.5369	19.5411	-0.206
RSA-7A	15.5237	17.6536	17.6579	-0.202
RSA-7B	17.5164	19.8135	19.8088	0.205
RSA-7C	25.5411	27.5754	27.5763	-0.044
RSA-8	24.3169	26.6402	26.6349	0.228
RSA-9	17.4748	19.4933	19.4932	0.005
RSA-10	16.3228	18.501	18.508	-0.321
RSA-11	15.9623	18.0421	18.0454	-0.159
RSA-12	17.0502	19.1374	19.1353	0.101
RSA-13	15.5346	17.6721	17.6759	-0.178

XRF quality standards. Oreas reproducibility data.

Table S2. Reproducibility data for Oreas 24c.

Oreas 24c	SiO_2 (%)	Al_2O_3 (%)	TiO_2 (%)	MnO (%)	Fe_2O_3 (%)	MgO (%)	CaO (%)	Na_2O (%)	K_2O (%)	P_2O_5 (%)
Measured value	52.01	14.87	1.88	0.15	11.20	7.14	8.77	3.40	0.92	0.41
Certified value	52.95	14.08	1.77	0.14	10.89	6.52	8.20	3.26	0.89	0.36
Accuracy (%)	1.78	5.65	6.33	5.38	2.79	9.49	6.94	4.26	3.91	13.29
Mean	52.00	14.78	1.88	0.15	11.29	6.99	8.76	3.32	0.88	0.36
2SD	0.49	0.14	0.02	0.00	0.15	0.07	0.07	0.05	0.01	0.03
3SD	0.74	0.21	0.04	0.01	0.22	0.11	0.10	0.08	0.02	0.05

The mean and standard deviation (SD) values were calculated from previous analyses at the same laboratory.

Table S3. Reproducibility data for Oreas 24b.

Oreas 24b	SiO_2 (%)	Al_2O_3 (%)	TiO_2 (%)	MnO (%)	Fe_2O_3 (%)	MgO (%)	CaO (%)	Na_2O (%)	K_2O (%)	P_2O_5 (%)
Measured value	66.67	15.35	0.80	0.06	6.40	2.95	1.51	1.20	3.41	0.21
Certified value	66.00	15.15	0.80	0.06	6.35	2.75	1.47	1.15	3.39	0.16
Accuracy (%)	1.02	1.32	0.13	6.78	0.72	7.27	2.65	4.17	0.59	30.43
Mean	66.22	15.23	0.80	0.06	6.38	2.81	1.49	1.11	3.38	0.17
2SD	0.74	0.20	0.01	0.00	0.10	0.08	0.02	0.04	0.04	0.04
3SD	1.10	0.30	0.02	0.01	0.16	0.12	0.03	0.06	0.06	0.06

The mean and standard deviation (SD) values were calculated from previous analyses at the same laboratory.

EPMA quality standards

Table S4. EPMA standard material and diffracting crystals used for the Oxide-ZAF method.

	Academia Sinica			Tohoku University		
Oxide	**Type of Crystal**	**Standard**	**Reference Value (%)**	**Type of Crystal**	**Standard**	**Reference Value (%)**
SiO_2	TAPJ	Wollastonite ($CaSiO_3$)[1]	50.94	TAPL	Wollastonite ($CaSiO_3$)[1]	50.94
TiO_2	PETJ	Rutile (TiO_2)[1]	99.99	PETL	Rutile (TiO_2)[1]	99.99
Al_2O_3	TAPJ	Corundum (Al_2O_3)[1]	99.99	TAPL	Corundum (Al_2O_3)[1]	99.99
Cr_2O_3	PETJ	Eskolaite (Cr_2O_3)[1]	99.99	LIFH	Eskolaite (Cr_2O_3)[1]	99.99
FeO	LIFH	Hematite (FeO)[1]	89.98	LIFL	Hematite (FeO)[1]	89.98
MnO	PETJ	Manganosite (MnO)[1]	99.99	LIFL	Manganosite (MnO)[1]	99.99
MgO	TAPH	Periclase (MgO)[1]	99.99	TAPL	Periclase (MgO)[1]	99.99
NiO	LIFH	Ni-oxide (NiO)*[1]	99.99	LIFH		
CaO	PETH	Wollastonite ($CaSiO_3$)[1]	48	PETL	Wollastonite ($CaSiO_3$)[1]	48
Na_2O	TAPH	Jadeite ($NaAlSi_2O_6$)[1]	15.1	TAPL	Albite ($NaAlSi_3O_8$)[1]	11.48
K_2O	PETH	Sanidine ($KAlSi_3O_8$)[2]	12.11	PETH	Orthoclase ($KAlSi_3O_8$)[1]	5.62
P2O5				PETH	Potassium titanium phosphate ($KTiOPO_4$)[1]	35.87

* Synthetic material. Standard materials provided by JEOL (JAPAN)[1] and Spi suppilers (USA)[2]

LA-ICP-MS quality standards

Table S5. LA-ICP-MS accuracy and precision standard data for groundmass analyses. Data collected in 2024.

Standard		Na	Mg	Al	Si	P	K	Ca	Ti	Cr	Mn	Fe
G_BCR2G	Mean (ppm)	23955.60	21464.07	70926.65	254355.92	1617.22	14922.81	50451.44	14103.93	17.02	1548.97	96356.16
	2SD (ppm)	908.38	632.06	2191.69	9731.89	77.51	740.69	2023.48	607.66	1.19	62.53	3954.09
	2SD (%)	3.79	2.94	3.09	3.83	4.79	4.96	4.01	4.31	6.97	4.04	4.10
	2SE (ppm)	302.79	210.69	730.56	3243.96	25.84	246.90	674.49	202.55	0.40	20.84	1318.03
	2SE (%)	1.26	0.98	1.03	1.28	1.60	1.65	1.34	1.44	2.32	1.35	1.37
	Reference Values (ppm)	23962.00	21467.00	70913.00	254270.00	1615.00	14900.00	50429.00	14100.00	17.00	1550.00	96385.00
	Accuracy (%)	0.15	0.04	0.02	0.03	0.02	0.03	0.04	0.07	0.03	0.02	0.03
	Precision (%)	1.10	1.14	1.17	3.83	1.06	1.27	1.18	1.64	3.64	0.83	0.96
G_BHVO2G	Mean (ppm)	16031.68	41831.75	68547.59	229381.77	1213.93	4105.62	77203.82	16313.70	312.94	1270.16	82720.70
	2SD (ppm)	801.85	1741.18	2750.99	11426.46	72.44	266.90	4566.74	925.65	16.50	72.12	4272.32
	2SD (%)	5.00	4.16	4.01	4.98	5.97	6.50	5.92	5.67	5.27	5.68	5.16
	2SE (ppm)	267.28	580.39	917.00	3808.82	24.15	88.97	1522.25	308.55	5.50	24.04	1424.11
	2SE (%)	1.67	1.39	1.34	1.66	1.99	2.17	1.97	1.89	1.76	1.89	1.72
	Reference Values (ppm)	17806.00	42994.00	71971.00	230428.00	1266.00	4270.00	81430.00	16300.00	293.00	1317.00	87835.00
	Accuracy (%)	9.35	2.21	4.39	0.45	3.90	3.68	4.70	0.75	7.34	2.90	5.22
	Precision (%)	1.42	1.16	1.22	4.96	1.10	1.57	1.76	1.84	1.87	0.94	1.17
G_GSD_2G	Mean (ppm)	29070.22	21188.52	69021.22	260584.84	1436.61	22128.49	45948.90	7632.19	48.63	654.14	93451.24
	2SD (ppm)	1045.04	589.88	1567.99	8260.05	62.68	943.74	1998.15	365.34	2.57	31.72	4527.61
	2SD (%)	3.59	2.78	2.27	3.17	4.36	4.26	4.35	4.79	5.28	4.85	4.84
	2SE (ppm)	348.35	196.63	522.66	2753.35	20.89	314.58	666.05	121.78	0.86	10.57	1509.20
	2SE (%)	1.20	0.93	0.76	1.06	1.45	1.42	1.45	1.60	1.76	1.62	1.61
	Reference Values (ppm)	28900.00	21200.00	70200.00	261000.00	1400.00	21700.00	45900.00	6900.00	44.30	641.00	92100.00
	Accuracy (%)	0.98	0.12	1.57	0.16	2.75	2.00	0.37	11.01	9.93	2.39	1.73
	Precision (%)	1.24	1.23	1.01	3.16	1.29	1.33	1.65	2.19	2.52	2.05	2.11

BCR2G was used as the calibration standard, while BHVO2G, GSD1G and GSD2G as the secondary standards.

Table S6. LA-ICP-MS accuracy and precision standard data for groundmass analyses. Data collected in 2025.

Standard		Na	Mg	Al	Si	P	K	Ca	Ti	Cr	Mn	Fe
G_BCR2G	Mean (ppm)	24006.68	21477.86	70937.75	254609.40	1616.92	14928.13	50447.65	14117.79	17.01	1551.54	96514.31
	2SD (ppm)	541.13	319.90	1031.40	5170.02	32.90	426.06	1058.51	327.82	0.48	45.40	2568.77
	2SD (%)	2.25	1.49	1.45	2.03	2.04	2.85	2.10	2.32	2.79	2.93	2.66
	2SE (ppm)	144.62	85.50	275.65	1381.75	8.79	113.87	282.90	87.61	0.13	12.13	686.53
	2SE (%)	0.60	0.40	0.39	0.54	0.54	0.76	0.56	0.62	0.75	0.78	0.71
	Reference Values (ppm)	23962.00	21467.00	70913.00	254270.00	1615.00	14900.00	50429.00	14100.00	17.00	1550.00	96385.00
	Accuracy (%)	0.19	0.05	0.03	0.13	0.12	0.19	0.04	0.13	0.07	0.10	0.13
	Precision (%)	0.60	0.40	0.39	0.54	0.54	0.76	0.56	0.62	0.75	0.78	0.71
G_BHVO2G	Mean (ppm)	16214.73	41650.58	68238.67	225491.12	1170.88	4087.62	76997.53	16274.49	296.74	1264.28	82880.74
	2SD (ppm)	621.90	1078.42	1884.79	7540.00	47.19	164.41	2482.63	588.00	9.26	39.12	2513.20
	2SD (%)	3.84	2.59	2.76	3.34	4.03	4.02	3.22	3.61	3.12	3.09	3.03
	2SE (ppm)	160.57	278.45	486.65	1946.82	12.18	42.45	641.01	151.82	2.39	10.10	648.90
	2SE (%)	0.99	0.67	0.71	0.86	1.04	1.04	0.83	0.93	0.81	0.80	0.78
	Reference Values (ppm)	17806.00	42994.00	71971.00	230428.00	1266.00	4270.00	81430.00	16300.00	293.00	1317.00	87835.00
	Accuracy (%)	8.94	3.12	5.19	2.14	7.51	4.27	5.44	0.16	1.28	4.00	5.64
	Precision (%)	0.90	0.65	0.68	0.84	0.96	0.99	0.79	0.93	0.82	0.77	0.74
G_GSD1G	Mean (ppm)	27939.93	21355.94	70585.29	248541.95	1026.38	26010.62	49661.51	8013.53	46.51	233.10	99565.14
	2SD (ppm)	657.82	508.55	1390.12	5547.24	28.01	704.64	1175.81	254.96	1.26	7.50	2470.01
	2SD (%)	2.35	2.38	1.97	2.23	2.73	2.71	2.37	3.18	2.71	3.22	2.48
	2SE (ppm)	175.81	135.92	371.53	1482.56	7.49	188.32	314.25	68.14	0.34	2.00	660.14
	2SE (%)	0.63	0.64	0.53	0.60	0.73	0.72	0.63	0.85	0.72	0.86	0.66
	Reference Values (ppm)	26706.96	21711.60	70919.50	248678.00	860.00	25300.00	51458.40	7433.92	42.00	220.00	103382.23
	Accuracy (%)	4.62	1.64	0.47	0.05	19.35	2.81	3.49	7.80	10.73	5.95	3.69
	Precision (%)	0.66	0.63	0.52	0.60	0.87	0.74	0.61	0.92	0.80	0.91	0.64

BCR2G was used as the calibration standard, while BHVO2G, GSD1G and GSD2G as the secondary standards.

Table S7. LA-ICP-MS accuracy and precision standard data for crystal mapping of pyroxene using a spot size of 16 µm.

Standard		Na	Al	Si	Ca	Sc	Ti	Cr	Ni	Zr	La	Ce	Nd	Sm	Eu	Gd	Yb
G_NIST612	Mean (ppm)	103812.69	11162.86	336209.97	85004.18	39.88	43.99	36.41	38.77	37.90	35.96	38.39	35.44	37.66	35.59	37.24	39.14
	2SD (ppm)	611.07	69.91	2226.48	310.96	0.20	1.96	0.99	0.57	0.20	0.40	0.15	0.53	0.54	0.16	0.57	0.48
	2SD (%)	0.59	0.63	0.66	0.37	0.50	4.45	2.71	1.47	0.54	1.11	0.39	1.51	1.44	0.44	1.53	1.24
	2SE (ppm)	122.21	13.98	445.30	62.19	0.04	0.39	0.20	0.11	0.04	0.08	0.03	0.11	0.11	0.03	0.11	0.10
	2SE (%)	0.12	0.13	0.13	0.07	0.10	0.89	0.54	0.29	0.11	0.22	0.08	0.30	0.29	0.09	0.31	0.25
	Reference Values (ppm)	103858.00	11167.00	336061.00	85002.00	39.90	44.00	36.40	38.80	37.90	36.00	38.40	35.50	37.70	35.60	37.30	39.20
	Accuracy (%)	0.04	0.04	0.04	0.00	0.04	0.03	0.03	0.08	0.00	0.12	0.01	0.16	0.12	0.04	0.15	0.16
	Precision (%)	0.29	0.31	0.33	0.18	0.25	2.22	1.35	0.73	0.27	0.56	0.19	0.75	0.72	0.22	0.77	0.62
G_BCR2G	Mean (ppm)	22904.10	74610.13	258963.05	50795.87	32.62	14236.98	15.03	13.90	175.18	24.37	51.15	27.44	6.44	1.92	6.40	3.31
	2SD (ppm)	1102.60	3175.59	15300.18	3771.23	1.61	765.51	0.75	1.97	12.97	1.10	3.05	1.41	0.44	0.13	0.37	0.15
	2SD (%)	4.81	4.26	5.91	7.42	4.93	5.38	4.96	14.15	7.40	4.53	5.95	5.12	6.85	6.78	5.73	4.59
	2SE (ppm)	416.74	1200.26	5782.92	1425.39	0.61	289.34	0.28	0.74	4.90	0.42	1.15	0.53	0.17	0.05	0.14	0.06
	2SE (%)	1.82	1.61	2.23	2.81	1.86	2.03	1.88	5.35	2.80	1.71	2.25	1.94	2.59	2.56	2.17	1.74
	Reference Values (ppm)	23962.00	70913.00	254270.00	50429.00	33.00	14100.00	17.00	13.00	184.00	24.70	53.30	28.90	6.59	1.97	6.71	3.39
	Accuracy (%)	4.41	5.21	1.85	0.73	1.16	0.97	11.57	6.93	4.79	1.35	4.03	5.05	2.31	2.32	4.64	2.48
	Precision (%)	2.30	2.24	3.01	3.74	2.44	2.71	2.19	7.57	3.52	2.23	2.86	2.43	3.34	3.31	2.73	2.24
G_BHVO2G	Mean (ppm)	15118.09	69214.48	228543.99	74749.73	28.74	15973.26	267.43	110.51	146.66	13.46	32.88	21.17	5.59	1.83	5.37	1.76
	2SD (ppm)	2368.91	10964.52	32959.61	11110.88	4.33	2277.01	40.77	18.60	24.02	2.07	5.11	3.29	0.90	0.29	0.83	0.24
	2SD (%)	15.67	15.84	14.42	14.86	15.06	14.26	15.24	16.83	16.38	15.34	15.56	15.53	16.09	15.73	15.54	13.61
	2SE (ppm)	837.54	3876.54	11652.98	3928.29	1.53	805.04	14.41	6.58	8.49	0.73	1.81	1.16	0.32	0.10	0.29	0.08
	2SE (%)	5.54	5.60	5.10	5.26	5.32	5.04	5.39	5.95	5.79	5.43	5.50	5.49	5.69	5.56	5.49	4.81
	Reference Values (ppm)	17806.00	71971.00	230428.00	81430.00	33.00	16300.00	293.00	116.00	170.00	15.20	37.60	24.50	6.10	2.07	6.16	2.01
	Accuracy (%)	15.10	3.83	0.82	8.20	12.91	2.00	8.73	4.73	13.73	11.43	12.56	13.58	8.35	11.64	12.84	12.19
	Precision (%)	6.65	7.62	7.15	6.82	6.56	6.98	6.96	8.02	7.06	6.80	6.80	6.71	7.37	6.95	6.77	5.97
G_GSD1G	Mean (ppm)	27361.11	77113.54	262126.56	51794.09	47.42	8188.54	42.55	56.17	41.86	39.08	41.07	43.90	47.65	40.84	48.28	51.31
	2SD (ppm)	1611.66	4222.49	12166.03	3587.80	3.78	488.12	3.00	4.66	3.07	1.90	2.70	3.04	2.76	2.66	2.53	2.59
	2SD (%)	5.89	5.48	4.64	6.93	7.97	5.96	7.04	8.30	7.32	4.86	6.58	6.92	5.80	6.51	5.24	5.04
	2SE (ppm)	609.15	1595.95	4598.33	1356.06	1.43	184.49	1.13	1.76	1.16	0.72	1.02	1.15	1.04	1.00	0.96	0.98
	2SE (%)	2.23	2.07	1.75	2.62	3.01	2.25	2.66	3.14	2.77	1.84	2.49	2.62	2.19	2.46	1.98	1.91
	Reference Values (ppm)	26706.96	70919.50	248678.00	51458.40	52.00	7433.92	42.00	58.00	42.00	39.10	41.40	44.70	47.80	41.00	50.70	50.90
	Accuracy (%)	2.45	8.73	5.41	0.65	8.80	10.15	1.31	3.15	0.33	0.04	0.80	1.79	0.31	0.38	4.78	0.80
	Precision (%)	3.02	2.98	2.45	3.49	3.63	3.28	3.57	4.02	3.65	2.43	3.26	3.40	2.89	3.24	2.49	2.54

G_NIST612 was used as the calibration standard BCR2G, BHVO2G and GSD1G were used as secondary standards.

Table S8. LA-ICP-MS accuracy and precision standard data for crystal mapping of pyroxene using a spot size of 10 µm.

Standard		Na	Al	Si	Ca	Sc	Ti	Cr	Ni	Zr	La	Ce	Nd	Sm	Eu	Gd	Yb
G_NIST612	Mean (ppm)	103841.92	11167.80	336693.02	84995.95	39.92	44.02	36.35	38.76	37.89	36.02	38.41	35.48	37.71	35.60	37.29	39.22
	2SD (ppm)	2494.15	181.56	13939.41	2104.25	1.36	2.13	3.71	1.51	0.83	0.83	0.94	0.76	1.12	0.74	1.15	0.72
	2SD (%)	2.40	1.63	4.14	2.48	3.40	4.83	10.21	3.90	2.19	2.32	2.45	2.14	2.98	2.09	3.09	1.84
	2SE (ppm)	720.00	52.41	4023.96	607.44	0.39	0.61	1.07	0.44	0.24	0.24	0.27	0.22	0.32	0.21	0.33	0.21
	2SE (%)	0.69	0.47	1.20	0.71	0.98	1.40	2.95	1.13	0.63	0.67	0.71	0.62	0.86	0.60	0.89	0.53
	Reference Values (ppm)	103858.00	11167.00	336061.00	85002.00	39.90	44.00	36.40	38.80	37.90	36.00	38.40	35.50	37.70	35.60	37.30	39.20
	Accuracy (%)	0.02	0.01	0.19	0.01	0.06	0.04	0.15	0.10	0.02	0.04	0.04	0.05	0.04	0.01	0.02	0.05
	Precision (%)	1.20	0.81	2.07	1.24	1.70	2.42	5.10	1.95	1.10	1.16	1.22	1.07	1.49	1.04	1.54	0.92
G_BCR2G	Mean (ppm)	25390.17	79764.27	282076.00	57007.41	37.09	16391.19	17.34	14.69	198.12	27.28	56.09	30.71	7.23	2.12	7.27	3.83
	2SD (ppm)	1352.68	3076.93	10634.49	3011.24	1.68	649.22	3.30	2.11	8.92	1.21	2.84	0.83	0.44	0.11	0.44	0.16
	2SD (%)	5.33	3.86	3.77	5.28	4.53	3.96	19.05	14.38	4.50	4.42	5.06	2.71	6.03	5.17	6.03	4.07
	2SE (ppm)	676.34	1538.47	5317.25	1505.62	0.84	324.61	1.65	1.06	4.46	0.60	1.42	0.42	0.22	0.05	0.22	0.08
	2SE (%)	2.66	1.93	1.89	2.64	2.27	1.98	9.53	7.19	2.25	2.21	2.53	1.36	3.01	2.58	3.01	2.04
	Reference Values (ppm)	23962.00	70913.00	254270.00	50429.00	33.00	14100.00	17.00	13.00	184.00	24.70	53.30	28.90	6.59	1.97	6.71	3.39
	Accuracy (%)	5.96	12.48	10.94	13.04	12.39	16.25	1.97	13.03	7.68	10.44	5.23	6.26	9.69	7.48	8.35	12.99
	Precision (%)	2.82	2.17	2.09	2.99	2.55	2.30	9.71	8.13	2.42	2.44	2.66	1.44	3.31	2.78	3.27	2.30
G_BHVO2G	Mean (ppm)	17249.74	75117.75	247502.71	85060.95	33.17	18636.93	302.78	126.77	169.14	15.38	36.79	24.14	6.36	2.08	6.13	2.07
	2SD (ppm)	557.54	2159.15	8835.50	3186.64	1.04	534.22	25.07	6.75	4.01	0.46	1.06	0.83	0.06	0.05	0.12	0.05
	2SD (%)	3.23	2.87	3.57	3.75	3.14	2.87	8.28	5.33	2.37	3.02	2.88	3.44	1.02	2.29	2.01	2.60
	2SE (ppm)	278.77	1079.57	4417.75	1593.32	0.52	267.11	12.53	3.38	2.01	0.23	0.53	0.42	0.03	0.02	0.06	0.03
	2SE (%)	1.62	1.44	1.78	1.87	1.57	1.43	4.14	2.66	1.19	1.51	1.44	1.72	0.51	1.14	1.01	1.30
	Reference Values (ppm)	17806.00	71971.00	230428.00	81430.00	33.00	16300.00	293.00	116.00	170.00	15.20	37.60	24.50	6.10	2.07	6.16	2.01
	Accuracy (%)	3.12	4.37	7.41	4.46	0.52	14.34	3.34	9.29	0.50	1.15	2.15	1.47	4.24	0.56	0.45	2.96
	Precision (%)	1.57	1.50	1.92	1.96	1.58	1.64	4.28	2.91	1.18	1.53	1.41	1.69	0.53	1.15	1.00	1.34
G_GSD1G	Mean (ppm)	29855.88	82822.54	287150.00	59364.64	54.06	9480.21	46.99	61.51	47.80	44.20	45.69	49.55	54.42	46.07	55.23	59.01
	2SD (ppm)	523.28	1792.20	12762.34	2553.79	1.35	292.89	9.67	2.80	1.80	1.80	1.71	2.50	2.10	1.46	2.40	2.30
	2SD (%)	1.75	2.16	4.44	4.30	2.49	3.09	20.57	4.55	3.76	4.07	3.75	5.05	3.85	3.18	4.34	3.91
	2SE (ppm)	261.64	896.10	6381.17	1276.89	0.67	146.44	4.83	1.40	0.90	0.90	0.86	1.25	1.05	0.73	1.20	1.15
	2SE (%)	0.88	1.08	2.22	2.15	1.24	1.54	10.28	2.28	1.88	2.03	1.87	2.52	1.92	1.59	2.17	1.95
	Reference Values (ppm)	26706.96	70919.50	248678.00	51458.40	52.00	7433.92	42.00	58.00	42.00	39.10	41.40	44.70	47.80	41.00	50.70	50.90
	Accuracy (%)	11.79	16.78	15.47	15.36	3.96	27.53	11.89	6.05	13.81	13.04	10.37	10.86	13.85	12.36	8.93	15.93
	Precision (%)	0.98	1.26	2.57	2.48	1.29	1.97	11.51	2.41	2.14	2.30	2.07	2.80	2.19	1.78	2.37	2.26

G_NIST612 was used as the calibration standard BCR2G, BHVO2G and GSD1G were used as secondary standards.

Table S9. LA-ICP-MS accuracy and precision standard data for crystal mapping of plagioclase using a spot size of 16 µm.

Standard		Li	Mg*	Si	Ca	Fe*	Rb	Sr	Ba	La	Ce	Nd	Sm	Eu	Gd	Dy
G_NIST612	Mean (ppm)	40.16	90.25	336089.81	84974.59	174.83	31.39	78.38	39.26	35.99	38.39	35.50	37.69	35.60	37.29	35.50

	2SD (ppm)	0.31	6.02	1941.93	488.77	18.39	0.15	0.30	0.47	0.10	0.12	0.11	0.21	0.03	0.10	0.04
	2SD (%)	0.77	6.67	0.58	0.58	10.52	0.47	0.39	1.19	0.29	0.32	0.32	0.55	0.08	0.26	0.12
	2SE (ppm)	0.06	1.20	388.39	97.75	3.68	0.03	0.06	0.09	0.02	0.02	0.02	0.04	0.01	0.02	0.01
	2SE (%)	0.15	1.33	0.12	0.12	2.10	0.09	0.08	0.24	0.06	0.06	0.06	0.11	0.02	0.05	0.02
	Reference Values (ppm)	40.20	68.00	336061.00	85002.00	51.00	31.40	78.40	39.30	36.00	38.40	35.50	37.70	35.60	37.30	35.50
	Accuracy (%)	0.11	32.72	0.01	0.03	242.81	0.03	0.02	0.11	0.02	0.03	0.01	0.03	0.00	0.02	0.00
	Precision (%)	0.39	4.43	0.29	0.29	18.03	0.24	0.19	0.60	0.14	0.16	0.16	0.28	0.04	0.13	0.06
G_BCR2G	Mean (ppm)	8.58	21465.61	259271.40	51288.51	100191.42	44.07	337.66	658.29	24.38	50.91	27.63	6.39	1.91	6.40	6.15
	2SD (ppm)	0.79	481.66	18061.57	3361.69	2848.88	3.39	20.78	51.69	1.59	3.19	1.64	0.46	0.14	0.35	0.43
	2SD (%)	9.18	2.24	6.97	6.55	2.84	7.69	6.15	7.85	6.54	6.26	5.93	7.20	7.09	5.54	6.99
	2SE (ppm)	0.28	170.29	6385.73	1188.54	1007.23	1.20	7.35	18.27	0.56	1.13	0.58	0.16	0.05	0.13	0.15
	2SE (%)	3.25	0.79	2.46	2.32	1.01	2.72	2.18	2.78	2.31	2.21	2.10	2.55	2.51	1.96	2.47
	Reference Values (ppm)	9.00	21467.00	254270.00	50429.00	96385.00	47.00	342.00	683.00	24.70	53.30	28.90	6.59	1.97	6.71	6.44
	Accuracy (%)	4.64	0.01	1.97	1.70	3.95	6.24	1.27	3.62	1.30	4.48	4.39	3.02	3.26	4.56	4.55
	Precision (%)	4.38	1.12	3.55	3.33	1.48	3.61	3.04	3.78	3.23	2.99	2.84	3.49	3.43	2.64	3.34
G_BHVO2G	Mean (ppm)	4.10	41475.61	234665.94	78127.54	87815.05	8.14	370.47	120.08	13.93	33.84	22.02	5.67	1.87	5.55	4.77
	2SD (ppm)	0.34	1265.30	16604.60	5064.90	1558.34	0.60	26.00	10.17	0.96	2.42	1.70	0.36	0.15	0.41	0.34
	2SD (%)	8.34	3.05	7.08	6.48	1.77	7.34	7.02	8.47	6.87	7.14	7.71	6.42	8.03	7.34	7.14
	2SE (ppm)	0.12	447.35	5870.61	1790.71	550.96	0.21	9.19	3.60	0.34	0.85	0.60	0.13	0.05	0.14	0.12
	2SE (%)	2.95	1.08	2.50	2.29	0.63	2.60	2.48	3.00	2.43	2.52	2.72	2.27	2.84	2.60	2.53
	Reference Values (ppm)	4.40	42994.00	230428.00	81430.00	87835.00	9.20	396.00	131.00	15.20	37.60	24.50	6.10	2.07	6.16	5.28
	Accuracy (%)	6.89	3.53	1.84	4.06	0.02	11.57	6.45	8.34	8.33	10.01	10.10	7.12	9.49	9.94	9.73
	Precision (%)	3.88	1.47	3.60	3.11	0.89	3.25	3.28	3.88	3.15	3.21	3.46	2.98	3.63	3.31	3.22
G_GSD1G	Mean (ppm)	42.36	22283.06	260061.14	52623.45	105315.52	36.30	71.61	69.90	39.24	40.98	44.19	48.01	40.68	48.82	51.66
	2SD (ppm)	3.95	723.79	18729.78	3829.44	3700.66	2.35	5.24	5.66	2.72	2.95	3.00	3.49	3.25	3.02	3.65
	2SD (%)	9.33	3.25	7.20	7.28	3.51	6.47	7.32	8.10	6.93	7.20	6.78	7.26	7.99	6.18	7.07
	2SE (ppm)	1.40	255.90	6621.98	1353.91	1308.38	0.83	1.85	2.00	0.96	1.04	1.06	1.23	1.15	1.07	1.29
	2SE (%)	3.30	1.15	2.55	2.57	1.24	2.29	2.59	2.86	2.45	2.55	2.40	2.57	2.82	2.18	2.50
	Reference Values (ppm)	43.00	21711.60	248678.00	51458.40	103382.23	37.30	69.40	67.00	39.10	41.40	44.70	47.80	41.00	50.70	51.20
	Accuracy (%)	1.50	2.63	4.58	2.26	1.87	2.67	3.19	4.32	0.36	1.01	1.13	0.43	0.78	3.72	0.90
	Precision (%)	4.60	1.67	3.77	3.72	1.79	3.15	3.77	4.22	3.48	3.57	3.35	3.65	3.96	2.97	3.57

G_NIST612 was used as the calibration standard BCR2G, BHVO2G and GSD1G were used as secondary standards.

* Due to low accuracy found for Mg and Fe using NIST612 as calibration standard in the plagioclases, the calibration standard was change to BCR2G for Mg and to BHVO2G for Fe.

Appendix 2 CSD Data

Crystal measurement data

The crystal mesurements used in Chappter 4 and 5 can be found in the the following repository https://doi.org/10.6084/m9.figshare.30906542

ShapeCalc uncertainties

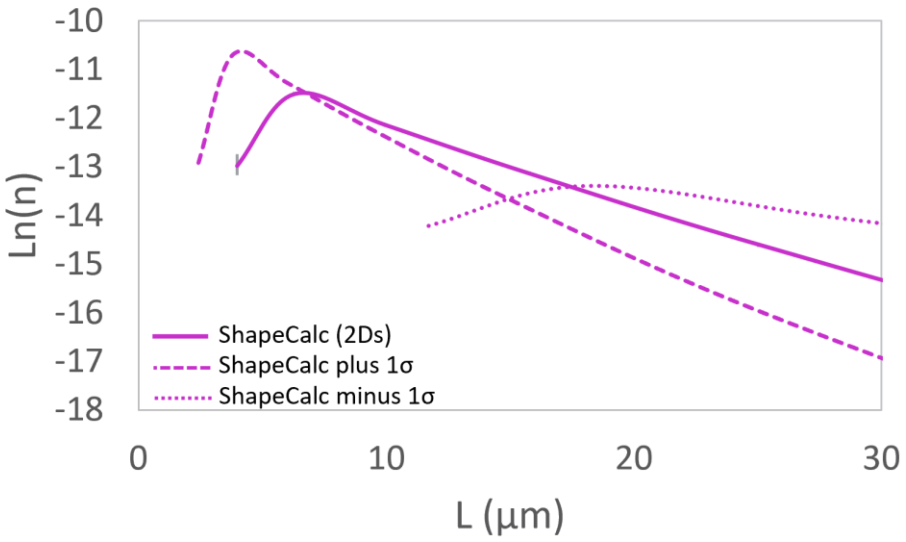

Figure S1. CSD obtained using ShapeCalc (Mangler et al., 2022) estimated aspect ratios, and their standard deviations (1σ). The three plots represent the CSDs calculated using: estimated aspect ratio (2Ds) provided by the tool (solid line), the estimated aspect ratio plus 1σ (dashed line), and the estimated aspect ratio minus 1σ (dotted line). The 1σ of the aspect ratio estimation is provided by ShapeCalc for the I/L (1σ = ±0.21) and S/I (1σ = ±0.06) ratios (Table 3). The CSDs were calculated in CSDCorrections v1.61 (Higgins, 2000).

CSD results using ShapeCalc v1.0 (Mangler et al., 2022) estimated ratio, and their standard uncertainties are presented in the tables below and were used to plot Figure S1. CSDs were determined using CSDCorections v1.61 (Higgins, 2000).

Table S10. CSD calculated using ShapeCalc estimated ratio.

Interval	Intersections	Mid Inter	Ln (n)	Min Ln (n)	Max L (n)
39.8	3	99.7			
25.1	25	62.9	-19.36	-19.59	-19.18
15.8	153	39.7	-16.64	-16.72	-16.56
10	473	25.04	-14.6	-14.64	-14.55
6.31	821	15.8	-13.14	-13.18	-13.11
3.98	930	9.97	-12.14	-12.17	-12.1
2.51	768	6.29	-11.5	-11.54	-11.46
1.58	155	3.97	-12.98	-13.22	-12.79
1	0				

Table S11. CSD calculated using ShapeCalc estimated ratio plus 1σ.

Interval	Intersections	Mid Inter	Ln (n)	Min Ln (n)	Max L (n)
39.8	3	60.3			
25.1	25	38.1	-18.47	-18.7	-18.29
15.8	153	24	-15.75	-15.83	-15.67
10	473	15.15	-13.71	-13.76	-13.67
6.31	821	9.56	-12.27	-12.31	-12.23
3.98	930	6.03	-11.28	-11.32	-11.25
2.51	768	3.81	-10.69	-10.74	-10.64
1.58	155	2.4	-12.94	-13.64	-12.54
1	0				

Table S12. CSD calculated using ShapeCalc estimated ratio minus 1σ.

Interval	Intersections	Mid Inter	Ln (n)	Min Ln (n)	Max L (n)
39.8	3	287.1			
25.1	25	181.2	-21.4	-21.62	-21.21
15.8	153	114.3	-18.67	-18.75	-18.59
10	473	72.12	-16.62	-16.67	-16.58
6.31	821	45.51	-15.16	-15.19	-15.12
3.98	930	28.71	-14.13	-14.16	-14.09
2.51	768	18.12	-13.43	-13.47	-13.4
1.58	155	11.43	-14.37	-14.49	-14.26
1	0				

Table S13. CSD calculated using 3D data measurements from SLICE.

RSA1A

Mid Interval (μm)	Number of crystals	Ln(n)	Max Ln(n)	Min Ln(n)
2.22953239	12	-11.97907686	-11.75038734	-12.80200708
3.329472863	48	-11.05020734	-10.70272908	-11.68839086
5.079183206	104	-10.7344423	-10.34568134	-11.31995162
7.810015528	125	-11.00794431	-10.61130643	-11.58394696
12.07469443	99	-11.69856304	-11.31202692	-12.28678766
18.47412853	39	-13.0875461	-12.75377239	-13.74435624
29.14638756	9	-15.01130801	-14.8166859	-15.8990773
51.828458	1	-17.66595744	-17.87680043	

RSA1B

Mid Interval	Number of crystals	Ln(n)	Max Ln(n)	Min Ln(n)
1.5387789	1	-13.85247552	-13.79571566	
2.112385714	26	-11.05180383	-10.59449626	-11.90649162
3.239430889	76	-10.43659188	-9.908796923	-11.19481679
5.195210067	186	-9.999003389	-9.433376031	-10.71154152
7.806166813	187	-10.45106629	-9.885256015	-11.1633926
11.81473714	87	-11.67369164	-11.13914879	-12.42348425
18.773865	20	-13.60129233	-13.1667079	-14.49077583
31.7194365	4	-15.66815509	-15.43723288	-16.99768959

RSA2

Mid Interval	Number of crystals	Ln(n)	Max Ln(n)	Min Ln(n)
1.480025612	5	-13.96915144	-12.50978488	-14.46609435
2.152160516	77	-11.69220878	-10.49456052	-12.66094145
3.244169883	290	-10.82355812	-9.676769073	-11.85276785
5.033308781	416	-10.92017863	-9.782587117	-11.95963339
7.746621538	332	-11.60315377	-10.45999823	-12.63643465
11.92557263	130	-12.99817914	-11.82438192	-13.99611289
18.48526769	20	-15.32740616	-14.03587676	-16.16403648
28.54322	2	-18.0874161	-16.46288959	-18.22563677

RSA3

Mid Interval	Number of crystals	Ln(n)	Max Ln(n)	Min Ln(n)
1.45959586	1	-13.47830726	-13.16089886	
2.235721544	14	-11.29667478	-10.52297727	-12.6181964
3.389466523	52	-10.44191324	-9.561223004	-11.60175225
4.997471871	112	-10.13208293	-9.211816872	-11.24189671
7.828709685	110	-10.60752628	-9.688041233	-11.71828488
12.21777292	55	-11.75809831	-10.87403438	-12.91349468
17.35402473	14	-13.58379901	-12.8101015	-14.90532064
25.053742	1	-16.68028119	-16.36287279	

RSA4

Mid Interval	Number of crystals	Ln(n)	Max Ln(n)	Min Ln(n)
1.47690648	3	-12.07890433	-11.22330451	-14.25146206
2.168179769	16	-10.86235275	-9.774150077	-12.46138104
3.268314285	47	-10.24221871	-9.067032296	-11.71123094
5.130911157	115	-9.804859035	-8.582668165	-11.21409429
7.837007222	153	-9.976778089	-8.743175203	-11.37242505
12.04531787	98	-10.87967338	-9.66455987	-12.29750881
18.39250142	24	-12.74401187	-11.61841811	-14.28367016
29.13868914	7	-14.4335804	-13.44284157	-16.21968469
38.913878	1	-16.8369154	-16.21871636	

RSA5

Mid Interval	Number of crystals	Ln(n)	Max Ln(n)	Min Ln(n)

2.22255481	21	-11.44703691	-11.18969762	-12.14794446
3.219219585	65	-10.77459693	-10.43679324	-11.36175411
5.030755791	68	-11.18690134	-10.84663302	-11.77090478
7.892882523	96	-11.2994857	-10.9419404	-11.86186838
11.84802431	72	-12.04459262	-11.70127249	-12.62471541
18.62912289	15	-14.07063338	-13.84558629	-14.82403584
30.38948567	6	-15.44434896	-15.33196721	-16.42374544

RSA6A

Mid Interval	Number of crystals	Ln(n)	Max Ln(n)	Min Ln(n)
2.070059152	20	-11.75931641	-11.74875253	-12.2036516
3.284496214	70	-10.96397829	-10.88564186	-11.28250861
5.139444155	111	-10.96036818	-10.85980664	-11.25133448
7.809669969	169	-10.99742451	-10.88029348	-11.26870622
12.02404533	86	-12.13040078	-12.04156742	-12.43574147
18.35981371	20	-14.04644065	-14.03587676	-14.49077583
34.19224133	3	-16.40098548	-16.13647809	-17.45343599

RSA6B

Mid Interval	Number of crystals	Ln(n)	Max Ln(n)	Min Ln(n)
2.182026487	38	-12.27906788	-11.15836834	-13.0724328
3.290234956	100	-11.7689087	-10.70323217	-12.63391454
4.96115386	143	-11.86865911	-10.81798159	-12.75169672
7.641702421	150	-12.27829329	-11.2294396	-13.16348332
11.99604638	96	-13.18200524	-12.11445585	-14.04471726
19.60058017	38	-14.56619212	-13.44549257	-15.35955703
28.9517452	10	-16.35861803	-15.11348179	-16.94885398
47.168578	1	-19.11862797	-17.45511444	
77.827174	2			

RSA7A

Mid Interval	Number of crystals	Ln(n)	Max Ln(n)	Min Ln(n)
1.491668061	16	-12.92272528	-11.49313057	-13.84149437
2.085382094	85	-11.71008759	-10.40066005	-12.80172791
3.240337477	261	-11.04564329	-9.779133836	-12.18819738
5.040794054	353	-11.20112049	-9.942812793	-12.35287823
7.677771308	314	-11.7756204	-10.51427086	-12.92398338
11.99296481	193	-12.71974805	-11.44378801	-13.85149552
19.299068	72	-14.16319697	-12.8453376	-15.24425367
29.00833962	21	-15.85276549	-14.44892529	-16.81303744
46.3973504	5	-17.74527487	-16.16918366	-18.35894242
79.519048	1			

RSA7B

Mid Interval	Number of crystals	Ln(n)	Max Ln(n)	Min Ln(n)
1.44028607	6	-14.11597534	-12.35475679	-15.01017916
2.097471455	68	-12.14565195	-10.61231996	-13.43524881
3.198464157	192	-11.56508913	-10.07653367	-12.90905565
4.957988638	219	-11.89093762	-10.40667711	-13.23984438
7.80894641	185	-12.51707837	-11.02726207	-13.85958594
12.20093819	106	-13.53141995	-12.01985159	-14.84811678
18.6648546	43	-14.89108377	-13.33027955	-16.14449298
30.3973362	20	-16.11397646	-14.49330161	-17.27975224
47.910046	3	-18.46852129	-16.59390294	-19.02618176
74.34955771	7			

RSA7C

Mid Interval	Number of crystals	Ln(n)	Max Ln(n)	Min Ln(n)
1.36317592	1	-13.45053881	-13.10536196	
2.092514393	27	-10.61212679	-9.74981285	-11.86420124
3.264171772	65	-10.19100124	-9.269601858	-11.36175411
5.004948592	98	-10.23784587	-9.295754555	-11.38265912
7.929958781	105	-10.62627785	-9.681070692	-11.76728821
12.24837358	67	-11.53297043	-10.60991021	-12.70159615
18.71070507	36	-12.61156896	-11.7273956	-13.83221454
29.279644	8	-14.5730712	-13.83748044	-16.0476599
42.2752384	5	-15.50049968	-14.83181569	-17.13160731
73.73914133	3	-16.46875015	-15.88617251	-18.36828568

RSA8

Mid Interval	Number of crystals	Ln(n)	Max Ln(n)	Min Ln(n)
1.40310985	8	-13.84074858	-12.10668803	-14.8358112
2.138336184	82	-11.97089573	-10.43481974	-13.28520421
3.164019567	203	-11.52183384	-10.02267387	-12.88039015
5.041575	224	-11.88081862	-10.38481347	-13.24299375
7.867931451	216	-12.37461111	-10.87745734	-13.73547152
12.13375213	121	-13.41152382	-11.89318516	-14.74754092
18.98681305	27	-15.36890234	-13.76156497	-16.58647921
32.379182	5	-17.51272614	-15.71175881	-18.35126983
47.542319	2	-18.88644172	-16.92031444	-19.08982183
76.35549	1	-20.03701375	-17.91253929	

RSA9

Mid Interval	Number of crystals	Ln(n)	Max Ln(n)	Min Ln(n)
1.488207303	6	-13.86135595	-12.35475679	-14.50094039
2.120929478	81	-11.71609111	-10.44647802	-12.76256066
3.202540563	229	-11.13424311	-9.906000419	-12.2301292
4.979173814	268	-11.43440298	-10.2108587	-12.53562553
7.799802916	211	-12.13095668	-10.90012749	-13.22388205
12.0264014	97	-13.36552868	-12.10457179	-14.42271416
18.4285751	29	-15.03036867	-13.69578671	-15.98920055
30.94315873	11	-16.45719408	-15.02941534	-17.26261031
53.36228667	3	-18.21390191	-16.59390294	-18.51694299

RSA10

Mid Interval	Number of crystals	Ln(n)	Max Ln(n)	Min Ln(n)
1.435440719	58	-9.462220416	-8.6193941	-10.56918467
2.077862018	355	-8.107970484	-7.193485038	-9.128704747
3.154089913	516	-8.191406355	-7.268288023	-9.20262672
4.861498839	351	-9.034151744	-8.119952621	-10.05520452
7.599192244	151	-10.33508298	-9.447120497	-11.38616387
11.85132754	58	-11.74934465	-10.90651833	-12.85630891
19.0682631	25	-13.04833668	-12.26445882	-14.23767965
31.16234194	7	-14.77872721	-14.13313518	-16.21968469
	0			
64.435936	1			

RSA11

Mid Interval	Number of crystals	Ln(n)	Max Ln(n)	Min Ln(n)
1.45822234	6	-13.64960211	-12.35475679	-14.0774327
2.135455804	82	-11.49206718	-10.43481974	-12.32754712
3.25552708	264	-10.78026217	-9.768037337	-11.66923974
4.978934761	304	-11.09660842	-10.08834018	-11.99004276
7.815516599	219	-11.88198924	-10.86410196	-12.76452277
11.80469716	90	-13.22867614	-12.17596177	-14.06978595
19.25289899	38	-14.5483245	-13.44549257	-15.3238218
28.45942586	14	-16.00427818	-14.81492137	-16.64581087
48.63082067	3	-18.00214807	-16.59390294	-18.0934353
75.820147	4	-18.17189084	-16.813927	-18.4312424

RSA12

Mid Interval	Number of crystals	Ln(n)	Max Ln(n)	Min Ln(n)
1.42090704	42	-13.03885504	-10.60769622	-15.1589223
2.112984714	320	-11.46562851	-9.123571601	-13.69576534
3.234176901	717	-11.11629851	-8.791971472	-13.36589943
4.960783388	839	-11.41658849	-9.09498542	-13.66911644
7.776720857	599	-12.21096245	-9.883254402	-14.45690719
12.19558072	281	-13.42529422	-11.07968903	-15.65144759
19.31057757	114	-14.78487529	-12.4076849	-16.9741979
29.89966024	25	-16.75962276	-14.28963939	-18.82414102
44.739795	6	-18.64416396	-16.01415556	-20.40715764
84.199104	1	-20.89334828	-17.91253929	

RSA13

Mid Interval	Number of crystals	Ln(n)	Max Ln(n)	Min Ln(n)
1.447827432	30	-9.673441322	-8.426910759	-11.28926059
2.095780299	146	-8.548456929	-7.213746671	-10.04906783
3.135174902	216	-8.61420999	-7.265812338	-10.098901
4.874195374	152	-9.423032724	-8.086797534	-10.9218465
7.684308197	61	-10.79346423	-9.499718937	-12.34469652
12.02956718	23	-12.22626872	-11.00143643	-13.87433647
21.0094531	4	-14.43289342	-13.42413439	-16.54026474
30.6444534	2	-15.58346545	-14.70404131	-18.22563677
57.083336	1	-16.73403748	-16.01296052	
80.265948	1	-17.19146233	-16.47038537	

Figure S2. CSD plots from 3D measurements per sample (Next page).

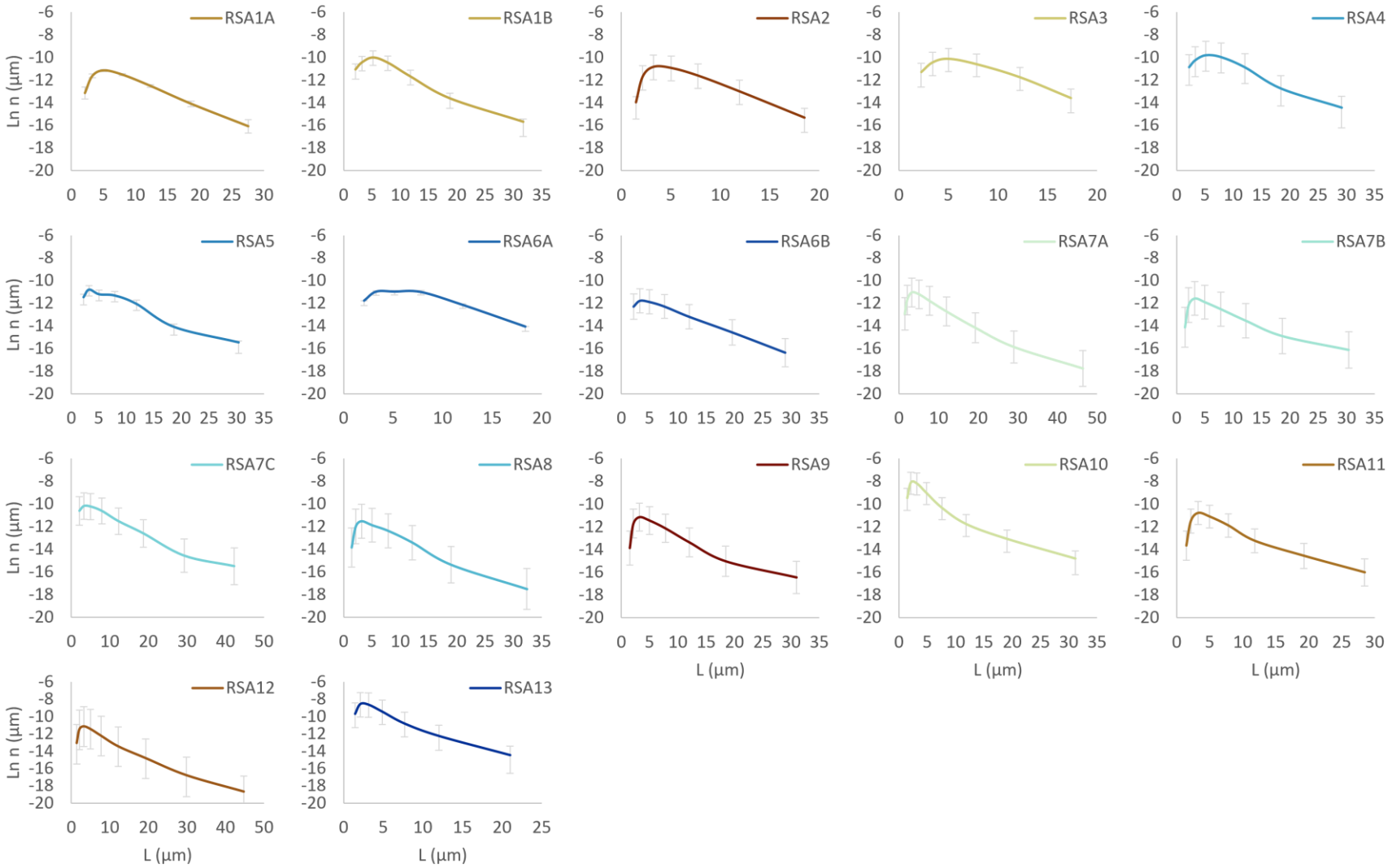

Table S14. Slope calculation for the range 5 - 30 µm compared to the slopes calculated for the range 10 - 20 µm.

	$Slope_{5 - 30\ \mu m}$				$Slope_{10 - 20\ \mu m}$				
Sample	Slope	Error	Intercept	R2	Sample	Slope	Error	Intercept	R2	Δslope
RSA1A	-0.22	0.007	-10.01	1.00	RSA1A	-0.20	0.003	-9.59	1.00	0.02
RSA1B	-0.22	0.014	-9.07	0.98	RSA1B	-0.28	0.004	-8.29	1.00	0.06
RSA2	-0.31	0.009	-9.44	1.00	RSA2	-0.35	0.007	-8.86	1.00	0.04
RSA3	-0.35	0.017	-8.03	0.99	RSA3	-0.33	0.048	-7.97	0.98	0.01
RSA4	-0.20	0.014	-8.79	0.98	RSA4	-0.28	0.009	-7.69	1.00	0.08
RSA5	-0.18	0.018	-10.22	0.96	RSA5	-0.28	0.017	-8.86	1.00	0.10
RSA6A	-0.21	0.017	-9.89	0.97	RSA6A	-0.30	0.006	-8.61	1.00	0.09
RSA6B	-0.19	0.002	-10.93	1.00	RSA6B	-0.19	0.014	-10.94	0.99	0.00
RSA7A	-0.19	0.005	-10.34	1.00	RSA7A	-0.20	0.002	-10.27	1.00	0.01
RSA7B	-0.17	0.015	-11.28	0.97	RSA7B	-0.21	0.030	-10.79	0.98	0.04
RSA7C	-0.18	0.003	-9.33	1.00	RSA7C	-0.18	0.017	-9.34	0.99	0.00
RSA8	-0.22	0.013	-10.85	0.99	RSA8	-0.28	0.019	-10.07	1.00	0.06
RSA9	-0.20	0.020	-10.72	0.96	RSA9	-0.27	0.043	-9.98	0.97	0.06
RSA10	-0.21	0.021	-8.51	0.96	RSA10	-0.21	0.066	-8.86	0.91	0.01
RSA11	-0.20	0.012	-10.39	0.99	RSA11	-0.21	0.018	-10.51	0.99	0.00
RSA12	-0.21	0.007	-10.22	1.00	RSA12	-0.21	0.010	-8.86	1.00	0.00
RSA13	-0.24	0.024	-8.77	0.96	RSA13	-0.26	0.072	-8.72	0.93	0.02

Δslope represents the difference between the slopes calculated, i.e., Δslope = slope5 - 30 µm - slope10 - 20 µm

Appendix 3 Geochemical and thermodynamic modelling data

Repositories

The geochemical data for whole rock, groundmass and crystals data that supports the findings in this thesis is available in the FAIR data repository EarthChem Library at: doi:10.60520/IEDA/113914.

The hygrothermobarometry and crystal-melt equilibrium data per individual crystals analysed is available at: https://doi.org/10.6084/m9.figshare.30906779

Crystal-Melt equilibrium

Table S15. Representative groundmass compositions used for crystal-melt equilibrium determination, and hygrothermobarometry calculations.

Sample	Raster ID	Year of collection	SiO_2 wt%	TiO_2 wt%	Al_2O_3 wt%	FeO^T wt%	MnO wt%	MgO wt%	CaO wt%	Na_2O wt%	K_2O wt%	P_2O_5 wt%	Cr_2O_3 wt%	Total
RSA1A	RSA1A_GM-7	2024	62.95	0.94	15.62	6.13	0.11	2.64	5.13	4.04	2.25	0.19	0.00	100.00
RSA1B	RSA1B_GM - 4	2025	62.70	0.97	15.88	6.14	0.10	2.61	5.16	4.02	2.22	0.19	0.00	100.00
RSA2	RSA2_GM-8	2024	69.72	0.78	14.05	3.90	0.06	0.83	2.89	4.03	3.58	0.17	0.00	100.00
RSA3	RSA3_GM - 4	2025	62.55	0.95	15.79	6.22	0.11	2.65	5.21	3.97	2.34	0.20	0.00	100.00
RSA4	RSA4_GM-1	2024	63.08	0.93	15.57	5.93	0.10	2.74	5.56	3.69	2.20	0.18	0.00	100.00
RSA5	RSA5_GM - 5	2025	62.53	0.95	16.77	5.42	0.09	2.18	5.83	3.83	2.22	0.18	0.00	100.00
RSA6A	RSA6A_GM - 4	2025	62.18	0.95	16.23	6.01	0.11	2.70	5.71	3.77	2.18	0.17	0.00	100.00
RSA6B	RSA6B_GM - 1	2025	63.05	1.00	15.26	6.25	0.11	2.90	5.31	3.67	2.27	0.19	0.00	100.00
RSA7A	RSA7A_GM - 1	2025	62.68	1.03	15.49	6.43	0.11	2.58	5.12	3.93	2.42	0.20	0.00	100.00
RSA7B	RSA7B_GM - 6	2025	62.66	0.91	16.09	5.81	0.11	2.53	5.41	3.93	2.34	0.20	0.00	100.00
RSA7C	RSA7C_GM - 6	2025	62.51	0.99	15.11	6.74	0.12	3.15	5.09	3.77	2.33	0.20	0.00	100.00
RSA8	RSA8_GM-4	2024	62.79	0.99	15.33	6.49	0.11	2.72	5.19	3.81	2.36	0.20	0.00	100.00
RSA9	RSA9_GM - 5	2025	69.85	0.82	14.21	3.79	0.06	0.81	2.53	4.03	3.72	0.17	0.00	100.00
RSA10	RSA10_GM - 2	2025	63.07	0.97	15.92	5.95	0.10	2.39	5.12	3.98	2.30	0.19	0.00	100.00
RSA11	RSA11_GM - 8	2025	65.52	1.08	15.04	5.29	0.09	1.64	4.28	3.70	3.12	0.24	0.00	100.00
RSA12	RSA12_GM - 7	2025	67.61	0.82	15.37	3.90	0.07	1.13	3.60	4.36	2.96	0.18	0.00	100.00
RSA13	RSA13_GM - 6	2025	62.11	1.06	16.47	5.52	0.09	2.39	5.83	3.88	2.44	0.21	0.00	100.00

[T] Fe expressed as FeO.

Melts Modelling

Table S16. Representative groundmass compositions used for MELTS modelling.

Sample	SiO_2	TiO_2	Al_2O_3	Fe_2O_3	Cr_2O_3	FeO	MgO	MnO	CaO	Na_2O	K_2O	P_2O_5
RSA1A	63.36	0.98	15.61	2.23	0.00	3.42	2.38	0.10	4.92	4.08	2.34	0.20
RSA1B	63.09	1.02	15.53	2.30	0.00	3.55	2.51	0.11	4.90	4.04	2.35	0.20
RSA2	70.23	0.73	14.01	1.50	0.00	1.91	0.79	0.06	2.68	4.02	3.70	0.15
RSA3	63.30	0.99	15.20	2.33	0.00	3.58	2.65	0.11	4.82	3.96	2.46	0.21
RSA4	63.29	0.95	15.58	2.12	0.00	3.40	2.50	0.10	5.44	3.77	2.27	0.19
RSA5	63.31	1.00	16.24	1.97	0.00	3.07	2.05	0.09	5.47	3.89	2.38	0.19
RSA6A	63.25	0.99	15.82	2.07	0.00	3.28	2.33	0.10	5.46	3.82	2.34	0.19
RSA6B	63.69	0.98	16.37	1.88	0.00	2.92	1.81	0.08	5.43	3.92	2.38	0.20
RSA7A	63.36	0.90	16.61	1.88	0.00	2.84	1.93	0.09	5.31	4.17	2.39	0.20
RSA7B	63.62	0.90	16.68	1.80	0.00	2.69	1.66	0.08	5.42	4.12	2.51	0.21
RSA7C	64.06	0.97	14.88	2.22	0.00	3.36	2.69	0.11	4.63	3.82	2.66	0.23
RSA8	63.88	0.95	14.37	2.40	0.00	3.72	2.91	0.12	4.74	3.75	2.54	0.22
RSA9	71.35	0.59	13.88	1.30	0.00	1.58	0.65	0.05	2.26	3.90	4.15	0.12
RSA10	63.74	0.98	15.35	2.23	0.00	3.40	2.30	0.10	4.88	4.03	2.40	0.21
RSA11	65.97	1.11	14.42	2.12	0.00	3.04	1.83	0.09	3.98	3.61	3.24	0.24
RSA12	68.27	0.81	15.08	1.52	0.00	2.04	1.09	0.07	3.36	4.32	3.04	0.17
RSA13	62.70	1.13	15.35	2.21	0.00	3.40	2.73	0.10	5.34	3.82	2.62	0.23

Table S17. Representative average compositions from Ruapehu Group units and Waimarino and Kakuki basalts used for MELTS modelling.

Unit	SiO_2	TiO_2	Al_2O_3	Fe_2O_3	Cr_2O_3	FeO	MgO	MnO	CaO	Na_2O	K_2O	P_2O_5
Mangaehuehu Member (Conway, 2016)	59.94	0.73	14.90	2.16	0.04	3.97	6.05	0.11	6.51	3.15	1.88	0.16
Makotuku Member (Conway, 2016)	60.92	0.79	17.47	2.12	0.00	3.61	2.67	0.09	6.12	3.73	1.92	0.16
Waitonga Member (Conway, 2016)	62.06	0.69	16.18	2.02	0.01	3.47	3.63	0.10	5.79	3.50	2.02	0.16
Whakapapaiti Member (Conway, 2016)	64.99	0.63	15.46	1.73	0.02	2.83	3.36	0.08	4.70	3.70	2.07	0.14
Turoa Member (Conway, 2016)	58.99	0.73	16.77	2.33	0.00	4.35	4.24	0.11	6.89	3.31	1.65	0.14
Waimarino Basalt (Hackett, 1985)	52.18	0.47	12.68	1.96	0.00	6.58	13.15	0.16	9.60	1.64	0.43	0.05
Kakuki Basalt (Gamble et al., 1993)	48.52	0.89	18.09	1.05	0.00	6.99	9.12	0.13	11.16	2.49	0.27	0.14

Appendix 4 Crystal Mapping

Crystal mapping

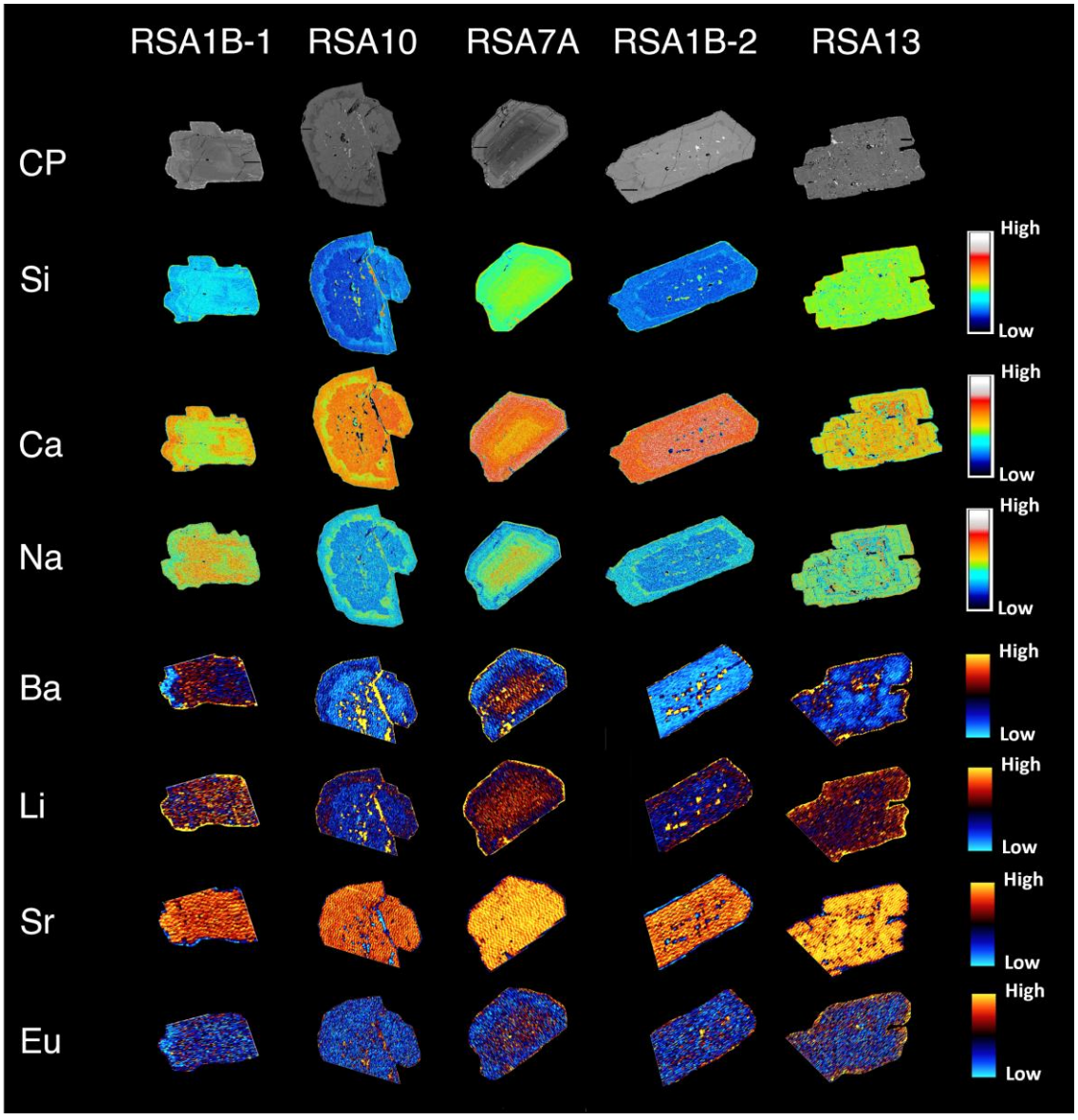

Figure S3. Plagioclase mapping. The calibration bars on the left indicates variations of the elements on the right within the crystal, however, do not indicate the elements content. CP: Backscatter electron composite image - EPMA. Si, Na and Ca from EPMA mapping. Ba, Li, Sr and Eu from LA-ICP-MS mapping.

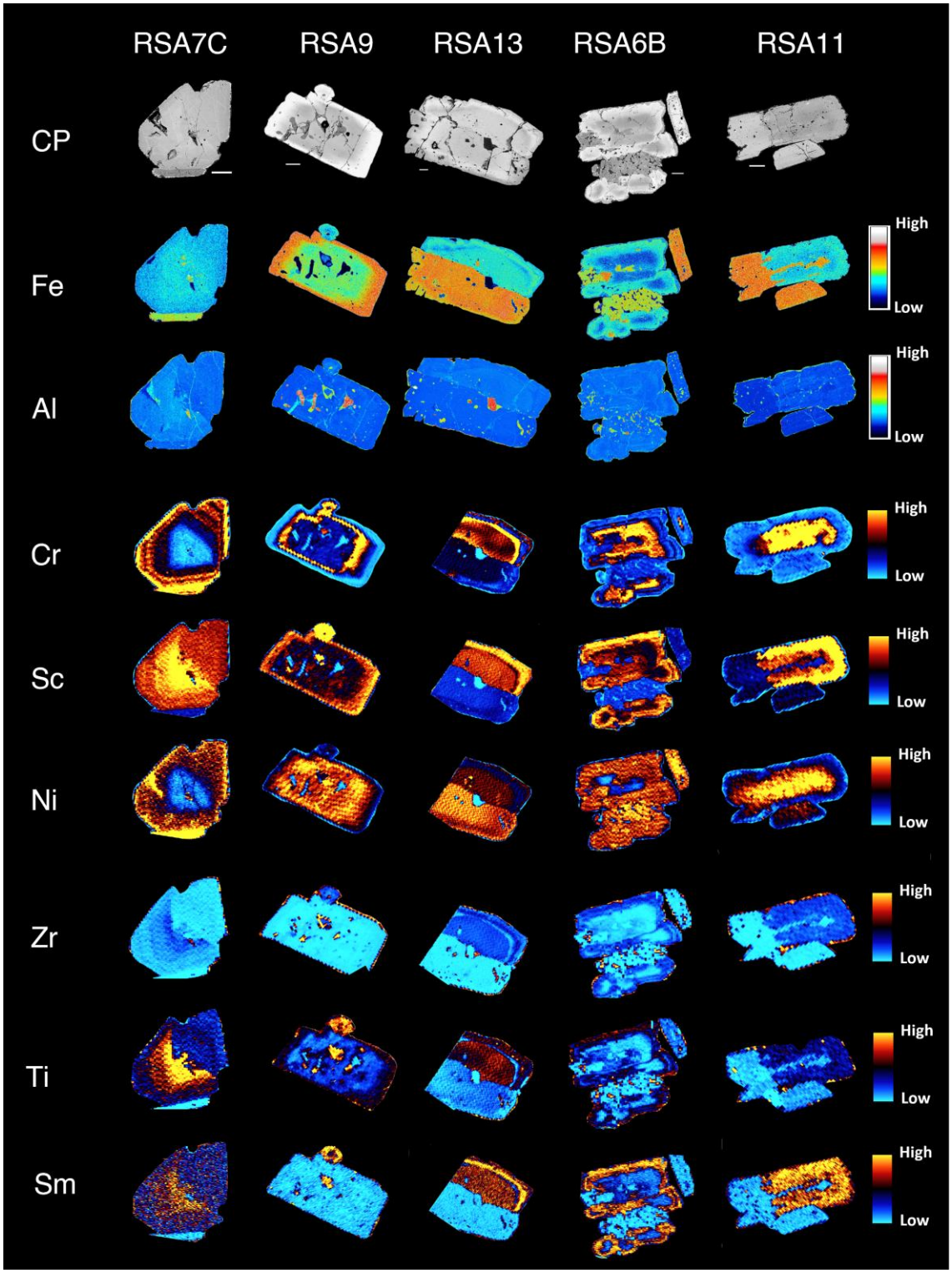

Figure S4. Pyroxene mapping. The calibration bars on the left indicates variations of the elements on the right within the crystal, however, do not indicate the elements content. CP: Backscatter electron composite image – EPMA Fe and Al from EPMA mapping. Cr, Sc, Ni, Zr, Ti and Sm from LA-ICP-MS mapping.

Element profiles

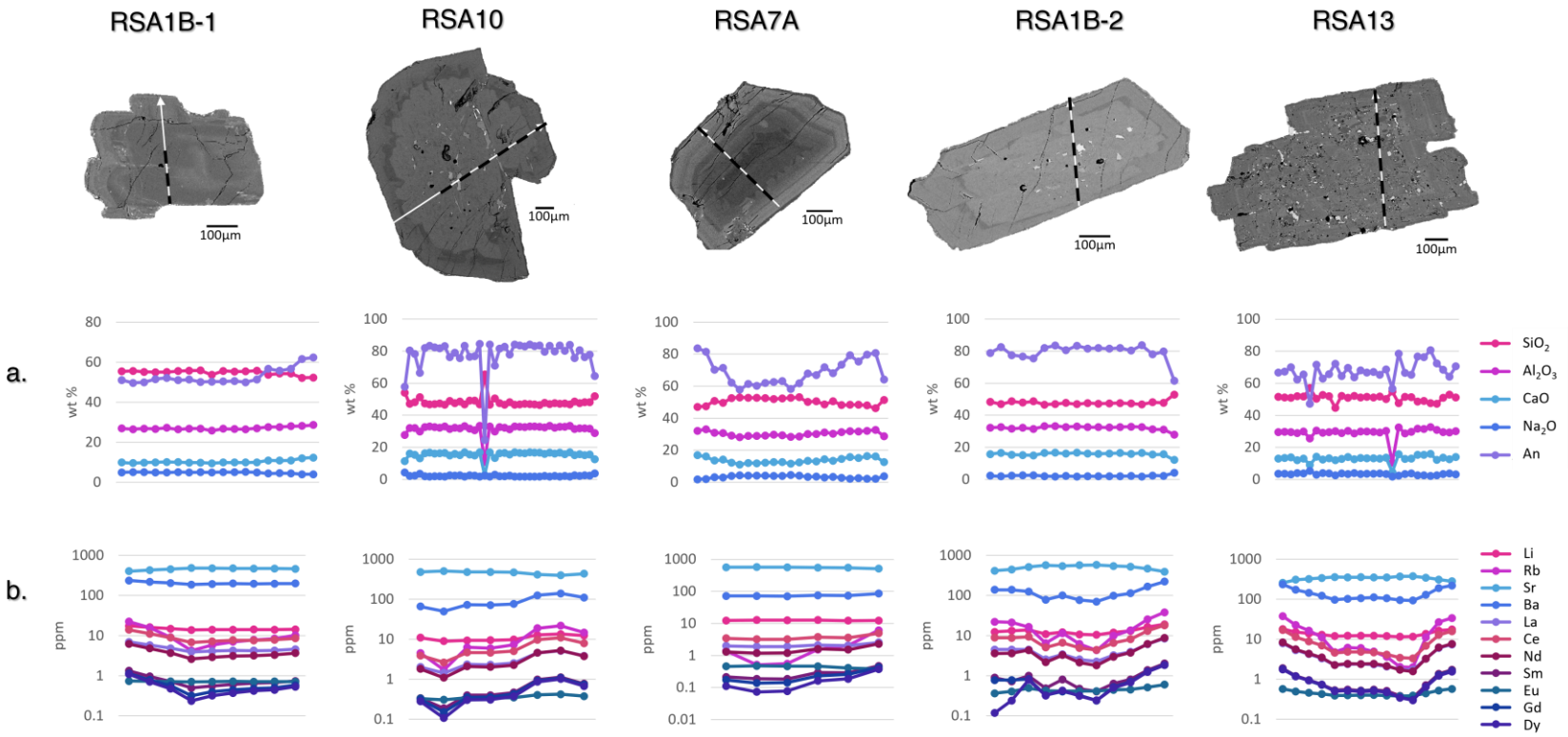

Figure S5. Compositional profiles of plagioclase per element. a. Major elements oxides profile lines from EPMA data. b. Trace elements profile lines from LA-ICPMS data. Each line represents the measurements of major oxides (a), An (a) and trace elements (b) alongside the profile. On top are the images of the crystals used in Figure 6.11. The arrow indicates the direction and trajectory of the profile line. The dashed line indicates the length of the profile for the trace elements.

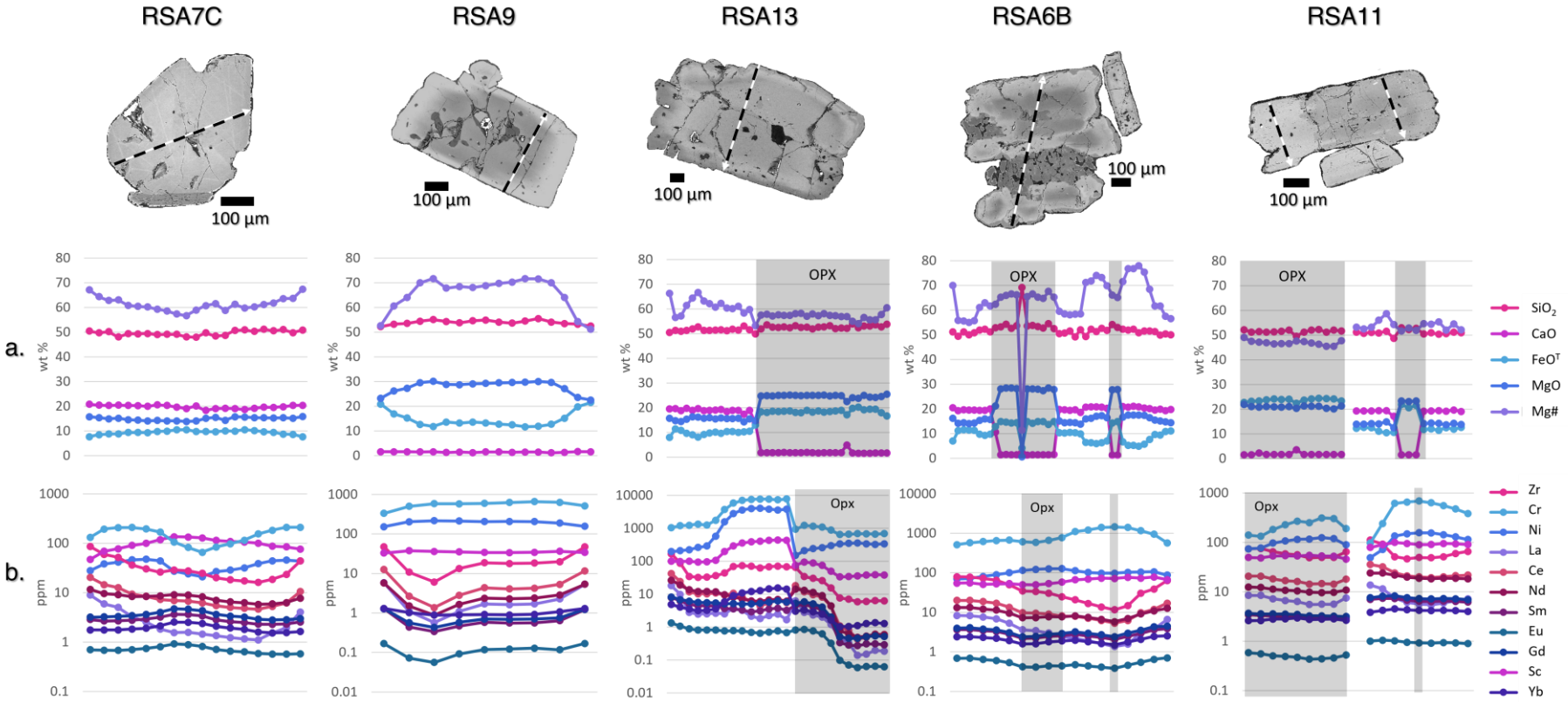

Figure S6. Compositional profiles of pyroxene per element. a. Major elements oxides profile lines from EPMA data. b. Trace elements profile lines from LA-ICPMS data. Each line represents the measurements of major oxides (a), Mg# (a) and trace elements (b) alongside the profile. On top are the images of the crystals used in Figure 6.12. The arrow indicates the direction and trajectory of the profile line. The dashed line indicates the length of the profile for the trace elements. For the glomerocrysts the part of the profile related to orthopyroxene (OPX) is highlighted in grey. For sample RSA11 two profiles were measured one in the clinopyroxene part (right) and another in the orthopyroxene part (left) of the crystal.

Appendix 5 Statements of Contribution

MASSEY UNIVERSITY
TE KUNENGA KI PŪREHUROA
UNIVERSITY OF NEW ZEALAND

GRADUATE RESEARCH SCHOOL

STATEMENT OF CONTRIBUTION
DOCTORATE WITH PUBLICATIONS/MANUSCRIPTS

We, the student and the student's main supervisor, certify that all co-authors have consented to their work being included in the thesis and they have accepted the student's contribution as indicated below in the Statement of Originality.

Student name:	Silvia Catalina Moreno Alfonso
Name and title of main supervisor:	Stuart Mead, Senior Lecturer
In which chapter is the manuscript/published work?	Chapter 4

Describe the contribution that the student and members of the supervisory team have made to the manuscript/published work:[1]

Silvia Moreno Alfonso: conceptualization, methodology, data collection, curation, visualization and analysis, writing original draft, review and editing.
Satoshi Okumura: writing review and editing, supervision
Stuart Mead: writing review and editing, supervision
Georg Zellmer: supervision, funding acquisition
Yoshiyuki Iizuka, Masahiro Yasutake, Kentaro Uesugi, Akira Miyake: data collection

Please select one of the following three options:

- ○ **The manuscript/published work is published or in press**
  Please provide the full reference of the research output:

- ◉ **The manuscript is currently under review for publication**
  Please provide the name of the journal:
  American Mineralogist

- ○ **It is intended that the manuscript will be published, but it has not yet been submitted to a journal**

Student's signature:	Silvia Catalina Moreno Alfonso Digitally signed by Silvia Catalina Moreno Alfonso DN: cn=Silvia Catalina Moreno Alfonso, email=s.morenoalfonso@massey.ac.nz Date: 2025.12.16 12:19:29 +13'00'	Main supervisor's signature:	Stuart Mead Digitally signed by Stuart Mead Date: 2025.12.18 15:01:26 +13'00'

This form should be placed at the beginning of each relevant thesis chapter.

[1] Refer to the Massey University Publishing and Authorship guidelines (OneMassey for staff, Stream for students) and/ or Contributor Roles Taxonomy (CRediT) guidelines for guidance.

MASSEY UNIVERSITY
TE KUNENGA KI PŪREHUROA
UNIVERSITY OF NEW ZEALAND

GRADUATE RESEARCH SCHOOL

STATEMENT OF CONTRIBUTION
DOCTORATE WITH PUBLICATIONS/MANUSCRIPTS

We, the student and the student's main supervisor, certify that all co-authors have consented to their work being included in the thesis and they have accepted the student's contribution as indicated below in the Statement of Originality.	
Student name:	Silvia Catalina Moreno Alfonso
Name and title of main supervisor:	Stuart Mead, Senior Lecturer
In which chapter is the manuscript/published work?	Chapter 5

Describe the contribution that the student and members of the supervisory team have made to the manuscript/published work:[1]

Silvia Moreno Alfonso: conceptualization, methodology, investigation, data collection, curation, visualization and analysis, writing original draft, review and editing.
Satoshi Okumura, Geoff Kilgour, Teresa Ubide: writing review and editing, supervision
Georg Zellmer: writing review and editing, supervision, funding acquisition
Stuart Mead: Supervision
Yoshiyuki Iizuka, Masahiro Yasutake, Kentaro Uesugi, Yujin Jegal: data collection

Please select one of the following three options:

○	**The manuscript/published work is published or in press** Please provide the full reference of the research output:
◉	**The manuscript is currently under review for publication** Please provide the name of the journal: Journal of Petrology
○	**It is intended that the manuscript will be published, but it has not yet been submitted to a journal**

Student's signature:	Silvia Catalina Moreno Alfonso Digitally signed by Silvia Catalina Moreno Alfonso DN: cn=Silvia Catalina Moreno Alfonso, email=s.morenoalfonso@massey.ac.nz Date: 2025.12.16 12:23:30 +13'00'	Main supervisor's signature:	Stuart Mead Digitally signed by Stuart Mead Date: 2025.12.18 15:01:43 +13'00'

This form should be placed at the beginning of each relevant thesis chapter.

[1] Refer to the Massey University Publishing and Authorship guidelines (OneMassey for staff, Stream for students) and/ or Contributor Roles Taxonomy (CRediT) guidelines for guidance.

MASSEY UNIVERSITY
TE KUNENGA KI PŪREHUROA
UNIVERSITY OF NEW ZEALAND

GRADUATE RESEARCH SCHOOL

STATEMENT OF CONTRIBUTION
DOCTORATE WITH PUBLICATIONS/MANUSCRIPTS

We, the student and the student's main supervisor, certify that all co-authors have consented to their work being included in the thesis and they have accepted the student's contribution as indicated below in the Statement of Originality.	
Student name:	Silvia Catalina Moreno Alfonso
Name and title of main supervisor:	Stuart Mead, Senior Lecturer
In which chapter is the manuscript/published work?	Chapter 6

Describe the contribution that the student and members of the supervisory team have made to the manuscript/published work:[1]

Silvia Moreno Alfonso: conceptualization, methodology, investigation, data collection, curation, visualization and analysis, writing original draft, review and editing.
Satoshi Okumura, Geoff Kilgour, Teresa Ubide: writing review and editing, supervision
Georg Zellmer: writing review and editing, supervision, funding acquisition
Stuart Mead: Supervision
Yoshiyuki Iizuka: data collection

Please select one of the following three options:

○	**The manuscript/published work is published or in press** Please provide the full reference of the research output:
○	**The manuscript is currently under review for publication** Please provide the name of the journal:
◉	**It is intended that the manuscript will be published, but it has not yet been submitted to a journal**

Student's signature:	Silvia Catalina Moreno Alfonso Digitally signed by Silvia Catalina Moreno Alfonso DN: cn=Silvia Catalina Moreno Alfonso, email=s.morenoalfonso@massey.ac.nz Date: 2025.12.16 12:32:47 +13'00'	Main supervisor's signature:	Stuart Mead Digitally signed by Stuart Mead Date: 2025.12.18 15:02:00 +13'00'

This form should be placed at the beginning of each relevant thesis chapter.

[1] Refer to the Massey University Publishing and Authorship guidelines (OneMassey for staff, Stream for students) and/ or Contributor Roles Taxonomy (CRediT) guidelines for guidance.